A new physically motivated thermoviscoelastic model for filled elastomers

Dissertation

zur Erlangung des akademischen Grades

Doktoringenieur
(Dr.-Ing.)

von M.Sc. Rathan Raghunath
geb. am 27.08.1985 in Sakaleshpur, Indien

genehmigt durch die Fakultät für Maschinenbau
der Otto-von-Guericke-Universität Magdeburg

Gutachter:

Jun.-Prof.Dr.-Ing. Daniel Juhre
Institut für Mechanik (IFME)
Otto-von-Guericke-Universität, Magdeburg

Prof. Dr.-Ing. Markus Böl
Institut für Festkörpermechanik (IFM)
Technische Universität, Braunschweig

Prof. Dr. habil. Manfred Klüppel
Abteilung Materialkonzepte und Modellierung (MM)
Deutsches Institut für Kautschuktechnologie e.V., Hannover

Promotionskolloquium am: 07.12.2017

This work was carried out in the department of simulation and continuum mechanics at the Deutsches Institut für Kautschuktechnologie e.V. (DIK), Hannover, Germany in association with Goodyear Innovation Center (GIC*L), Luxembourg and Fonds National de la Recherche (FNR), Luxembourg.

Acknowledgement

Foremost, I would like to express my sincere gratitude to my supervisor Jun.-Prof.Dr.-Ing. Daniel Juhre and Prof. Dr. habil. Manfred Klüppel for the continuous support to my doctoral thesis. Their guidance and knowledge sharing helped me throughout the time of work and writing this thesis.

Besides my supervisors and DIK, I would like to thank GIC*L and FNR, Luxembourg for offering this project and providing financial support. My special thanks goes to Dr. Stephan Westermann, Dr. Benoit Duez, Dr. Frank Petry of GIC*L for the encouragement, knowledge sharing and cooperation, which were essential for the success of this doctoral thesis. I also thank Mr. Tom Jakobs, the administrative assistant of FNR for helping with the administrative tasks of AFR grant program.

My sincere thanks also goes to Dr. Nils Kröger of DIK, Hannover and Prof. Dr.-Ing. Markus Böl for their necessary guidance. I would like to thank all the colleagues of DIK, especially Abdulghani, Abhiram Sarmukaddam, Andrej Lang, Anuj Jain, Dirk Schellenberg, Fares Hussein, Hamid El Manaaoui, Joachim Heier, Jürgen Hamann, Kevin Krause, Mohammed El-Yaagoubi, Monika Gille, Peter Erren, Sahbi Aloui, Sam Al-Afif and Tatiana Dilman and Niels Goldberg of TU Chemnitz for the support in conducting experiments, technical discussions, model implementation and simulations, etc.

Last but not the least, I would like to thank all those who are responsible for making this thesis a success.

Contents

Nomenclature and abbreviation

Abbreviation

CB	**C**arbon **B**lack
DFM	**D**ynamic **F**locculation **M**odel
DMA	**D**ynamic **M**echanical **A**nalysis
DSC	**D**ifferential **S**canning **C**alorimetry
FEM	**F**inite **E**lement **M**ethod
MD	**M**olecular **D**ynamics
NMR	**N**uclear **M**agnetic **R**esonance
NR	**N**atural **R**ubber
TEM	**T**ransmission **E**lectron **M**icroscopy

Scalar

α_T	Coefficient of thermal expansion $[K^{-1}]$
C_{10}	Material parameter $[MPa]$
C_p	Mass heat capacity $[J/(tonne\,K)]$
$\mathscr{D}_{int}$	Internal dissipation $[W/mm^3]$
$\mathscr{D}^m$	Mechanical dissipation $[W/mm^3]$
E_a	Activation energy $[J/mol]$
E_d, E_v	Activation energies of damaged and virgin clusters bonds $[J/mol]$
E_{diss}	Energy dissipation $[N-mm]$
f	Frequency $[Hz]$
G_0, G_∞	Small and large strain moduli $[MPa]$
G', G''	Storage and loss moduli $[MPa]$
G_c	Cross-link modulus $[MPa]$
G_e	Entanglement modulus $[MPa]$
η_d, η_v	Material parameters refer to coefficient of viscosity $[Pa^N \cdot s]$
θ, θ_s, θ_{amb}, θ_{ref}	Absolute, surface, ambient and reference temperatures $[K]$
θ_g	Glass transition temperature $[K]$
I_1, I_2, I_3	Principal invariants of deformation $[-]$
J	Jacobian (determinant of $\mathbf{F}$) $[-]$
$\dot{J}$	Jacobian rate $[s^{-1}]$
κ	Heat conductivity $[W/(mm\,K)]$
K_{mod}	Compression modulus $[MPa]$
k_{stat}	Static heat exchange coefficient $[W/(mm^2\,K)]$

k_{conv}	Convective heat exchange coefficient $[W\,s/(mm^3\,K)]$
μ	Material parameter (Zener model) $[MPa]$
n	Number of chain segments $[-]$
N_d, N_v	Material parameters refer to exponent $[-]$
n_e	Number of segments $[-]$
ρ	Density $[tonne/mm^3]$
p_v	Volumetric/hydrostatic pressure $[MPa]$
ς	Thermal diffusivity $[mm^2/s]$
R	Universal gas constant $[J/(K\,mol)]$
s_d, s_v	Strengths of cluster bonds $[MPa]$
$s_{d,eq}$, $s_{v,eq}$	Equilibrium strengths of cluster bonds $[MPa]$
$s_{d,ref}$, $s_{v,ref}$	reference strengths of cluster bonds $[MPa]$
$s_{d,t}$, $s_{v,t}$	Time dependent strengths of cluster bonds $[MPa]$
t	time $[s]$
T_e	Langley trapping factor $[-]$
τ	Relaxation time (Zener model) $[s]$
τ_d, τ_v	Material parameters refer to relaxation times of clusters bonds $[Pa^{N-1} \cdot s]$
W	Strain-energy density $[J/mm^3]$
W_R, W_A	Rubber and filler cluster strain-energy densities $[J/mm^3]$
$\mathscr{W}_{int}$	Internal stress power $[W/mm^3]$
U	Internal thermal energy per unit mass $[J/tonne]$
v	Test velocity $[mm/min]$
X	Amplification factor $[-]$
$T_{set,0}$	Material parameter for set stress $[MPa]$
Υ	Entropy $[J/(mm^3\,K)]$
Φ_{eff}	Effective filler volume fraction $[-]$
χ_0	Average cluster size $[-]$
Ψ	Helmholtz free energy $[J/mm^3]$

Vector

$\boldsymbol{\lambda}$	Principal stretch ratio $[-]$
$\mathbf{X}$	Undeformed position $[mm]$
$\mathbf{x}$	Deformed position $[mm]$
$\mathbf{Q}$, $\mathbf{q}$	Piola-Kirchhoff and Cauchy heat fluxes $[W/mm^2]$
$\mathbf{u}$	Displacement $[mm]$
$\dot{\mathbf{u}}$	Velocity $[mm/s]$

Tensor

$\mathbf{b}$	Left Cauchy-Green deformation $[-]$
$\mathbf{C}$	Right Cauchy-Green deformation $[-]$
$\dot{\mathbf{C}}$	Right Cauchy-Green deformation rate $[s^{-1}]$
$\mathbf{d}$	Symmetric part of deformation rate $[s^{-1}]$
$\mathbf{E}$	Green-Lagrange strain $[-]$
$\dot{\mathbf{E}}$	Green-Lagrange strain rate $[s^{-1}]$

$\mathbf{e}$	Almansi strain [–]
$\boldsymbol{\varepsilon}$	Engineering/nominal strain [–]
$\boldsymbol{\varepsilon}^H$	Hencky or logarithmic strain [–]
$\mathbf{F}$	Deformation gradient [–]
$\mathbb{K}^{Lag}$, $\mathbb{K}^{Eul}$	4^{th} order Lagrangian and Eulerian material tangents $[MPa]$
$\mathbf{l}$	Spatial velocity $[s^{-1}]$
$\boldsymbol{\sigma}$	Cauchy stress $[MPa]$
$\mathbf{T}$	1^{st} Piola-Kirchhoff stress $[MPa]$
$\tilde{\mathbf{T}}$	2^{nd} Piola-Kirchoff stress $[MPa]$

Abaqus symbols

$DDSDDE$	Mechanical material tangent $[MPa]$
$DDSDDT$	dSigma/dTEMP $[MPa/K]$
$DFLUX$	Subroutine for user defined surface flux boundary condition
RPL	Volumetric heat generation per unit time $[W/mm^3]$
$UMAT$	Subroutine for user defined mechanical material laws
$UMATHT$	Subroutine for user defined thermal material laws

Abstract

The Dynamic Flocculation Model (DFM) is a micro-structure based model of rubber reinforcement which is developed on a physical framework to describe the non-linear and inelastic mechanical behaviour of filled elastomers [Klüppel, 2003]. This one-dimensional material law has been implemented into the finite element code using the concept of representative directions [Freund et al., 2011], which allows the generalization of one-dimensional model to compute three dimensional stress-strain states. The model shows very good agreement with the standard quasi-static multi-hysteresis tests on CB-filled elastomers like NR, SBR or EPDM. An extension of this model to include time dependent effects allows to consider the filler induced dynamic response such as strain rate dependency, amplitude dependency and stress relaxation. The physical hypothesis of characterizing the filler clusters as time-dependent parameters is described in Juhre et al. [2013] and Raghunath et al. [2016]. In this work contribution, the quasi-static DFM model was extended to include the time-dependent effects using first-order differential relaxation equation which evolves as a function of time. Subsequently, the corresponding parameters were identified through curve fitting and the model was further validated against associated experiments. The influence of each parameter on the course of change in material behaviour has been investigated. The major advantage of the model is its physically meaningful parameters and the ability to reproduce the material response at different loading rates under arbitrary deformation using the single parameter set for each rubber compound. The Grosch wheel simulations with static and dynamic loading cases were done to analyse the foot print lengths and reaction displacements/velocities, respectively. A further extension of DFM was considered to include temperature effects on the mechanical behaviour. Model prediction was substantiated by temperature controlled experiments. The potential to couple thermo-mechanical quantities of DFM is presented. The implementation of thermo-viscoelastic model in FE program is described. At the end of the work, the temperature-displacement simulation using Zener model and a subsequent analytical simulation along with dynamic cyclic loading experiment was carried out to estimate the evolution of inner and surface temperatures due to self-heating of rubber component.

Keywords

Filled elastomer, inelasticity, stress relaxation, strain-rate dependency, amplitude dependency, representative directions, self-heating, thermo-mechanical coupling

Zusammenfassung

Das Dynamische Flockulationsmodell (DFM) ist ein mikrostrukturbasiertes Modell der Kautschukverstärkung, das auf einem physikalischen Rahmen entwickelt wird, um das nichtlineare und inelastische mechanische Verhalten von Elastomeren zu beschreiben [Klüppel, 2003]. Dieses eindimensionale Materialgesetz wurde in der finite-Elemente-Code mit dem Konzept der repräsentativen Richtungen umgesetzt [Freund et al., 2011], die die Berechnung der dreidimensionalen Spannungs-Dehnungszustände aus dem eindimensionalen Stoffgesetz ermöglicht. Das Modell zeigt eine sehr gute Übereinstimmung mit den standardmäßigen quasi-statischen Multihysterese-Versuchen an rußgefüllten Elastomeren wie NR, SBR oder EPDM. Die Erweiterung dieses Modells durch Einbeziehung zeitabhängiger Effekte ermöglicht die Berücksichtigung von füllstoffinduzierten dynamischen Antworten wie die Dehnungsratenabhängigkeit, die Amplitudenabhängigkeit und die Spannungsrelaxation. Die physikalische Hypothese der Charakterisierung der Füllstoffcluster als zeitabhängige Parameter ist in Juhre et al. [2013] und Raghunath et al. [2016] beschrieben. In dieser Arbeit wurde das quasi-statische DFM-Modell um die zeitabhängigen Effekte durch eine zeitabhängige Relaxations-Differentialgleichung der erster Ordnung erweitert. die sich als Funktion der Zeit entwickelt, erweitert. Anschließend wurden die entsprechenden Parameter an experimentelle Messergebnisse angepasst. Das Modell wurde daraufhin an weiteren Experimenten validiert. Der Einfluss eines jeden Parameters auf das Materialverhalten wurde untersucht. Die Hauptvorteile des erweiterten DFM-Modells sind seine physikalisch sinnvollen Parameter und die Reproduzierbarkeit des Materialverhaltens jeder Gummimischung für unterschiedliche Belastungsraten unter beliebiger Verformung bei Verwendung nur eines Parametersatzes. Die Grosch-Rad-Simulationen wurden unter statischer und dynamischer Belastung durchgeführt, um die Länge der Auflageflächen und die erreichten Verschiebungen bzw. Geschwindigkeiten zu analysieren. Eine weitere Erweiterung des DFM-Modells bezieht sich auf die Temperatureffekte und deren Einflüsse auf das mechanische Verhalten der verwendeten Gummimischungen. Die Modellvorhersagen wurden durch temperaturgesteuerte Experimente bestätigt. Die Fähigkeit der Kopplung thermo-mechanischer Größen im DFM-Modell wird vorgestellt. Die Implementierung des thermo-viskoelastischen Modells im FE-Programm wird beschrieben. Am Ende der Arbeit wurden die Temperaturverlagerungssimulation mit dem Zener-Modell und eine anschließende analytische Simulation zusammen mit einem dynamischen zyklischen Belastungsexperiment durchgeführt, um die Entwicklung von Innen- und Oberflächentemperaturen durch Selbsterhitzung der Kautschukkomponente abzuschätzen.

Schlagworte

Gefüllte Elastomere, Inelastizität, Spannungsrelaxation, Dehnungsratenabhängigkeit, Amplitudenabhängigkeit, repräsentative Richtungen, Selbsterhitzung, Thermomechanische Kopplung

Chapter 1

Introduction

An elastomer when reinforced with fillers such as carbon black or silica shows an improved characteristics with enhanced properties to work under various operating loads. Besides making the elastomer stiffer and tougher, the incorporation of fillers result in a strong non-linear behaviour with inelastic effects as shown in Fig.1.1. One of the effect is stress softening or the Mullin's effect [Mullins and Tobin, 1965], where the stress drop occurs not only during the multi-cyclic deformation loop, but also after the loading history has gone beyond the previous maximum. In addition to this, hysteresis is another characteristic effect caused by fillers which is related to the dissipation of mechanical energy. The non-linear dynamic-mechanical response of the material also increases and most of these effects are interrelated due to their common origin, the interaction between polymer and filler.

1.1 Hyperelastic model for filled elastomer

During vulcanization of rubber, in addition to the process of polymer network cross-linking, the filler particles form clusters due to high process temperature. The process of formation of cluster-cluster aggregation can also be called flocculation. The resulting filler structure essentially determines the mechanical behaviour of the entire polymer filler network. Unlike phenomenological models, the so-called Dynamic Flocculation Model (DFM) which is developed on a physically motivated framework, is able to describe a wide range of non-linear and inelastic material properties of filled elastomers [Klüppel, 2003, Klüppel et al., 2005, Lorenz et al., 2011]. It couples the entropic driven material behaviour of the polymer network with the polymer-filler and filler-filler interaction by considering the breakage and re-agglomeration of filler clusters in the polymer matrix during repeated deformation cycles [Lorenz and Klüppel, 2012]. The finite element implementation of the model has been realized using concept of representative directions [Freund et al., 2011]. The main advantage is that the constitutive behaviour of the model mimics the material response of the filled elastomer with its material parameters aligned to real physical quantities.

The physical motivation of the DFM has been addressed in several papers. On the one hand side, the DFM considers the rubber elastic matrix by the extended non-affine tube model, delivering a very good description of the stress-stain response of unfilled rubbers up to large deformations [Klüppel and Schramm, 2000, Klüppel et al., 2001]. In addition, the significance of non-affine tube deformation (with exponent 1/2 instead of 1) was demonstrated directly by static neutron

scattering of stretched rubber samples [Straube et al., 1994, Pyckhout-Hintzen et al., 2013]. On the other hand side, the structure and dynamics of the filler network was studied by various techniques, like TEM [Klüppel, 2003], dielectric spectroscopy [Klüppel, 2003, Meier et al., 2007], tomography inspections based on 3D-TEM micro-graphs [Kohjiya et al., 2006] and transverse NMR relaxation spectroscopy [Luo et al., 2004, Litvinov et al., 2011]. Recently, the rupture of glassy-like polymer bridges under tension was also investigated by molecular dynamics (MD) simulations, which have shown that the temperature dependent strength of virgin filler-filler bonds obtained from fits with the DFM is well reproduced [Froltsov et al., 2012]. The dynamics of filler flocculation in stretched samples was analysed by mechanical relaxation and time dependent X-ray scattering techniques, showing that the filler clusters break and particles move on ballistic trajectories during relaxation [Ehrburger-Dolle et al., 2012]. All these results are in close agreement with the assumptions of the DFM regarding the stress-strain response and rupture mechanism of filler clusters in strained samples.

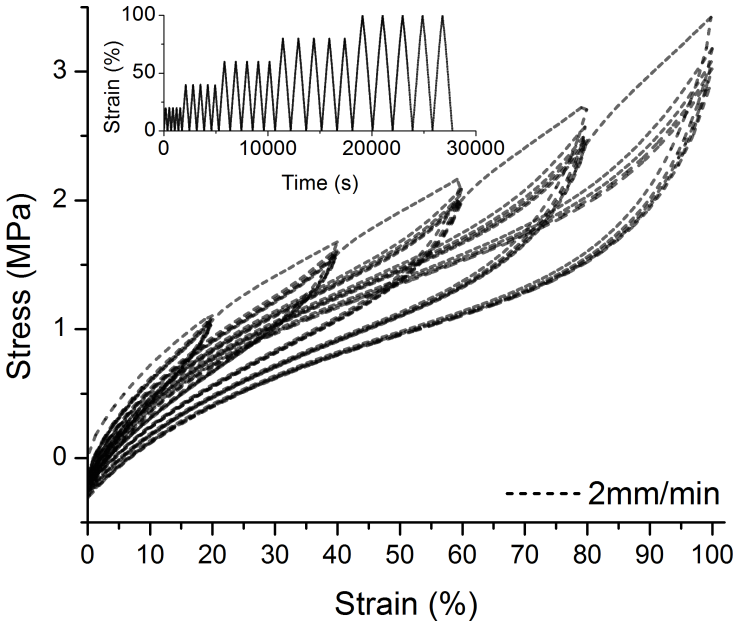

Figure 1.1: Uniaxial multi-hysteresis measurement of a CB-filled NR sample; the inset shows the strain history.

1.2 Viscoelastic material models

In this contribution, the DFM has been further developed to include time dependent effects where the limit of frequency and temperature range is given by the glass transition of the polymer composite. Generally the viscoelastic models are constituted with basic hyperelastic model in parallel with series of Maxwell elements [Johnson and Quigley, 1992, Kaliske and Heinrich, 2000]. The basic three parameter model is popularly known as Zener model. The constitutive theory is based on the phenomenological approach decomposes the stress into an equilibrium stress that corresponds to the stress response at an infinite slow rate of deformation ($t \to \infty$) and a viscosity-induced over-stress. Another possibility for the phenomenological approach is hyperelastic model in series with Kelvin element known as Poynting-Thomson rheological model [Laiarinandrasana et al., 2003] which is based on the instantaneous elasticity or infinitely high strain rate ($t \to 0$). Both models reproduce linear viscoelastic response and their extension to finite viscoelasticity

requires a large number of material parameters that are difficult to estimate. Another innovative approach in Haupt and Lion [2002] uses compact relaxation function based on power law, the Mittag-Leffler function which involves only a very few number of material parameters. As the constitutive hypothesis of DFM is based on the thermodynamical equilibrium state, we restrict our survey of literatures to the ones based on infinite slow rate of deformation.

On referring to the developments in non-linear viscoelastic framework, finite strain models of viscoelasticity are constructed by considering the multiplicative decomposition of the deformation gradient into elastic and inelastic parts [Bergstrom and Boyce, 1998, Lion, 2000, Reese and Govindjee, 1998a]. In this approach, a suitable hyperelastic model is employed to reproduce the elastic responses represented by the springs, while the dashpot represents the inelastic or the so-called internal strain. Its temporal behaviour is determined by an evolution equation that is consistent with the second law of thermodynamics. The similar kind of approach can also be seen in Amin et al. [2006] where the model follows the concept of the Zener model.

In contrast to the most common approach of multiplicative decomposition of the deformation gradient into elastic and inelastic parts, some of the constitutive models are formulated with microstructure-dependent viscosity or intrinsic time scales which are equivalent to variable viscosities and are available in the time- and the frequency-domain. These intrinsic time scales are driven by internal state variables, which can be interpreted as phenomenological measures for the current state of the filler network. Taking the amplitude-induced non-linearities into account, a three-dimensional constitutive approach in the time domain based on non-linear Maxwell elements (i.e. Prony series) is developed for the CB filled elastomer [Lion and Kardelky, 2004, Höfer and Lion, 2009]. The finite strain model is based on the general concept proposed by Haupt and Lion [2002] which was developed on the theory of finite linear viscoelasticity for incompressible materials. To simulate the frequency-dependent behaviour of non-linear viscoelastic structures under loadings which consist of a finite pre-deformation in combination with a superimposed harmonic deformation with small amplitude, frequency-domain formulations of the constitutive models are used [Lion et al., 2009]. As the main focus is on the pre-deformation and frequency dependent material behaviour, amplitude-dependency is not taken into account. The constitutive approach in Wollscheid and Lion [2013] is based on the proposed model of Lion et al. [2009] which is modified to represent the frequency- and pre-deformation-dependent behaviour of both moduli by using a deformation-dependent relaxation function.

The scientific publication of Marvalova [2007] presents a phenomenological material model for the viscoelastic stress response at large strains. The model is used for the simulation of carbon-black filled rubber in monotonic and cyclic deformation processes under isothermal conditions. The material stress response is decomposed into an elastic equilibrium stress response and a rate-dependent viscoelastic overstress response. Billon [2012] has focused on proposing constitutive equations to model the time-dependent mechanical behaviour of polymers close to their θ_g. In addition to the Edward and Vilgis model [Edwards and Vilgis, 1986] which is based on the non-Gaussian statistic approach of entangled polymer network, the author assumed specific evolution equations for internal state variables related to slip-link and related disentanglement as a source of inelastic mechanisms. Therefore, a phenomenological modelling of disentanglement was used to reproduce the viscoelastic behaviour of polymers.

A statistical hyper-visco-elasto-plastic model based on a meso-physically motivated approach is presented by Martinez et al. [2011], which covers a wide loading frequency spectrum and requires identifying only a few characteristic parameters which consists both statistical and phenomeno-

logical constants. The method followed to identify the parameters in Martinez et al. [2011] is comparable to our work, wherein the time-dependent parameters of DFM are identified using successive partial identifications using cyclic quasi-static and relaxation tests. In addition to that, the results of the model predictions in the shear mode under harmonic loading and the experimental data used to investigate the frequency and amplitude dependency is similar to the work of Martinez et al. [2011].

As most of the above stated models predict the material response in macroscopic level, the contribution of Reese [2003] present a so-called transient network theory which is extended in order to obtain a more general concept of viscoelasticity at the micromechanical level to include also the breaking and reforming of chains. Using certain assumptions for the chain distributions, one arrives at a continuum mechanical model of finite viscoelasticity which is based on the multiplicative decomposition of the deformation gradient.

In contrast to so far mentioned phenomenological approaches, there are some micromechanical models which are physically motivated. In Miehe et al. [2004] a micromechanical based non-affine network model for finite rubber elasticity incorporating topological constraints has been discussed. This micro-sphere model was further extended by Miehe and Göktepe [2005] towards the description of time-dependent viscoelastic effects. Although the base model is physically motivated, the extension to viscoelasticity involves a phenomenological form.

The Kröger et al. [2016] presents an approach to extend the Dynamic Flocculation Model (DFM) and the MOdel for Rubber PHenomenology (MORPH, [Ihlemann, 2003]) to include viscous effects through Prony series. In contrast to general conventional hyperelastic models, the DFM and the MORPH can reproduce complex elastomer behaviours such as material non-linearity, hysteresis, Mullin's effect and permanent set under quasi-static loading conditions. The additive composition of either DFM or MORPH with Prony series produces the desired visco-hyperelastic effects.

1.3 Payne-effect

A well-known inelastic phenomena of filler-reinforced rubber are the frequency and the amplitude dependence (Payne-effect) [Rendek and Lion, 2010]. A standard way to investigate the dynamic properties of viscoelastic materials is via the dynamic modulus, which is obtained from stress signals due to harmonic strain excitations. If rubber is unfilled, the dynamic moduli depend only on the frequency of the dynamic excitation. In the case of reinforcement with active fillers like carbon black, the moduli also depend on the amplitude of deformation [Lion, 2005].

After adding the filler, the instantaneous modulus G_0 increases more than the equilibrium modulus G_∞, resulting in a non-linear viscoelastic behaviour, known as Payne-effect. This increase is caused by the formation of filler-filler interactions, which are formed with carbon black loading. The probability for the formation of a filler network increases due to the fact that the inter-aggregate distances become smaller with rising filler content. With increasing carbon black loading filler networking develops and stabilizes the viscous polymer fluid yielding a diminished hysteresis behaviour at small and intermediate strains. At high strains, when the filler network is broken down, the viscous polymer is no longer stabilized and the $\tan\delta$ rises drastically. It can be stated that this hysteresis results from the breakdown of the increased filler network whose disruption during straining dissipates energy.

If filler-reinforced rubber is cyclically deformed the Payne-effect comes to light in the form of a monotonically decreasing storage modulus (in-phase modulus) and a sigmoidal-shaped loss modulus (out-of-phase modulus) with increasing strain amplitude. In contrast to the Mullins effect, which is irreversible at room temperature and occurs at filled and unfilled elastomers, the Payne effect is reversible [Wang et al., 1996, Wollscheid and Lion, 2013]. On a molecular level, the Payne-effect can be attributed to dynamic reversible breakdown and recovery processes of carbon black aggregate structures (Rendek and Lion [2010], Lion and Kardelky [2004]). According to Höfer and Lion [2009] two important phenomena related to frequency and amplitude are observed. Increasing frequencies lead to a higher storage and loss modulus and increasing amplitudes lead to a decrease in the storage modulus and a maximum in the loss modulus. As an increased amount of network-links are destroyed at medium strains, a maximum can be found within the loss modulus.

1.4 Temperature dependency

Elastomers are often described by so-called entropy-elastic property due to a significant change in its entropy when compared to internal energy. Where as materials like metal and glass are described by energy elasticity with a significant change in their internal energy [Holzapfel, 2000, Aboudi, 2004]. Another notable character of rubber is the Gough-Joule effect. In case of metals, the gradient of stress is always negative and the gradient of deformation is always positive with respect to temperature. But in case of rubber, beyond a so-called thermoelastic inversion point the gradient of stress becomes positive and the gradient of deformation becomes negative with respect to temperature. That means when rubber is heated, instead of expanding, it contracts and vice-versa and therefore rubber has a negative thermal expansion coefficient within certain temperature range.

Therefore the constitutive model has to be developed in such a way that it can be able to predict the thermoelastic behaviour of rubber-like materials. The free-energy functions that are capable to describe the thermo-viscoelastic behaviour at finite strains of rubber-like materials at elevated temperatures has to be determined.

Generally the thermo-viscoelastic constituent is modelled by a free-energy function which is given by a sum of a long-term contribution, that is based on the entropic elasticity for thermoelastic polymers and a non-equilibrium part which characterizes the viscoelastic (dissipative) mechanism which depends on deformation, temperature and a set of internal variables. A second important assumption in the model is a multiplicative decomposition of the material deformation gradient into an elastic and an inelastic part [Reese and Govindjee, 1998b, Dippel et al., 2014, Johlitz et al., 2015, Boukamel et al., 2001, Christ and Reese, 2009, Behnke et al., 2012, Rodas et al., 2015]. This decomposition is often applied in elasto-viscoplasticity [Balzani et al., 2015, Anand et al., 2009]. For the thermo-mechanical coupling, the free-energy function is further divided into a thermal-volume coupling part and a thermal part [Johlitz et al., 2015]. In another approach the split of free energy into thermal-volume coupling part is replaced by multiplicative decomposition of deformation gradient into thermal expansion and mechanical parts [Dippel et al., 2014, Rodas et al., 2015, Naumann and Ihlemann, 2012]. In such case the thermal part is purely volumetric and the mechanical part is again decomposed into intermediate configurations of elastic and inelastic parts.

The temperature dependency of a body can be analysed in three ways. The first one is the uncou-

pled heat transfer analysis, in which the temperature field (that include conduction, boundary convection, and boundary radiation) is calculated without consideration of the stress/deformation in the bodies being studied. The second one is sequentially coupled thermal-stress analysis. If the stress/displacement solution is dependent on a temperature field but there is no inverse dependency, a sequentially coupled thermal-stress analysis can be conducted. Sequentially coupled thermal-stress analysis is performed by first solving the pure heat transfer problem, then reading the temperature solution into a stress analysis. The last one is fully coupled thermal-stress analysis. A coupled temperature-displacement procedure is used to solve simultaneously for the stress/displacement and the temperature fields. A coupled analysis is used when the thermal and mechanical solutions affect each other strongly.

In our work we consider the fully coupled thermal-stress analysis as temperature influences the deformation via thermal expansion and temperature dependent material parameters and on the other hand, the temperature is affected by dissipative (self heating) and thermo-elastic effects.

1.5 Thesis outline

To study the phenomenon like viscoelasticity at microscopic level, the DFM is extended to consider time dependent effects using physically meaningful parameters. Since the time dependent effects are mainly driven by filler-filler interactions, their influence is described explicitly by the parameters s_d and s_v in the DFM as the strengths of damaged and virgin filler clusters, respectively. Henceforth these material parameters can be decoupled into equilibrium constants ($s_{d,eq}$ & $s_{v,eq}$) and time dependent functions ($s_{d,t}$ & $s_{v,t}$). The time-dependent function can be described by a relaxation function [Juhre et al., 2013, Raghunath et al., 2016]. The prediction of the extended DFM model involves comparing strain rate-dependency, stress relaxation, and Payne effect with comprehensive experiments.

Due to low conductivity of rubber in comparison with metals, internal dissipation phenomena lead to a high temperature increase which is called self heating. Therefore another aim of this work is to study thermal response of elastomeric materials by means of thermo-mechanical material model. Similar to the time-dependent effects, the temperature dependency of the filled elastomer is more pronounced with respect to the filler volume fraction. The dynamic effect of the material reduces with respect to an increase in temperature where as the static effect increases due to an increase in entropy of matrix rubber. As the dynamic behaviour is mainly contributed by the filler clusters, $s_{d,t}$ and $s_{v,t}$, they are made temperature dependent by using the relaxation time τ. In order to include the entropy-elastic behaviour of matrix rubber, the parameters of the tube model are made temperature dependent. This completes the one-way coupling of temperature effects on the mechanical deformation. In order to fully couple the temperature-displacement effects, the stress power due to $\dot{s}_{d,t}$ and $\dot{s}_{v,t}$ and the entropy from the energy inequality are determined.

The static/viscoelastic DFM has been implemented in a finite element program Abaqus by using user subroutine UMAT. The so-called Grosch wheel was simulated under static loading conditions to predict the foot print length and visualise stress softening phenomenon. The thermo-mechanically coupled theory has been implemented in a finite element program Abaqus by combining the user subroutines UMAT, UMATHT and DFLUX. The predictive capabilities of the theory and its numerical implementation are validated by comparing the results from a suite of validation experiments such as temperature-dependent quasi-static and rate-dependent

experiments at a temperature controlled chamber. These cyclic isothermal experiments at different level of temperatures are used to compare the thermal effects on material deformation. For the full thermo-viscoelastic coupling of DFM requires entropy contribution of filler clusters that is not included in the formulation due to unavailable quantities to fulfil the balance equations. Hence a simple viscoelstic phenomenological model like Zener was used for thermo-mechanical coupling simulations. Although the results of the simulation can not be compared to the actual test results (because the chosen parameters for the simulations are not identified based on the actual material behaviour), it can be viewed as an attempt towards the thermo-mechanical coupling approach. In addition to numerical approach, an analytical model has been presented to estimate the internal and surface temperatures evolution during cyclic loading and the results are compared with thermal images and curves.

Chapter 2

Continuum mechanics

In this chapter a brief introduction to matrix, tensor and continuum mechanics involved in this work are discussed. For deep understanding of concepts, the reader can refer Holzapfel [2000], Bonet and Wood [2008] and Haupt [2002] or any other continuum mechanics reference material. The basic concept of continuum mechanics is also referred from the university lecture script of Juhre [2010].

2.1 Tensor algebra

2.1.1 Symbols and description

The vectors and tensors are in consistent to the literatures with bold and special symbol depictions compared to the widespread usage of underscores by other literatures.

α	zero order tensor (scalar)
$\mathbf{a} = a_i$	1^{st} order tensor (vector)
$\mathbf{A} = A_{ij}$	2^{nd} order tensor
$\boldsymbol{\mathcal{A}} = \mathcal{A}_{ijk}$	3^{rd} order tensor
$\mathbb{A} = \mathbb{A}_{ijkl}$	4^{th} order tensor

where a_i, A_{ij}, $\mathcal{A}_{ijk}$ and $\mathbb{A}_{ijkl}$ are the matrix components of tensors $\mathbf{a}$, $\mathbf{A}$, $\boldsymbol{\mathcal{A}}$ and $\mathbb{A}$, respectively.

2.1.2 Dot product

The dot product or scalar product of combination of scalars or vectors or higher order tensors results in scalar, vector or tensor.

The dot product of scalar and vector:

$$\begin{aligned} &\alpha \cdot \mathbf{a} \qquad \text{or simply,} \qquad \alpha\,\mathbf{a} = \mathbf{b} \\ &\alpha\, a_i\, \mathbf{e}_i = b_i\, \mathbf{e}_i \qquad \text{(in index notation).} \end{aligned} \tag{2.1}$$

A Euclidean vector space is characterized by an orthonormal (cartesian) basis $\mathbf{e}_i$ (i = 1, 2, 3) and the Kronecker delta δ_{ij} can be expressed as

$$\delta_{ij} := \mathbf{e}_i \cdot \mathbf{e}_j = \begin{cases} 1, & \text{if } i = j \\ 0, & \text{otherwise.} \end{cases} \tag{2.2}$$

The dot product of two vectors:

$$\mathbf{a} \cdot \mathbf{b} = (a_i\, \mathbf{e}_i) \cdot (b_j\, \mathbf{e}_j) = a_i\, b_j\, \delta_{ij} = a_i\, b_i = \alpha. \tag{2.3}$$

The dot product of vector and 2^{nd} order tensor:

$$\mathbf{B} \cdot \mathbf{a} = (B_{jk}\, \mathbf{e}_j \otimes \mathbf{e}_k) \cdot (a_i\, \mathbf{e}_i) = B_{jk}\, a_i\, \delta_{ki}\, \mathbf{e}_j = B_{jk}\, a_k\, \mathbf{e}_j = c_j\, \mathbf{e}_j = \mathbf{c}. \tag{2.4}$$

$$\mathbf{B} \cdot \mathbf{a} \neq \mathbf{a} \cdot \mathbf{B} \qquad \text{unless } \mathbf{B} \text{ is symmetric.} \tag{2.5}$$

The dot product of two 2^{nd} order tensors:

$$\begin{aligned} \mathbf{A} \cdot \mathbf{B} &= (A_{ij}\, \mathbf{e}_i \otimes \mathbf{e}_j) \cdot (B_{kl}\, \mathbf{e}_k \otimes \mathbf{e}_l) \\ &= A_{ij}\, B_{kl}\, \delta_{jk}\, \mathbf{e}_i \otimes \mathbf{e}_l = A_{ij}\, B_{jl}\, \mathbf{e}_i \otimes \mathbf{e}_l = C_{il}\, \mathbf{e}_i \otimes \mathbf{e}_l = \mathbf{C}. \end{aligned} \tag{2.6}$$

$$\mathbf{A} \cdot \mathbf{B} \neq \mathbf{B} \cdot \mathbf{A} \qquad \text{unless both } \mathbf{A} \text{ and } \mathbf{B} \text{ are symmetric.} \tag{2.7}$$

The dot product of 2^{nd} order and 4^{th} order tensors:

$$\begin{aligned} \mathbb{B} \cdot \mathbf{A} &= (\mathbb{B}_{ijkl}\, \mathbf{e}_i \otimes \mathbf{e}_j \otimes \mathbf{e}_k \otimes \mathbf{e}_l) \cdot (A_{mn}\, \mathbf{e}_m \otimes \mathbf{e}_n) \\ &= \mathbb{B}_{ijkl}\, A_{mn}\, \delta_{lm}\, \mathbf{e}_i \otimes \mathbf{e}_j \otimes \mathbf{e}_k \otimes \mathbf{e}_n = \mathbb{B}_{ijkl}\, A_{ln}\, \mathbf{e}_i \otimes \mathbf{e}_j \otimes \mathbf{e}_k \otimes \mathbf{e}_n \\ &= \mathbb{C}_{ijkn}\, \mathbf{e}_i \otimes \mathbf{e}_j \otimes \mathbf{e}_k \otimes \mathbf{e}_n = \mathbb{C}. \end{aligned} \tag{2.8}$$

2.1.3 Cross product

The cross product or vector product of two vectors gives vector.

$$\mathbf{a} \times \mathbf{b} = a_i\, \mathbf{e}_i \times b_j\, \mathbf{e}_j = a_i\, b_j\, \mathcal{E}_{ijk}\, \mathbf{e}_k = c_k\, \mathbf{e}_k = \mathbf{c} \tag{2.9}$$

where $\mathcal{E}_{ijk}$ is called permutation symbol which is defined by

$$\mathcal{E}_{ijk} = \begin{cases} 1, & \text{for cyclic permutations of i, j, k} \\ -1, & \text{for anti-cyclic permutations of i, j, k} \\ -1, & \text{if at least two of the indices are equal.} \end{cases} \tag{2.10}$$

2.1.4 Dyadic product

The dyadic product or tensor product of vectors or lower order tensors gives a higher order tensor.

The dyadic product of two vectors:

$$\mathbf{a} \otimes \mathbf{b} = a_i\, \mathbf{e}_i \otimes b_j\, \mathbf{e}_j = a_i\, b_j\, \mathbf{e}_i \otimes \mathbf{e}_j = C_{ij}\, \mathbf{e}_i \otimes \mathbf{e}_j = \mathbf{C} \tag{2.11}$$

The dyadic product of two 2^{nd} order tensors:

$$\begin{aligned} \mathbf{A} \otimes \mathbf{B} &= (A_{ij}\, \mathbf{e}_i \otimes \mathbf{e}_j) \otimes (B_{kl}\, \mathbf{e}_k \otimes \mathbf{e}_l) \\ &= A_{ij}\, B_{kl}\, \mathbf{e}_i \otimes \mathbf{e}_j \otimes \mathbf{e}_k \otimes \mathbf{e}_l = \mathbb{C}_{ijkl}\, \mathbf{e}_i \otimes \mathbf{e}_j \otimes \mathbf{e}_k \otimes \mathbf{e}_l = \mathbb{C} \end{aligned} \tag{2.12}$$

2.1.5 Double dot product

The double dot product of vectors or tensors gives scalar or tensor.

The inner double dot product of two 2^{nd} order tensors:

$$\mathbf{A} : \mathbf{B} = A_{ij}\, B_{ji}. \tag{2.13}$$

In index notation,

$$\begin{aligned} (A_{ij}\, \mathbf{e}_i \otimes \mathbf{e}_j) : (B_{kl}\, \mathbf{e}_k \otimes \mathbf{e}_l) &= (A_{ij}\, \mathbf{e}_i)\delta_{jk} \cdot (B_{kl}\, \mathbf{e}_l) = A_{ij}\, B_{kl}\, \delta_{jk}\, \delta_{il} \\ &= A_{ij}\, B_{jl}\, \delta_{il} = A_{ij}\, B_{ji} = \alpha. \end{aligned} \tag{2.14}$$

In contrast, the outer double dot product of two 2^{nd} order tensors is not equal to inner product unless $\mathbf{A}$ is symmetric.

$$\mathbf{A} \cdot\cdot \mathbf{B} = \mathbf{A}^T : \mathbf{B} = A_{ji} B_{ji}. \tag{2.15}$$

In index notation,

$$\begin{aligned} (A_{ji}\, \mathbf{e}_i \otimes \mathbf{e}_j) : (B_{kl}\, \mathbf{e}_k \otimes \mathbf{e}_l) &= (A_{ji}\, \mathbf{e}_i)\delta_{jk} \cdot (B_{kl}\, \mathbf{e}_l) = A_{ji}\, B_{kl}\, \delta_{jk}\, \delta_{il} \\ &= A_{ji}\, B_{jl}\, \delta_{il} = A_{ji}\, B_{ji} = \beta. \end{aligned} \tag{2.16}$$

The inner double dot product of 4^{th} order and 2^{nd} order tensors:

$$\begin{aligned} \mathbb{A} : \mathbf{B} &= (\mathbb{A}_{ijkl}\, \mathbf{e}_i \otimes \mathbf{e}_j \otimes \mathbf{e}_k \otimes \mathbf{e}_l) : (B_{mn}\, \mathbf{e}_m \otimes \mathbf{e}_n) \\ &= \mathbb{A}_{ijkl}\, B_{mn}\, \delta_{lm}\, \delta_{kn}\, \mathbf{e}_i \otimes \mathbf{e}_j = \mathbb{A}_{ijkl}\, B_{ln}\, \delta_{kn}\, \mathbf{e}_i \otimes \mathbf{e}_j \\ &= \mathbb{A}_{ijkn}\, B_{lk}\, \mathbf{e}_i \otimes \mathbf{e}_j = C_{ij}\, \mathbf{e}_i \otimes \mathbf{e}_j = \mathbf{C}. \end{aligned} \tag{2.17}$$

Similarly in case of two 4^{th} order tensors:

$$\mathbb{A} : \mathbb{B} = \mathbb{A}_{ijkl}\, \mathbb{B}_{lkop}\, \mathbf{e}_i \otimes \mathbf{e}_j \otimes \mathbf{e}_o \otimes \mathbf{e}_p = \mathbb{C}_{ijop}\, \mathbf{e}_i \otimes \mathbf{e}_j \otimes \mathbf{e}_o \otimes \mathbf{e}_p = \mathbb{C}. \tag{2.18}$$

The double-double dot product of two 4^{th} order tensors:

$$\mathbb{A} :: \mathbb{B} = \mathbb{A}_{ijkl}\, \mathbb{B}_{lkji} = \alpha. \tag{2.19}$$

2.1.6 Transpose and inverse

The dot product transpose of two 2^{nd} order tensors:

$$(\mathbf{A} \cdot \mathbf{B})^T = \mathbf{B}^T \cdot \mathbf{A}^T. \tag{2.20}$$

The dot product inverse of two 2^{nd} order tensors:

$$(\mathbf{A} \cdot \mathbf{B})^{-1} = \mathbf{B}^{-1} \cdot \mathbf{A}^{-1}. \tag{2.21}$$

The dot product inverse of three 2^{nd} order tensors:

$$(\mathbf{A} \cdot \mathbf{B} \cdot \mathbf{C})^{-1} = \mathbf{C}^{-1} \cdot \mathbf{B}^{-1} \cdot \mathbf{A}^{-1}. \tag{2.22}$$

2.1.7 Trace

The trace of two 2^{nd} order tensors:

$$tr(\mathbf{A} \cdot \mathbf{B}) = \mathbf{A} : \mathbf{B} = A_{ij}\, B_{ji}. \tag{2.23}$$

The trace of three 2^{nd} order tensors:

$$\begin{aligned} &\text{if, } \mathbf{A}' = \mathbf{B} \cdot \mathbf{A} \cdot \mathbf{B}^{-1} \\ &A'_{ij} = (B\, A\, B^{-1})_{ij} = B_{il}\, A_{lk}\, B^{-1}_{kj} \\ &\text{then, } tr(\mathbf{A}') = tr(\mathbf{B} \cdot \mathbf{A} \cdot \mathbf{B}^{-1}) = B_{il}\, A_{lk}\, B^{-1}_{ki} \\ &= (B^{-1}\, B)_{kl}\, A_{lk} = \delta_{kl}\, A_{lk} = A_{kk}. \end{aligned} \tag{2.24}$$

2.2 Continuum mechanics

Continuum body assumes that the substance of the object completely fills the space it occupies. Continuum mechanics deals with physical properties of solids and fluids which are defined by using mathematical objects in the form of tensors. These tensors are independent of any particular coordinate system in which they are observed. For the sake of computational convenience, these tensors can be expressed in coordinate systems. Here the relation between various forms of mechanical measurements are described.

2.2.1 Deformation gradient

The deformation gradient $\mathbf{F}$ measures the deformation of a line element at an arbitrary position and time. From Fig.2.1, the deformation gradient $\mathbf{F}$ can be written as

$$\mathbf{F} = \frac{d\mathbf{x}}{d\mathbf{X}} \tag{2.25}$$

where, $d\mathbf{X}$ is a line element before deformation and $d\mathbf{x}$ is a line element after deformation.

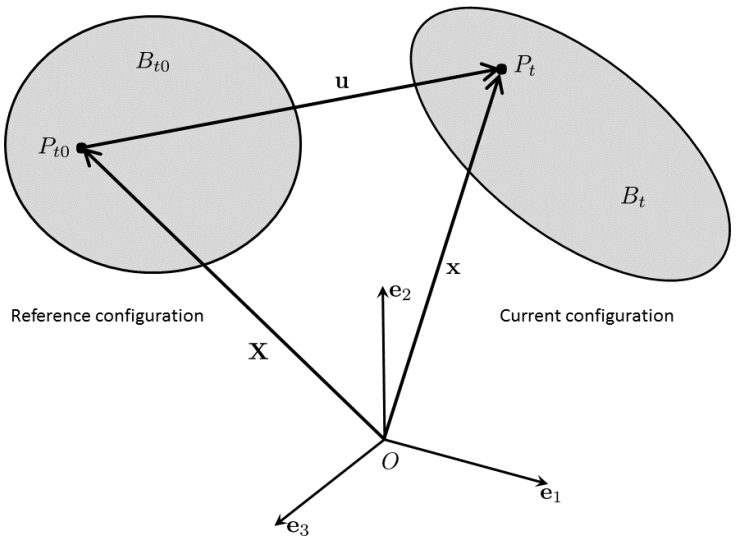

Figure 2.1: Deformation and motion of a continuum body.

The matrix notation of the deformation gradient $\mathbf{F}$:

$$\begin{pmatrix} dx_1 \\ dx_2 \\ dx_3 \end{pmatrix} = \begin{pmatrix} F_{11} & F_{12} & F_{13} \\ F_{21} & F_{22} & F_{23} \\ F_{31} & F_{32} & F_{33} \end{pmatrix} \begin{pmatrix} dX_1 \\ dX_2 \\ dX_3 \end{pmatrix}$$

Therefore,

$$d\mathbf{x} = \mathbf{F}d\mathbf{X} \quad or \quad d\mathbf{X} = \mathbf{F}^{-1}d\mathbf{x} \tag{2.26}$$

$$det\mathbf{F} = det\frac{\partial \mathbf{x}}{\partial \mathbf{X}} := J \neq 0. \tag{2.27}$$

2.2.2 Strain measures

The strain measure can be used for computing the stress in the material. The deformation gradient $\mathbf{F}$ uniquely describes the deformation state of the material.

We know from the latter definitions that the terms

$$\mathbf{F}^T\mathbf{F} := \mathbf{C} \tag{2.28}$$

$$\mathbf{F}\mathbf{F}^T := \mathbf{b} \tag{2.29}$$

are symmetric. Here, we have introduced the so-called right Cauchy-Green tensor $\mathbf{C}$ and the left Cauchy-Green tensor $\mathbf{b}$.

From the above we can define the strain tensors as

$$\mathbf{E} = \frac{1}{2}(\mathbf{F}^T\mathbf{F} - \mathbf{1}) \quad \text{or} \quad \mathbf{E} = \frac{1}{2}(\mathbf{C} - \mathbf{1}) \tag{2.30}$$

$$\mathbf{e} = \frac{1}{2}(\mathbf{1} - \mathbf{F}^{-1}\mathbf{F}^{-T}) \quad \text{or} \quad \mathbf{e} = \frac{1}{2}(\mathbf{1} - \mathbf{b}^{-1}) \tag{2.31}$$

where $\mathbf{E}$ is the Green Lagrange strain tensor and $\mathbf{e}$ is the Almansi strain tensor.

The so called engineering strain $\boldsymbol{\varepsilon}$ or the nominal strain can be expressed as

$$\boldsymbol{\varepsilon} = \boldsymbol{\lambda} - \mathbf{1} \tag{2.32}$$

where $\boldsymbol{\lambda}$ is the principal stretch ratio vector and $\mathbf{1}$ is the unit vector.

In uniaxial extension the logarithmic strain $\boldsymbol{\varepsilon}^H$ or the Hencky strain or true strain is related to stretch ratio by

$$\boldsymbol{\varepsilon}^H = ln\boldsymbol{\lambda}. \tag{2.33}$$

The engineering strain considers only the final state compared to the initial state, where as the logarithmic strain takes into account the continuous variation of length. So engineering strain and logarithmic strain give the same value for small deformations but they differ a lot if one considers large deformation. When large deformation are encountered, the initial length can be no more taken as reference to compute every strain increments (like in engineering strain), one have to take in account the value of length just before each strain increment (that is the idea of the logarithmic strain).

The detailed derivation of logarithmic strain and it's rate for different deformation modes is provided in chapter 8.

2.2.3 Deformation rate

The spatial velocity gradient $\mathbf{l}$ can be written as

$$\mathbf{l} = \dot{\mathbf{F}}\,\mathbf{F}^{-1} \tag{2.34}$$

and its transpose

$$\mathbf{l}^T = \mathbf{F}^{-T}\,\dot{\mathbf{F}}^T. \tag{2.35}$$

The symmetric part of $\mathbf{l}$ is called rate of deformation $\mathbf{d}$

$$\mathbf{d} = \frac{1}{2}\left(\mathbf{l} + \mathbf{l}^T\right). \tag{2.36}$$

The time derivative of the Green-Lagrange tensor $\dot{\mathbf{E}}$ can be written as

$$\dot{\mathbf{E}} = \frac{1}{2}\,\dot{\mathbf{C}} = \mathbf{F}^T\,\mathbf{d}\,\mathbf{F}. \tag{2.37}$$

A further important rate is the time derivative of the determinant of the deformation gradient:

$$\dot{J} = \overline{\dot{det}\mathbf{F}} = J\,tr\mathbf{d}. \tag{2.38}$$

2.2.4 Invariants

An invariant is a property of a class of mathematical objects that remains unchanged when transformations of a certain type are applied to the objects or in other words they are independent of chosen basis. The principal invariants of deformation tensors can be given as

$$I_1 = tr\mathbf{C} = \mathbf{CI} = tr\mathbf{b} = \mathbf{bI}, \tag{2.39}$$

$$I_2 = \frac{1}{2}((tr\mathbf{C})^2 - tr\mathbf{C^2}) = \frac{1}{2}((tr\mathbf{b})^2 - tr\mathbf{b^2}), \tag{2.40}$$

$$I_3 = det\mathbf{C} = det\mathbf{b} = (det\mathbf{F})^2 = J^2. \tag{2.41}$$

Derivatives of principal invariants,

$$\frac{\partial I_1}{\partial \mathbf{C}} = \mathbf{I}, \qquad \frac{\partial I_1}{\partial \mathbf{b}} = \mathbf{I}, \tag{2.42}$$

$$\frac{\partial I_2}{\partial \mathbf{C}} = tr\mathbf{C}\,\mathbf{I} - \mathbf{C}, \qquad \frac{\partial I_2}{\partial \mathbf{b}} = tr\mathbf{b}\,\mathbf{I} - \mathbf{b}, \tag{2.43}$$

$$\frac{\partial I_3}{\partial \mathbf{C}} = det\mathbf{C}\mathbf{C^{-1}} = I_3\mathbf{C^{-1}} = J^2\mathbf{C^{-1}}, \qquad \frac{\partial I_3}{\partial \mathbf{b}} = det\mathbf{b}\mathbf{b^{-1}} = I_3\mathbf{b^{-1}} = J^2\mathbf{b^{-1}}. \tag{2.44}$$

2.2.5 Stress measures

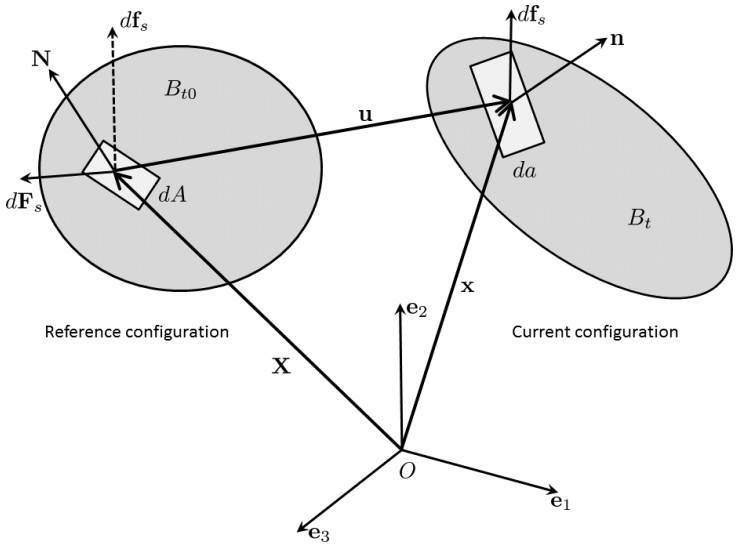

Figure 2.2: Continuum body with area element and corresponding deformation vectors.

The stress is expressed by the Cauchy traction vector $\mathbf{t}_s$ which is defined as the traction force $\mathbf{f}_s$ between the neighbouring continuum points of the body divided by the area of an imaginary separating surface s. In case of fluid at rest, the force will be perpendicular to the surface, and hence the resulting stress is a scalar quantity. In contrast, the force $\mathbf{f}_s$ may not be perpendicular to the surface in a solid, or in a flow of viscous liquid. Therefore the stress across a surface must be regarded a vector quantity. The direction and magnitude of the vector generally depend on the orientation of the surface. Thus the stress state of the material must be described by tensor, called the Cauchy stress tensor $\boldsymbol{\sigma}$. The Cauchy stress is a linear function which relates the normal vector $\mathbf{n}$ of a surface s to the stress $\mathbf{t}_s$ across s. Moreover, the Cauchy stress tensor can be represented as a symmetric matrix with respect to any chosen coordinate system. This stress tensor even within a homogeneous body can vary from place to place and can change over

time. In general, the Cauchy stress within a material is a time-varying tensor field. Hence from the definition, the Cauchy traction vector can be defined as

$$\mathbf{t}_s = \boldsymbol{\sigma}\mathbf{n}. \tag{2.45}$$

The Cauchy stress tensor $\boldsymbol{\sigma}$ is defined as

$$\boldsymbol{\sigma} = \frac{d\mathbf{f}_s}{d\mathbf{a}} \tag{2.46}$$

where $d\mathbf{f}_s$ is the force acting on the surface area d$\mathbf{a}$ of the material at current configuration.

Similarly the 1^{st} Piola-Kirchhoff (PK) or engineering or nominal stress $\mathbf{T}$ is defined as

$$\mathbf{T} = \frac{d\mathbf{f}_s}{d\mathbf{A}} \tag{2.47}$$

where $d\mathbf{f}_s$ is the force acting on the surface area $d\mathbf{A}$ of the material at reference configuration.

The 1^{st} Piola-Kirchhoff (PK) stress tensor is connected to $\boldsymbol{\sigma}$ via

$$\mathbf{T} = J\boldsymbol{\sigma}\mathbf{F}^{-T}. \tag{2.48}$$

If we consider material to be incompressible ($J = 1$), then

$$\mathbf{T} = \frac{\boldsymbol{\sigma}}{\boldsymbol{\lambda}}. \tag{2.49}$$

By pulling-back the force vector $d\mathbf{f}_s$ to the reference configuration, we get the 2^{nd} PK stress tensor $\tilde{\mathbf{T}}$,

$$\tilde{\mathbf{T}} = \frac{d\mathbf{F}_s}{d\mathbf{A}}. \tag{2.50}$$

The 2^{nd} PK stress tensor is connected to $\boldsymbol{\sigma}$ via

$$\tilde{\mathbf{T}} = \mathbf{F}^{-1}\mathbf{T} = J\mathbf{F}^{-1}\boldsymbol{\sigma}\mathbf{F}^{-T}. \tag{2.51}$$

2.2.6 Conjugate quantities

There comes a question *why all these different type of stresses and strains are required?* The principle of virtual work which is expressed as mathematical weak formulation in continuum mechanics states that the internal work done by an infinitesimal strain variation operating on the current stresses equals the external work done by a corresponding virtual displacement operating on the loads. The stress and strain measures must then be selected so that their product gives an accurate energy density. This energy density may be related either to the undeformed or deformed volume, depending on whether the internal virtual work is integrated over the original or the deformed geometry. The conjugate pairs of stresses and stains are shown in Tab.2.1 and the corresponding material stiffness curve is shown in Fig.2.3.

The total Lagrangian is formulated in terms of 2^{nd} Piola-Kirchhoff stresses and the Green-Lagrangian strains and the updated Lagrangian is formulated in terms of the Cauchy stresses and the logarithmic strains.

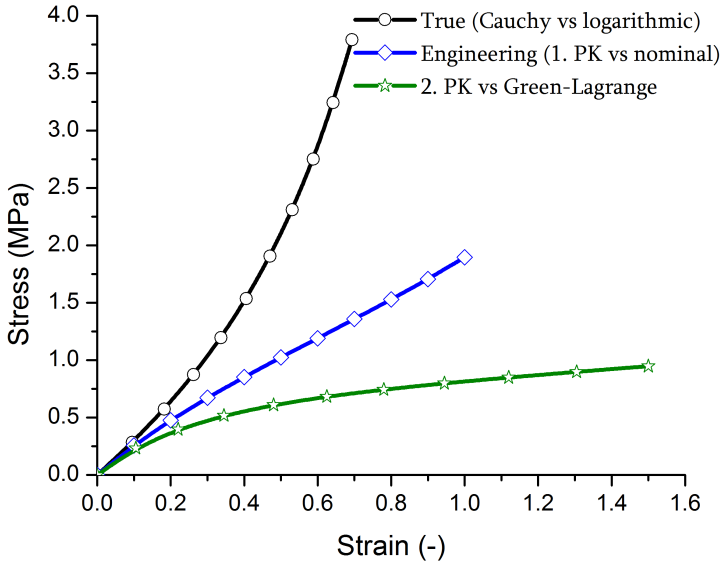

Figure 2.3: Stress-strain pairs for the uniaxial tensile stretch of 100%.

Table 2.1: The stress-strain pairs that can be conjugared.

Stress	Strain	Deformation state
Cauchy (true)	logarithmic (true) or Almansi	deformed
1^{st} Piola-Kirchhoff (nominal)	Nominal or deformation gradient	original
2^{nd} Piola-Kirchhoff	Green-Lagrange	original

2.2.7 Continuum thermodynamics

A continuum which possesses both mechanical and thermal energy is called a thermodynamic continuum. A non-equilibrium state in the continuum is a state of imbalance (i.e. there exists a gradient of temperature and velocity), while an equilibrium state is a state of balance (i.e. of uniform temperature and zero velocity). Heat is the form of thermal energy that is transferred between a system and its surroundings (or between two systems) by virtue of a temperature gradient.

In discussing deformations of elastic materials it is convenient to extract the part of the internal energy which includes processes due to reversible deformations. Therefore we subtract the entropic term from the internal energy

$$\Psi = U - \theta\,\Upsilon. \tag{2.52}$$

which determines the so-called Helmholtz free energy Ψ in terms of internal energy U, entropy Υ and temperature θ.

The rate of Helmholtz free energy Ψ in Eq.(2.52) is then

$$\dot{\Psi} = \dot{U} - \Upsilon\,\dot{\theta} - \theta\,\dot{\Upsilon}. \tag{2.53}$$

The Clausius-Duhem inequality from the 2^{nd} law of thermodynamics for the undeformed or reference configuration can be written as

$$(\dot{U} - \theta\,\dot{\Upsilon}) - \tilde{\mathbf{T}} : \dot{\mathbf{E}} \leq -\frac{1}{\theta}\,\mathbf{Q}\,\nabla\theta \tag{2.54}$$

where $\tilde{\mathbf{T}}$ is 2^{nd} PK stress, $\dot{\mathbf{E}}$ is the time derivative of the Green-Lagrange tensor and $\mathbf{Q}$ is the PK heat flux.

Substiting Eq.(2.53) in Eq.(2.54) yields

$$-\dot{\Psi} - \Upsilon\,\dot{\theta} + \tilde{\mathbf{T}} : \dot{\mathbf{E}} - \frac{1}{\theta}\,\mathbf{Q}\,\nabla\theta \geq 0 \tag{2.55}$$

Similarly in case of deformed or spatial configuration

$$\begin{aligned} &J^{-1}\,(\dot{U} - \theta\,\dot{\Upsilon}) - \boldsymbol{\sigma} : \mathbf{d} \leq -\frac{1}{\theta}\,\mathbf{q}\,\nabla\theta \\ &-J^{-1}\,\dot{\Psi} - J^{-1}\,\Upsilon\,\dot{\theta} + \boldsymbol{\sigma} : \mathbf{d} - \frac{1}{\theta}\,\mathbf{q}\,\nabla\theta \geq 0 \end{aligned} \tag{2.56}$$

where $\boldsymbol{\sigma}$ is Cauchy stress and $\mathbf{d}$ is rate of deformation. In case of current configuration the stress, entropy and flux are scaled by the volume ratio J. $\mathbf{q}$ is the Cauchy heat flux and is related to PK heat flux by

$$\mathbf{q} = J^{-1}\,F^{T}\,\mathbf{Q}. \tag{2.57}$$

The Clausius-Duhem inequality leads to an alternative strong form of the second law of thermodynamics, often referred to as the Clausius-Planck inequality

$$\mathscr{D}_{int} = \tilde{\mathbf{T}} : \dot{\mathbf{E}} - \dot{\Psi} - \Upsilon\,\dot{\theta} \geq 0 \qquad \text{in reference configuration,} \tag{2.58}$$

$$\mathscr{D}_{int} = \boldsymbol{\sigma} : \mathbf{d} - J^{-1}\,\dot{\Psi} - J^{-1}\,\Upsilon\,\dot{\theta} \geq 0 \qquad \text{in current configuration,} \tag{2.59}$$

where $\mathscr{D}_{int}$ is the internal dissipation which is required to be non-negative at any particle of a body for all times t. In equations (2.58) and (2.59), $\tilde{\mathbf{T}} : \dot{\mathbf{E}}$ and $\boldsymbol{\sigma} : \mathbf{d}$ are rate of internal mechanical work $\mathscr{W}_{int}$ which is often referred as internal stress power. The internal dissipation $\mathscr{D}_{int}$ is zero for reversible processes while the inequality holds for irreversible processes.

From the first law of thermodynamics, the reduced form of balance of internal energy without external heat source can be expressed as

$$\dot{U} = \tilde{\mathbf{T}} : \dot{\mathbf{E}} - Div\mathbf{Q} \qquad \text{in reference configuration.} \tag{2.60}$$

Substiting Eq.(2.53) in Eq.(2.60) yields

$$\dot{\Psi} + \Upsilon\,\dot{\theta} + \theta\,\dot{\Upsilon} = \tilde{\mathbf{T}} : \dot{\mathbf{E}} - Div\mathbf{Q}. \tag{2.61}$$

Similarly in case of current configuration

$$\begin{aligned} &J^{-1}\,\dot{U} = \boldsymbol{\sigma} : \mathbf{d} - div\mathbf{q} \\ &J^{-1}\,\dot{\Psi} + J^{-1}\,\Upsilon\,\dot{\theta} + J^{-1}\,\theta\,\dot{\Upsilon} = \boldsymbol{\sigma} : \mathbf{d} - div\mathbf{q}. \end{aligned} \tag{2.62}$$

By means of the Clausius-Planck inequality in equations (2.58) and (2.59), the local form of the balance of energy can be rewritten in the entropy form

$$\theta\,\dot{\Upsilon} = \mathscr{D}_{int} - Div\mathbf{Q} \qquad \text{in reference configuration,} \tag{2.63}$$

$$J^{-1}\,\theta\,\dot{\Upsilon} = \mathscr{D}_{int} - div\mathbf{q} \qquad \text{in current configuration.} \tag{2.64}$$

In case of an adiabatic process, i.e. thermal energy can neither cross (enter or leave) the boundary surface nor be generated or destroyed within the body so that the thermal power $\frac{d\mathscr{D}}{dt}$ is zero, the entropy form degenerates to

$$\theta\,\dot{\Upsilon} \text{ or } J^{-1}\,\theta\,\dot{\Upsilon} = \mathscr{D}_{int}. \tag{2.65}$$

If, in addition, an adiabatic process is reversible, i.e. no entropy is produced, the balance equation reduces further to

$$\theta\,\dot{\Upsilon} \text{ or } J^{-1}\,\theta\,\dot{\Upsilon} = \mathscr{D}_{int} = 0. \tag{2.66}$$

which is called isentropic process. A further important type of thermodynamic processes is the isothermal process, i.e. no temperature change ($\dot{\theta} = 0$).

Therefore for the case of a purely mechanical theory, that is, if thermal effects are ignored, the free energy Ψ coincides with the internal energy U and the Clausius-Planck inequality in equations (2.58) and (2.59) degenerates to

$$\mathscr{D}_{int} = \tilde{\mathbf{T}} : \dot{\mathbf{E}} - \dot{\Psi} \geq 0 \qquad \text{in reference configuration,} \tag{2.67}$$

$$\mathscr{D}_{int} = \boldsymbol{\sigma} : \mathbf{d} - J^{-1}\,\dot{\Psi} \geq 0 \qquad \text{in current configuration.} \tag{2.68}$$

Further on for a reversible process in which the internal dissipation $\mathscr{D}_{int}$ is zero, the rate of internal mechanical work $\mathscr{W}_{int}$ equals the time derivative of the Helmholtz free energy $\dot{\Psi}$

$$\dot{\Psi} = \mathscr{W}_{int} = \tilde{\mathbf{T}} : \dot{\mathbf{E}} \qquad \text{in reference configuration} \tag{2.69}$$

$$J^{-1}\,\dot{\Psi} = \mathscr{W}_{int} = \boldsymbol{\sigma} : \mathbf{d} \qquad \text{in current configuration.} \tag{2.70}$$

Table 2.2: Summary of sub-section 2.2.7.

1. Hyperelasticity and viscoelasticity: adiabatic, isentropic and isothermal processes

$$\tilde{\mathbf{T}} : \dot{\mathbf{E}} = \dot{\Psi} \qquad \text{in reference configuration} \tag{2.71}$$

$$\left(\tilde{\mathbf{T}} - \frac{\partial \Psi}{\partial \mathbf{C}}\right) : \frac{1}{2}\,\dot{\mathbf{C}} = 0 \tag{2.72}$$

$$\tilde{\mathbf{T}} = 2\,\frac{\partial \Psi}{\partial \mathbf{C}}. \tag{2.73}$$

Similarly in case of current configuration

$$\boldsymbol{\sigma} = 2\,J^{-1}\,\frac{\partial \Psi}{\partial \mathbf{b}}\,\mathbf{b} \tag{2.74}$$

2. Coupled temperature-displacement: non-adiabatic, non-isentropic and non-isothermal processes

$$\tilde{\mathbf{T}} : \dot{\mathbf{E}} - \dot{\Psi} - \Upsilon\dot{\theta} - \frac{1}{\theta}\,\mathbf{Q}\,\nabla\theta \geq 0 \qquad \text{in reference configuration} \tag{2.75}$$

$$\left(\tilde{\mathbf{T}} - \frac{\partial \Psi}{\partial \mathbf{C}}\right) : \frac{1}{2}\,\dot{\mathbf{C}} - \left(\Upsilon + \frac{\partial \Psi}{\partial \theta}\right)\dot{\theta} - \frac{1}{\theta}\,\mathbf{Q}\,\nabla\theta \geq 0 \tag{2.76}$$

$$\tilde{\mathbf{T}} = 2\,\frac{\partial \Psi}{\partial \mathbf{C}} \quad \text{and} \quad \Upsilon = -\frac{\partial \Psi}{\partial \theta} \tag{2.77}$$

It is assumed that heat conduction follows Fourier's law

$$\mathbf{Q} = -\kappa_0\,\nabla\theta \tag{2.78}$$

where κ_0 is a positive definite thermal conductivity in reference configuration.

Similarly in case of current configuration

$$\boldsymbol{\sigma} = 2\,J^{-1}\,\frac{\partial \Psi}{\partial \mathbf{b}}\,\mathbf{b} \quad \text{and} \quad \Upsilon = -J^{-1}\,\frac{\partial \Psi}{\partial \theta} \tag{2.79}$$

$$\mathbf{q} = -\kappa\,\nabla\theta \tag{2.80}$$

where κ is a positive definite thermal conductivity in current configuration.

Chapter 3

Dynamic Flocculation Model (DFM)

In this chapter the theoretical aspects and essential equations of DFM are briefly described and then the thought of extending the existing model to include the time dependent effects is discussed in the chapter 5. The detailed formulation of this model including incomplete (inner) cycles appearing in arbitrary strain hysteresis can be referred in Lorenz et al. [2012].

As we consider a purely mechanical theory where thermal effects are ignored, for the sake of clarity, the Helmholtz free energy Ψ is replaced by W which is called energy density under adiabatic, isentropic and isothermal conditions.

The free Helmholtz energy density

$$W = (1 - \Phi_{\text{eff}})\, W_R + \Phi_{\text{eff}}\, W_A \tag{3.1}$$

of a filled elastomer can be considered as the sum of a matrix and a filler contribution [Klüppel, 2003]. In this case W_R is calculated for the entropy-elastic rubber phase including hydrodynamic reinforcement by a fraction of rigid filler clusters and W_A denotes the energy-elastic contribution of the fragile agglomerates of filler particles. Furthermore, the quantity Φ_{eff} is the mechanically effective filler volume fraction which is larger than the real volume fraction because of the rubber occluded in the aggregates (non-spherical secondary particles).

3.1 Rubber Elasticity

The material behaviour of the rubber matrix is assumed to be hyperelastic, so that we use the non-affine tube model with non-Gaussian extension [Heinrich et al., 1988, Klüppel and Schramm, 2000] which exhibits the following energy density as a function of the stretch λ_μ:

$$\begin{aligned} W_R(\lambda_\mu) \;=\; & \frac{G_c}{2}\left[\frac{\left(\sum_{\mu=1}^{3}\lambda_\mu^2 - 3\right)\left(1 - n^{-1}\right)}{1 - n^{-1}\left(\sum_{\mu=1}^{3}\lambda_\mu^2 - 3\right)} + \ln\left(1 - n^{-1}\left(\sum_{\mu=1}^{3}\lambda_\mu^2 - 3\right)\right)\right] \\ & + 2\,G_e\left(\sum_{\mu=1}^{3}\lambda_\mu^{-1} - 3\right) \end{aligned} \tag{3.2}$$

The index μ denotes the three main axes whereas the direction $\mu = 1$ is the tensile axis and the directions $\mu = 2$ and $\mu = 3$ are the orthogonal axes. Since this model is strongly physically motivated its free parameters G_c, G_e and n are closely related to the structure of a polymer chain network.

- G_c: cross-link modulus (proportional to the density of network junctions)
- G_e: modulus of topological constraints (proportional to the density of entanglements)
- $\frac{n_e}{T_e} \equiv n$: number of chain segments between two successive trapped entanglements (n_e is the number of segments between entanglements, and T_e is the Langley trapping factor)

The first Piola-Kirchhoff stresses $T_{R,\mu}$ (engineering stresses) is then obtained by differentiating the energy density W_R with respect to the stretch λ_μ. In case of uniaxial extension this yields:

$$\begin{aligned} T_{R,1}(\lambda_1) &= G_c(\lambda_1 - \lambda_1^{-2}) \cdot \left(\frac{1 - 1/n}{\left(1 - \frac{1}{n}\left(\lambda_1^2 + \frac{2}{\lambda_1} - 3\right)\right)^2} - \frac{1/n}{1 - \frac{1}{n}\left(\lambda_1^2 + \frac{2}{\lambda_1} - 3\right)} \right) \\ &\quad + 2G_e(\lambda_1^{-1/2} - \lambda_1^{-2}) \end{aligned} \tag{3.3}$$

3.2 Cluster mechanics in strained rubbers

The presence of filler clusters dispersed in the rubber matrix is considered by a Smoluchowski type of cluster size distribution according to the kinetics of cluster-cluster aggregation processes [Klüppel, 2003]

$$\phi_\mu(\chi) = \frac{4\chi}{\langle\chi_\mu\rangle^2}\, e^{-2\frac{\chi}{\langle\chi_\mu\rangle}}. \tag{3.4}$$

Here the cluster size distribution ϕ is a function of χ which denotes the relative cluster size, and $\chi = \xi/d$ is a ratio of cluster size to particle size. $\langle\chi_\mu\rangle$ denotes the average cluster size in space direction μ. To account for the preconditioning of clusters under compression, it is appropriate to use an anisotropic size distribution as derived by Witten et al. [1993] which states that the clusters deform like the specimen as a whole.

$$\langle\chi_1\rangle = \langle\chi_0\rangle\, \lambda_{1,min} \quad \text{and} \quad \langle\chi_2\rangle = \langle\chi_3\rangle = \frac{\langle\chi_0\rangle}{\sqrt{\lambda_{1,max}}} \tag{3.5}$$

The material parameter χ_0 denotes the initial isotropic average cluster size whereas $\lambda_{1,min}$ and $\lambda_{1,max}$ are the minimum and maximum stretches occurred during the whole loading history.

For a quantitative evaluation of elasticity and strength of filler clusters in elastomers we refer to a concept for the mechanical response of flexible, curved chains as proposed by Kantor and Webman [1984] and extended to percolation clusters by Lin and Lee [1996, 1997]. According to this linear elastic model the force constant k_s of a fractal, flexible filler cluster, relating the force to the displacement, is given by (refer figures 3.1, 3.2 and 3.3):

$$k_s = \frac{F}{\Delta\xi} = \frac{\kappa\,\overline{E}}{d^2}\left(\frac{d}{\xi}\right)^{2+d_{f,b}} \tag{3.6}$$

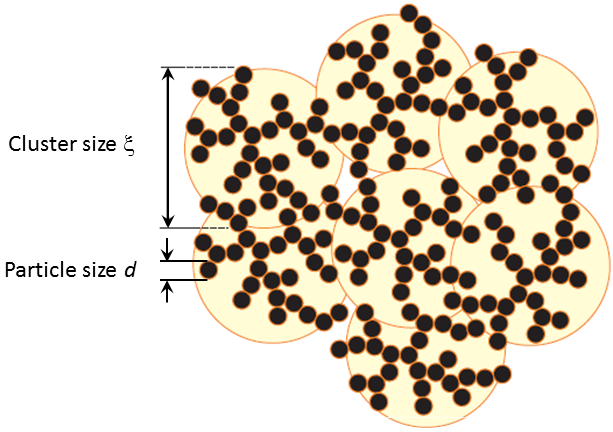

Figure 3.1: Network of overlapped clusters

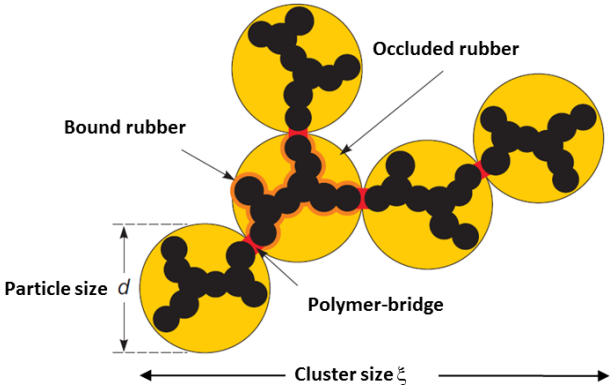

Figure 3.2: Schematic diagram of clusters with filler-filler bonds between primary aggregates; due to the occluded rubber, the effective filler volume fraction is greater than the actual filler fraction [Klüppel, 2003].

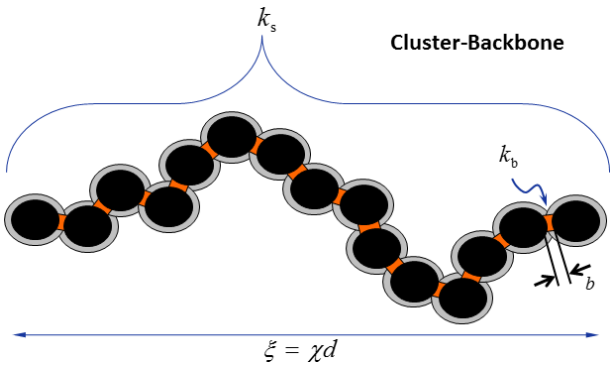

Figure 3.3: Micro-mechanical model of a cluster backbone [Juhre et al., 2013].

Here, $\overline{E}$ is an elastic constant, related to the bending and twisting mode of the filler-filler bonds, κ is a geometry factor of order one, d is particle size and $d_{f,b}$ is the fractal dimension of the cluster backbone that is considered to be non-branched. The elastic modulus of the cluster is then found as:

$$E_A = \xi^{-1} k_s = \frac{\kappa\,\overline{E}}{d^3}\left(\frac{d}{\xi}\right)^{3+d_{f,b}} \tag{3.7}$$

Note that in the case of a linear cluster backbone with $d_{f,b}$=1, equations (3.6) and (3.7) correspond to the well known elastic behaviour of a linear, flexible rod, where the bending modulus falls with the 4th power of the length ξ. The equations (3.6) and (3.7) represent a generalization of this behavior to the case of flexible, curved rods.

The yield stretch λ_s of the cluster follows from the stress equilibrium between the whole cluster and a single bond:

$$(\lambda_s - 1) = \frac{k_b}{k_s}(\lambda_b - 1) = \frac{Q\,(\lambda_b - 1)}{\kappa\,\overline{E}}\left(\frac{\xi}{d}\right)^{2+d_{f,b}} \tag{3.8}$$

where $k_b = \frac{F}{\Delta b} = \frac{Q}{d^2}$ is the force constant and λ_b is the yield stretch of a bond. The elastic constant Q is related to the tension mode of filler-filler bonds. Eq.(3.8) implies that the yield stretch of a filler cluster increases with the size ξ, i. e., large clusters show a high extensibility due to the ability to bend and twist around the single bonds.

To analyse the fracture behaviour of filler clusters in strained polymer networks, we have to evaluate the stretch $\lambda_{A,\mu}$ of the filler clusters relative to the external stretch λ_μ of the sample. At medium and large strains, when a stress induced gel-sol transition of the pervading filler network has taken place, the stress on the filler clusters is transmitted by the rubber matrix. Then, $\lambda_{A,\mu}$ follows from the stress equilibrium between the clusters and the rubber matrix $E_A\ (\lambda_{A,\mu} - 1) = \hat{T}_{R,\mu}(\lambda_\mu)$. This yields with Eq.(3.7) [Klüppel, 2003]:

$$(\lambda_{A,\mu} - 1) = \frac{d^3}{\kappa\,\overline{\overline{E}}} \left(\frac{\xi_\mu}{d}\right)^{3+d_{f,b}} \hat{T}_{R,\mu}(\lambda_\mu), \tag{3.9}$$

where, the stress $\hat{T}_{R,\mu}(\lambda_\mu)$ is the relative stress of the rubber matrix determined by means of Eq.(3.3). It is related to the initial stress at the beginning of each strain cycle, where $\lambda_\mu = \lambda_{\mu,min}$:

$$\hat{T}_{R,\mu}(\lambda_\mu) = T_{R,\mu}(\lambda_\mu) - T_{R,\mu}(\lambda_{\mu,min}) \tag{3.10}$$

A comparison between equations (3.8) and (3.9) makes clear that the stretch $\lambda_{A,\mu}$ of the filler clusters increases faster with their size ξ_μ than the yield stretch λ_s. Accordingly, with increasing strain the large clusters in the system break first followed by the smaller ones. The maximum size ξ_μ of clusters surviving at exposed external stretch λ_μ is estimated by the stress equilibrium between the rubber matrix and the yield stress $T_s = E_A\ (\lambda_s - 1)$ of the clusters [Klüppel, 2003]:

$$\xi_\mu = \frac{Q\,(\lambda_b - 1)}{d^2\,\hat{T}_{R,\mu}(\lambda_\mu)} \tag{3.11}$$

This allows for an evaluation of the boundaries of the integrals in equations (3.15) and (3.20) using the critical cluster size:

$$\chi_{\mu,min}(\lambda_\mu) = \frac{\xi_\mu}{d} = \frac{Q\,(\lambda_b - 1)}{d^3\,\hat{T}_{R,\mu}(\lambda_\mu)} \equiv \frac{s}{\hat{T}_{R,\mu}(\lambda_\mu)} \tag{3.12}$$

Here, Q is the elastic constant due to tensile deformation of cluster bonds and λ_b is the ultimate stretch of the bonds under tensile loading. Accordingly, s is the tensile strength of cluster bonds, which is treated as a fitting parameter. This cluster mechanics holds for the virgin and damaged filler-filler bonds which is shown in the later sections.

3.3 Hydrodynamic Strain Amplification and Stress Softening

The part that is caused by hydrodynamic effects leads to a strain amplification resulting from the fact that the fillers are rigid (undeformable) particles, and consequently, the intrinsic strain

of the polymer is higher than the externally applied strain and therefore only a certain part of rubber matrix would deform under external (global) stretch λ_μ. Thus, the local stretch κ_μ of the rubber matrix is obtained by multiplying the global deformation by the strain amplification factor X_μ:

$$\kappa_\mu = 1 + X_\mu(\lambda_\mu - 1) \tag{3.13}$$

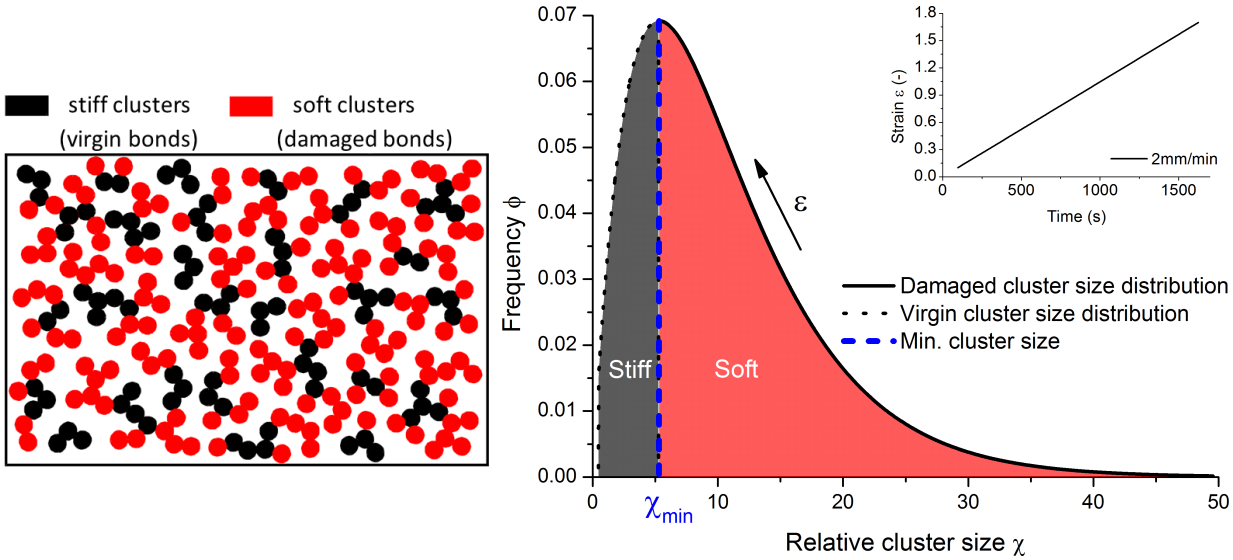

Figure 3.4: Left: schematic representation of stiff and soft clusters in a pre-strained sample [Klüppel, 2003]; right: corresponding location within the cluster size distribution under quasi-static loading ($\dot{\varepsilon} = 0.0017/s$). Inset shows the loading history.

Huber and Vilgis [1999] calculated an amplification factor X for overlapping aggregates of primary spherical filler particles, assuming a fractal aggregate geometry. They found that X is proportional to powers of filler volume fraction and relative aggregate diameter. Because clusters of secondary particles also show a fractal geometry, we can use the same result. Virgin (undamaged) clusters are relatively stiff and immobilize a certain amount of rubber, according to their diameter. The damage of stiff clusters causes stress softening by decreasing X, because soft clusters do not significantly contribute to X. Accordingly, X is expressed as an integral over the stiff section of the cluster size distribution $\phi(\chi(\xi))$ (Fig.3.4) surviving the maximum deformation which the material has been subjected to, so that X is a function of the minimum and maximum deformation.

$$\begin{aligned} X_{max} &= X(\lambda_{\mu,min}, \lambda_{\mu,max}) \\ &= 1 + c\,\phi_{eff}^{\frac{2}{3-d_f}} \cdot \left(\int_0^{\chi_{\mu,min}(\lambda)} \chi^{d_w - d_f} \phi_\mu(\chi) d\chi + \int_{\chi_{\mu,min}(\lambda)}^{\infty} \phi_\mu(\chi) d\chi \right) \end{aligned} \tag{3.14}$$

The constant c is taken from the Einstein relation for spherical inclusions [Einstein, 1906] and is set to c=2.5. The quantity d_w denotes the anomalous diffusion exponent and amounts to $d_w \approx 3.1$ and d_f is the fractal-dimension of the filler cluster with $d_f \approx 1.8$ [Klüppel et al., 1997]. To solve the integrals analytically we make use of the following approximation:

$$d_w - d_f = 1 \Rightarrow X_{max} = 1 + c\,\phi_{eff}^{\frac{2}{3-d_f}} \cdot \left(1 + \int_0^{\chi_{\mu,min}(\lambda)} (\chi - 1)\phi_\mu(\chi) d\chi \right) \tag{3.15}$$

The upper integration limit $\chi_{\mu,min}$ depends on the tensile strength s_v of virgin filler-filler bonds which represents another material parameter (from Eq.(3.12)). The stresses $T_{R,\mu}$ are calculated with the local deformation κ_μ by using the extended non-affine tube model as stated by Eq.(3.3) [Klüppel, 2003]:

$$\chi_{\mu,min}(\lambda_\mu) = \frac{Q_v\,(\lambda_{v,b}-1)}{d^3\,\hat{T}_{R,\mu}(\lambda_{\mu,max})} \equiv \frac{s_v}{T_{R,\mu}(\lambda_{\mu,max}) - T_{R,\mu}(\lambda_{\mu,min})} \tag{3.16}$$

We point out that according to the amplification factor given in equations (3.14) or (3.15) the mechanical reinforcement of clustered and non clustered fillers is much different since the strain amplification factor is larger for clustered fillers. This takes into account that part of the polymer between the spanning arms of the clusters is not deformed and acts as additional filler provided the clusters behave almost rigid. If the clusters break into smaller parts this occluded polymer will also deform more and more, which corresponds to a decrease of the effective filler volume fraction. Accordingly, there is a significant difference between the mechanical reinforcement of clustered and non clustered fillers. Recently, this effect has also been shown experimentally by preparing silica filled rubbers with clusters and without clusters, which was proven to be realized by a special small angle neutron scattering technique combined with reverse Monte Carlo modelling. Interestingly, the modulus of the non-clustered samples was found to be much smaller than that of the clustered one and a Payne effect could only be measured for the clustered samples [Papon et al., 2012]. This demonstrates that the Payne effect is closely related to the breakdown of clustered filler structures.

3.4 Micro-Mechanics of Filler Clusters and Filler-Induced Hysteresis

Concerning the inelastic behaviour it is assumed that the cyclic stretching, breakdown and re-aggregation of soft clusters is the reason for hysteresis, because clusters release potential energy when they break. This can be expressed by the following energy density:

$$W_A(\lambda_\mu) = \sum_{\mu}^{\dot{\lambda}_\mu>0} \frac{1}{2} \int_{\chi_\mu(\lambda_{min},\lambda_{max})}^{\chi_\mu(\lambda)} E_A(\chi)\;(\lambda_{A,\mu}-1)^2\;\phi_\mu(\chi)\,d\chi \tag{3.17}$$

Here, E_A denotes the elastic modulus and $\lambda_{A,\mu}$ the stretch of soft filler clusters. The time derivative appearing in the upper limit of the sum implies, that the sum is taken over stretching directions with $\dot{\lambda}_\mu > 0$, only. Consequently, clusters are strained and successively broken in stretching directions alone. Recovery of the clusters takes place in the directions of compression implying that a cyclic breakdown and re-aggregation of clusters can be described.

The strain of the filler clusters is determined by a stress equilibrium between the rubber matrix and the clusters. For simplicity, we assume linear elastic behaviour of the clusters:

$$E_A(\chi)\;(\lambda_{A,\mu}-1) = \hat{T}_{R,\mu}(\lambda_\mu), \tag{3.18}$$

where, the stress $\hat{T}_{R,\mu}(\lambda_\mu)$ is the relative stress of the rubber matrix determined by means of Eq.(3.3). It is related to the initial stress at the beginning of each strain cycle, where $\lambda_\mu = \lambda_{\mu,min}$:

$$\hat{T}_{R,\mu}(\lambda_\mu) = T_{R,\mu}(\lambda_\mu) - T_{R,\mu}(\lambda_{\mu,min}) \tag{3.19}$$

Finally we calculate the cluster stress $T_{A,\nu}$ in spatial direction ν by differentiating the energy density W_A with respect to the cluster deformation $\lambda_{A,\nu}$. Due to the restriction of the sum in Eq.(3.17) to stretching directions, $T_{A,\nu}$ differs for the up and down cycle since the lateral directions are stretched during the down cycle.

$$\begin{aligned} T_{A,\nu}(\lambda_{A,\nu}) &= \frac{\partial W_A}{\partial \lambda_{A,\nu}} = \sum_\mu \frac{\partial W_A}{\partial \lambda_{A,\mu}} \frac{\partial \lambda_{A,\mu}}{\partial \lambda_{A,\nu}} \\ &= \sum_\mu^{\dot{\lambda}_\mu > 0} \hat{T}_{R,\mu}(\lambda_\mu) \int_{\chi_\mu(\lambda_{min},\lambda_{max})}^{\chi_\mu(\lambda)} \frac{\partial \lambda_{A,\mu}(\chi)}{\partial \lambda_{A,\nu}(\chi)} \, \phi_\mu(\chi) \, d\chi \end{aligned} \tag{3.20}$$

The integration is performed over the fraction of soft filler clusters with a cluster size lying in the interval $\chi_\mu(\lambda_{max}) < \chi_\mu < \chi_\mu(\lambda)$ which are not broken at exposed deformation λ of the actual cycle. The boundary cluster size $\chi_\mu(\lambda)$ is obtained similar to Eq.(3.16), but in this case the tensile strength s_d of damaged filler-filler bonds enters as an additional material parameter (from Eq.(3.12)):

$$\chi_\mu(\lambda_\mu) = \frac{Q_d \, (\lambda_{d,b} - 1)}{d^3 \, \hat{T}_{R,\mu}(\lambda_\mu)} \equiv \frac{s_d}{T_{R,\mu}(\lambda_\mu) - T_{R,\mu}(\lambda_{\mu,min})} \tag{3.21}$$

3.5 Residual Stress

The mechanical behaviour of filled elastomers is also characterized by residual stresses after the material is brought back into its initial configuration. The corresponding stress contribution T_{set} is a function of the minimum and maximum deformation and contains the material parameter $T_{set,0}$ which is always negative:

$$T_{set} = T_{set,0} \left((\lambda_{max} - 1)^{1/2} - |(\lambda_{min} - 1)|^{1/2} \right). \tag{3.22}$$

Thus, the total stresses of the dynamic flocculation model are given by the following three stress contributions:

$$T = (1 - \Phi_{\text{eff}}) \, T_R + \Phi_{\text{eff}} \, T_A + T_{\text{set}} \tag{3.23}$$

To establish a physical relation to the real structure of the material the development of constitutive models considering the microstructure of polymer chains and filler networks are desired. This usually means a huge amount of work, so that physically-based models are often restricted to a one-dimensional formulation describing uniaxial tension only. But the finite element method requires completely three-dimensional constitutive models. Thus, most of the existing material models for filled elastomers are derived phenomenologically. In our case we take the benefit of concept of representative directions for the implementation of the material model into the finite element code [Freund et al., 2011]. The concept of representative directions is briefly discussed in the chapter 4.

Chapter 4

The concept of representative directions

The Dynamic Flocculation Model (DFM) in chapter 3 describes the material behaviour under uniaxial extensions only. In its present form it is not possible to implement it directly into the finite element method. The finite element method requires a tensorial formulation of constitutive model to compute 3-D stress-strain states. Therefore most of the phenomenological models are derived in this form so that they can be directly implemented into FEM. In order to fulfil these conditions the presented model has to be generalized to such a three-dimensional stress-strain relation. This is possible by using the so-called concept of representative directions [Freund et al., 2011]. A brief description of the essential equations with respect to the application of the concept is presented in this chapter. For more detailed description the reader can refer Freund and Ihlemann [2010].

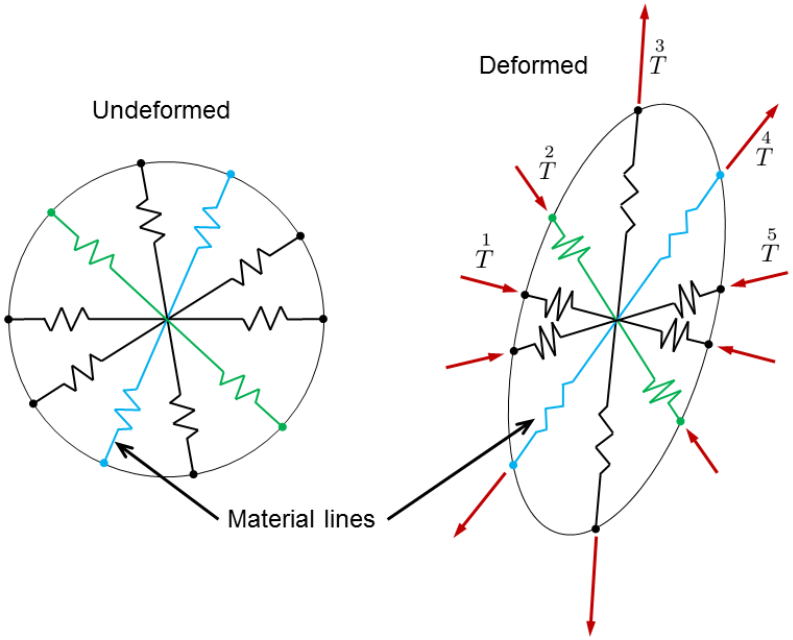

Figure 4.1: Schematic representation of generalization of uniaxial material law into fully three-dimensional stress-states with each material lines representing the uniaxial model in 3-D space.

During the deformation of a component, at each material point there exists an individual state of strain which is fully described by the right Cauchy-Green tensor $\mathbf{C}$ (within the framework of

idealization of continuum mechanics). By using this symmetrical strain tensor the local stretch ratio $\overset{\alpha}{\lambda}$ of any assumed material line along the associated direction $\overset{\alpha}{\mathbf{e}}$ (given in terms of the undeformed configuration) can be calculated for each material point:

$$\overset{\alpha}{\lambda} = \sqrt{\overset{\alpha}{\mathbf{e}}\ \mathbf{C}\ \overset{\alpha}{\mathbf{e}}} \tag{4.1}$$

where α is the space direction.

Similarly the local stretch ratio $\overset{\alpha}{\lambda}_{old}$ from the previous time step (in numerical simulation) is

$$\overset{\alpha}{\lambda}_{old} = \sqrt{\overset{\alpha}{\mathbf{e}}\ \mathbf{C}_{old}\ \overset{\alpha}{\mathbf{e}}}. \tag{4.2}$$

The rate of local stretch ratio $\dot{\overset{\alpha}{\lambda}}$ is then

$$\dot{\overset{\alpha}{\lambda}} = \frac{\overset{\alpha}{\lambda} - \overset{\alpha}{\lambda}_{old}}{\Delta t}. \tag{4.3}$$

For each of the directions $\overset{\alpha}{\mathbf{e}}$ a corresponding uniaxial stress response can be identified by the one-dimensional dynamic flocculation model that is intended to be generalized. As DFM also includes inelastic material characteristics, the 1^{st} PK stresses $\overset{\alpha}{T}$ also depend on some internal variables $\overset{\alpha}{\Gamma}_i$ which relate to each space direction α:

$$\overset{\alpha}{T} = \overset{\alpha}{T}\left(\overset{\alpha}{\lambda}, \dot{\overset{\alpha}{\lambda}}, \overset{\alpha}{\Gamma}_i\right). \tag{4.4}$$

For further numerical calculations it is beneficial to switch to 2^{nd} PK stress in each space direction $\overset{\alpha}{\mathbf{e}}$

$$\overset{\alpha}{\tilde{T}} = \frac{\overset{\alpha}{T}}{\overset{\alpha}{\lambda}}. \tag{4.5}$$

It is postulated that all the uniaxial stress responses achieve the same stress power as the overall stress power concerning the actual external deformation which is given by deformation tensor $\mathbf{C}$. Finally with several conversions yield an equation for calculating the unknown 2^{nd} PK stress tensor

$$\tilde{\mathbf{T}} = \sum_{\alpha=1}^{n} \overset{\alpha}{w}\, \overset{\alpha}{\tilde{T}}\, \overset{\alpha}{\mathbf{e}} \otimes \overset{\alpha}{\mathbf{e}} \tag{4.6}$$

where $\overset{\alpha}{w}$ is the weighting factor.

From a mathematical point of view this equation describes a type of numerical integration on the surface of a sphere. For an efficient integration the so-called representative directional unit vectors $\overset{\alpha}{\mathbf{e}}$ are selected in such a way, that they are evenly distributed in space. If the distribution is not perfectly even, the uniaxial stresses are balanced with appropriate weighting factors $\overset{\alpha}{w}$ which depends on the individual orientation of the associated representative direction. In order to have the same elastic constants for the original and the generalized model, these factors are additionally scaled by a unitary constant w which has a value of 5 for incompressible materials Freund and Ihlemann [2010].

By linearising the constitutive model of Eq.(4.6) it can be shown, that it always describes a compressible material behaviour due to a constant Poisson's ratio of $\nu = 0.25$. Therefore the concept of representative directions can also be extended for the application of quasi incompressible materials like elastomers as well. This is done by limiting the concept itself to pure isochoric deformations while the stress response concerning volume strains is modelled separately.

Therefore, the deviatoric part of deformation tensor $\mathbf{C}$ is considered to calculate the deviatoric stretch ratios

$$\overset{\alpha}{\lambda^*} = \sqrt{\overset{\alpha}{\mathbf{e}}\,\overset{D}{\mathbf{C}}\,\overset{\alpha}{\mathbf{e}}} \tag{4.7}$$

where $\overset{D}{\mathbf{C}}$ is the deviatoric deformation tensor which is

$$\overset{D}{\mathbf{C}} = J^{-2/3}\,\mathbf{C}. \tag{4.8}$$

The corresponding modified stress in each representative direction is

$$\overset{\alpha}{\tilde{T}^*} = \frac{\overset{\alpha}{T^*}\left(\overset{\alpha}{\lambda^*}, \dot{\overset{\alpha}{\lambda^*}}, \overset{\alpha}{\Gamma_i}\right)}{\overset{\alpha}{\lambda^*}}. \tag{4.9}$$

The total stresses of the modified constitutive model are given by

$$\tilde{\mathbf{T}}^* = \sum_{\alpha=1}^{n} \overset{\alpha}{w}\,\overset{\alpha}{\tilde{T}^*}\,\overset{\alpha}{\mathbf{e}} \otimes \overset{\alpha}{\mathbf{e}}\,. \tag{4.10}$$

Finally the deviatoric stresses are calculated using

$$\overset{D}{\tilde{\mathbf{T}}} = Dev\left(\tilde{\mathbf{T}}^* \cdot \overset{D}{\mathbf{C}}\right) \cdot \mathbf{C}^{-1} = J^{-2/3}\,\tilde{\mathbf{T}}^* - \frac{1}{3}\,tr\left(\tilde{\mathbf{T}}^* \cdot \overset{D}{\mathbf{C}}\right) \cdot \mathbf{C}^{-1}. \tag{4.11}$$

On the other hand the volumetric stress tensor

$$\overset{V}{\tilde{\mathbf{T}}} = -p_v\,J\,\mathbf{C}^{-1} \tag{4.12}$$

where the compressibility can be freely adjusted by the hydrostatic pressure function $p_v = -\frac{\partial \psi^V}{\partial J} = -K_{mod}\,(J-1)$ of the volume ratio J. ψ^V is the volumetric part of free energy density and it is considered to be of the form $\frac{K_{mod}}{2}\,(J-1)^2$. For the numerical calculations, the compression modulus K_{mod} can be set to $1000MPa$, so that we have nearly incompressible behaviour.

The equations (4.11) and (4.12) yield the total stress

$$\tilde{\mathbf{T}} = \overset{D}{\tilde{\mathbf{T}}} + \overset{V}{\tilde{\mathbf{T}}}\,. \tag{4.13}$$

Because the derivation of Eq.(4.6) is based on the correspondence between the continuum-mechanical stress power and the summed up uniaxial stress powers, the generalization procedure retains the thermodynamic consistency of the original model. Hence, the concept of representative directions is applicable to any inelastic material model without the need of knowing the associated free energy.

Chapter 5

Extended Dynamic Flocculation Model

5.1 Viscoelasticity

In order to include the time dependent properties into the material model we have to highlight some important relations in the constitutive equations of the model, i.e. the filler-filler interaction during the loading process. The experimental investigation of microstructure of filled NR by Omnes et al. [2008] considering the increase of both the filler volume fraction and the filler specific surface on the reinforcement effect shows an increase of the elastic modulus, the tensile strength and the hysteresis. In addition, the work contribution of Fröhlich et al. [2005], Leblanc [2002], Donnet [2003] characterize the rubber reinforcement phenomenon through rubber process analysis, rheological analysis and physical experiments, which influences the dynamic and mechanical properties of the material. All these investigations relate the cause to filler-filler and filler-rubber interactions.

Further on the investigations of Fritzsche and Klüppel [2011a] in Fig.5.1 show that the storage modulus G' of unfilled elastomer above glass transition temperature θ_g of matrix rubber shows no dependency over the temperature/frequency (time) domain, where it remains nearly constant in this region (rubber elastic plateau). In contrast, the loss modulus G'' is very small and remains decreasing even above θ_g thereby showing its temperature/frequency dependency. The temperature/frequency dependency of G' for filled elastomers is more pronounced with respect to the amount of filler concentration in the material and it is vise versa in case of G'' where the dependency reduces with increase in filler content. The G'' data of rubber compounds with low/no filler content i.e., 0phr and 20phr in Fig.5.1, which is measured at low frequencies contains noise in data. This is because of the limitations of the machine which can not be able to measure such a low value of loss factor $\tan\delta = \frac{G''}{G'}$ of order 10^{-2}. The vertical line above the glass transition temperature θ_g in Fig.5.1 shows the limit of the model which coincides with the end of plateau of unfilled rubber (here it is approximately $500 - 600Hz$). The loss modulus G'' which corresponds to the hysteresis is more pronounced with the increase of filler content and in the Fig.5.1 the difference of G'' data of unfilled to highly filled rubber compound is approximately a factor of 10^2. The viscoelastic response of filled elastomers in the low frequency regime (Fig.5.1) reflects the viscoelastic nature of filler-filler bonds that can be traced back to the mechanical response of glassy-like polymer bridges which become stiffer with increasing frequency [Fritzsche and Klüppel, 2011a]. Hence, the matrix rubber does not give a significant contribution to the time-dependent stress contribution of the filled elastomer due to the fact that the origin of time-dependent phenomenon can be traced to filler-filler interaction. In addition, the range of

material response is restricted to above θ_g as the material only couples the entropy-elastic part of polymer network with the filler-filler interaction. Therefore in this paper the parameters of DFM representing the strength of damaged (s_d) and virgin (s_v) clusters are being made time-dependent. The detailed description of necessary relations derived for the constitutive equations of the model can be referred in Juhre et al. [2013].

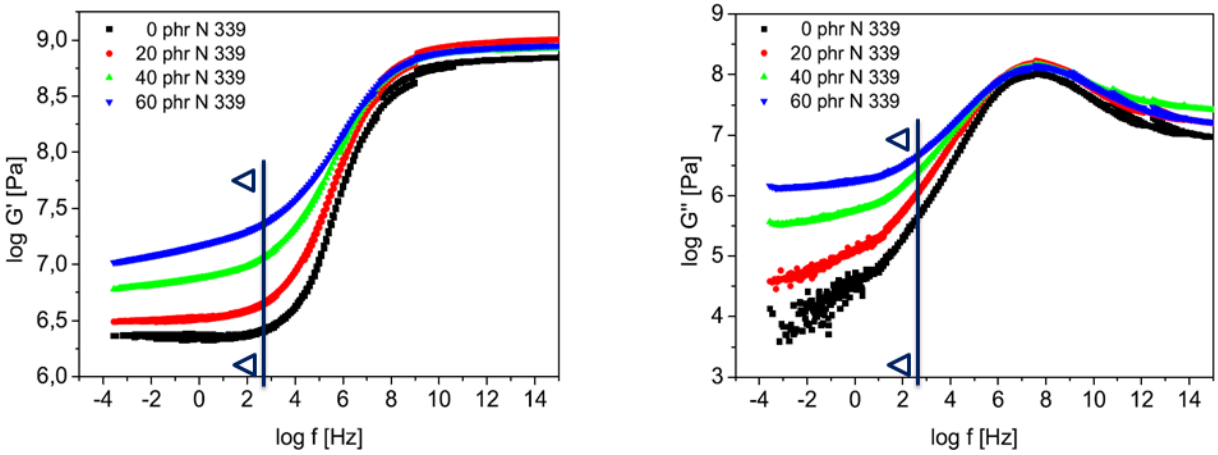

Figure 5.1: Frequency dependent master curve of filled and unfilled S-SBR compounds at amplitude of 0.5% [Fritzsche and Klüppel, 2011a]. The vertical line above θ_g showing the limit of model.

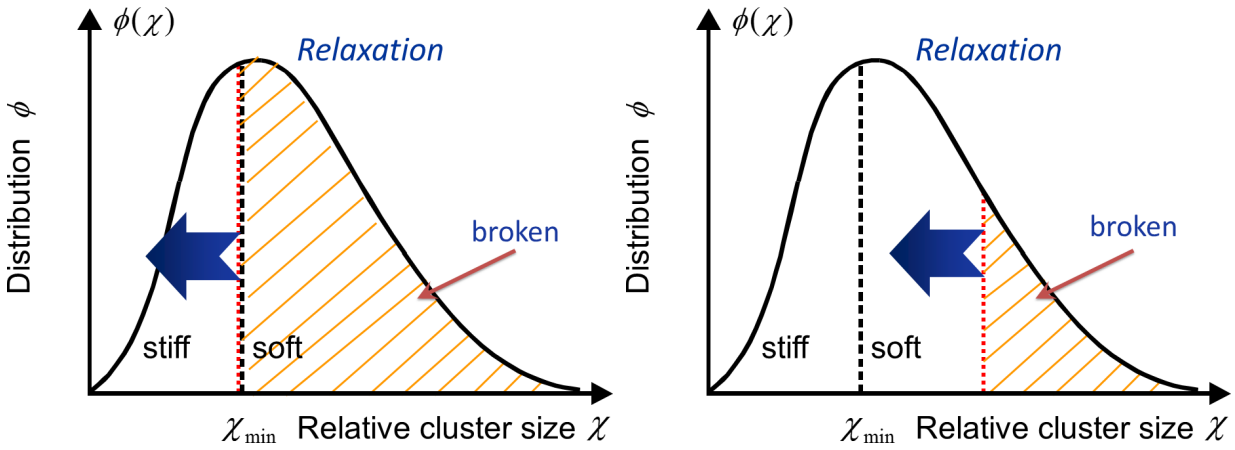

Figure 5.2: Left: relaxation of stiff clusters when $\dot{\varepsilon} = 0$ at the maximum load (upper boundary); right: relaxation of soft clusters when $\dot{\varepsilon} = 0$ between the max-min loading history.

For realizing these considerations in the model, in Eq.(3.15) we integrate over the stiff section of the cluster size distribution $\phi(\chi)$ surviving the maximum deformation which the material has been subjected to and where as in Eq.(3.20) the integral is over the re-aggregated section of the cluster size distribution $\phi(\chi)$ which has sustained under the currently acting stress, in each space direction μ where clusters are being stretched. Here the cluster size distribution ϕ is a function of χ, where $\chi = \xi/d$ is a ratio of cluster size to particle size. At the maximum load where ξ is minimum, represents the upper boundary of broken clusters where they have no stress contribution. Therefore it is assumed that at this boundary the stress relaxation is mainly contributed by stiff clusters (Fig.5.2-left and Fig.5.3). Hence rewriting the Eq.(3.15) and

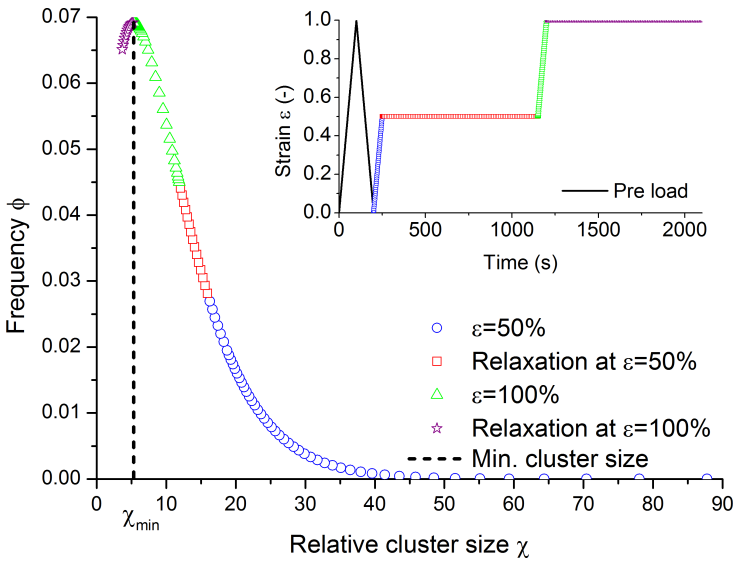

Figure 5.3: Relaxation of stiff and soft clusters under time dependent loading ($\dot{\varepsilon} = 0.017/s$); red squares: relaxation of soft clusters ($\dot{\varepsilon} = 0$) between the max-min loading history; purple stars: relaxation of stiff clusters ($\dot{\varepsilon} = 0$) at the maximum load (upper boundary). Inset shows the loading history ($v = 20mm/min$).

Eq.(3.16) as

$$X_{max} = 1 + c\ \phi_{eff}^{\frac{2}{3-d_f}} \cdot \left(1 + \int_0^{\chi_{\mu,min}(\lambda,t)} (\chi - 1)\phi_\mu(\chi) d\chi\right) \tag{5.1}$$

$$\chi_{\mu,min}(\lambda_\mu, t) = \frac{s_v(t)}{T_{R,\mu}(\lambda_{\mu,max}) - T_{R,\mu}(\lambda_{\mu,min})} \tag{5.2}$$

where $s_v(t)$ is the time-dependent parameter of DFM representing stiff or virgin cluster strength.

Analogous to this, when the loading on the material is between the maximum-minimum boundaries of the entire deformation history, then the stress relaxation is mainly because of the contribution of damaged clusters as the virgin clusters do not play an influential role at this region (Fig.5.2-right and Fig.5.3). Following the footsteps of virgin clusters, we can rewrite Eq.(3.20) and Eq.(3.21) as

$$T_{A,\nu}(\lambda_{A,\nu}, t) = \sum_{\mu}^{\dot{\lambda}_\mu > 0} \hat{T}_{R,\mu}(\lambda_\mu, t) \int_{\chi_\mu(\lambda_{min},\lambda_{max})}^{\chi_\mu(\lambda,t)} \frac{\partial \lambda_{A,\mu}(\chi)}{\partial \lambda_{A,\nu}(\chi)} \phi_\mu(\chi)\, d\chi \tag{5.3}$$

$$\chi_\mu(\lambda_\mu, t) = \frac{s_d(t)}{T_{R,\mu}(\lambda_\mu) - T_{R,\mu}(\lambda_{\mu,min})} \tag{5.4}$$

where $s_d(t)$ is the time-dependent parameter of DFM representing damaged or soft cluster strength.

In this case we assume that the time-dependent relative stress of the rubber matrix is approximately equal to the equilibrium stress between rubber matrix and the clusters:

$$\hat{T}_{R,\mu}(\lambda_\mu, t) \approx \hat{T}_{R,\mu}(\lambda_\mu) \tag{5.5}$$

and only the integral over cluster size distribution $\phi(\chi)$ will be time dependent.

The continuous rupture of filler bondings during the application of a constant load, which is macroscopically observed as a relaxation process can be implemented into the present DFM model either by a steady decrease of the ultimate cluster strain ε_A or by a reduction of the elastic stiffness. If we consider a filler-filler bonding under tension, either the potential energy of several clusters is dissipated during breakage of bondings or the potential energy of all clusters decreases due to a reduced elastic stiffness. Both effects can appear at the same time, but it is very difficult to separate and independently characterize these effects. Thus, in Juhre et al. [2013] and Raghunath et al. [2016] the focus was on an approach to build up a time-dependent function of the cluster strength s. For this purpose s is additively decomposed into an equilibrium part and a time-dependent part, respectively:

$$s(t) = s_{eq} + s_t. \tag{5.6}$$

The change of s_t during time is not explicitly measurable because there is no physical experimental investigation available to characterize this quantity. However, the cluster stress $T_{A,1}(t)$ in tension can be characterized e.g. by stress-relaxation tests at different strain levels and temperatures. Experimental studies at 40% strain indicate that the stress relaxation can be very well approximated by the power function [Lorenz, 2012, Juhre et al., 2013]:

$$T(t) = T_\infty + at^{-\beta}. \tag{5.7}$$

Due to the entropic properties of the matrix, the equilibrium stress T_∞ is depending on the strain level λ and the temperature θ. The cluster stress $T_{A,1}(t) = at^{-\beta}$ correlates with the upper integration limit $\chi_1(t)$ in Eq.(5.1) and Eq.(5.3), which is changing in time.

The time dependent part of the cluster strength can be written as

$$s_t \Rightarrow s(\dot{\lambda}, t) = \dot{s}_t \cdot \Delta t. \tag{5.8}$$

As the time dependent cluster stress $T_{A,1}(t)$ follows a power law, it makes sense to assume that the time-dependent integration boundary and hence the cluster strength s_t of the glassy-like polymer bridge also fulfills a power law. In addition, s_t should increase with the strain rate $|\dot{\lambda}|$, because faster deformation of the glass-like polymer bridges should deliver higher strength values. This motivates the following differential equation for the cluster strength s_t:

$$\dot{s}_t = -\frac{1}{\tau} s_t^N, \quad \text{when} \quad \dot{\lambda} = 0 \tag{5.9}$$

$$\dot{s}_t = \frac{1}{\tau}\left(\eta|\dot{\lambda}| - s_t^N\right), \quad \text{when} \quad \dot{\lambda} \neq 0, \tag{5.10}$$

where τ and η are the fitting parameters describing the relaxation behaviour and viscous response of the polymer bridges. N is a fitting exponent. Here s_t corresponds to an internal variable of the model. At $\dot{\lambda} = 0$, the differential equation $\dot{s}_t$ in Eq.(5.9) shows power law type of relaxation behaviour.

Therefore, based on Eq.(5.6), decomposing the strengths of damaged and virgin clusters into an equilibrium part and a time-dependent part as

$$s_d(t) = s_{d,eq} + s_{d,t} \tag{5.11}$$

$$s_v(t) = s_{v,eq} + s_{v,t}. \tag{5.12}$$

The corresponding time-dependent part can be written as

$$s_d(\dot{\lambda}, t + \Delta t) = \frac{1}{\tau_d}\left(\eta_d|\dot{\lambda}| - s_d^N(\dot{\lambda}, t)\right) \cdot \Delta t. \tag{5.13}$$

Similarly for virgin cluster,

$$s_v(\dot{\lambda}, t + \Delta t) = \frac{1}{\tau_v}\left(\eta_v|\dot{\lambda}| - s_v^N(\dot{\lambda}, t)\right) \cdot \Delta t. \tag{5.14}$$

We point out that the dynamical response of the cluster strengths given by equations (5.13) and (5.14) are dominating the stress-strain properties of the samples as long as the modulus of the rubber matrix exhibits no pronounced temperature or frequency dependency, i.e. in the rubber elastic plateau regime. This low frequency regime is indicated by the vertical lines (with arrows) in Fig.5.1, where the modulus of the unfilled sample shows almost no frequency response. For larger frequencies in the glass transition range the viscoelastic modulus of the rubber matrix increases substantially and delivers additional contributions to the dynamic response of filled rubber samples, which are not considered in the present theory. Instead, the theory delivers the hysteresis response at medium and large strains which normally play a role for technical applications up to several hundred Hertz. The combination of large frequencies and high amplitudes may appear in extreme cases, only.

5.2 Thermo-hyperelasticity

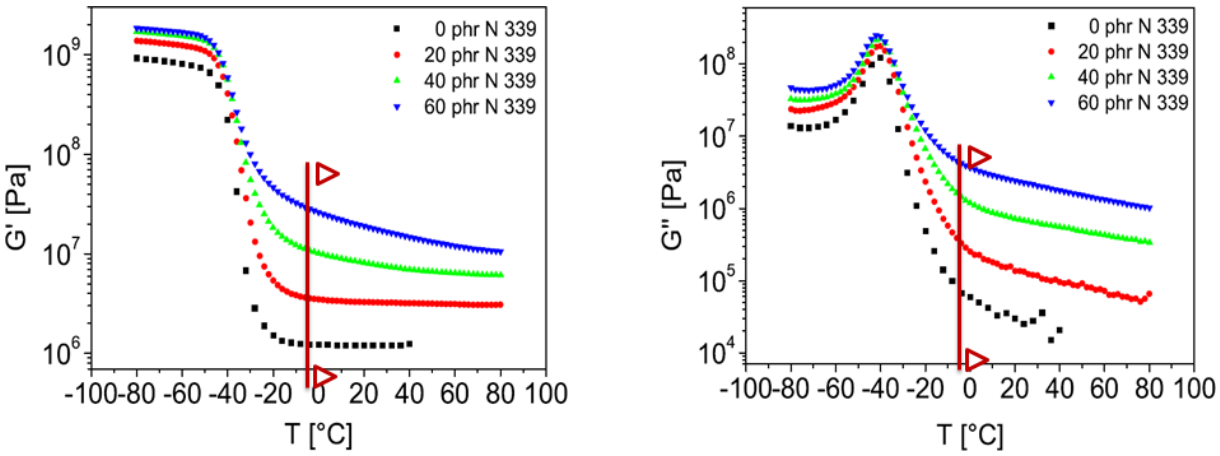

Figure 5.4: Temperature dependent master curve of filled and unfilled S-SBR compounds at frequency of $f = 1Hz$ and amplitude of 0.5% [Fritzsche and Klüppel, 2011a]. The vertical line above θ_g showing the limit of model.

In this section the temperature dependency of DFM parameters without time-dependent effects are considered. The master curves in Fig.5.4 are the same as in Fig.5.1 which describes the mechanical behaviour of filled and unfilled polymers on temperature scale. Accordingly, the rubber matrix can be considered to be independent of temperature in the range that is well

above θ_g (marked as a vertical line in Fig.5.4). Hence the temperature dependence of filled elastomer has been linked to the filler-filler bonds [Klüppel et al., 2005, Lorenz et al., 2012] and the rubber matrix is largely kept out of the equation. But this assumption is reconsidered because, in reference to the relaxation experiments in Lorenz [2012], the long term relaxation stress in the finite strain region increases with respect to temperature. This stress corresponds to T_∞ in Eq.(5.7). This phenomenon is due to change in entropic properties of matrix depending on temperature.

Therefore in addition to the Arrhenius dependence of filler-filler bonds (determined at small strain amplitudes), moduli of rubber matrix are also considered to be temperature dependent. According to thermo-physical properties of polymers [Klüppel, 2003] the moduli of rubber elasticity G_c and G_e in Eq.(3.3) and their relationship with temperature can be written as

$$G_c = \frac{1}{2}\nu_c\, k_B\, \theta, \tag{5.15}$$

$$G_e = \frac{1}{\sqrt{6}} R\, \theta\, \frac{\rho}{M_s\, n_e}, \tag{5.16}$$

where ν_c is the chain density, k_B is Boltzmann constant, R is Gas constant, M_s is the molar mass, n_e is the number of segments between entanglements and θ is the temperature. In both the cases, moduli are directly proportional and linearly dependent on temperature.

The experimental study of filled elastomers have shown an Arrhenius dependent temperature behaviour of elastic modulus [Kraus, 1965]. In agreement with the small strain dynamic behaviour, the thermal dependency of mechanical properties such as stress softening and filler induced hysteresis results from the thermal activation energy of glassy-like polymer bridges (detailed description in subsection 8.5.2). In the DFM, the Arrhenius-like dependence of filler-filler bonds with respect to change in temperature can be characterised as the Arrhenius dependency of virgin and damaged cluster strengths in the form

$$s_d(\theta) = s_{d,ref} \cdot e^{\frac{E_d}{R}\left(\frac{1}{\theta} - \frac{1}{\theta_{ref}}\right)}, \tag{5.17}$$

$$s_v(\theta) = s_{v,ref} \cdot e^{\frac{E_v}{R}\left(\frac{1}{\theta} - \frac{1}{\theta_{ref}}\right)}, \tag{5.18}$$

where E_d and E_v are the activation energies of damaged and virgin clusters bonds, respectively. $s_{d,ref}$ and $s_{v,ref}$ are the reference strengths of damaged and virgin clusters bonds at reference temperature θ_{ref}. R is the gas constant and θ is the current temperature.

In addition to the filler-filler bonds, the inelastic behaviour like set stress is also temperature dependent and using the empirical form in Eq.(3.22) we can write $T_{set,0}(\theta)$ as

$$T_{set,0}(\theta) = T_{set,0,ref} \cdot \left(\frac{\theta_{ref} - \theta_g}{\theta - \theta_g}\right), \tag{5.19}$$

where $T_{set,0,ref}$ is the reference material parameter and θ_g is the glass transition temperature.

5.3 Thermo-viscoelasticity

The experimental studies of Lorenz [2012] at different temperatures and the corresponding approximation of stress relaxation behaviour using power function leads to rewriting of the Eq.(5.7)

as

$$T(t,\theta) = T_{\infty}(\theta) + a(\theta)\, t^{-\beta}. \tag{5.20}$$

The second part in the Eq.(5.20) not only corresponds to the time dependent deformation of cluster bonds but also to the temperature dependency. Therefore from the time-temperature superposition principle, the Arrhenius-like dependence of filler-filler bonds with respect to change in temperature can be characterised using the relaxation time τ. Therefore the equations (5.13) and (5.14) can be rewritten as

$$s_d(\dot{\lambda}, t+\Delta t, \theta) = \frac{1}{\tau_d(\theta)} \left(\eta_d |\dot{\lambda}| - s_d^N(\dot{\lambda}, t, \theta) \right) \cdot \Delta t, \tag{5.21}$$

$$s_v(\dot{\lambda}, t+\Delta t, \theta) = \frac{1}{\tau_v(\theta)} \left(\eta_v |\dot{\lambda}| - s_v^N(\dot{\lambda}, t, \theta) \right) \cdot \Delta t. \tag{5.22}$$

The relaxation times $\tau_d(\theta)$ and $\tau_v(\theta)$ are therefore of the form

$$\tau_d(\theta) = \tau_{d,ref} \cdot e^{\frac{E_d}{R}\left(\frac{1}{\theta} - \frac{1}{\theta_{ref}}\right)}, \tag{5.23}$$

$$\tau_v(\theta) = \tau_{v,ref} \cdot e^{\frac{E_v}{R}\left(\frac{1}{\theta} - \frac{1}{\theta_{ref}}\right)}. \tag{5.24}$$

Chapter 6

Coupled temperature-displacement

From the cited literatures in introductory text, it has been mentioned that not only the mechanical properties of elastomers significantly depend on the temperature, but also the material heats up under large dynamic deformations there by affecting the temperature fields. Therefore, an elastomer's behaviour can not be described sufficiently by an isothermal approach, but a detailed thermo-viscoelastic modelling is required.

In this chapter the coupling of mechanical dissipation to the temperature rise and the temperature to the change in mechanical properties are considered. In the first section of the chapter a simple phenomenological model called Zener is formulated for fully coupled thermo-viscoelastic simulation. This is useful in understanding the development and implementation of the necessary constitutive equations into the finite element package. Detailed explanation on the implementation of stresses, material tangent, dissipation and entropy is given in the next chapter.

6.1 Zener model

The self heating due to loss of energy during viscoelastic deformation of the material is modelled generally with a additive split of free energy function as well as multiplicative split of deformation gradient into an elastic and inelastic or plastic parts [Reese and Govindjee, 1998b, Johlitz et al., 2015, Dippel et al., 2014, Balzani et al., 2015]. The stress power of the viscous part from the energy inequality is then considered to calculate the self heating driven by the energy dissipation. The formulation is provided in both Lagrangian and Eulerian configurations.

6.1.1 Kinematics

In a first step, a twofold multiplicative split of the deformation gradient is performed to be able to describe both mechanical and thermal deformations. As most of the rubber-like materials are nearly incompressible ($\nu = 0.499$ and $J \neq 1$), it is numerically more efficient to split the energy function into a volumetric and a deviatoric parts. Accordingly the multiplicative decomposition of deformation gradient $\mathbf{F}$ into deviatoric $\hat{\mathbf{F}}$ and volumetric $\bar{\mathbf{F}}$ parts is given by

$$\mathbf{F} = \hat{\mathbf{F}}\,\bar{\mathbf{F}}, \tag{6.1}$$

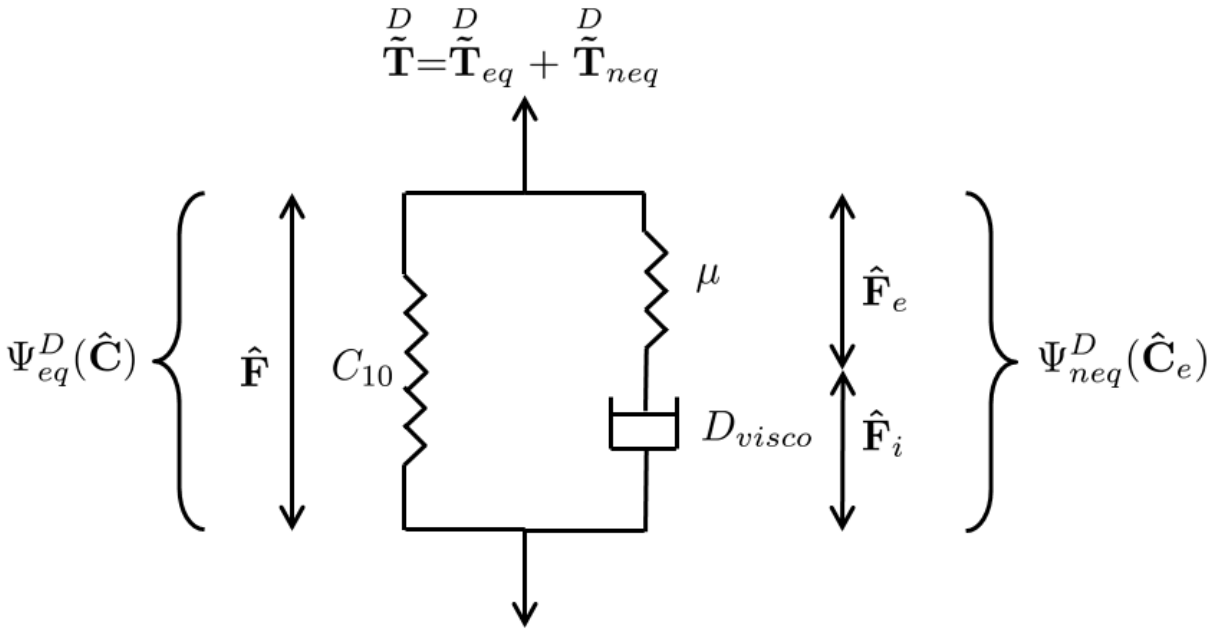

Figure 6.1: Schematic representation of Zener type model consisting of an equilibrium resistance acting in parallel with a time-dependent resistance.

and the determinant is

$$det\mathbf{F} = J. \tag{6.2}$$

The deviatoric part of $\mathbf{F}$ is

$$\hat{\mathbf{F}} = J^{-1/3}\,\mathbf{F}. \tag{6.3}$$

As is standard, we assume that

$$det\hat{\mathbf{F}} = 1. \tag{6.4}$$

The volumetric part of $\mathbf{F}$ and its determinant is

$$\bar{\mathbf{F}} = J^{1/3}\,\mathbf{I} \tag{6.5}$$

$$det\bar{\mathbf{F}} = J. \tag{6.6}$$

The right Cauchy-Green deformation tensor and its determinant is

$$\mathbf{C} = \mathbf{F}^T\,\mathbf{F} \tag{6.7}$$

$$det\mathbf{C} = J^2. \tag{6.8}$$

The deviatoric part of $\mathbf{C}$ and its determinant is

$$\hat{\mathbf{C}} = J^{-2/3}\,\mathbf{C} = \hat{\mathbf{F}}^T\,\hat{\mathbf{F}} \tag{6.9}$$

$$det\hat{\mathbf{C}} = 1. \tag{6.10}$$

Now further decomposition of deviatoric deformation gradient $\hat{\mathbf{F}}$ into an another intermediate configuration of elastic $\hat{\mathbf{F}}_e$ and inelastic $\hat{\mathbf{F}}_i$ parts yields

$$\hat{\mathbf{F}} = \hat{\mathbf{F}}_e \, \hat{\mathbf{F}}_i. \tag{6.11}$$

The associated inelastic right Cauchy-Green deformation tensor $\hat{\mathbf{C}}_i$ and its inverse can be given as

$$\hat{\mathbf{C}}_i = \hat{\mathbf{F}}_i^T \, \hat{\mathbf{F}}_i \tag{6.12}$$

$$\hat{\mathbf{C}}_i^{-1} = \hat{\mathbf{F}}_i^{-1} \, \hat{\mathbf{F}}_i^{-T}. \tag{6.13}$$

The corresponding elastic right Cauchy-Green deformation tensor $\hat{\mathbf{C}}_e$ can be given as

$$\hat{\mathbf{C}}_e = \hat{\mathbf{F}}_e^T \, \hat{\mathbf{F}}_e = \hat{\mathbf{F}}_i^{-T} \, \hat{\mathbf{F}}^T \, \hat{\mathbf{F}} \, \hat{\mathbf{F}}_i^{-1} = \hat{\mathbf{F}}_i^{-T} \, \hat{\mathbf{C}} \, \hat{\mathbf{F}}_i^{-1}. \tag{6.14}$$

6.1.2 Helmholtz free energy

In this subsection a thermodynamically consistent constitutive relations for thermo-viscoelastic Zener model undergoing finite deformations is presented. Although the Zener model reproduces linear viscoelasticity, as an initial approach towards thermo-mechanical coupling we could apply finite deformations. Accordingly, the Helmholtz free energy function for the Zener model can be given as

$$\Psi = \Psi^D + \Psi^V + \Psi^C + \Psi^\theta \tag{6.15}$$

where Ψ^D is the deviatoric part of Ψ which consists of long-term free-energy at equilibrium Ψ^D_{eq} (at time $t \to \infty$) when the material responds perfectly elastic, and Ψ^D_{neq} represents the free-energy that characterizes the non-equilibrium state which provides the creep and relaxation behaviour. The Ψ^D function can be written as

$$\Psi^D = \Psi^D_{eq} + \Psi^D_{neq} = C_{10} \, (\widehat{\mathbf{I}}_\mathbf{1} - 3) + \frac{\mu(\theta)}{2} \, (\widehat{\mathbf{I}}^\mathbf{e}_\mathbf{1} - 3) \tag{6.16}$$

where $\widehat{\mathbf{I}}_\mathbf{1}$ and $\widehat{\mathbf{I}}^e_\mathbf{1}$ are the first invariants of equilibrium and non-equilibrium parts of Ψ^D and they can be written as

$$\widehat{\mathbf{I}}_\mathbf{1} = (J^{-2/3} \, \mathbf{C}) : \mathbf{I}, \tag{6.17}$$

$$\widehat{\mathbf{I}}^e_\mathbf{1} = (J^{-2/3} \, \mathbf{C}_e) : \mathbf{I}. \tag{6.18}$$

Similarly in current state or Eulerian form can be written as

$$\widehat{\mathbf{I}}_\mathbf{1} = (J^{-2/3} \, \mathbf{b}) : \mathbf{I}, \tag{6.19}$$

$$\widehat{\mathbf{I}}^e_\mathbf{1} = (J^{-2/3} \, \mathbf{b}_e) : \mathbf{I}. \tag{6.20}$$

C_{10} and $\mu(\theta)$ are the material parameters of equilibrium and non-equilibrium parts and the Arrhenius dependency of the parameter $\mu(\theta)$ can be given as

$$\mu(\theta) = \mu_0 \, e^{\frac{E_a}{R} \left(\frac{1}{\theta} - \frac{1}{\theta_{ref}} \right)} \tag{6.21}$$

where E_a is the activation energy, R is universal gas constant, θ is the absolute temperature and θ_{ref} is the reference temperature.

The volumetric part can be given as

$$\Psi^V = \frac{K_{mod}}{2}\,(J-1)^2. \tag{6.22}$$

The so-called thermoelastic effect which describes the correlation between the temperature and a volume change in the material can be given as

$$\Psi^C = -3\,\alpha_T\,(\theta-\theta_{ref})\,\frac{\partial \Psi^V}{\partial J}. \tag{6.23}$$

This coupled part depends on θ and J. The material parameter α_T is the thermal expansion coefficient.

The last term in Eq.(6.15) only depends on the temperature θ and can be given as

$$\Psi^\theta = C_p\,\rho\,\left[\theta\left\{1-ln\left(\frac{\theta}{\theta_{ref}}\right)\right\}-\theta_{ref}\right] \tag{6.24}$$

where C_p is the heat capacity and ρ is the material density.

6.1.3 Clausius-Duhem inequality (Lagrangian)

From here on the constitutive equations are derived in both Lagrangian as well as Eulerian formulations. The Clausius-Duhem inequality from Eq.(2.55) in reference state can be rewritten as

$$\tilde{\mathbf{T}} : \dot{\mathbf{E}} - \dot{\Psi} - \Upsilon\,\dot{\theta} - \frac{1}{\theta}\,\mathbf{Q}\,\nabla\theta \geq 0$$

Accordingly the rate of free energy function in Eq.(6.15) is

$$\begin{aligned}\dot{\Psi} &= \frac{\partial \Psi^D_{eq}}{\partial \mathbf{C}} : \dot{\mathbf{C}} + \frac{\partial \Psi^D_{neq}}{\partial \mathbf{C}_e} : \dot{\mathbf{C}}_e + \frac{\partial \Psi^D_{neq}}{\partial \theta}\,\dot{\theta} \\ &+ \frac{1}{2}\,J\,\frac{\partial \Psi^V}{\partial J}\,\mathbf{C}^{-1} : \dot{\mathbf{C}} + \frac{1}{2}\,J\,\frac{\partial \Psi^C}{\partial J}\,\mathbf{C}^{-1} : \dot{\mathbf{C}} + \frac{\partial \Psi^C}{\partial \theta}\dot{\theta} + \frac{\partial \Psi^\theta}{\partial \theta}\dot{\theta}.\end{aligned} \tag{6.25}$$

The elastic right Cauchy-Green deformation tensor $\mathbf{C}_e$ can be written as

$$\mathbf{C}_e = \mathbf{F}_i^{-T}\,\mathbf{C}\,\mathbf{F}_i^{-1}, \tag{6.26}$$

and therefore,

$$\mathbf{C} = \mathbf{F}_i^T\,\mathbf{C}_e\,\mathbf{F}_i. \tag{6.27}$$

The rate of $\mathbf{C}$ is then

$$\begin{aligned}\dot{\mathbf{C}} &= \mathbf{F}_i^T\,\mathbf{C}_e\,\dot{\mathbf{F}}_i + \mathbf{F}_i^T\,\dot{\mathbf{C}}_e\,\mathbf{F}_i + \dot{\mathbf{F}}_i^T\,\mathbf{C}_e\,\mathbf{F}_i \\ &= \mathbf{F}_i^T\,\mathbf{C}_e\,\underbrace{\dot{\mathbf{F}}_i\,\mathbf{F}_i^{-1}}_{=\mathbf{l}_i}\,\mathbf{F}_i + \mathbf{F}_i^T\,\dot{\mathbf{C}}_e\,\mathbf{F}_i + \mathbf{F}_i^T\,\underbrace{\mathbf{F}_i^{-T}\,\dot{\mathbf{F}}_i^T}_{=\mathbf{l}_i^T}\,\mathbf{C}_e\,\mathbf{F}_i \\ &= \mathbf{F}_i^T\,\dot{\mathbf{C}}_e\,\mathbf{F}_i + \mathbf{F}_i^T\,(\mathbf{C}_e\,\mathbf{l}_i + \mathbf{l}_i^T\,\mathbf{C}_e)\,\mathbf{F}_i \\ &= \mathbf{F}_i^T\,\dot{\mathbf{C}}_e\,\mathbf{F}_i + \mathbf{F}_i^T\,2\,\mathbf{C}_e\,\mathbf{d}_i\,\mathbf{F}_i.\end{aligned} \tag{6.28}$$

Rewriting the previous equation results in

$$\dot{\mathbf{C}}_e = \mathbf{F}_i^{-T}\,\dot{\mathbf{C}}\,\mathbf{F}_i^{-1} - 2\,\mathbf{C}_e\,\mathbf{d}_i. \tag{6.29}$$

Equating Eq.(6.29) into Eq.(6.25) yields

$$\begin{aligned}\dot{\Psi} &= \frac{\partial \Psi^D_{eq}}{\partial \mathbf{C}} : \dot{\mathbf{C}} + \left(\frac{\partial \Psi^D_{neq}}{\partial \mathbf{C}_e} : (\mathbf{F}_i^{-T}\,\dot{\mathbf{C}}\,\mathbf{F}_i^{-1}) - 2\,\mathbf{C}_e\,\frac{\partial \Psi^D_{neq}}{\partial \mathbf{C}_e} : \mathbf{d}_i \right) + \frac{\partial \Psi^D_{neq}}{\partial \theta}\,\dot{\theta} \\ &+ \frac{1}{2}\,J\,\frac{\partial \Psi^V}{\partial J}\,\mathbf{C}^{-1} : \dot{\mathbf{C}} + \frac{1}{2}\,J\,\frac{\partial \Psi^C}{\partial J}\,\mathbf{C}^{-1} : \dot{\mathbf{C}} + \frac{\partial \Psi^C}{\partial \theta}\dot{\theta} + \frac{\partial \Psi^\theta}{\partial \theta}\dot{\theta}.\end{aligned} \tag{6.30}$$

Rearranging the previous equation gives

$$\begin{aligned}\dot{\Psi} &= \frac{\partial \Psi^D_{eq}}{\partial \mathbf{C}} : \dot{\mathbf{C}} + \left(\mathbf{F}_i^{-1}\frac{\partial \Psi^D_{neq}}{\partial \mathbf{C}_e}\,\mathbf{F}_i^{-T} : \dot{\mathbf{C}} - 2\,\mathbf{C}_e\,\frac{\partial \Psi^D_{neq}}{\partial \mathbf{C}_e} : \mathbf{d}_i \right) + \frac{\partial \Psi^D_{neq}}{\partial \theta}\,\dot{\theta} \\ &+ \frac{1}{2}\,J\,\frac{\partial \Psi^V}{\partial J}\,\mathbf{C}^{-1} : \dot{\mathbf{C}} + \frac{1}{2}\,J\,\frac{\partial \Psi^C}{\partial J}\,\mathbf{C}^{-1} : \dot{\mathbf{C}} + \frac{\partial \Psi^C}{\partial \theta}\dot{\theta} + \frac{\partial \Psi^\theta}{\partial \theta}\dot{\theta}.\end{aligned} \tag{6.31}$$

Equating Eq.(6.31) into Eq.(2.55) leads to

$$\begin{aligned}&\left(\tilde{\mathbf{T}} - 2\,\frac{\partial \Psi^D_{eq}}{\partial \mathbf{C}} - 2\,\mathbf{F}_i^{-1}\frac{\partial \Psi^D_{neq}}{\partial \mathbf{C}_e}\,\mathbf{F}_i^{-T} - J\,\frac{\partial \Psi^V}{\partial J}\,\mathbf{C}^{-1} - J\,\frac{\partial \Psi^C}{\partial J}\,\mathbf{C}^{-1} \right) : \frac{1}{2}\dot{\mathbf{C}} \\ &+ 2\,\mathbf{C}_e\,\frac{\partial \Psi^D_{neq}}{\partial \mathbf{C}_e} : \mathbf{d}_i - \left(\Upsilon + \frac{\partial \Psi^D_{neq}}{\partial \theta} + \frac{\partial \Psi^C}{\partial \theta} + \frac{\partial \Psi^\theta}{\partial \theta} \right)\dot{\theta} - \frac{1}{\theta}\,\mathbf{Q}\,\nabla\theta \geq 0\end{aligned} \tag{6.32}$$

Therefore, the resulting constitutive equations of stresses and entropy can be written as

$$\tilde{\mathbf{T}} = 2\,\frac{\partial \Psi^D_{eq}}{\partial \mathbf{C}} + 2\,\mathbf{F}_i^{-1}\frac{\partial \Psi^D_{neq}}{\partial \mathbf{C}_e}\,\mathbf{F}_i^{-T} + J\,\frac{\partial \Psi^V}{\partial J}\,\mathbf{C}^{-1} + J\,\frac{\partial \Psi^C}{\partial J}\,\mathbf{C}^{-1}, \tag{6.33}$$

$$\Upsilon = -\left(\frac{\partial \Psi^D_{neq}}{\partial \theta} + \frac{\partial \Psi^C}{\partial \theta} + \frac{\partial \Psi^\theta}{\partial \theta} \right). \tag{6.34}$$

6.1.4 Stress equations (Lagrangian)

We introduce a following operator from Weiss [1994],

$$DEV(\cdot) = (\cdot) - \frac{1}{3}\,[(\cdot) : \mathbf{C}]\;\mathbf{C}^{-1} \tag{6.35}$$

where $DEV(\cdot)$ is an operator extracting the deviatoric part of a tensor in the reference configuration.

Using Eq.(6.35), we can derive the equilibrium stress from the Eq.(6.32) as

$$\begin{aligned}DEV\left(\frac{\partial \Psi^D_{eq}}{\partial \mathbf{C}}\right) &= \left(\frac{\partial \Psi^D_{eq}}{\partial \mathbf{C}}\right) - \frac{1}{3}\left[\left(\frac{\partial \Psi^D_{eq}}{\partial \mathbf{C}}\right) : \mathbf{C}\right]\mathbf{C}^{-1} \\ &= C_{10}\,J^{-2/3}\,\mathbf{I} - \frac{1}{3}\left[C_{10}\,J^{-2/3}\,\mathbf{I} : \mathbf{C}\right]\mathbf{C}^{-1} \\ &= C_{10}\,J^{-2/3}\left(\mathbf{I} - \frac{1}{3}\,[\mathbf{I} : \mathbf{C}]\;\mathbf{C}^{-1}\right) \\ &= C_{10}\,J^{-2/3}\left(\mathbf{I} - \frac{1}{3}\,\mathbf{I}_1\,\mathbf{C}^{-1}\right).\end{aligned} \tag{6.36}$$

Similarly, the non-equilibrium stress from the Eq.(6.32) can be derived as

$$\begin{aligned} DEV\left(\mathbf{F}_i^{-1}\frac{\partial\Psi^D_{neq}}{\partial\mathbf{C}_e}\mathbf{F}_i^{-T}\right) &= \left(\mathbf{F}_i^{-1}\frac{\partial\Psi^D_{neq}}{\partial\mathbf{C}_e}\mathbf{F}_i^{-T}\right) - \frac{1}{3}\left[\left(\mathbf{F}_i^{-1}\frac{\partial\Psi^D_{neq}}{\partial\mathbf{C}_e}\mathbf{F}_i^{-T}\right):\mathbf{C}\right]\mathbf{C}^{-1} \\ &= \mathbf{F}_i^{-1}\frac{\mu(\theta)}{2}J^{-2/3}\mathbf{F}_i^{-T} - \frac{1}{3}\left[\mathbf{F}_i^{-1}\frac{\mu(\theta)}{2}J^{-2/3}\mathbf{F}_i^{-T}:\mathbf{C}\right]\mathbf{C}^{-1} \\ &= \frac{\mu(\theta)}{2}J^{-2/3}\left(\mathbf{C}_i^{-1} - \frac{1}{3}tr\left(\mathbf{C}_i^{-1}\mathbf{C}\right)\mathbf{C}^{-1}\right). \end{aligned} \tag{6.37}$$

As $\mathbf{d}_i$ in Eq.(6.32) is the rate of inelastic deformation in current state, from Weiss [1994] an operator to extract the deviatoric part of a tensor in the current configuration can be given as

$$dev(\cdot) = (\cdot) - \frac{1}{3}\left[(\cdot):\mathbf{I}\right]\mathbf{I}. \tag{6.38}$$

Using Eq.(6.38) we derive the dissipation stress from inequality in Eq.(6.32):

$$\begin{aligned} dev\left(\mathbf{C}_e\frac{\partial\Psi^D_{neq}}{\partial\mathbf{C}_e}\right) &= \left(\mathbf{C}_e\frac{\partial\Psi^D_{neq}}{\partial\mathbf{C}_e}\right) - \frac{1}{3}\left[\left(\mathbf{C}_e\frac{\partial\Psi^D_{neq}}{\partial\mathbf{C}_e}\right):\mathbf{I}\right]\mathbf{I} \\ &= \mathbf{C}_e\,\mu(\theta)\,J^{-2/3} - \frac{1}{3}\left[\mathbf{C}_e\,\mu(\theta)\,J^{-2/3}:\mathbf{I}\right]\mathbf{I} \\ &= \frac{\mu(\theta)}{2}J^{-2/3}\left(\mathbf{C}_e - \frac{1}{3}\left(\mathbf{C}_e:\mathbf{I}\right)\mathbf{I}\right) \\ &= \frac{\mu(\theta)}{2}J^{-2/3}\left(\mathbf{C}_e - \frac{1}{3}tr(\mathbf{C}_i^{-1}\mathbf{C})\,\mathbf{I}\right) \end{aligned} \tag{6.39}$$

where $\mathbf{C}_e$ is

$$\begin{aligned} &\mathbf{C}_e = \mathbf{F}_i^{-T}\cdot\mathbf{C}\cdot\mathbf{F}_i^{-1} \\ &(C_e)_{ij} = (F_i^{-T}\cdot C\cdot F_i^{-1})_{ij} = (F_i^{-T})_{il}\,C_{lk}\,(F_i^{-1})_{kj}, \end{aligned} \tag{6.40}$$

and its trace using Eq.(2.24) is

$$\begin{aligned} tr(\mathbf{C}_e) &= tr(\mathbf{F}_i^{-T}\cdot\mathbf{C}\cdot\mathbf{F}_i^{-1}) = (F_i^{-T})_{il}\,C_{lk}\,(F_i^{-1})_{ki} \\ &= (F_i^{-1}\,F_i^{-T})_{kl}\,C_{lk} = (C_i^{-1})_{kl}\,C_{lk} = tr(\mathbf{C}_i^{-1}\,\mathbf{C}) \end{aligned} \tag{6.41}$$

6.1.5 Evolution law (Lagrangian)

The inelastic deformation rate can be given as

$$\begin{aligned} \mathbf{d}_i &= \frac{2}{D_{visco}}\mathbf{C}_e\frac{\partial\Psi^D_{neq}}{\partial\mathbf{C}_e} \\ &= \frac{2}{\tau}J^{-2/3}\left(\mathbf{C}_e - \frac{1}{3}tr(\mathbf{C}_i^{-1}\mathbf{C})\,\mathbf{I}\right) \end{aligned} \tag{6.42}$$

where D_{visco} and τ are the material parameters namely, viscous co-efficient and relaxation time of damper in the Zener model.

Using the arithmetic operation

$$\dot{\mathbf{C}}_i = 2\,\mathbf{F}_i^T\cdot\mathbf{d}_i\cdot\mathbf{F}_i, \tag{6.43}$$

a representation of the evolution equation is calculated in terms of the material time derivative of the inelastic deviatoric right Cauchy-Green deformation tensor:

$$\begin{aligned}\dot{\mathbf{C}}_i &= \frac{4}{\tau}\, J^{-2/3}\, \mathbf{F}_i^T \left(\mathbf{C}_e - \frac{1}{3}\, tr(\mathbf{C}_i^{-1}\, \mathbf{C})\, \mathbf{I}\right) \mathbf{F}_i \\ &= \frac{4}{\tau}\, J^{-2/3} \left(\mathbf{C} - \frac{1}{3}\, tr(\mathbf{C}_i^{-1}\, \mathbf{C})\, \mathbf{C}_i\right). \end{aligned} \tag{6.44}$$

Finally the increment of inelastic deviatoric right Cauchy-Green deformation tensor:

$$\mathbf{C}_i = \mathbf{C}_i + \Delta t \left[\frac{4}{\tau}\, J^{-2/3} \left(\mathbf{C} - \frac{1}{3}\, tr(\mathbf{C}_i^{-1}\, \mathbf{C})\, \mathbf{C}_i\right)\right]. \tag{6.45}$$

6.1.6 Thermo-mechanical formulation (Lagrangian)

In this section we present two kinds of approaches for the implementation of thermo-mechanical coupling in the finite element package. In some of the software tools, the constitutive equations of coupled thermal and mechanical fields and their corresponding derivatives with respect to strain and temperature for the coupled material tangent have to be defined. This is generally derived from the first law of thermodynamics. On the other hand, the FE software package like Abaqus has a different approach. Here the volumetric heat generation per unit time corresponding to the mechanical work has to be derived from the mechanical dissipative power and entropy in the Clausius-Duhem inequality. This scalar field automatically takes care of temperature rise due to self heating and simultaneously it couples this effect to the temperature fields. Therefore, in Abaqus the thermal and mechanical constitutive equations have to be defined separately in two user-subroutines such as UMAT for mechanical and UMATht for thermal laws.

First we start with the strong form of the balance equations from the first law of thermodynamics in Eq.(2.60)

$$\dot{\Psi} + \Upsilon\dot{\theta} + \theta\dot{\Upsilon} = \tilde{\mathbf{T}} : \dot{\mathbf{E}} - Div\mathbf{Q},$$

and this yields the form

$$\begin{aligned}&\overbrace{\left(\frac{\partial \Psi^D_{eq}}{\partial \mathbf{C}} + \mathbf{F}_i^{-1} \frac{\partial \Psi^D_{neq}}{\partial \mathbf{C}_e}\, \mathbf{F}_i^{-T} + \frac{1}{2}\, J\, \frac{\partial \Psi^V}{\partial J}\, \mathbf{C}^{-1} + \frac{1}{2}\, J\, \frac{\partial \Psi^C}{\partial J}\, \mathbf{C}^{-1}\right) : \dot{\mathbf{C}}}^{=\tilde{\mathbf{T}}:\dot{\mathbf{E}}} \\ &+ \overbrace{\left(\frac{\partial \Psi^D_{neq}}{\partial \theta} + \frac{\partial \Psi^C}{\partial \theta} + \frac{\partial \Psi^\theta}{\partial \theta}\right)\dot{\theta}}^{=-\Upsilon\dot{\theta}} + \Upsilon\dot{\theta} - 2\, \mathbf{C}_e\, \frac{\partial \Psi^D_{neq}}{\partial \mathbf{C}_e} : \mathbf{d}_i \\ &\underbrace{-\theta \left(\mathbf{F}_i^{-1} \frac{\partial^2 \Psi^D_{neq}}{\partial\theta \partial \mathbf{C}_e}\, \mathbf{F}_i^{-T} : \dot{\mathbf{C}} + \frac{1}{2}\, J\, \frac{\partial^2 \Psi^C}{\partial\theta \partial J}\, \mathbf{C}^{-1} : \dot{\mathbf{C}} + \frac{\partial^2 \Psi^C}{\partial \theta^2}\dot{\theta} + \frac{\partial^2 \Psi^\theta}{\partial \theta^2}\dot{\theta}\right)}_{=\theta\dot{\Upsilon}} \\ &= \tilde{\mathbf{T}} : \dot{\mathbf{E}} - Div\mathbf{Q}. \end{aligned} \tag{6.46}$$

After rearranging the previous equation we get

$$\overbrace{-2\,\mathbf{C}_e\,\frac{\partial \Psi^D_{neq}}{\partial \mathbf{C}_e} : \mathbf{d}_i}^{=\mathscr{W}_{int}} \underbrace{-\theta \overbrace{\left(\mathbf{F}_i^{-1}\frac{\partial^2 \Psi^D_{neq}}{\partial\theta\partial\mathbf{C}_e}\,\mathbf{F}_i^{-T} + \frac{1}{2}\,J\,\frac{\partial^2\Psi^C}{\partial\theta\partial J}\,\mathbf{C}^{-1}\right)}^{=\frac{1}{2}\frac{\partial\tilde{\mathbf{T}}}{\partial\theta}} : \dot{\mathbf{C}}}_{=\mathscr{W}_{ext}}$$

$$\underbrace{-\theta\left(\frac{\partial^2\Psi^C}{\partial\theta^2} + \frac{\partial^2\Psi^\theta}{\partial\theta^2}\right)\dot{\theta}}_{=C_p\,\dot{\theta}} = -Div\mathbf{Q} \tag{6.47}$$

Finally, we can write the energy balance equation as

$$C_p\,\dot{\theta} - (\mathscr{W}_{int} + \mathscr{W}_{ext}) = -Div\mathbf{Q} \tag{6.48}$$

where the term $\mathscr{W}_{int}$ represents the inner dissipation which stems from the power of the viscous part and $\mathscr{W}_{ext}$ is the thermo-mechanical coupling term of the system. C_p is the heat capacity and is equals to $\dfrac{\partial U}{\partial\theta}$. That means the internal thermal energy depends on this parameter. The flux $\mathbf{Q}$ is defined by Fourier's law which depends on parameter thermal conductivity κ_0.

The second approach of deriving thermo-mechanical constitutive equations from Clausius-Planck inequality is as follows

$$\tilde{\mathbf{T}} : \dot{\mathbf{E}} - \dot{\Psi} - \Upsilon\dot{\theta} \geq 0.$$

After mathematical handling the remaining inequality is

$$2\,\mathbf{C}_e\,\frac{\partial\Psi^D_{neq}}{\partial\mathbf{C}_e} : \mathbf{d}_i - \left(-\frac{\partial\Psi^D_{neq}}{\partial\theta} - \frac{\partial\Psi^C}{\partial\theta} - \frac{\partial\Psi^\theta}{\partial\theta}\right)\dot{\theta} \geq 0 \tag{6.49}$$

is the volumetric heat generation per time caused by mechanical work in reference state. After converting this Lagrangian formulation to Eulerian form, the inequality can be implemented into Abaqus as *RPL* in UMAT.

6.1.7 Clausius-Duhem inequality (Eulerian)

Similar to the Lagrangian formulations we now derive the constitutive equations in Eulerian formulations.

Hemholtz free energy rate of Zener model in spatial state can be given as

$$\begin{aligned}\dot{\Psi} &= \frac{\partial\Psi^D_{eq}}{\partial\mathbf{b}} : \dot{\mathbf{b}} + \frac{\partial\Psi^D_{neq}}{\partial\mathbf{b}_e} : \dot{\mathbf{b}}_e + \frac{\partial\Psi^D_{neq}}{\partial\theta}\,\dot{\theta} \\ &+ \frac{\partial\Psi^V}{\partial J}\,\dot{J} + \frac{\partial\Psi^C}{\partial J}\,\dot{J} + \frac{\partial\Psi^C}{\partial\theta}\,\dot{\theta} + \frac{\partial\Psi^\theta}{\partial\theta}\,\dot{\theta}.\end{aligned} \tag{6.50}$$

The rate of left Cauchy-green deformation tensor $\mathbf{b}$ and volume ratio J can be given as

$$\dot{\mathbf{b}} = \dot{\mathbf{F}}\,\mathbf{F}^T + \mathbf{F}\,\dot{\mathbf{F}}^T = \underbrace{\dot{\mathbf{F}}\,\mathbf{F}^{-1}}_{=\mathbf{l}}\,\underbrace{\mathbf{F}\,\mathbf{F}^T}_{=\mathbf{b}} + \underbrace{\mathbf{F}\,\mathbf{F}^T}_{=\mathbf{b}}\,\underbrace{\mathbf{F}^{-T}\,\dot{\mathbf{F}}^T}_{=\mathbf{l}^T} = \mathbf{l}\,\mathbf{b} + \mathbf{b}\,\mathbf{l}^T = 2\,\mathbf{b}\,\mathbf{d}, \tag{6.51}$$

$$\dot{J} = \frac{d(\sqrt{det\mathbf{b}})}{dt} = J\ \mathbf{d}. \tag{6.52}$$

The elastic left Cauchy-Green deformation tensor $\mathbf{b}_e$ of the non-equilibrium part can be written as

$$\mathbf{b}_e = \mathbf{F}_e\,\mathbf{F}_e^T = \mathbf{F}\,\mathbf{F}_i^{-1}\ \mathbf{F}_i^{-T}\,\mathbf{F}^T = \mathbf{F}\,\mathbf{C}_i^{-1}\,\mathbf{F}^T, \tag{6.53}$$

and its rate

$$\begin{aligned}
\dot{\mathbf{b}}_e &= \mathbf{F}\,\mathbf{C}_i^{-1}\,\dot{\mathbf{F}}^T + \mathbf{F}\,\dot{\mathbf{C}}_i^{-1}\,\mathbf{F}^T + \dot{\mathbf{F}}\,\mathbf{C}_i^{-1}\,\mathbf{F}^T \\
&= \mathbf{F}\,\mathbf{C}_i^{-1}\,\mathbf{F}^T\underbrace{\mathbf{F}^{-T}\,\dot{\mathbf{F}}^T}_{=\mathbf{l}^T} + \mathbf{F}\,\dot{\mathbf{C}}_i^{-1}\,\mathbf{F}^T + \underbrace{\dot{\mathbf{F}}\,\mathbf{F}^{-1}}_{=\mathbf{l}}\,\mathbf{F}\,\mathbf{C}_i^{-1}\,\mathbf{F}^T \\
&= \mathbf{F}\,\dot{\mathbf{C}}_i^{-1}\,\mathbf{F}^T + \mathbf{F}\,\mathbf{C}_i^{-1}\,\mathbf{F}^T\,(\mathbf{l}^T + \mathbf{l}) \\
&= \underbrace{\mathbf{F}\,\dot{\mathbf{C}}_i^{-1}\,\mathbf{F}^T}_{=\mathscr{L}_v\mathbf{b}_e} + 2\,\mathbf{b}_e\,\mathbf{d}
\end{aligned} \tag{6.54}$$

where $\mathscr{L}_v\mathbf{b}_e$ is the Lie-derivative of the contra-variant tensor $\mathbf{b}_e$ along the flow of the material motion [Reese and Govindjee, 1998b].

Equating equations (6.54), (6.51) and (6.52) in Eq.(6.50) yields

$$\begin{aligned}
\dot{\Psi} &= 2\,\frac{\partial\Psi^D_{eq}}{\partial\mathbf{b}}\,\mathbf{b} : \mathbf{d} + \left(2\,\frac{\partial\Psi^D_{neq}}{\partial\mathbf{b}_e}\,\mathbf{b}_e : \mathbf{d} + \frac{\partial\Psi^D_{neq}}{\partial\mathbf{b}_e} : (\mathbf{F}\,\dot{\mathbf{C}}_i^{-1}\,\mathbf{F}^T)\right) + \frac{\partial\Psi^D_{neq}}{\partial\theta}\,\dot{\theta} \\
&+ J\,\frac{\partial\Psi^V}{\partial J}\,\mathbf{I} : \mathbf{d} + J\,\frac{\partial\Psi^C}{\partial J}\,\mathbf{I} : \mathbf{d} + \frac{\partial\Psi^C}{\partial\theta}\dot{\theta} + \frac{\partial\Psi^\theta}{\partial\theta}\dot{\theta}.
\end{aligned} \tag{6.55}$$

Rearranging the previous equation yields

$$\begin{aligned}
\dot{\Psi} &= 2\,\frac{\partial\Psi^D_{eq}}{\partial\mathbf{b}}\,\mathbf{b} : \mathbf{d} \\
&+ \left(2\,\frac{\partial\Psi^D_{neq}}{\partial\mathbf{b}_e}\,\mathbf{b}_e : \mathbf{d} + \frac{1}{2}\left(2\,\frac{\partial\Psi^D_{neq}}{\partial\mathbf{b}_e}\,\mathbf{b}_e\right) : (\mathscr{L}_v\mathbf{b}_e\cdot\mathbf{b}_e^{-1})\right) \\
&+ \frac{\partial\Psi^D_{neq}}{\partial\theta} + J\,\frac{\partial\Psi^V}{\partial J}\,\mathbf{I} : \mathbf{d} + J\,\frac{\partial\Psi^C}{\partial J}\,\mathbf{I} : \mathbf{d} + \frac{\partial\Psi^C}{\partial\theta}\dot{\theta} + \frac{\partial\Psi^\theta}{\partial\theta}\dot{\theta}.
\end{aligned} \tag{6.56}$$

Clausius-Duhem Inequality in spatial state

$$-J^{-1}\,\dot{\Psi} - J^{-1}\,\Upsilon\dot{\theta} + \boldsymbol{\sigma} : \mathbf{d} - \frac{1}{\theta}\,\mathbf{q}\,\nabla\theta \geq 0,$$

and therefore,

$$\begin{aligned}
&\left(\boldsymbol{\sigma} - \frac{2}{J}\frac{\partial\Psi^D_{eq}}{\partial\mathbf{b}}\,\mathbf{b} - \frac{2}{J}\,\frac{\partial\Psi^D_{neq}}{\partial\mathbf{b}_e}\,\mathbf{b}_e - \frac{\partial\Psi^V}{\partial J}\,\mathbf{I} - \frac{\partial\Psi^C}{\partial J}\,\mathbf{I}\right) : \mathbf{d} \\
&- \overset{D}{\boldsymbol{\sigma}}_{neq} : (\frac{1}{2}\,\mathscr{L}_v\mathbf{b}_e\cdot\mathbf{b}_e^{-1}) - \left(\Upsilon + \frac{1}{J}\,\frac{\partial\Psi^D_{neq}}{\partial\theta} + \frac{1}{J}\,\frac{\partial\Psi^C}{\partial\theta} + \frac{1}{J}\,\frac{\partial\Psi^\theta}{\partial\theta}\right)\dot{\theta} \\
&- \frac{1}{\theta}\,\mathbf{q}\,\nabla\theta \geq 0.
\end{aligned} \tag{6.57}$$

Resulting equations of stress and entropy

$$\boldsymbol{\sigma} = \frac{2}{J}\frac{\partial\Psi^D_{eq}}{\partial\mathbf{b}}\,\mathbf{b} + \frac{2}{J}\,\frac{\partial\Psi^D_{neq}}{\partial\mathbf{b}_e}\,\mathbf{b}_e + \frac{\partial\Psi^V}{\partial J}\,\mathbf{I} + \frac{\partial\Psi^C}{\partial J}\,\mathbf{I}, \tag{6.58}$$

$$\Upsilon = -\frac{1}{J}\left(\frac{\partial \Psi^{D}_{neq}}{\partial \theta} + \frac{\partial \Psi^{C}}{\partial \theta} + \frac{\partial \Psi^{\theta}}{\partial \theta}\right). \tag{6.59}$$

The assumed evolution law from Reese and Govindjee [1998b] for the case of current state can be given as

$$-\frac{1}{2}\,\mathscr{L}_v \mathbf{b}_e \cdot \mathbf{b}_e^{-1} = \frac{1}{2\,\tau}\;\overset{D}{\boldsymbol{\sigma}}_{neq} \tag{6.60}$$

where the $\overset{D}{\boldsymbol{\sigma}}_{neq}$ represents the non-equilibrium deviatoric Cauchy stress tensor.

6.1.8 Thermo-mechanical formulation (Eulerian)

The balance of energy without external heat source from first law of thermodynamics can be given as

$$J^{-1}\,\dot{\Psi} + J^{-1}\,\Upsilon\dot{\theta} + J^{-1}\,\theta\dot{\Upsilon} = \boldsymbol{\sigma} : \mathbf{d} - div\mathbf{q},$$

and this yields

$$\begin{aligned}
&\overbrace{\left(\frac{2}{J}\frac{\partial \Psi^{D}_{eq}}{\partial \mathbf{b}}\,\mathbf{b} + \frac{2}{J}\frac{\partial \Psi^{D}_{neq}}{\partial \mathbf{b}_e}\,\mathbf{b}_e + \frac{\partial \Psi^{V}}{\partial J}\,\mathbf{I} + \frac{\partial \Psi^{C}}{\partial J}\,\mathbf{I}\right) : \mathbf{d}}^{=\boldsymbol{\sigma}:\mathbf{d}} \\
&+ \overbrace{\left(\frac{1}{J}\frac{\partial \Psi^{D}_{neq}}{\partial \theta} + \frac{1}{J}\frac{\partial \Psi^{C}}{\partial \theta} + \frac{1}{J}\frac{\partial \Psi^{\theta}}{\partial \theta}\right)\dot{\theta}}^{=-J^{-1}\Upsilon\dot{\theta}} + J^{-1}\,\Upsilon\dot{\theta} + \overset{D}{\boldsymbol{\sigma}}_{neq} : \left(\frac{1}{2}\,\mathscr{L}_v \mathbf{b}_e \cdot \mathbf{b}_e^{-1}\right) \\
&\underbrace{-\theta\left(\frac{2}{J}\frac{\partial^2 \Psi^{D}_{neq}}{\partial \theta \partial \mathbf{b}_e}\,\mathbf{b}_e : \mathbf{d} + \frac{\partial^2 \Psi^{C}}{\partial \theta \partial J}\,\mathbf{I} : \mathbf{d} + \frac{1}{J}\frac{\partial^2 \Psi^{C}}{\partial \theta^2}\dot{\theta} + \frac{1}{J}\frac{\partial^2 \Psi^{\theta}}{\partial \theta^2}\dot{\theta}\right)}_{=-J^{-1}\theta\dot{\Upsilon}} \\
&= \boldsymbol{\sigma} : \mathbf{d} - div\mathbf{q}.
\end{aligned} \tag{6.61}$$

After rearranging the previous equation we get

$$\begin{aligned}
&\overbrace{\overset{D}{\boldsymbol{\sigma}}_{neq} : \left(\frac{1}{2}\,\mathscr{L}_v \mathbf{b}_e \cdot \mathbf{b}_e^{-1}\right)}^{=-\mathscr{W}_{int}} - \theta\,\overbrace{\left(\frac{2}{J}\frac{\partial^2 \Psi^{D}_{neq}}{\partial \theta \partial \mathbf{b}_e}\,\mathbf{b}_e + \frac{\partial^2 \Psi^{C}}{\partial \theta \partial J}\,\mathbf{I}\right) : \mathbf{d}}^{=\frac{\partial \boldsymbol{\sigma}}{\partial \theta}}}_{=\mathscr{W}_{ext}} \\
&\underbrace{-\theta\left(\frac{1}{J}\frac{\partial^2 \Psi^{C}}{\partial \theta^2} + \frac{1}{J}\frac{\partial^2 \Psi^{\theta}}{\partial \theta^2}\right)\dot{\theta}}_{=C_p\,\dot{\theta}} = -div\mathbf{q}.
\end{aligned} \tag{6.62}$$

Finally we can write the energy balance equation as

$$C_p\,\dot{\theta} - (\mathscr{W}_{int} + \mathscr{W}_{ext}) = -div\mathbf{q} \tag{6.63}$$

where the term $\mathscr{W}_{int}$ represents the inner dissipation which stems from the power of the viscous part and $\mathscr{W}_{ext}$ is the thermo-mechanical coupling term of the system. C_p is the heat capacity

and is $= \dfrac{\partial U}{\partial \theta}$. That means the internal thermal energy depends on this parameter. The flux $\mathbf{q}$ is defined by Fourier's law which depends on parameter thermal conductivity κ.

The second approach of deriving thermo-mechanical constitutive equations from Clausius-Planck inequality is as follows

$$\boldsymbol{\sigma} : \mathbf{d} - J^{-1}\,\dot{\Psi} - J^{-1}\,\Upsilon\dot{\theta} \geq 0 \tag{6.64}$$

After mathematical handling, the remaining inequality

$$\overset{D}{\boldsymbol{\sigma}}_{neq} \colon \left(-\frac{1}{2}\,\mathscr{L}_v \mathbf{b}_e \cdot \mathbf{b}_e^{-1}\right) - \frac{1}{J}\left(-\frac{\partial \Psi^D_{neq}}{\partial \theta} - \frac{\partial \Psi^C}{\partial \theta} - \frac{\partial \Psi^\theta}{\partial \theta}\right)\dot{\theta} \geq 0 \tag{6.65}$$

is the volumetric heat generation per time caused by mechanical work in current state. This Eulerian formulation has been implemented into Abaqus as *RPL* in UMAT. This scalar field automatically takes care of temperature rise due to self heating and simultaneously it couples this effect to the temperature fields. This completes the thermo-viscoelastic modelling and coupling for the case of Zener model and in the next section we discuss the thermo-viscoelastic modelling and coupling of DFM. In the following chapter the implementation of constitutive models into Abaqus user-subroutines UMAT and UMATht are discussed in detail.

6.2 Thermo-mechanical coupling of DFM using representative directions

In case of thermo-mechanical theory, the temperature-dependent quantities of constitutive model has to be derived. Accordingly the temperature-dependent modified stress in each representative direction is

$$\overset{\alpha}{\tilde{T}}{}^{*} = \frac{\overset{\alpha}{T}{}^{*}\left(\overset{\alpha}{\lambda}{}^{*}, \dot{\overset{\alpha}{\lambda}}{}^{*}, \overset{\alpha}{\Gamma}_i, \theta\right)}{\overset{\alpha}{\lambda}{}^{*}}. \tag{6.66}$$

The total stresses of the modified constitutive model are given by

$$\tilde{\mathbf{T}}^{*} = \sum_{\alpha=1}^{n} \overset{\alpha}{w}\,\overset{\alpha}{\tilde{T}}{}^{*}\,\overset{\alpha}{\mathbf{e}} \otimes \overset{\alpha}{\mathbf{e}}\,. \tag{6.67}$$

Finally the deviatoric stresses are calculated using

$$\overset{D}{\tilde{\mathbf{T}}} = Dev\left(\tilde{\mathbf{T}}^{*} \cdot \overset{D}{\mathbf{C}}\right) \cdot \mathbf{C}^{-1} = J^{-2/3}\,\tilde{\mathbf{T}}^{*} - \frac{1}{3}\,tr\left(\tilde{\mathbf{T}}^{*} \cdot \overset{D}{\mathbf{C}}\right) \cdot \mathbf{C}^{-1}. \tag{6.68}$$

The total stress can be calculated using

$$\tilde{\mathbf{T}} = \overset{D}{\tilde{\mathbf{T}}} + \overset{V}{\tilde{\mathbf{T}}} + \overset{C}{\tilde{\mathbf{T}}}\,. \tag{6.69}$$

The volumetric stress tensor can be derived using

$$\overset{V}{\tilde{\mathbf{T}}} = -p_v\,J\,\mathbf{C}^{-1} \tag{6.70}$$

$$p_v = -\frac{\partial \psi^V}{\partial J} = -K_{mod}\,(J-1), \tag{6.71}$$

where ψ^V is the volumetric part of free energy density and it is considered to be of the form $\frac{K_{mod}}{2}(J-1)^2$.

The coupled volume-temperature part of the stress can be derived using

$$\overset{C}{\tilde{\mathbf{T}}} = -p_c\, J\, \mathbf{C}^{-1} \tag{6.72}$$

$$p_c = -\frac{\partial \psi^C}{\partial J} = 3\,\alpha_T\,(\theta - \theta_{ref})\,K_{mod}, \tag{6.73}$$

where p_c is the coupled hydrostatic-thermal pressure function. ψ^C is the coupled volume-temperature part of free energy density and it is considered to be of the form $-3\,\alpha_T\,(\theta - \theta_{ref})\,\frac{\partial \Psi^V}{\partial J}$.

The viscous over-stress that is responsible for the hysteresis dissipation and the entropy of DFM model can be written in agreement with the Clausius-Planck inequality as,

$$\mathscr{D}^m - J^{-1}\,\Upsilon\dot{\theta} \geq 0. \tag{6.74}$$

The mechanical dissipation of DFM implies to the stress power of cluster bond deformation and can be written as

$$\mathscr{D}^m = \overset{D}{\boldsymbol{\sigma}}_{A,\mu}\,(\lambda, t, \theta)\, : \overset{D}{\mathbf{d}}\,. \tag{6.75}$$

The cluster viscous stress $\overset{D}{\boldsymbol{\sigma}}_{A,\mu}$ is calculated using the Eq.(6.68) and is only influenced by the time- and rate-dependent evolution part of the damaged and virgin cluster strengths as in equations (5.21) and (5.22), respectively.

In addition to the stresses, entropy of the proposed constitutive model have to be derived for the uniaxial loading by using

$$\Upsilon^* = \sum_{\alpha=1}^{n} \overset{\alpha}{w} \cdot \overset{\alpha}{\Upsilon^*}\left(\overset{\alpha}{\lambda^*}, \theta\right) \tag{6.76}$$

The total entropy can be calculated using

$$\Upsilon = \overset{D}{\Upsilon} + \overset{C}{\Upsilon} + \overset{\theta}{\Upsilon} = \Upsilon^* - \frac{\partial \psi^C}{\partial \theta} - \frac{\partial \psi^\theta}{\partial \theta}. \tag{6.77}$$

The entropy Υ^* consists of two parts. First one is the rubber matrix entropy $\Upsilon_R(\lambda_1, \theta)$ and the next one is the entropy contribution of cluster bonds $\Upsilon_{A,1}(\lambda_1, \theta)$. Although the matrix entropy can be calculated using the energy density in Eq.(3.2) as

$$\Upsilon_R(\lambda_1, \theta) = \frac{\partial W_R(\lambda_1, \theta)}{\partial \theta}, \tag{6.78}$$

the entropy contribution of cluster bonds $\Upsilon_{A,1}(\lambda_1, \theta)$ can not be easily determined due to the absence of energy function for cluster part of DFM. The stresses of filler clusters are determined using an estimation of stress equilibrium between the rubber matrix and the clusters. Such an estimation is also applicable in case of entropy is a question. In addition to that, what kind of cluster size distribution function needs to be considered for the determination of filler cluster entropy. Due to unavailability of sufficient information in this regard, Υ^* is not included in the implementation of thermo-mechanical coupling of the DFM. This leads to the incompleteness of the Clausius-Planck inequality and therefore results in overestimation of temperature. Due to this deviation in material behaviour prediction, the results of thermo-mechanical coupling of DFM is not included or discussed in the subsequent chapters.

Chapter 7

FE-implementation

In this chapter the implementation of DFM in combination with concept of representative directions into the finite element system Abaqus is discussed. Along with that the Zener model with complete 3-D formulation as well as in combination with concept of representative directions is also described only for the case of thermo-mechanical coupling. Although Abaqus requires Cauchy stresses and the corresponding material tangent, we prefer the Lagrangian constitutive formulations to be derived first as they are easy compared to Eulerian formulations and then using push forward technique (in continuum mechanics) to convert them to Eulerian form.

7.1 Hyperelasticity & viscoelasticity

In this section both time-independent and time-dependent DFM is clubbed together as the implementation procedure is similar.

7.1.1 Lagrangian formulation

The total 2^{nd} PK stress can be given as

$$\tilde{\mathbf{T}} = \overset{D}{\tilde{\mathbf{T}}} + \overset{V}{\tilde{\mathbf{T}}} \,. \tag{7.1}$$

where $\overset{D}{\tilde{\mathbf{T}}}$ and $\overset{V}{\tilde{\mathbf{T}}}$ are the deviatoric and volumetric stress tensors, respectively, and are calculated using equations (4.11) and (4.12).

The rate of 2^{nd} PK stress can be given as

$$\dot{\tilde{\mathbf{T}}} = 2\,\frac{\partial^2 \Psi}{\partial \mathbf{C}^2} : \dot{\mathbf{C}} = 4\,\frac{\partial^2 \Psi}{\partial \mathbf{C}^2} : \dot{\mathbf{E}} = 4\,\frac{\partial^2 \Psi}{\partial \mathbf{C}^2} : \frac{1}{2}\,\dot{\mathbf{C}} \tag{7.2}$$

The incremental form of Eq.(7.2) is

$$\Delta\tilde{\mathbf{T}} = \underbrace{4\,\frac{\partial^2 \Psi}{\partial \mathbf{C}^2}}_{=\mathbb{K}^{Lag}} : \frac{1}{2}\,\Delta\mathbf{C}, \tag{7.3}$$

which is a linear relation between the increments of $\tilde{\mathbf{T}}$ and $\mathbf{C}$, and so it is commonly referred to as linearised constitutive equation. $\mathbb{K}^{Lag}$ refers to the 4^{th} order Lagrangian material tangent and can be defined as

$$\mathbb{K}^{Lag} = 4\,\frac{\partial^2 \Psi}{\partial \mathbf{C}^2} = 2\,\frac{\partial \tilde{\mathbf{T}}}{\partial \mathbf{C}} \tag{7.4}$$

Thus, the total stresses of Eq.(7.1) have to be differentiated with respect to the right Cauchy-Green tensor $\mathbf{C}$:

$$\mathbb{K}^{Lag} = \overset{D}{\mathbb{K}}{}^{Lag} + \overset{V}{\mathbb{K}}{}^{Lag} = 2\,\frac{\partial \overset{D}{\tilde{\mathbf{T}}}}{\partial \mathbf{C}} + 2\,\frac{\partial \overset{V}{\tilde{\mathbf{T}}}}{\partial \mathbf{C}}. \tag{7.5}$$

The first part of Eq.(7.5), $\overset{D}{\mathbb{K}}{}^{Lag}$ contains the uniaxial Dynamic Flocculation Model (DFM) within the intermediate stress tensor $\tilde{\mathbf{T}}^*$ in Eq.(4.10) for which an analytical derivation has not been found yet. Thus, this scalar stress-strain relation is the only part of the constitutive model that has to be differentiated numerically by means of a difference quotient. On the other hand $\overset{V}{\mathbb{K}}{}^{Lag}$ can be computed completely analytically using the function

$$\overset{V}{\mathbb{K}}{}^{Lag} = \mathfrak{f}_2\,(\mathbf{C^{-1}} \otimes \mathbf{C^{-1}}) + \mathfrak{f}_3\,(\mathbf{C^{-1}} \odot \mathbf{C^{-1}}) \tag{7.6}$$

where the coefficients $\mathfrak{f}_2$ and $\mathfrak{f}_3$ can be defined as

$$\begin{aligned} \mathfrak{f}_2 &= 2\,J\,\frac{\partial \psi^V}{\partial J} + J\,\frac{\partial^2 \psi^V}{\partial J^2} \\ \mathfrak{f}_3 &= -2\,J\,\frac{\partial \psi^V}{\partial J}. \end{aligned} \tag{7.7}$$

The fourth order tensors $(\mathbf{C^{-1}} \odot \mathbf{C^{-1}})$ can be defined as

$$\frac{\partial \mathbf{C^{-1}}}{\partial \mathbf{C}} = -\mathbf{C^{-1}} \odot \mathbf{C^{-1}} \tag{7.8}$$

$$-\,(\mathbf{C^{-1}} \odot \mathbf{C^{-1}})_{ijkl} = -\frac{1}{2}(\mathbf{C^{-1}}_{ik}\mathbf{C^{-1}}_{jl} + \mathbf{C^{-1}}_{il}\mathbf{C^{-1}}_{jk}) = \frac{\partial \mathbf{C^{-1}}_{ij}}{\partial \mathbf{C}_{kl}} \tag{7.9}$$

7.1.2 Numerical differentiation techniques

In this sub-section we briefly describe the numerical approximations for first-order derivatives such as 4^{th} order material tangent tensor $\overset{D}{\mathbb{K}}{}^{Lag}$. For illustration, we assume the derivative of a function f at a point x and the expression for the approximation scheme is obtained by evaluating the Taylor series expansion.

For the classical forward difference scheme the expansion along the real axis, i.e. $f(x+\Delta)$ is taken into account where Δ is a small perturbation about the point of interest x. The Taylor series expansion for forward difference scheme can be given as

$$f(x+\Delta) = f(x) + f'(x)\,\frac{\Delta}{1!} + f''(x)\,\frac{\Delta^2}{2!} + f'''(x)\,\frac{\Delta^3}{3!} + \cdots \tag{7.10}$$

With the assumption that Δ is small enough to be able to neglect the higher order terms, from the Eq.(7.10), the approximation for $f'(x)$ can be obtained as

$$f'(x) = \frac{f(x+\Delta) - f(x)}{\Delta} + \mathcal{O}(\Delta). \tag{7.11}$$

Unfortunately, the difference in the numerator therein becomes source of round-off errors which is influenced by the size of Δ.

Similarly, the Taylor series expansion for backward difference scheme can be given as

$$f(x-\Delta) = f(x) - f'(x)\,\frac{\Delta}{1!} + f''(x)\,\frac{\Delta^2}{2!} - f'''(x)\,\frac{\Delta^3}{3!} + \cdots \tag{7.12}$$

Solving the Eq.(7.12), the backward derivative approximation for $f'(x)$ can be obtained as

$$f'(x) = \frac{f(x) - f(x-\Delta)}{\Delta} + \mathcal{O}(\Delta). \tag{7.13}$$

Subtracting the Eq.(7.12) from the Eq.(7.10) gives the Taylor series expansion for the central difference scheme:

$$f(x+\Delta) - f(x-\Delta) = 2\,f'(x)\,\frac{\Delta}{1!} + 2\,f'''(x)\,\frac{\Delta^3}{3!} + \cdots \tag{7.14}$$

Solving the Eq.(7.14) one can obtain the central derivative approximation

$$f'(x) = \frac{f(x+\Delta) - f(x-\Delta)}{2\,\Delta} + \mathcal{O}(\Delta^2). \tag{7.15}$$

Therefore from equations (7.11), (7.13) and (7.15) one can conclude that the central scheme is more accurate than the other two difference schemes.

Following are the central difference schemes for first- and second-order derivatives with respect to two variables x and y

$$f'_x = \frac{\partial f(x,y)}{\partial x} = \frac{f(x+\Delta,y) - f(x-\Delta,y)}{2\cdot\Delta} \tag{7.16}$$

$$f'_y = \frac{\partial f(x,y)}{\partial y} = \frac{f(x,y+\Delta) - f(x,y-\Delta)}{2\cdot\Delta} \tag{7.17}$$

$$f''_x = \frac{\partial^2 f(x,y)}{\partial x^2} = \frac{f(x+\Delta,y) - 2\,f(x,y) + f(x-\Delta,y)}{\Delta^2} \tag{7.18}$$

$$f''_y = \frac{\partial^2 f(x,y)}{\partial y^2} = \frac{f(x,y+\Delta) - 2\,f(x,y) + f(x,y-\Delta)}{\Delta^2}, \tag{7.19}$$

and finally,

$$\begin{aligned} f''_{xy} &= \frac{\partial^2 f(x,y)}{\partial y \partial x} = \frac{\partial^2 f(x,y)}{\partial x \partial y} \\ &= \frac{f(x+\Delta,y+\Delta) - f(x+\Delta,y-\Delta) - f(x-\Delta,y+\Delta) + f(x-\Delta,y-\Delta)}{4\cdot\Delta^2}. \end{aligned} \tag{7.20}$$

7.1.3 Eulerian formulation

As mentioned previously, the finite element program Abaqus requires the Cauchy stress tensor $\boldsymbol{\sigma}$ and the corresponding material tangent $\mathbb{K}^{Eul}$. Therefore we make use of push forward technique to convert the 2^{nd} PK stress $\tilde{\mathbf{T}}$ and the Lagrangian material tangent $\mathbb{K}^{Lag}$ to their equivalent Eulerian tensors.

The Cauchy stress can be calculated as

$$\boldsymbol{\sigma} = \frac{1}{J}\,\mathbf{F}\,\tilde{\mathbf{T}}\,\mathbf{F}^T = \frac{1}{J}\,\tilde{\mathbf{T}}\left(\mathbf{F}^T \otimes \mathbf{F}\right) \quad \text{or} \quad = \frac{1}{J}\,\left(\mathbf{F} \otimes \mathbf{F}^T\right)\,\tilde{\mathbf{T}} \tag{7.21}$$

where,

$$\mathbf{F}^T \otimes \mathbf{F} = \begin{bmatrix} F_{11}^2 & F_{21}^2 & F_{31}^2 & F_{21}\,F_{11} & F_{31}\,F_{21} & F_{31}\,F_{11} \\ F_{12}^2 & F_{22}^2 & F_{32}^2 & F_{22}\,F_{12} & F_{32}\,F_{22} & F_{32}\,F_{12} \\ F_{13}^2 & F_{23}^2 & F_{33}^2 & F_{23}\,F_{13} & F_{33}\,F_{23} & F_{33}\,F_{13} \\ 2\,F_{12}\,F_{11} & 2\,F_{22}\,F_{21} & 2\,F_{32}\,F_{31} & \begin{matrix} F_{22}\,F_{11} \\ +F_{12}\,F_{21} \end{matrix} & \begin{matrix} F_{32}\,F_{21} \\ +F_{22}\,F_{31} \end{matrix} & \begin{matrix} F_{32}\,F_{11} \\ +F_{12}\,F_{31} \end{matrix} \\ 2\,F_{13}\,F_{12} & 2\,F_{23}\,F_{22} & 2\,F_{33}\,F_{32} & \begin{matrix} F_{23}\,F_{12} \\ +F_{13}\,F_{22} \end{matrix} & \begin{matrix} F_{33}\,F_{22} \\ +F_{23}\,F_{32} \end{matrix} & \begin{matrix} F_{33}\,F_{12} \\ +F_{13}\,F_{32} \end{matrix} \\ 2\,F_{13}\,F_{11} & 2\,F_{23}\,F_{21} & 2\,F_{33}\,F_{31} & \begin{matrix} F_{23}\,F_{11} \\ +F_{13}\,F_{21} \end{matrix} & \begin{matrix} F_{33}\,F_{21} \\ +F_{23}\,F_{31} \end{matrix} & \begin{matrix} F_{33}\,F_{11} \\ +F_{13}\,F_{31} \end{matrix} \end{bmatrix} \tag{7.22}$$

and

$$\left(\mathbf{F} \otimes \mathbf{F}^T\right) = \left(\mathbf{F}^T \otimes \mathbf{F}\right)^T. \tag{7.23}$$

One important thing to be noted here is that the way Abaqus stores its stress components. It is bit different compared to other software packages where the fifth and sixth components (shear components) of stress are interchanged. The stress tensor storage is covered in section 1.2 of the "Abaqus Analysis User's Guide" (the section entitled "Abaqus syntax and conventions"). That is

$$\begin{pmatrix} \sigma_1 \\ \sigma_2 \\ \sigma_3 \\ \sigma_4 \\ \sigma_6 \\ \sigma_5 \end{pmatrix} = \begin{pmatrix} \sigma_{11} \\ \sigma_{22} \\ \sigma_{33} \\ \sigma_{12} \\ \sigma_{13} \\ \sigma_{23} \end{pmatrix} \text{ and } \neq \begin{pmatrix} \sigma_{11} \\ \sigma_{22} \\ \sigma_{33} \\ \sigma_{12} \\ \sigma_{23} \\ \sigma_{13} \end{pmatrix} \tag{7.24}$$

Furthermore, the Lagrangian material tangent $\mathbb{K}^{Lag}$ has to be changed to its equivalent $\mathbb{K}^{Eul}$.

For that we have to derive the time-derivative of the Cauchy stress and from the Eq.(7.21),

$$\begin{aligned}
\dot{\boldsymbol{\sigma}} &= \frac{1}{J}\left(\mathbf{F}\,\tilde{\mathbf{T}}\,\dot{\mathbf{F}}^T + \mathbf{F}\,\dot{\tilde{\mathbf{T}}}\,\mathbf{F}^T + \dot{\mathbf{F}}\,\tilde{\mathbf{T}}\,\mathbf{F}^T\right) \\
&= \frac{1}{J}\left(\mathbf{F}\,\tilde{\mathbf{T}}\,\mathbf{F}^T\,\mathbf{F}^{-T}\,\dot{\mathbf{F}}^T + \mathbf{F}\,\dot{\tilde{\mathbf{T}}}\,\mathbf{F}^T + \dot{\mathbf{F}}\,\mathbf{F}^{-1}\,\mathbf{F}\,\tilde{\mathbf{T}}\,\mathbf{F}^T\right) \\
&= \frac{1}{J}\left(\mathbf{F}\,\tilde{\mathbf{T}}\,\mathbf{F}^T\,\mathbf{l}^T + \mathbf{F}\,\dot{\tilde{\mathbf{T}}}\,\mathbf{F}^T + \mathbf{l}\,\mathbf{F}\,\tilde{\mathbf{T}}\,\mathbf{F}^T\right) \\
&= \underbrace{\frac{1}{J}\mathbf{F}\,\tilde{\mathbf{T}}\,\mathbf{F}^T}_{=\boldsymbol{\sigma}}\,\underbrace{\left(\mathbf{l}+\mathbf{l}^T\right)}_{=2\,\mathbf{d}} + \frac{1}{J}\mathbf{F}\,\dot{\tilde{\mathbf{T}}}\,\mathbf{F}^T \\
&= 2\,\boldsymbol{\sigma} : \mathbf{d} + \frac{1}{J}\mathbf{F}\,\underbrace{\left(2\,\frac{\partial\tilde{\mathbf{T}}}{\partial\mathbf{C}}\right)}_{=\mathbb{K}^{Lag}}\,\mathbf{F}^T : \frac{1}{2}\dot{\mathbf{C}} \\
&= \left(2\,\boldsymbol{\sigma}\otimes\mathbf{I} + \frac{1}{J}\left[\left(\mathbf{F}\otimes\mathbf{F}^T\right) : \mathbb{K}^{Lag} : \left(\mathbf{F}^T\otimes\mathbf{F}\right)\right]\right) : \mathbf{d}.
\end{aligned} \tag{7.25}$$

The incremental form of Eq.(7.25) can be given as

$$\Delta\boldsymbol{\sigma} = \underbrace{\left(2\,\boldsymbol{\sigma}\otimes\mathbf{I} + \frac{1}{J}\left[\left(\mathbf{F}\otimes\mathbf{F}^T\right) : \mathbb{K}^{Lag} : \left(\mathbf{F}^T\otimes\mathbf{F}\right)\right]\right)}_{=\mathbb{K}^{Eul}}\,\Delta\boldsymbol{\varepsilon}. \tag{7.26}$$

In finite-strain problems, $\boldsymbol{\varepsilon}^H$ is an approximation to the logarithmic strain which is also known as Hencky or true strain.

Therefore the transformation of the Lagrangian material tangent $\mathbb{K}^{Lag}$ to its equivalent $\mathbb{K}^{Eul}$ is possible with the relation

$$\mathbb{K}^{Eul} = 2\,\boldsymbol{\sigma}\otimes\mathbf{I} + \frac{1}{J}\left[\left(\mathbf{F}\otimes\mathbf{F}^T\right) : \mathbb{K}^{Lag} : \left(\mathbf{F}^T\otimes\mathbf{F}\right)\right] \tag{7.27}$$

where,

$$2\,\boldsymbol{\sigma}\otimes\mathbf{I} = \begin{bmatrix}
2\,\sigma_1 & 0 & 0 & \sigma_4 & 0 & \sigma_6 \\
 & 2\,\sigma_2 & 0 & \sigma_4 & \sigma_5 & 0 \\
 & & 2\,\sigma_3 & 0 & \sigma_5 & \sigma_6 \\
 & & & \frac{1}{2}\left(\sigma_2+\sigma_1\right) & \frac{1}{2}\sigma_6 & \frac{1}{2}\sigma_5 \\
 & sym & & & \frac{1}{2}\left(\sigma_3+\sigma_2\right) & \frac{1}{2}\sigma_4 \\
 & & & & & \frac{1}{2}\left(\sigma_1+\sigma_3\right)
\end{bmatrix} \tag{7.28}$$

This completes the implementation of mechanical constitutive equations for a purely mechanical theory ignoring thermal effects into finite element program Abaqus, which uses user-subroutine UMAT. In UMAT, the stresses have to be stored as *STRESS* and material tangent $\mathbb{K}^{Eul}$ as *DDSDDE*.

7.2 Thermo-viscoelasticity

Referring to the Abaqus documentation, in Abaqus the temperatures are integrated using a backward-difference scheme, and the non-linear coupled system is solved using Newton's method.

An exact implementation of Newton's method for fully coupled temperature-displacement analysis involves a non-symmetric Jacobian matrix as is illustrated in the following matrix representation of the coupled equations:

$$\begin{bmatrix} \mathbb{K}_{uu} & \mathbb{K}_{u\theta} \\ \mathbb{K}_{\theta u} & \mathbb{K}_{\theta\theta} \end{bmatrix} \begin{pmatrix} \Delta \mathbf{u} \\ \Delta\theta \end{pmatrix} = \begin{pmatrix} R_u \\ R_\theta \end{pmatrix} \tag{7.29}$$

where,

$\mathbb{K}_{ij}$ = submatrices of the fully coupled Jacobian matrix,

Δu_i = incremental displacement,

$\Delta\theta$ = incremental temperature,

R_u = mechanical residual vector,

R_θ = thermal residual vector.

Abaqus makes use of the non-symmetric matrix storage and solution scheme to solve the non-linear coupled system of equations in (7.29). The number of degrees of freedom for mechanical system is $nDOF_{mech} = 6$ and for thermal system is $nDOF_{thermal} = 1$.

7.2.1 Lagrangian formulation

The 2^{nd} PK stress which includes thermal effects can be written as

$$\tilde{\mathbf{T}} = \overset{D}{\tilde{\mathbf{T}}} + \overset{V}{\tilde{\mathbf{T}}} + \overset{C}{\tilde{\mathbf{T}}} \,. \tag{7.30}$$

where $\overset{C}{\tilde{\mathbf{T}}}$ is the coupled temperature-volume change part of stress tensor.

The time derivative of 2^{nd} PK stress can be given as

$$\dot{\tilde{\mathbf{T}}} = 2\,\frac{\partial \tilde{\mathbf{T}}}{\partial \mathbf{C}} : \frac{1}{2}\,\dot{\mathbf{C}} + \frac{\partial \tilde{\mathbf{T}}}{\partial \theta}\,\dot{\theta} \tag{7.31}$$

The linearised constitutive equation of (7.31) is

$$\Delta\tilde{\mathbf{T}} = \underbrace{2\,\frac{\partial \tilde{\mathbf{T}}}{\partial \mathbf{C}}}_{=\mathbb{K}^{Lag}_{uu}} : \frac{1}{2}\,\Delta\mathbf{C} + \underbrace{\frac{\partial \tilde{\mathbf{T}}}{\partial \theta}}_{=\mathbf{K}^{Lag}_{u\theta}}\,\Delta\theta, \tag{7.32}$$

where $\mathbb{K}^{Lag}_{uu}$ and $\mathbf{K}^{Lag}_{u\theta}$ refers to the mechanical and mechanical-thermal parts of coupled Lagrangian material tangent and can be defined as

$$\mathbb{K}^{Lag}_{uu} = 2\,\frac{\partial \tilde{\mathbf{T}}}{\partial \mathbf{C}} \tag{7.33}$$

$$\mathbf{K}^{Lag}_{u\theta} = \frac{\partial \tilde{\mathbf{T}}}{\partial \theta} \tag{7.34}$$

Thus, the stresses in Eq.(7.30) have to be differentiated with respect to the right Cauchy-Green tensor $\mathbf{C}$ and temperature θ:

$$\mathbb{K}_{uu}^{Lag} = \overset{D}{\mathbb{K}}_{uu}^{Lag} + \overset{V}{\mathbb{K}}_{uu}^{Lag} + \overset{C}{\mathbb{K}}_{uu}^{Lag} = 2\,\frac{\partial\,\overset{D}{\tilde{\mathbf{T}}}}{\partial \mathbf{C}} + 2\,\frac{\partial\,\overset{V}{\tilde{\mathbf{T}}}}{\partial \mathbf{C}} + 2\,\frac{\partial\,\overset{C}{\tilde{\mathbf{T}}}}{\partial \mathbf{C}} \tag{7.35}$$

$$\mathbf{K}_{u\theta}^{Lag} = \overset{D}{\mathbf{K}}_{u\theta}^{Lag} + \overset{C}{\mathbf{K}}_{u\theta}^{Lag} = \frac{\partial\,\overset{D}{\tilde{\mathbf{T}}}}{\partial \theta} + \frac{\partial\,\overset{C}{\tilde{\mathbf{T}}}}{\partial \theta}. \tag{7.36}$$

As stated in the previous section, in Eq.(7.36), $\overset{D}{\mathbb{K}}_{uu}^{Lag}$ and $\overset{D}{\mathbf{K}}_{u\theta}^{Lag}$ which contains the uniaxial Dynamic Flocculation Model (DFM) has to be differentiated numerically. On the other hand $\overset{V}{\mathbb{K}}_{uu}^{Lag}$, $\overset{C}{\mathbb{K}}_{uu}^{Lag}$ and $\overset{C}{\mathbf{K}}_{u\theta}^{Lag}$ can be computed completely analytically using the functions

$$\overset{V}{\mathbb{K}}_{uu}^{Lag} + \overset{C}{\mathbb{K}}_{uu}^{Lag} = \mathfrak{f}_2\,(\mathbf{C^{-1}} \otimes \mathbf{C^{-1}}) + \mathfrak{f}_3\,(\mathbf{C^{-1}} \odot \mathbf{C^{-1}}) \tag{7.37}$$

where co-efficients $\mathfrak{f}_2$ and $\mathfrak{f}_3$ can be defined as

$$\begin{aligned} \mathfrak{f}_2 &= 2\,J\,\frac{\partial \psi^V}{\partial J} + J\,\frac{\partial^2 \psi^V}{\partial J^2} + 2\,J\,\frac{\partial \psi^C}{\partial J} + J\,\frac{\partial^2 \psi^C}{\partial J^2} \\ \mathfrak{f}_3 &= -2\,J\,\frac{\partial \psi^V}{\partial J} - 2\,J\,\frac{\partial \psi^C}{\partial J}. \end{aligned} \tag{7.38}$$

7.2.2 Eulerian formulation

From the Eq.(7.21), the corresponding Cauchy stress for the second PK stress in Eq.(7.30) can be calculated. Furthermore, for converting the Lagrangian material tangent $\mathbb{K}^{Lag}$ which includes thermal effects to its equivalent $\mathbb{K}^{Eul}$, we consider the time-derivative of Cauchy stress as

$$\begin{aligned} \dot{\boldsymbol{\sigma}} &= \underbrace{\frac{1}{J}\,\mathbf{F}\,\tilde{\mathbf{T}}\,\mathbf{F}^T}_{=\boldsymbol{\sigma}}\,\underbrace{\left(\mathbf{l} + \mathbf{l}^T\right)}_{=2\,\mathbf{d}} + \frac{1}{J}\,\mathbf{F}\,\dot{\tilde{\mathbf{T}}}\,\mathbf{F}^T \\ &= 2\,\boldsymbol{\sigma} : \mathbf{d} + \frac{1}{J}\,\mathbf{F}\,\underbrace{\left(2\,\frac{\partial \tilde{\mathbf{T}}}{\partial \mathbf{C}}\right)}_{=\mathbb{K}_{uu}^{Lag}}\,\mathbf{F}^T : \frac{1}{2}\dot{\mathbf{C}} + \frac{1}{J}\,\mathbf{F}\,\underbrace{\left(\frac{\partial \tilde{\mathbf{T}}}{\partial \theta}\right)}_{=\mathbf{K}_{u\theta}^{Lag}}\,\mathbf{F}^T\,\dot{\theta} \\ &= \underbrace{\left(2\,\boldsymbol{\sigma} \otimes \mathbf{I} + \frac{1}{J}\,\left[\left(\mathbf{F} \otimes \mathbf{F}^T\right) : \mathbb{K}_{uu}^{Lag} : \left(\mathbf{F}^T \otimes \mathbf{F}\right)\right]\right) : \mathbf{d}}_{①} + \underbrace{\frac{1}{J}\,\mathbf{F}\,\mathbf{K}_{u\theta}^{Lag}\,\mathbf{F}^T\,\dot{\theta}}_{②} \end{aligned} \tag{7.39}$$

where ① is the purely mechanical part and ② is the coupled mechanical-thermal part of global stiffness tensor relating to mechanical constitutive equations.

As the numerical implementation in the previous section was only pertaining to purely mechanical theory, we had only considered the first part ① of the Eq.(7.39) and the latter part was ignored. But in this section, the second part ② of the Eq.(7.39) is also included.

The incremental form of ① and ② in Eq.(7.39) can be given as

$$\Delta\boldsymbol{\sigma} = \underbrace{\left(2\,\boldsymbol{\sigma}\otimes\mathbf{I} + \frac{1}{J}\left[\left(\mathbf{F}\otimes\mathbf{F}^{T}\right) : \mathbb{K}_{uu}^{Lag} : \left(\mathbf{F}^{T}\otimes\mathbf{F}\right)\right]\right)}_{=\mathbb{K}_{uu}^{Eul}} \Delta\boldsymbol{\varepsilon} \tag{7.40}$$

$$+ \underbrace{\frac{1}{J}\,\mathbf{F}\,\mathbf{K}_{u\theta}^{Lag}\,\mathbf{F}^{T}}_{=\mathbf{K}_{u\theta}^{Eul}} \Delta\theta. \tag{7.41}$$

Therefore the transformation of Lagrangian material tangent $\mathbb{K}^{Lag}$ to its equivalent $\mathbb{K}^{Eul}$ is possible with the relation

$$\mathbb{K}_{uu}^{Eul} = 2\,\boldsymbol{\sigma}\otimes\mathbf{I} + \frac{1}{J}\left[\left(\mathbf{F}\otimes\mathbf{F}^{T}\right) : \mathbb{K}_{uu}^{Lag} : \left(\mathbf{F}^{T}\otimes\mathbf{F}\right)\right] \tag{7.42}$$

$$\mathbf{K}_{u\theta}^{Eul} = \frac{1}{J}\,\mathbf{F}\,\mathbf{K}_{u\theta}^{Lag}\,\mathbf{F}^{T}. \tag{7.43}$$

In UMAT, the stresses $\boldsymbol{\sigma}$ have to be stored as $STRESS$, material tangent $\mathbb{K}_{uu}^{Eul}$ as $DDSDDE$ and $\mathbf{K}_{u\theta}^{Eul}$ as $DDSDDT$.

In addition to these, we also require to define dissipation caused by mechanical deformation to address the evolution of temperature as self heating. This is possible by defining RPL. According to Abaqus, RPL is the volumetric heat generation per unit time at the end of the increment caused by mechanical working of the material.

From the Eq.(2.59)

$$\mathscr{D}_{int} = \boldsymbol{\sigma} : \mathbf{d} - J^{-1}\,\dot{\Psi} - J^{-1}\,\Upsilon\,\dot{\theta} \geq 0,$$

RPL can be calculated.

Therefore, we can define RPL as

$$RPL = \mathscr{D}^{m} - \Upsilon\,\dot{\theta}. \tag{7.44}$$

$\mathscr{D}^{m}$ is the mechanical dissipation due to viscoelastic effects. $\mathscr{D}^{m}$ depends on the assumptions made for the development of constitutive equations of various models. The entropy can de given as

$$\begin{aligned}\Upsilon &= -\frac{1}{J}\frac{\partial\Psi}{\partial\theta} \\ &= -\frac{1}{J}\left(\frac{\partial\Psi^{D}}{\partial\theta} + \frac{\partial\Psi^{C}}{\partial\theta} + \frac{\partial\Psi^{\theta}}{\partial\theta}\right).\end{aligned} \tag{7.45}$$

This completes the implementation of mechanical constitutive equations for a coupled thermo-mechanical theory into finite element program Abaqus using user-subroutine UMAT.

7.3 Heat transfer process

7.3.1 UMATht

For fully coupled temperature-displacement analysis, we make use of user-subroutine UMATht in combination with UMAT. UMATht is used to solve the thermal constitutive equations for heat transfer processes. In our case we have to define internal thermal energy per unit mass U and its variation with respect to temperature. In addition to that the body heat flux vector $\mathbf{q}$ and its variation with respect to gradients of temperature has to be defined.

The strong form of thermal energy balance is

$$\int_B \rho \dot{U}\, dv + \int_B div\mathbf{q}\, dv = 0. \tag{7.46}$$

The weak form of Eq.(7.46) can be given as

$$\int_B \delta\theta\, \rho \dot{U}\, dv + \int_B (\delta\nabla\theta)\, \mathbf{q}\, dv = 0. \tag{7.47}$$

By introducing the backward difference integration algorithm for internal thermal energy, we get

$$\frac{1}{\Delta t} \int_B \delta\theta\, \rho\, \Delta U\, dv + \int_B (\delta\nabla\theta)\, \mathbf{q}\, dv = 0. \tag{7.48}$$

This non-linear system is solved by using Newton's method.

The Jacobian for Newton's method is given by

$$\frac{1}{\Delta t} \int_B \delta\theta\, \rho \frac{\partial U}{\partial \theta}\, d\theta\, dv + \int_B (\delta\nabla\theta) \frac{\partial \mathbf{q}}{\partial \nabla\theta}\, d\nabla\theta\, dv = 0. \tag{7.49}$$

This problem can be solved by specifying thermal conductivity and specific heat capacity. The rate of internal thermal energy can be given as

$$\dot{U} = \frac{\partial U}{\partial \theta} \frac{\partial \theta}{\partial t} = C_p\, \dot{\theta}, \tag{7.50}$$

$$\frac{\partial U}{\partial \theta} = C_p \tag{7.51}$$

where C_p is the specific heat capacity.

The increment of internal thermal energy can be given as

$$\Delta U = \frac{\partial U}{\partial \theta}\, \Delta\theta. \tag{7.52}$$

Finally the update of internal thermal energy can be given as

$$U(t + \Delta t) = U(t) + \Delta U(t + \Delta t). \tag{7.53}$$

The body heat flux vector can be given as

$$\mathbf{q} = -\kappa\, \nabla\theta \tag{7.54}$$

and its variation with respect to gradients of temperature is

$$\frac{\partial \mathbf{q}}{\partial \nabla\theta} = -\kappa. \tag{7.55}$$

where κ is the thermal conductivity.

7.3.2 DFLUX

To define the user specified surface boundary flux, we make use of another user subroutine DFLUX. From Behnke et al. [2012], the phenomenological heat transfer law for the heat flux through the boundary can be given as

$$q_{surf} = k_{stat}\,\Delta\theta + k_{conv}\,|\dot{u}_{\parallel surf}|\,\Delta\theta, \tag{7.56}$$

and

$$\Delta\theta = \theta_s - \theta_{amb}. \tag{7.57}$$

Where k_{stat} and k_{conv} are the static and convective heat exchange coefficients, respectively. θ_s and θ_{amb} are the surface temperature of the material and surrounding ambient temperature, respectively. $\dot{u}_{\parallel surf}$ is the tangential relative surface velocity of the considered surface point. The Eq.(7.56) contains both static heat conduction as well as dynamic heat convection phenomena for a surface displacement relative to its surrounding.

The initial operating temperature is defined in predefined field of initial analysis step and then the body temperature changes with respect to the Abaqus solver results.

7.4 Implementation of thermo-viscoelastic Zener Model

7.4.1 Complete 3-D Zener model

By solving the Eq.(6.33) using free energy functions in subsection 6.1.2 we get the 2^{nd} PK stress as

$$\begin{aligned}
\tilde{\mathbf{T}} &= \overset{D}{\tilde{\mathbf{T}}}_{eq} + \overset{D}{\tilde{\mathbf{T}}}_{neq} + \overset{V}{\tilde{\mathbf{T}}} + \overset{C}{\tilde{\mathbf{T}}} \\
&= 2\,C_{10}\,J^{-2/3}\left(\mathbf{I} - \frac{1}{3}(\mathbf{C} : \mathbf{I})\,\mathbf{C}^{-1}\right) \\
&+ \mu(\theta)\,J^{-2/3}\left(\mathbf{C}_i^{-1} - \frac{1}{3}(\mathbf{C}_i^{-1}\mathbf{C} : \mathbf{I})\,\mathbf{C}^{-1}\right) \\
&+ K_{mod}\,J\,(J-1)\,\mathbf{C}^{-1} \\
&- 3\,\alpha_T\,(\theta - \theta_{ref})\,K_{mod}\,J\,\mathbf{C}^{-1}.
\end{aligned} \tag{7.58}$$

Similarly solving the Eq.(6.58) we get the Cauchy stress as

$$\begin{aligned}
\boldsymbol{\sigma} &= \overset{D}{\boldsymbol{\sigma}}_{eq} + \overset{D}{\boldsymbol{\sigma}}_{neq} + \overset{V}{\boldsymbol{\sigma}} + \overset{C}{\boldsymbol{\sigma}} \\
&= 2\,C_{10}\,J^{-5/3}\left(\mathbf{b} - \frac{1}{3}(\mathbf{b} : \mathbf{I})\right) \\
&+ \mu(\theta)\,J^{-5/3}\left(\mathbf{b}_e - \frac{1}{3}(\mathbf{b}_e : \mathbf{I})\right) \\
&+ K_{mod}\,(J-1)\,\mathbf{I} \\
&- 3\alpha_T\,(\theta - \theta_{ref})\,K_{mod}\,\mathbf{I}.
\end{aligned} \tag{7.59}$$

Alternatively, the corresponding Cauchy stress for the second PK stress in Eq.(7.58) can also be calculated using Eq.(7.21).

The $\overset{D}{\mathbb{K}}{}^{Lag}_{uu}$ and $\overset{D}{\mathbf{K}}{}^{Lag}_{u\theta}$ are calculated numerically. $\overset{V}{\mathbb{K}}{}^{Lag}_{uu}$ and $\overset{C}{\mathbb{K}}{}^{Lag}_{uu}$ are calculated using the coefficients $\mathfrak{f}_2$ and $\mathfrak{f}_3$ in Eq.(7.38) as

$$\begin{aligned}\mathfrak{f}_2 &= 2\,K_{mod}\,J^2 - K_{mod}\,J - 6\,\alpha_T\,(\theta-\theta_{ref})\,K_{mod}\,J\\ \mathfrak{f}_3 &= -2\,K_{mod}\,J^2 + 2\,K_{mod}\,J + 6\,\alpha_T\,(\theta-\theta_{ref})\,K_{mod}\,J,\end{aligned} \tag{7.60}$$

and $\overset{C}{\mathbf{K}}{}^{Lag}_{u\theta}$ can be calculated using the equation

$$\overset{C}{\mathbf{K}}{}^{Lag}_{u\theta} = \mathfrak{f}_\theta\,\mathbf{C}^{-1}, \tag{7.61}$$

where $\mathfrak{f}_\theta$ is

$$\mathfrak{f}_\theta = -3\,\alpha_T\,K_{mod}\,J. \tag{7.62}$$

The corresponding Eulerian material tangents $\mathbb{K}^{Eul}_{uu}$ and $\mathbf{K}^{Eul}_{u\theta}$ can be calculated using the transformation functions in equations (7.42), and (7.43).

The variable RPL for the 3-D Zener model can be calculated using the Eq.(7.44). Accordingly,

$$\mathscr{D}^m = \overset{D}{\boldsymbol{\sigma}}_{neq} : (-\frac{1}{2}\,\mathscr{L}_v\mathbf{b}_e\cdot\mathbf{b}_e^{-1}) \tag{7.63}$$

where,

$$\overset{D}{\boldsymbol{\sigma}}_{neq} = \frac{1}{J}\,\mathbf{F}\,\tilde{\mathbf{T}}^D_{neq}\,\mathbf{F}^T. \tag{7.64}$$

Entropy can be calculated as

$$\begin{aligned}\Upsilon &= -\frac{1}{J}\left(\frac{\partial\Psi^D_{neq}}{\partial\theta}+\frac{\partial\Psi^C}{\partial\theta}+\frac{\partial\Psi^\theta}{\partial\theta}\right)\\ &= -\frac{\partial(\mu(\theta)/2)}{\partial\theta}\,(\widehat{\mathbf{I}}^{\mathbf{e}}_{\mathbf{1}}-3)+3\alpha_T\,K_{mod}\,(J-1)+C_p\,\rho\,ln\left(\frac{\theta}{\theta_{ref}}\right)\\ &= -\frac{\partial(\mu(\theta)/2)}{\partial\theta}\,\Big(tr(J^{-2/3}\,\mathbf{b}_e)-3\Big)+3\alpha_T\,K_{mod}\,(J-1)+C_p\,\rho\,ln\left(\frac{\theta}{\theta_{ref}}\right)\\ &= -\frac{\partial(\mu(\theta)/2)}{\partial\theta}\,\Big(J^{-2/3}\,tr(\mathbf{C}\,\mathbf{C}_i^{-1})-3\Big)+3\alpha_T\,K_{mod}\,(J-1)+C_p\,\rho\,ln\left(\frac{\theta}{\theta_{ref}}\right)\end{aligned} \tag{7.65}$$

where,

$$\frac{\partial\mu(\theta)}{\partial\theta} = -\frac{E_a\,\mu_0}{R\,\theta^2}\,e^{\frac{E_a}{R}\left(\frac{1}{\theta}-\frac{1}{\theta_{ref}}\right)}. \tag{7.66}$$

7.4.2 1-D Zener model using representative directions

Considering only the deviatoric part of the free energy function, the rate of free energy function can be written as

$$\dot\Psi^D = \frac{\partial\Psi^D_{eq}}{\partial\mathbf{F}} : \dot{\mathbf{F}} + \frac{\partial\Psi^D_{neq}}{\partial\mathbf{F}_e} : \dot{\mathbf{F}}_e + \frac{\partial\Psi^D_{neq}}{\partial\theta}\,\dot\theta. \tag{7.67}$$

The free energy function $\dot{\Psi}^D$ in the uniaxial direction can be written as

$$\dot{\Psi}^D = \frac{\partial \Psi^D_{eq}}{\partial \lambda}\,\dot{\lambda} + \frac{\partial \Psi^D_{neq}}{\partial \lambda_e}\,\dot{\lambda}_e + \frac{\partial \Psi^D_{neq}}{\partial \theta}\,\dot{\theta}. \tag{7.68}$$

The multiplicative decomposition of deformation gradient into elastic and inelastic parts leads to

$$\lambda = \lambda_e\,\lambda_i, \tag{7.69}$$

where λ_e and λ_i are the elastic and inelastic stretch ratios, respectively.

The rate of stretch ratio can be given as

$$\dot{\lambda} = \lambda_e\,\dot{\lambda}_i + \dot{\lambda}_e\,\lambda_i, \tag{7.70}$$

and therefore,

$$\dot{\lambda}_e = \lambda_i^{-1}\,\dot{\lambda} - \lambda_e\,\lambda_i^{-1}\,\dot{\lambda}_i. \tag{7.71}$$

Substituting Eq.(7.71) into Eq.(7.68) yields

$$\dot{\Psi}^D = \frac{\partial \Psi^D_{eq}}{\partial \lambda}\,\dot{\lambda} + \lambda_i^{-1}\,\frac{\partial \Psi^D_{neq}}{\partial \lambda_e}\,\dot{\lambda} - \lambda_e\,\lambda_i^{-1}\,\frac{\partial \Psi^D_{neq}}{\partial \lambda_e}\,\dot{\lambda}_i + \frac{\partial \Psi^D_{neq}}{\partial \theta}\,\dot{\theta}. \tag{7.72}$$

The assumed deviatoric energy function of the Zener model is

$$\Psi^D = \Psi^D_{eq} + \Psi^D_{neq} = C_{10}\,(\widehat{\mathbf{I}}_{\mathbf{1}} - 3) + \frac{\mu(\theta)}{2}\,(\widehat{\mathbf{I}}^{\mathbf{e}}_{\mathbf{1}} - 3). \tag{7.73}$$

And in uniaxial direction is

$$\Psi^D = C_{10}\left(\lambda^{*2} + \frac{2}{\lambda^*} - 3\right) + \frac{\mu(\theta)}{2}\left(\lambda_e^{*2} + \frac{2}{\lambda_e^*} - 3\right). \tag{7.74}$$

The modified stress and entropy to calculate the deviatoric stresses and entropy is given by

$$T^* = \frac{\partial \Psi^D_{eq}}{\partial \lambda^*} + \lambda_i^{-1}\,\frac{\partial \Psi^D_{neq}}{\partial \lambda_e^*} \tag{7.75}$$

$$\Upsilon^* = -\frac{\partial \Psi^D_{neq}}{\partial \theta}, \tag{7.76}$$

where,

$$\frac{\partial \Psi^D_{eq}}{\partial \lambda^*} = 2\,C_{10}\left(\lambda^* - \frac{1}{\lambda^{*2}}\right) \tag{7.77}$$

$$\frac{\partial \Psi^D_{neq}}{\partial \lambda_e^*} = \mu(\theta)\left(\lambda_e^* - \frac{1}{\lambda_e^{*2}}\right) \tag{7.78}$$

$$\frac{\partial \Psi^D_{neq}}{\partial \theta} = \frac{\partial(\mu(\theta)/2)}{\partial \theta}\left(\lambda_e^{*2} + \frac{2}{\lambda_e^*} - 3\right). \tag{7.79}$$

Finally the modified stress and entropy functions can be calculated using

$$T^* = 2\,C_{10}\left(\lambda^* - \frac{1}{\lambda^{*2}}\right) + \mu(\theta)\left(\lambda_e^* - \frac{1}{\lambda_e^{*2}}\right)\lambda_i^{*-1} \tag{7.80}$$

$$\Upsilon^* = -\frac{\partial(\mu(\theta)/2)}{\partial \theta}\left(\lambda_e^{*2} + \frac{2}{\lambda_e^*} - 3\right). \tag{7.81}$$

The evolution function for the 1-D Zener model can be given as

$$\lambda_i^* = \lambda_i^* + \Delta t \left[\frac{2}{\tau} \left(\frac{\lambda^{*2}}{\lambda_i^{*3}} - \frac{1}{\lambda^*} \right) \right] \tag{7.82}$$

$$\lambda_e^* = \frac{\lambda^*}{\lambda_i^*}. \tag{7.83}$$

Chapter 8

Experiments

8.1 Multi-modal test velocity and strain amplitudes

In order to characterize the material behaviour in multi-modal axes, the correlation of test velocity and strain amplitudes between different multi-modal physical experiments have to be determined. This correlation ensures a balanced influence of each test mode on the fitting parameter of the material model. In the following sections the test velocity and strain amplitudes are determined based on the logarithmic strain and its rate.

8.1.1 Rate of logarithmic strain

The deformation gradient $\mathbf{F}$ is

$$\mathbf{F} = \begin{bmatrix} \lambda_1 & 0 & 0 \\ 0 & \lambda_2 & 0 \\ 0 & 0 & \lambda_3 \end{bmatrix} \tag{8.1}$$

Principal stretch ratios: λ_1, λ_2 and λ_3

For incompressibility of the material: $J = det\mathbf{F} = \lambda_1\,\lambda_2\,\lambda_3 = 1$.

The right Cauchy-Green deformation tensor is

$$\mathbf{C} = \mathbf{F^T F} = \begin{bmatrix} \lambda_1^2 & 0 & 0 \\ 0 & \lambda_2^2 & 0 \\ 0 & 0 & \lambda_3^2 \end{bmatrix} \tag{8.2}$$

The rate of logarithmic strain is

$$\dot{\varepsilon}^H = \sqrt{\frac{1}{6}\ tr\left(\dot{\mathbf{C}} \cdot \mathbf{C}^{-1}\right)^2} \tag{8.3}$$

The question arises whether the logarithmic strain rates of all the multi axial load tests are equal or not. That means

$$\dot{\varepsilon}^h_{ux} \stackrel{?}{=} \dot{\varepsilon}^h_{bx} \stackrel{?}{=} \dot{\varepsilon}^h_{ps} \stackrel{?}{=} \dot{\varepsilon}^h_{ss}. \tag{8.4}$$

In order to find out that, we derive the strain rate of each test modes in the following sections.

8.1.2 Uniaxial tension

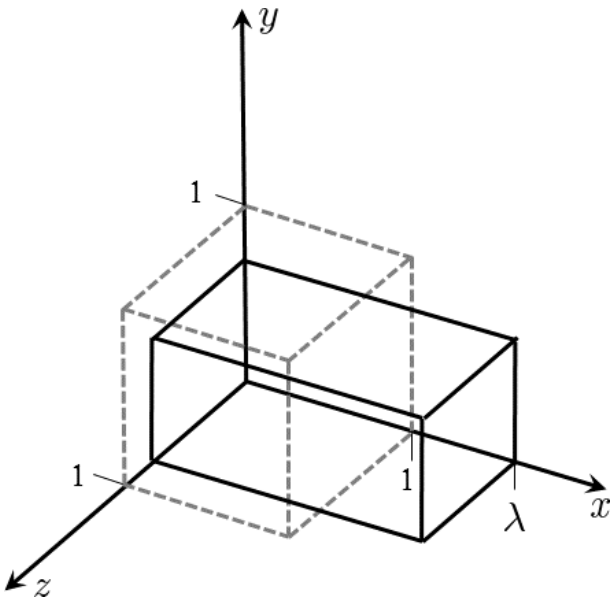

Figure 8.1: Schematic representation of uniaxial deformation state.

The principal stretches for the uniaxial tension deformation mode are $\lambda_1 = \lambda$ and $\lambda_2 = \lambda_3 = 1/\sqrt{\lambda}$. The deformation gradient $\mathbf{F}$ for uniaxial tension is

$$\mathbf{F} = \begin{bmatrix} \lambda & 0 & 0 \\ 0 & \frac{1}{\sqrt{\lambda}} & 0 \\ 0 & 0 & \frac{1}{\sqrt{\lambda}} \end{bmatrix} \tag{8.5}$$

The right Cauchy-Green deformation tensor is

$$\mathbf{C} = \mathbf{F}^{\mathbf{T}}\mathbf{F} = \begin{bmatrix} \lambda^2 & 0 & 0 \\ 0 & \frac{1}{\lambda} & 0 \\ 0 & 0 & \frac{1}{\lambda} \end{bmatrix} \tag{8.6}$$

The rate and inverse of right Cauchy-Green deformation tensor $\mathbf{C}$ can be written as

$$\dot{\mathbf{C}} = \begin{bmatrix} 2\lambda\dot{\lambda} & 0 & 0 \\ 0 & -\frac{\dot{\lambda}}{\lambda^2} & 0 \\ 0 & 0 & -\frac{\dot{\lambda}}{\lambda^2} \end{bmatrix} \tag{8.7}$$

$$\mathbf{C}^{-1} = \begin{bmatrix} \frac{1}{\lambda^2} & 0 & 0 \\ 0 & \lambda & 0 \\ 0 & 0 & \lambda \end{bmatrix} \tag{8.8}$$

The product of rate and inverse of right Cauchy-Green deformation tensor can be written as

$$\dot{\mathbf{C}} \cdot \mathbf{C}^{-1} = \begin{bmatrix} \frac{2\dot{\lambda}}{\lambda} & 0 & 0 \\ 0 & -\frac{\dot{\lambda}}{\lambda} & 0 \\ 0 & 0 & -\frac{\dot{\lambda}}{\lambda} \end{bmatrix} \tag{8.9}$$

The square of the matrix in the Eq.(8.9) can be written as

$$(\dot{\mathbf{C}} \cdot \mathbf{C}^{-1})^2 = \begin{bmatrix} \frac{4\dot{\lambda}^2}{\lambda^2} & 0 & 0 \\ 0 & \frac{\dot{\lambda}^2}{\lambda^2} & 0 \\ 0 & 0 & \frac{\dot{\lambda}^2}{\lambda^2} \end{bmatrix} \tag{8.10}$$

The trace of the Eq.(8.10) yields

$$tr\left(\dot{\mathbf{C}} \cdot \mathbf{C}^{-1}\right)^2 = \frac{4\dot{\lambda}^2}{\lambda^2} + \frac{\dot{\lambda}^2}{\lambda^2} + \frac{\dot{\lambda}^2}{\lambda^2} \tag{8.11}$$

Finally, substituting the the Eq.(8.11) in the Eq.(8.3) yields

$$\dot{\varepsilon}^h_{ux} = \sqrt{\frac{1}{6}\ tr\left(\dot{\mathbf{C}} \cdot \mathbf{C}^{-1}\right)^2} = \frac{\dot{\lambda}}{\lambda} \tag{8.12}$$

8.1.3 Biaxial tension

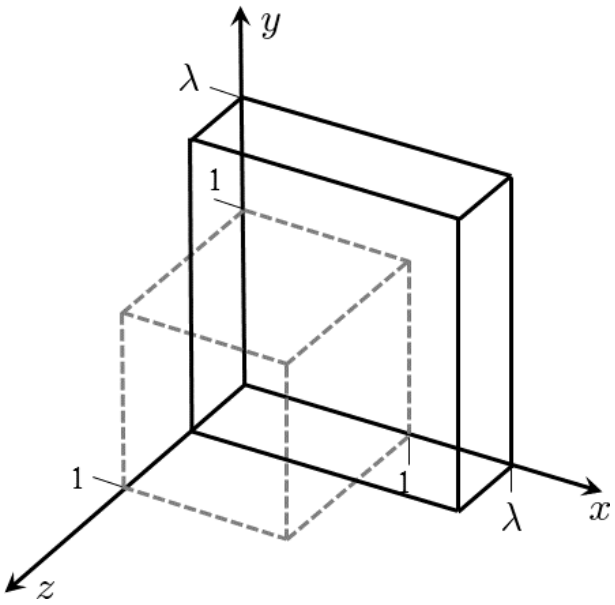

Figure 8.2: Schematic representation of biaxial deformation state.

The principal stretches for the biaxial tension deformation mode are $\lambda_1 = \lambda_2 = \lambda$ and $\lambda_3 = 1/\lambda^2$. The deformation gradient $\mathbf{F}$ for biaxial tension is

$$\mathbf{F} = \begin{bmatrix} \lambda & 0 & 0 \\ 0 & \lambda & 0 \\ 0 & 0 & \frac{1}{\lambda^2} \end{bmatrix} \tag{8.13}$$

The right Cauchy-Green deformation tensor is

$$\mathbf{C} = \mathbf{F}^{\mathbf{T}}\mathbf{F} = \begin{bmatrix} \lambda^2 & 0 & 0 \\ 0 & \lambda^2 & 0 \\ 0 & 0 & \frac{1}{\lambda^4} \end{bmatrix} \tag{8.14}$$

The rate and inverse of right Cauchy-Green deformation tensor $\mathbf{C}$ can be written as

$$\dot{\mathbf{C}} = \begin{bmatrix} 2\lambda\dot{\lambda} & 0 & 0 \\ 0 & 2\lambda\dot{\lambda} & 0 \\ 0 & 0 & -\frac{4\dot{\lambda}}{\lambda^5} \end{bmatrix} \tag{8.15}$$

$$\mathbf{C}^{-1} = \begin{bmatrix} \frac{1}{\lambda^2} & 0 & 0 \\ 0 & \frac{1}{\lambda^2} & 0 \\ 0 & 0 & \lambda^4 \end{bmatrix} \tag{8.16}$$

The product of rate and inverse of right Cauchy-Green deformation tensor can be written as

$$\dot{\mathbf{C}} \cdot \mathbf{C}^{-1} = \begin{bmatrix} \frac{2\dot{\lambda}}{\lambda} & 0 & 0 \\ 0 & \frac{2\dot{\lambda}}{\lambda} & 0 \\ 0 & 0 & -\frac{4\dot{\lambda}}{\lambda} \end{bmatrix} \tag{8.17}$$

The square of the matrix in the Eq.(8.17) can be written as

$$(\dot{\mathbf{C}} \cdot \mathbf{C}^{-1})^2 = \begin{bmatrix} \frac{4\dot{\lambda}^2}{\lambda^2} & 0 & 0 \\ 0 & \frac{4\dot{\lambda}^2}{\lambda^2} & 0 \\ 0 & 0 & \frac{16\dot{\lambda}^2}{\lambda^2} \end{bmatrix} \tag{8.18}$$

The trace of the Eq.(8.18) yields

$$tr\left(\dot{\mathbf{C}} \cdot \mathbf{C}^{-1}\right)^2 = \frac{4\dot{\lambda}^2}{\lambda^2} + \frac{4\dot{\lambda}^2}{\lambda^2} + \frac{16\dot{\lambda}^2}{\lambda^2} \tag{8.19}$$

Finally, substituting the the Eq.(8.19) in the Eq.(8.3) yields

$$\dot{\varepsilon}^h_{bx} = \sqrt{\frac{1}{6}\ tr\left(\dot{\mathbf{C}} \cdot \mathbf{C}^{-1}\right)^2} = \frac{2\dot{\lambda}}{\lambda} \tag{8.20}$$

8.1.4 Planar tension or pure shear

The principal stretches for the pure shear deformation mode are $\lambda_1 = \lambda$, $\lambda_2 = 1/\lambda$, $\lambda_3 = 1$. The deformation gradient $\mathbf{F}$ for pure shear is

$$\mathbf{F} = \begin{bmatrix} \lambda & 0 & 0 \\ 0 & \frac{1}{\lambda} & 0 \\ 0 & 0 & 1 \end{bmatrix} \tag{8.21}$$

The right Cauchy-Green deformation tensor is

$$\mathbf{C} = \mathbf{F}^{\mathbf{T}}\mathbf{F} = \begin{bmatrix} \lambda^2 & 0 & 0 \\ 0 & \frac{1}{\lambda^2} & 0 \\ 0 & 0 & 1 \end{bmatrix} \tag{8.22}$$

The rate and inverse of right Cauchy-Green deformation tensor $\mathbf{C}$ can be written as

$$\dot{\mathbf{C}} = \begin{bmatrix} 2\lambda\dot{\lambda} & 0 & 0 \\ 0 & -\frac{2\dot{\lambda}}{\lambda^3} & 0 \\ 0 & 0 & 0 \end{bmatrix} \tag{8.23}$$

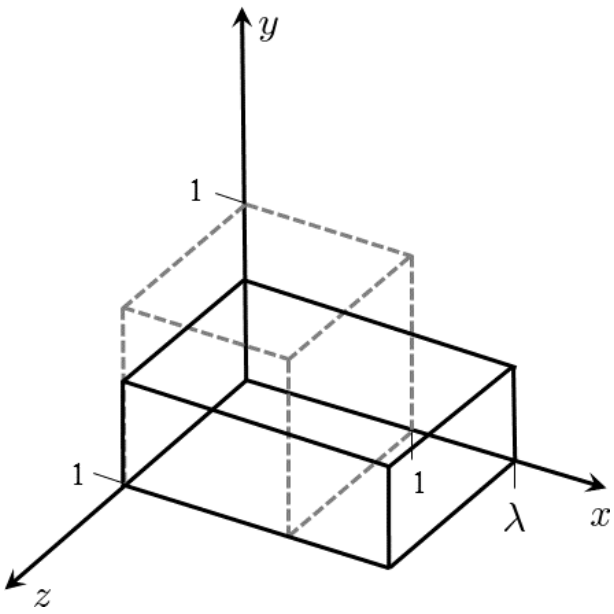

Figure 8.3: Schematic representation of pure shear deformation state.

$$\mathbf{C}^{-1} = \begin{bmatrix} \frac{1}{\lambda^2} & 0 & 0 \\ 0 & \lambda^2 & 0 \\ 0 & 0 & 1 \end{bmatrix} \tag{8.24}$$

The product of rate and inverse of right Cauchy-Green deformation tensor can be written as

$$\dot{\mathbf{C}} \cdot \mathbf{C}^{-1} = \begin{bmatrix} \frac{2\dot{\lambda}}{\lambda} & 0 & 0 \\ 0 & -\frac{2\dot{\lambda}}{\lambda} & 0 \\ 0 & 0 & 0 \end{bmatrix} \tag{8.25}$$

The square of the matrix in the Eq.(8.25) can be written as

$$(\dot{\mathbf{C}} \cdot \mathbf{C}^{-1})^2 = \begin{bmatrix} \frac{4\dot{\lambda}^2}{\lambda^2} & 0 & 0 \\ 0 & \frac{4\dot{\lambda}^2}{\lambda^2} & 0 \\ 0 & 0 & 0 \end{bmatrix} \tag{8.26}$$

The trace of the Eq.(8.26) yields

$$tr\left(\dot{\mathbf{C}} \cdot \mathbf{C}^{-1}\right)^2 = \frac{4\dot{\lambda}^2}{\lambda^2} + \frac{4\dot{\lambda}^2}{\lambda^2} \tag{8.27}$$

Finally, substituting the the Eq.(8.27) in the Eq.(8.3) yields

$$\dot{\varepsilon}^h_{ps} = \sqrt{\frac{1}{6}\ tr\left(\dot{\mathbf{C}} \cdot \mathbf{C}^{-1}\right)^2} = \sqrt{\frac{4}{3}}\frac{\dot{\lambda}}{\lambda} \tag{8.28}$$

8.1.5 Simple shear

The deformation gradient $\mathbf{F}$ for simple shear is

$$\mathbf{F} = \begin{bmatrix} 1 & \gamma & 0 \\ 0 & 1 & 0 \\ 0 & 0 & 1 \end{bmatrix} \tag{8.29}$$

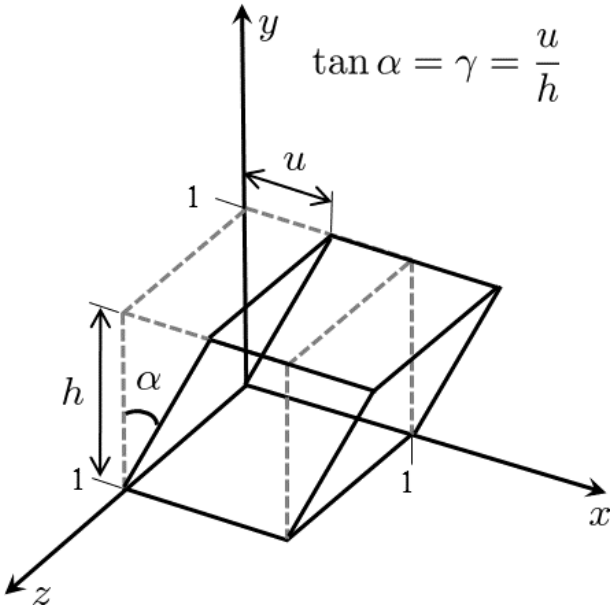

Figure 8.4: Schematic representation of simple shear deformation state.

The right Cauchy-Green deformation tensor is

$$\mathbf{C} = \mathbf{F}^{\mathbf{T}}\mathbf{F} = \begin{bmatrix} 1 & \gamma & 0 \\ \gamma & 1+\gamma^2 & 0 \\ 0 & 0 & 1 \end{bmatrix} \tag{8.30}$$

The rate and inverse of right Cauchy-Green deformation tensor $\mathbf{C}$ can be written as

$$\dot{\mathbf{C}} = \begin{bmatrix} 0 & \dot{\gamma} & 0 \\ \dot{\gamma} & 2\gamma\dot{\gamma} & 0 \\ 0 & 0 & 0 \end{bmatrix} \tag{8.31}$$

$$\mathbf{C}^{-1} = \begin{bmatrix} 1+\gamma^2 & -\gamma & 0 \\ -\gamma & 1 & 0 \\ 0 & 0 & 1 \end{bmatrix} \tag{8.32}$$

The product of rate and inverse of right Cauchy-Green deformation tensor can be written as

$$\dot{\mathbf{C}} \cdot \mathbf{C}^{-1} = \begin{bmatrix} -\gamma\dot{\gamma} & \dot{\gamma} & 0 \\ \dot{\gamma} - \gamma^2\dot{\gamma} & \gamma\dot{\gamma} & 0 \\ 0 & 0 & 0 \end{bmatrix} \tag{8.33}$$

The square of the matrix in the Eq.(8.33) can be written as

$$(\dot{\mathbf{C}} \cdot \mathbf{C}^{-1})^2 = \begin{bmatrix} \dot{\gamma}^2 & 0 & 0 \\ 0 & \dot{\gamma}^2 & 0 \\ 0 & 0 & 0 \end{bmatrix} \tag{8.34}$$

The trace of the Eq.(8.34) yields

$$tr\left(\dot{\mathbf{C}} \cdot \mathbf{C}^{-1}\right)^2 = \dot{\gamma}^2 + \dot{\gamma}^2 \tag{8.35}$$

Finally, substituting the the Eq.(8.35) in the Eq.(8.3) yields

$$\dot{\varepsilon}^h_{ss} = \sqrt{\frac{1}{6}\ tr\left(\dot{\mathbf{C}}\cdot\mathbf{C}^{-1}\right)^2} = \frac{\dot{\gamma}}{\sqrt{3}} \tag{8.36}$$

From the equations (8.12), (8.20), (8.28) and (8.36), we can write

$$\begin{aligned} &\dot{\varepsilon}^h_{ux} \neq \dot{\varepsilon}^h_{bx} \neq \dot{\varepsilon}^h_{ps} \neq \dot{\varepsilon}^h_{ss} \qquad \text{because} \\ &\frac{\dot{\lambda}}{\lambda} \neq \frac{2\dot{\lambda}}{\lambda} \neq \sqrt{\frac{4}{3}}\frac{\dot{\lambda}}{\lambda} \neq \frac{\dot{\gamma}}{\sqrt{3}}. \end{aligned} \tag{8.37}$$

The equivalent logarithmic strain rates of different modes can be calculated

$$\text{if, } \dot{\varepsilon}^h_{ux} = \frac{\dot{\lambda}}{\lambda},$$

$$\text{then, } \dot{\varepsilon}^h_{bx} = \frac{2\dot{\lambda}}{\lambda} = 2\,\dot{\varepsilon}^h_{ux}, \tag{8.38}$$

$$\text{and } \dot{\varepsilon}^h_{ps} = \sqrt{\frac{4}{3}}\frac{\dot{\lambda}}{\lambda} = \sqrt{\frac{4}{3}}\,\dot{\varepsilon}^h_{ux}. \tag{8.39}$$

If the stretch rate of one of the deformation mode is known, then the equivalent stretch rates of other modes can be calculated as

$$\dot{\lambda}_{ux} = \dot{\varepsilon}^h\ \lambda, \tag{8.40}$$

$$\dot{\lambda}_{bx} = \frac{1}{2}\,\dot{\varepsilon}^h\ \lambda, \tag{8.41}$$

$$\dot{\lambda}_{ps} = \sqrt{\frac{3}{4}}\,\dot{\varepsilon}^h\ \lambda, \tag{8.42}$$

$$\dot{\gamma} = \sqrt{3}\,\dot{\varepsilon}^h. \tag{8.43}$$

8.1.6 Rate of displacement or velocity

The relation between stretch λ, stretch rate $\dot{\lambda}$, and the velocity of deformation $\dot{u}$ for the uniaxial, biaxial and planar tension test modes can be written as

$$\lambda = \frac{u}{u_0}, \tag{8.44}$$

$$\dot{\lambda} = \frac{\dot{u}}{u_0} \iff \dot{u} = \dot{\lambda}\ u_0. \tag{8.45}$$

Where, u_0 is the initial length and u is the final length.

Similarly the relation between shear strain γ, shear strain rate $\dot{\gamma}$, and the velocity of deformation $\dot{u}$ for the simple shear test mode can be written as

$$\gamma = \frac{u}{h}, \tag{8.46}$$

$$\dot{\gamma} = \frac{\dot{u}}{h} \iff \dot{u} = \dot{\gamma}\ h. \tag{8.47}$$

Where, h is the thickness of the simple shear test sample.

With an assumption of constant strain rate $\dot{\varepsilon}$ and initial stretch ratio λ=1, we can calculate the test velocity for different test modes as given in Tab.8.1

Table 8.1: Correlation of unknown velocity for different load tests with constant strain rate calculated from a given input of uniaxial stretch velocity (arrows indicate the calculation sequence).

Parameters	uniaxial	biaxial	pure shear	simple shear
u_0 [mm]	20	80	20	
h [mm]				2
$\dot{u}$ [mm/min]	15 (given) $\Downarrow$	30	13	2.6
$\dot{\lambda}$ or $\dot{\gamma}$ [/min]	0.75 $\Downarrow$	0.375 $\Uparrow$	0.866 $\Uparrow$	1.3 $\Uparrow$
$\dot{\varepsilon}^h$ [/min]	0.75 $\Rightarrow$	0.75 $\Uparrow$	0.75 $\Uparrow$	0.75 $\Uparrow$
$\dot{u}$ [mm/min]	10 (given)	20	8.7	1.7
	20 (given)	40	17.3	3.5

Table 8.2: Correlation of unknown strain amplitudes for different load tests calculated from a given input of uniaxial strain (arrows indicate the calculation sequence).

ε_{ux} [%]	λ_{ux}	ε^h	λ_{bx}	ε_{bx} [%]	λ_{ps}	ε_{ps} [%]	γ [%]
20	1.2	0.1823 $\Rightarrow$	1.0954	9.5	1.171	17	32
40	1.4	0.3364 $\Rightarrow$	1.1831	18	1.3382	34	58
60	1.6	0.47 $\Rightarrow$	1.2649	26	1.5023	50	81
80	1.8	0.5877 $\Rightarrow$	1.3415	34	1.6635	66	102
100	2	0.6931 $\Rightarrow$	1.4141	41	1.8225	82	120

8.1.7 Stretch ratio and strain amplitude

The integration of equations (8.12), (8.20), (8.28) and (8.36) with respect to time leads to

$$\dot{\varepsilon}^h_{ux} = \frac{\dot{\lambda}}{\lambda} \quad \Longrightarrow \quad \varepsilon^h_{ux} = ln\lambda \quad \Longleftrightarrow \quad \lambda_{ux} = e^{\varepsilon^h} \tag{8.48}$$

$$\dot{\varepsilon}^h_{bx} = \frac{2\dot{\lambda}}{\lambda} \quad \Longrightarrow \quad \varepsilon^h_{bx} = 2ln\lambda \quad \Longleftrightarrow \quad \lambda_{bx} = e^{\varepsilon^h/2} \tag{8.49}$$

$$\dot{\varepsilon}^h_{ps} = \sqrt{\frac{4}{3}}\frac{\dot{\lambda}}{\lambda} \quad \Longrightarrow \quad \varepsilon^h_{ps} = \sqrt{\frac{4}{3}} ln\lambda \quad \Longleftrightarrow \quad \lambda_{ps} = e^{\sqrt{3/4}\,\varepsilon^h} \tag{8.50}$$

$$\dot{\varepsilon}^h_{ss} = \frac{\dot{\gamma}}{\sqrt{3}} \Longrightarrow \varepsilon^h_{ss} = \frac{\gamma}{\sqrt{3}} \Longleftrightarrow \gamma = \sqrt{3}\,\varepsilon^h \tag{8.51}$$

The calculated strain amplitudes for different deformation modes based on referential input of uniaxial strain is given in Tab.8.2. The engineering or nominal strain $\varepsilon = \lambda$-1.

8.2 Rubber compound

In this work, six NR blend compounds with two kinds of Carbon Black (CB) with varying filler contents are used for the investigation. The recipe of one of the compound is given in Tab.8.3. The test specimens are vulcanized within a press at a temperature of $160°C$ and pressure of $280bar$. The vulcanization time can be measured using Vulkameter or rheometer measurement. The Fig.8.5 shows the rheometer curve measured at $150°C$ for the compound S50N1 using Alpha Technologies MDR 2000 E. This curve is very important for both compound mixing as well as for

Table 8.3: Composition of investigated rubber compound.

Sample	Rubber			Filler	Stearic	ZnO	X-link/accelerator	
	SMR20	SBR1502	CIS BR	N121 (CB)	acid		Sulphur	CBS
	phr	phr	phr	phr	phr	phr	phr	phr
S50N1	80	10	10	50	3	3	1	2

vulcanization. T^q_{min} is the minimum torque which represents the viscosity of uncured compound. t_{min} is the point where the compound in cavity has rheometer temperature. $t_{\Delta+2}$ and $t_{\Delta+5}$ indicate the scorch time which is important for mixing. This scorch time helps to control the compound from curing so that even after mixing the compound stays uncured. t_{90}, t_{98} and t_{100} are the time required for 90%, 98% and 100% curing, respectively. T^q_{max} is the maximum torque which indicates the maximum crosslink density. The t_{98} for S50N1 is $11.77min$ and in addition to this time, an extra time, which depends on the thickness or diameter of the test specimen has to be added for vulcanisation of desired test samples or components. If for example the specimen is $2mm$ thick then the total vulcanization time is $t_{98} + 2min = 13.77min$. S50N1 is $75\,ShoreA$ hard.

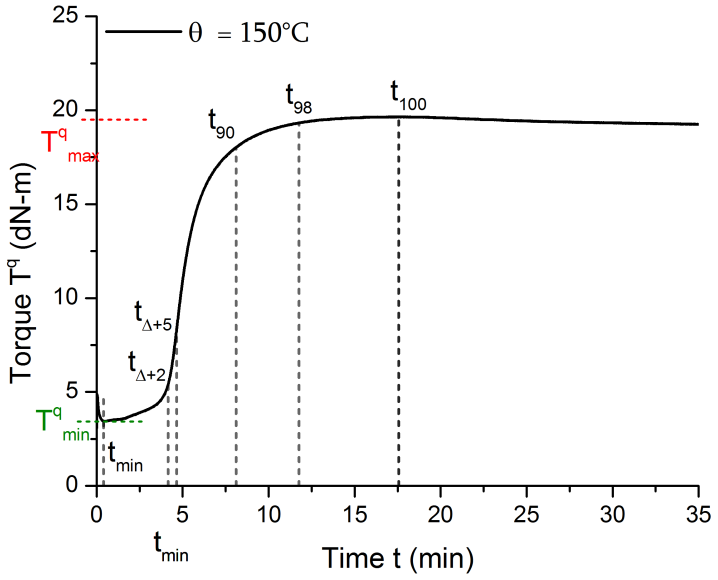

Figure 8.5: Vulkameter or rheometer curve of the S50N1 compound.

8.3 Quasi-static test

In order to identify the quasi-static material parameters, we have considered uniaxial multi-hysteresis measurements at a loading velocity of $v = 2mm/min$ (Fig.1.1) and double-sided shear tests with harmonic loading at frequency $f = 0.1Hz$ (Fig.9.2). Uniaxial tests were carried out on Zwick/Roell 1445 machine (Fig.8.6) and shear tests on MTS machine using $2mm$ thick discs of $20mm$ diameter, sandwiched between the double sided holders as shown in Fig.8.7.

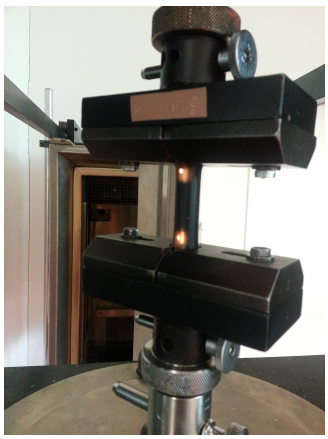

Figure 8.6: Dumb-bell shaped test specimen for uniaxial-tension/compression test

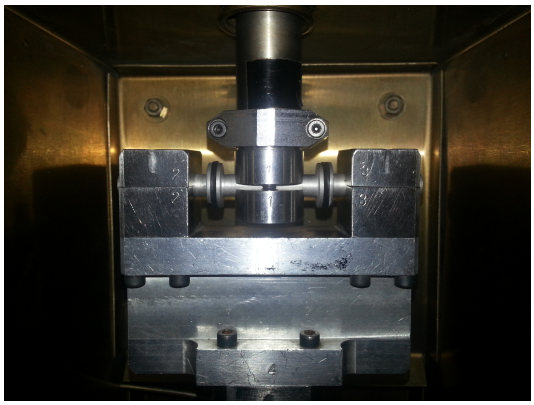

Figure 8.7: Double-sided shear test specimen.

8.4 Time-dependent test

For the time-dependent parameter identification, stepwise uniaxial loading and relaxation was applied on dumb-bell shaped test specimen which was also carried out on Zwick/Roell 1445 machine. In case of stepwise loading-relaxation test, the test sample was preconditioned with multi-hysteresis loading cycles followed by stepwise loading and relaxation. On two different test samples the loading was applied at velocities of $v = 20mm/min$ and $500mm/min$ from ε=0% to a maximum of 100% in steps of 20%, 40%, 60% and 80% with a holding time of $\Delta t = 900s$ when $\dot{\varepsilon} = 0/s$ at each strain amplitude (Fig.8.8). This is to have a similar deformation history as a preconditioning effect for the characterization of viscoelastic effect.

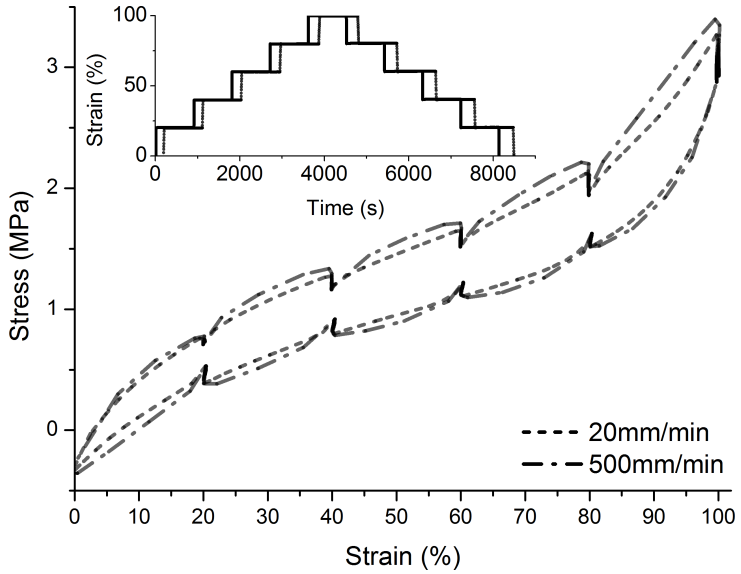

Figure 8.8: Stepwise loading and relaxation measurement @20mm/min ($\dot{\varepsilon} \approx 0.017/s$) and @500mm/min ($\dot{\varepsilon} \approx 0.42/s$) on different test samples; inset shows the strain history.

In the Fig.8.8 we can observe a difference between the material response to test velocities $v = 20mm/min$ and $500mm/min$. The contribution of the cluster stress to the total stress depends on the amount of cluster breakdown during loading and hence depends on the rate of loading.

In addition, the relaxation of polymer bridges during $\dot{\varepsilon} = 0/s$ with a holding time of $\Delta t = 900s$ and re-bonding of clusters during unloading, all these phenomena appears to be rate dependent. Between the maximum and minimum loading history, damaged cluster bonds play a major role in the stress relaxation behaviour, where as at the boundary of minimum cluster size, the broken cluster stress contribution can be considered to be zero or negligible. Therefore, virgin cluster bonds play a key role in the stress relaxation phenomenon at the boundary. In addition to rate dependency, material also shows amplitude dependent stress relaxation. During loading the amount of stress relaxation increases with increasing strain amplitude which is related to the amount of cluster breakdown, where as during unloading the same phenomenon is observed in the opposite way, where the amount of stress relaxation is more at lower strain amplitudes which is related to the re-bonding of broken filler clusters.

8.5 Temperature-dependent test

In order to gain informations about the temperature-dependent mechanical properties, the behaviour of filled elastomer compound S50N1 is experimentally investigated. We have performed different tests on NR blend rubber to emphasize the temperature dependence of the equilibrium, time-dependent stress-strain relation. As it is necessary for parameterising a material model, thermal tests such as Dynamic Mechanical Analysis (DMA), Differential Scanning Calorimetry (DSC) and thermal diffusivity tests were carried out to determine the thermal parameters.

The dynamic properties of an elastomer are determined by its glass transition temperature θ_g. Elastomers having the lowest θ_g will have the lowest $\tan\delta$ (or highest resilience). θ_g of an elastomer can be determined either using DMA test or DSC test. There is no complete consensus in the scientific community on the exact way of determining θ_g. In case of DMA test, some refer to the maximum of $\tan\delta$ and others to maximum of loss modulus G'' as θ_g.

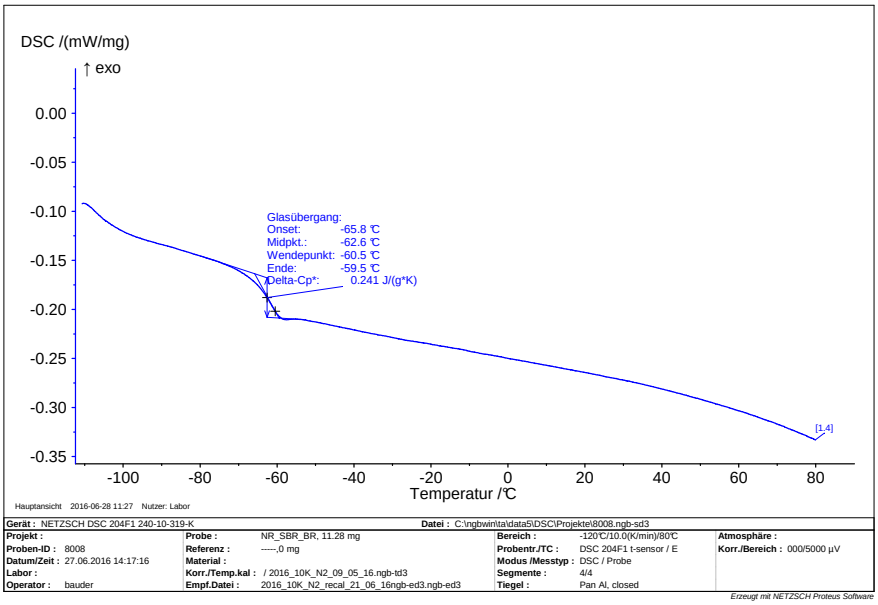

Figure 8.9: DSC measurement of sample A of the S50N1 compound subjected to temperature ranging from $-120°C$ to $80°C$ with a heating rate of $10K/min$.

8.5.1 Differential Scanning Calorimetry (DSC)

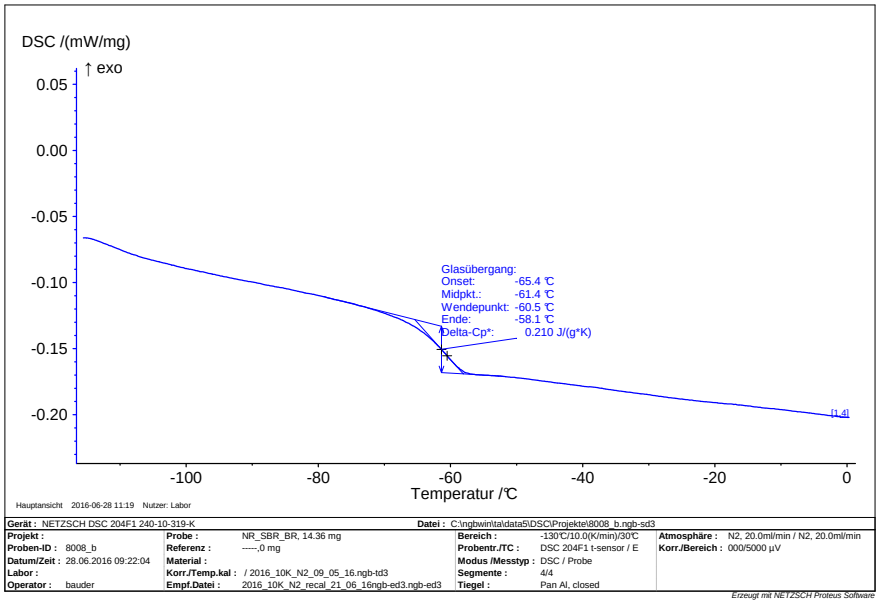

Figure 8.10: DSC measurement of sample B of the S50N1 compound subjected to temperature ranging from $-130°C$ to $30°C$ with a heating rate of $10K/min$.

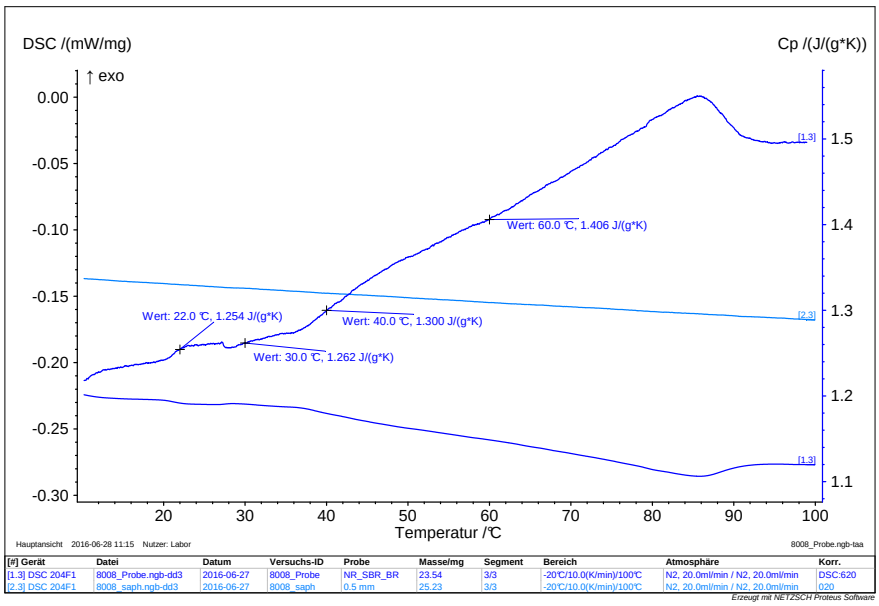

Figure 8.11: DSC test with a heating rate of $10K/min$ to measure the mass heat capacity C_p at different temperatures.

DSC tests were conducted on the rubber compound S50N1 using the machine Netzsch for the characterisation of material's θ_g and specific heat capacity C_p. Generally, natural rubber has a fairly low θ_g which is around $-60°C$. On the other hand SBR has θ_g in the range of $-40°C$ to $-20°C$ and BR in the range of $-120°C$ to $-100°C$. As the S50N1 compound has a large share

Table 8.4: Fit parameters of specific heat capacity $C_p(\theta)$.

Temperature θ [K]	273	283	295	303	313	333	353
C_p $[\frac{J}{tonne\,K}]$	1.164	1.208	1.260	1.296	1.339	1.428	1.516

of NR in its elastomer blend (80phr), NR will dominate the compound's mechanical and thermal properties. This is evident from the DSC measurements with a heating rate of $10K/min$ on two different samples in Fig.8.9 and Fig.8.10. From the measurements θ_g for the investigated compound is around $-60.5°C$ which is near to the natural rubber θ_g.

Another DSC measurement in Fig.8.11 shows the temperature-dependency of specific heat capacity C_p in the temperature range between $-20°C$ to $80°C$, in which it is approximately linearly depending on the temperature. An empirical model is given by the equation

$$C_p(\theta) = A_{C_p} + B_{C_p}\,\theta \tag{8.52}$$

where θ represents the absolute temperature in Kelvin and A_{C_p} and B_{C_p} are fitting parameters, which are determined to be A_{C_p} = - 0.0376 x 10^6 $\frac{J}{tonne\,K}$ and B_{C_p} = 0.0044 x 10^6 $\frac{J}{tonne\,K^2}$. The fit parameters of $C_p(\theta)$ is given in Tab.8.4.

8.5.2 Dynamic Mechanical Analysis (DMA)

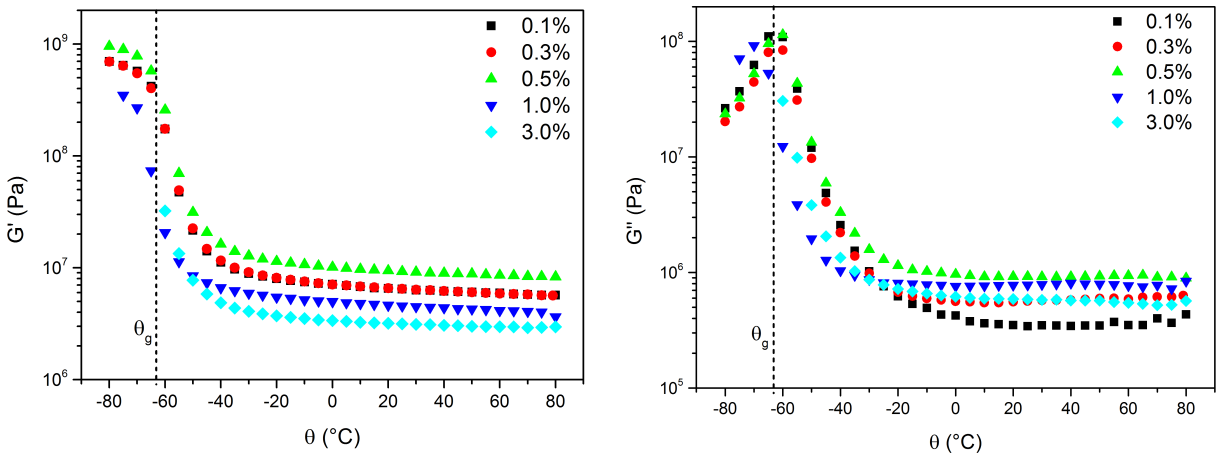

Figure 8.12: Temperature dependent master curves of dynamic moduli G' and G'' of S50N1 compound at frequency of $f = 1Hz$. The vertical line showing θ_g with respect to maximum of G''.

The dynamic-mechanical measurements were performed in the torsion-rectangular mode with strip specimen of $2mm$ thickness and $\approx 30mm$ length with an ARES rheometer. The dynamic moduli were measured using the temperature-frequency sweep program. Normally for a temperature sweep, if the compound contains only one type of elastomer then the minimum temperature is taken to be $\theta_g - 10°C$. But in case of a blend rubber like S50N1, θ_g shifts depending on the amount of other kind of elastomers in the compound. Considering this point, the temperature range from $80°C$ to $-80°C$ and the frequencies of 0.1, 0.2, 0.4, 1, 2, 4 and $10Hz$ were taken for the tests. In order to determine the activation energy E_a for S50N1 compound, five temperature-frequency sweep experiments were conducted with five strain amplitudes of 0.1, 0.3, 0.5, 1 and 3% which is as shown in Fig.8.12. The measurements have been performed by varying the frequency

at various constant temperatures from $80°C$ to $-80°C$ (see Fig.8.13). At lower temperatures the transducer of the machine experiences a very high force due to the glassy-stiffness of elastomer, particularly at large strain amplitudes. This leads to an overload mode of machine which forces it to stop the measurement. This can be observed in 1 and 3% curves of Fig.8.12 which could not measure till $-80°C$. Therefore the measurements were started from higher temperature ($80°C$) to the lower one ($-80°C$). From the Fig.8.12 we can observe the glass transition temperature θ_g of S50N1 compound is just below $-60°C$ which can be correlated to the θ_g measured using DSC. This θ_g actually corresponds to the material's state change from an energy-elastic to an entropy-elastic state.

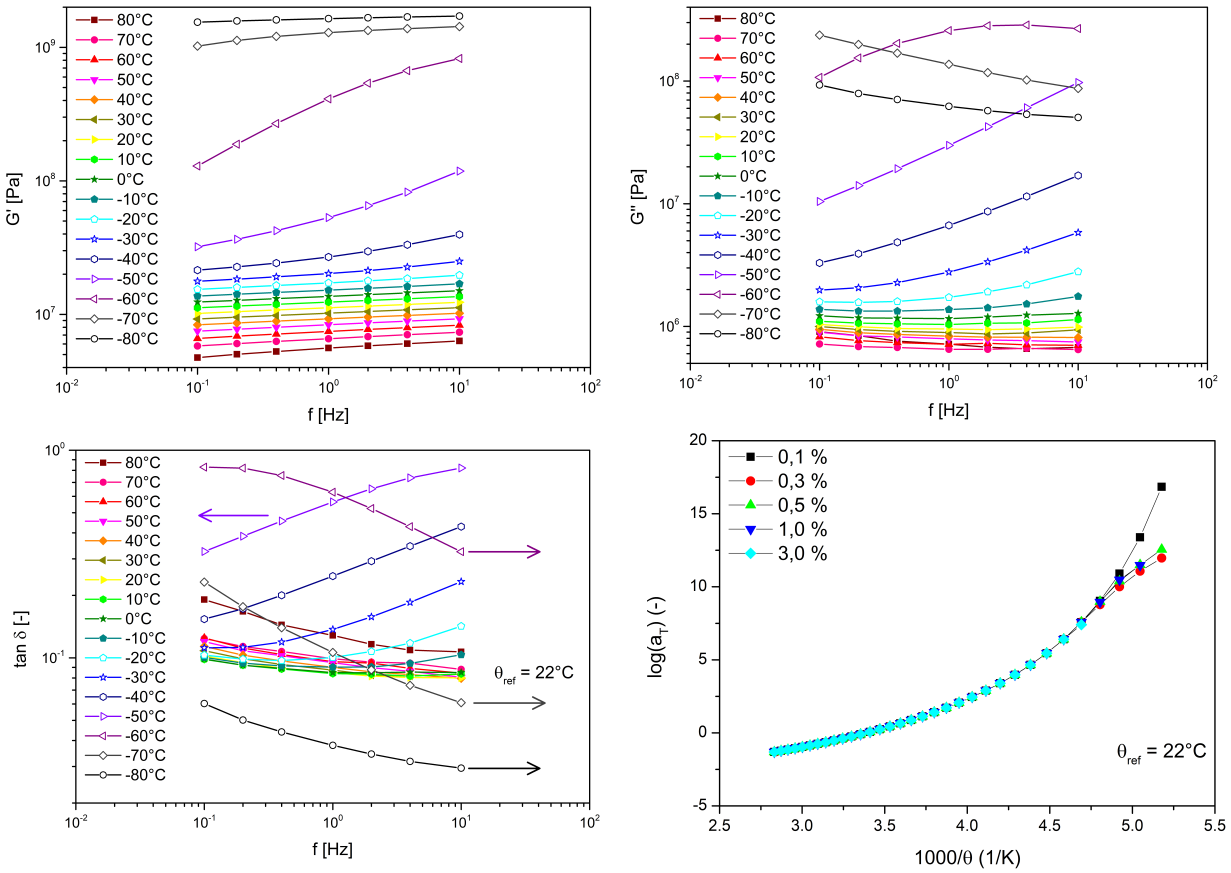

Figure 8.13: Temperature-frequency sweep experiment at strain amplitude of 0.3%. Top-left: storage modulus G', top-right: loss modulus G'', bottom-left: $tan\,\delta$ curves with arrows showing the horizontal shift with respect to reference temperature θ_{ref}=22°C and bottom-right: applied arrhenius dependent WLF horizontal shift factors $log(a_T)$ for different strain amplitude experiments.

Since the frequency range for dynamic mechanical measurements is very limited, it generally uses the time-temperature superposition principle, which is the well known WLF method to create master curves over a wider frequency range. The viscoelastic behaviour of polymers means that there is often a time dependence of their properties in addition to any temperature effects. The underlying basis for the time-temperature superposition is the demonstrated equivalence between time and temperature. It has been demonstrated that viscoelastic data collected at one temperature can be superimposed upon data obtained at a different temperature simply by shifting one of the curves along the time or frequency axis. In the normal practice, the $tan\,\delta$ curves at different temperatures are superimposed over the frequency scale with respect to a reference

temperature θ_{ref}=22°C which is shown in the bottom-left graph of Fig.8.13. The relationship between temperature and frequency for the glassy process is given by the Williams-Landel-Ferry (WLF) equation

$$log(a_T) = \frac{-C_1(\theta - \theta_{ref})}{C_2 + \theta - \theta_{ref}}. \tag{8.53}$$

Regarding the chain mobility which is a temperature change equivalent to a shift in the time and frequency axis. The displacements occur along the logarithmic frequency axis and are described by temperature-dependent shift factor a_T which transform the original frequency values by multiplying the master curves. The bottom-right graph of Fig.8.13 shows the applied arrhenius dependent WLF horizontal shift factors $log(a_T)$ to obtain the partial G' and G'' master-curves for filled elastomer. The word partial refers to the step prior to vertical shift, which is necessary to achieve the final master curve for filled elastomer. The parameters C_1 and C_2 in the Eq.(8.53) are the polymer specific constants.

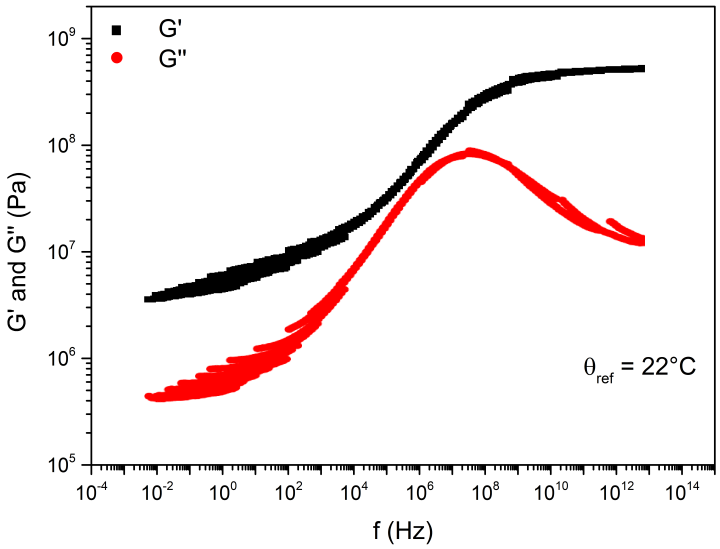

Figure 8.14: The 0.3% strain amplitude G' and G'' master-curves after horizontal shift.

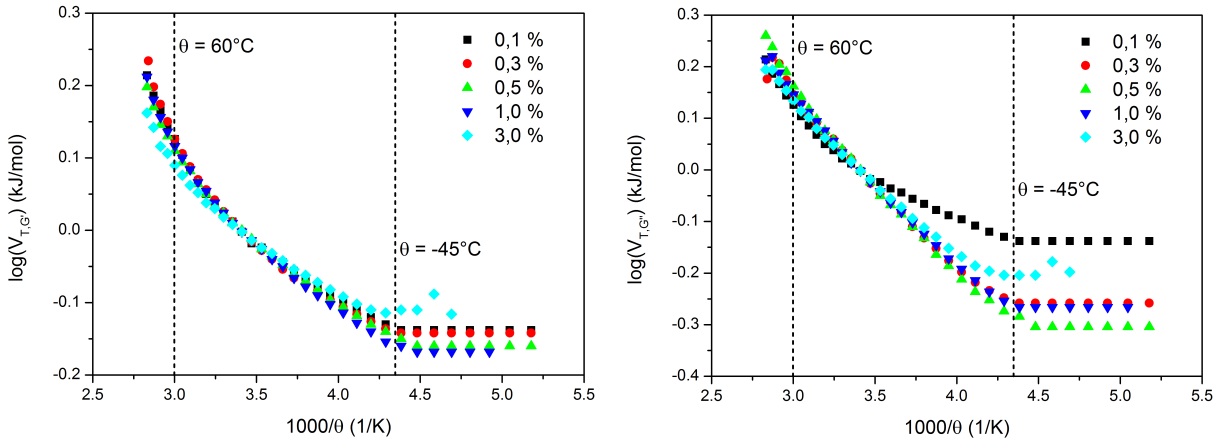

Figure 8.15: Arrhenius dependence of the vertical shift factors necessary to obtain G' and G'' master-curves for the S50N1 compound samples.

In case of unfilled polymer, the different branches of temperature-frequency measurements can be shifted horizontally to obtain the viscoelastic master curves by applying the time-temperature

superposition principle. However, for filled polymers, the horizontal shift is not sufficient, but an additional vertical shift of branches are required [Fritzsche and Klüppel, 2011a]. This is because, in case of filled samples, an increase in the filler content leads to an increase in the discontinuity of the single branches at low frequencies which is as shown in the Fig.8.14. In the case of filler reinforced elastomers, the mechanical response at low temperature or at high frequency is mainly due to the glassy polymer matrix, while at high temperature or at low frequency regime the response is dominated by the filler network, provided the filler network is significantly stiffer than the polymer matrix [Klüppel, 2003]. Accordingly, at low frequencies the Arrhenius like thermal activation of the filler network, resulting from the rigid polymer bridges between the adjacent filler particles, can not be compensated by the WLF-like horizontal shifting factors of the polymer matrix. Therefore an Arrhenius-dependent vertical shift factors are required to obtain G' and G'' master-curves for the S50N1 compound samples which is as shown in Fig.8.15. The horizontal shift is done with respect to the reference temperature θ_{ref}=22°C.

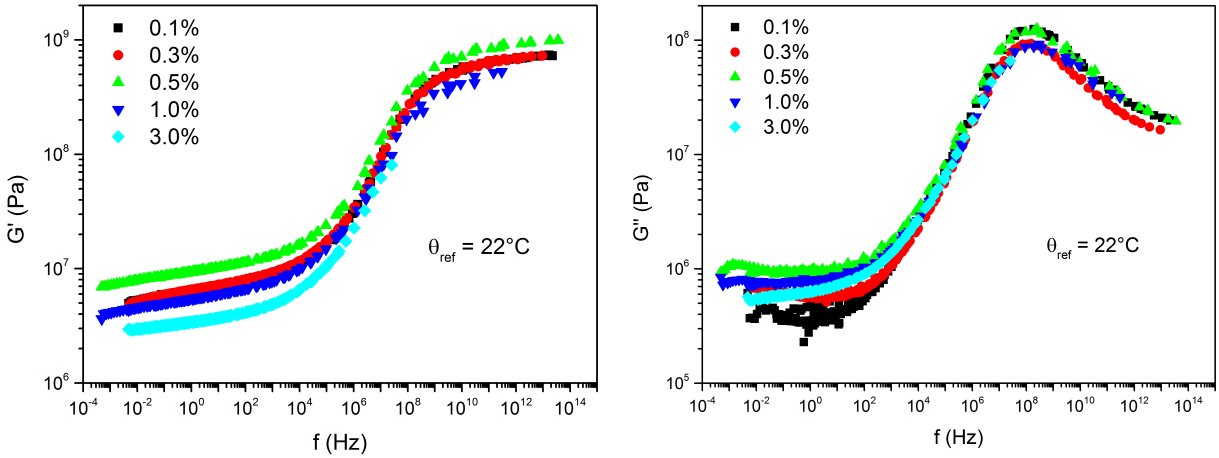

Figure 8.16: The G' and G'' master curves of compound S50N1 after vertical shift.

In the Fig.8.15 we can observe a linear behaviour of the vertical shift factors between the temperature range above the glass transition of the matrix indicating a thermally activated process which causes the deviation in the master curves. The temperature range is marked in the Fig.8.15 as $-45°C$ to $60°C$ within which WLF method is normally valid and beyond these temperatures it looses its relevance. The slope between these temperature range can be interpreted as an apparent activation energy E_a of the filler network, resulting from glassy-like polymer bridges between adjacent filler particles which form the filler-filler bonds [Klüppel, 2003]. Fig.8.17 and Tab.8.5 shows the activation energy for different strain amplitudes. As the θ_g of the matrix, indicated by the loss maxima, is not affected by the presence of filler. Accordingly, all samples can be described by a single set of horizontal shift factors and therefore in Tab.8.5 constants C_1 and C_2 remains unchanged.

The final dynamic-mechanical G' and G'' master-curves for the S50N1 compound samples after applying horizontal and vertical shifting as in Tab.8.5 are shown in Fig.8.16. The summarised activation energies in Tab.8.5 increase at first till it reaches a peak (in our case which appears to be 0.5%) and then start to decrease linearly. The tendency is same for both the dynamic moduli G' and G''. This phenomena of strain dependency can also be observed in the G' and G'' master-curves in Fig.8.16. This phenomena can be related to the mobility of polymer chains which increases beyond the peak strain thereby decreasing the energy it requires for the flow. The activation energies of moduli G' and G'' are the same for 0.1% strain amplitude, but as the

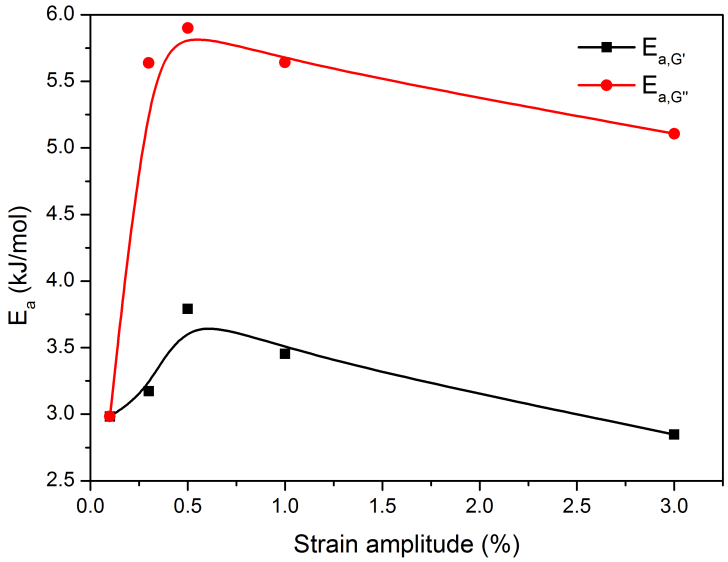

Figure 8.17: Strain amplitude dependence of activation energy.

Table 8.5: Activation energy and WLF shift constants for different strain amplitudes.

Strain amplitude	θ_{ref}	C_1	C_2	$E_{a,G'}$	$E_{a,G''}$
%	$°C$		$°C$	kJ/mol	kJ/mol
0.1				2.98	2.98
0.3				3.17	5.64
0.5	22	4.2	127.41	3.79	5.91
1				3.45	5.64
3				2.85	5.11

strain amplitude increases the activation energies vary due to different vertical shifting factor for G''.

8.5.3 Thermal diffusivity and conductivity

The Fig.8.18 shows the measurement of thermal diffusivity using Tematec temperature sensor and vulcanisation press. For the measurement, two test samples of dimension 350x150x10mm were prepared. Blocks of vulcanisation press were stabilised at a temperature $\theta_{max} = 100°C$ and then the sandwich of two samples with Tematec temperature sensor at the centre was placed between the blocks. The temperature increase over time was recorded as shown in Fig.8.19.

Using simplified Fick's law of diffusion, the temperature change over time can be calculated according to equation

$$\frac{\partial \theta}{\partial t} = \varsigma \frac{\partial^2 \theta}{\partial t^2}. \tag{8.54}$$

Solving the differential equation (8.54) results in

$$\theta(t) - \theta_{max} = -(\theta_{max} - \theta_0)\, e^{-\left(\frac{\pi}{2h}\right)^2 \varsigma t}, \tag{8.55}$$

$$ln\left(\frac{\theta(t)-\theta_{max}}{\theta_0-\theta_{max}}\right) = -\left(\frac{\pi}{2h}\right)^2 \varsigma\, t. \tag{8.56}$$

The left hand side of the Eq.(8.56) $ln\left(\frac{\theta(t)-\theta_{max}}{\theta_0-\theta_{max}}\right) = ln(\theta)$ and the slope of the linear regression line to $ln(\theta)$ is plotted in Fig.8.20.

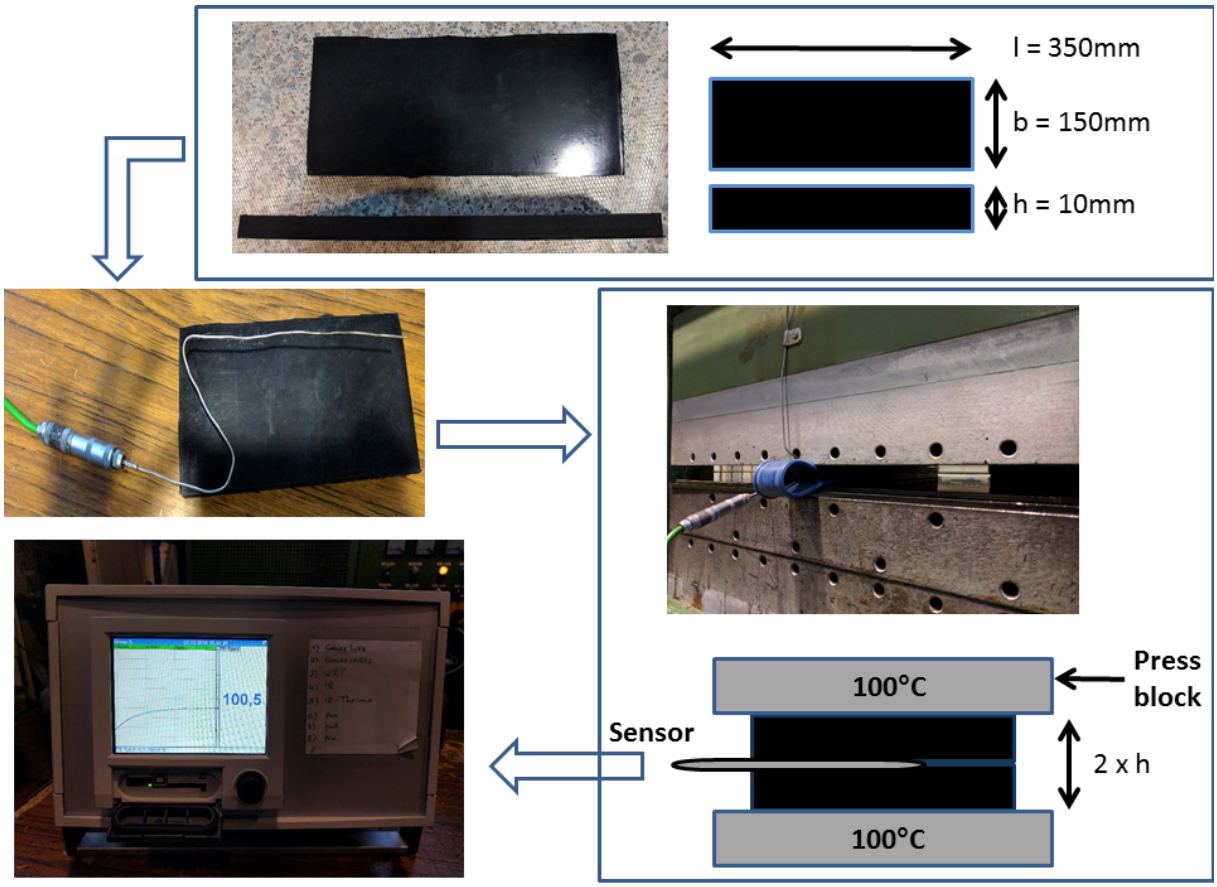

Figure 8.18: Thermal diffusivity measurement.

The left hand side of the Eq.(8.56)

$$-\left(\frac{\pi}{2h}\right)^2 \varsigma\, t = \text{Slope} \cdot t, \tag{8.57}$$

where,

$$\text{Slope} = -\left(\frac{\pi}{2h}\right)^2 \varsigma, \tag{8.58}$$

and finally the thermal diffusivity can be calculated using,

$$\varsigma = -\left(\frac{2h}{\pi}\right)^2 \cdot \text{Slope}. \tag{8.59}$$

Using thermal diffusivity ς in Eq.(8.59), the thermal conductivity κ can be calculated by,

$$\kappa = \varsigma \cdot C_p \cdot \rho, \tag{8.60}$$

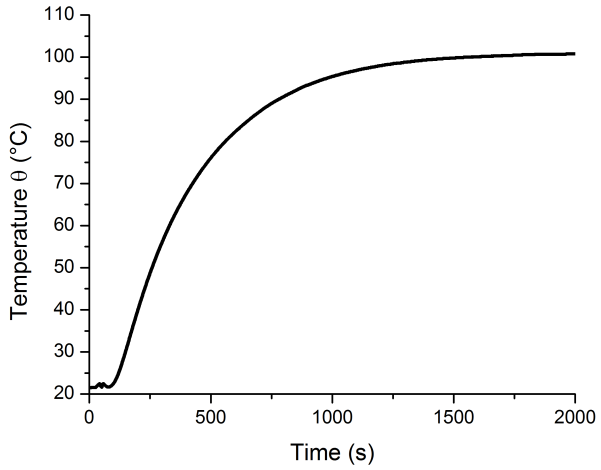

Figure 8.19: Temperature measurement over time in vulcanisation press.

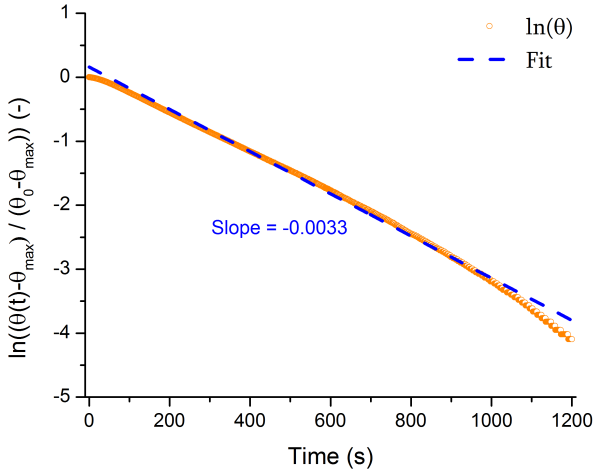

Figure 8.20: ln of temperature increase factor and slope of the regression line.

where C_p and ρ are the specific heat capacity and density, respectively.

The calculated value of thermal diffusivity from the experiment is $\varsigma = 0.1339 mm^2/s$ and the corresponding thermal conductivity is $\kappa = 0.221 \text{ x } 10^{-3} W/(mm\,K)$ with $C_p = 1.52 \text{ x } 10^{-6} J/(tonne\,K)$ and $\rho = 1.1 \text{ x } 10^{-9} tonne/mm^3$.

8.5.4 Temperature-controlled quasi-static & time-dependent tests

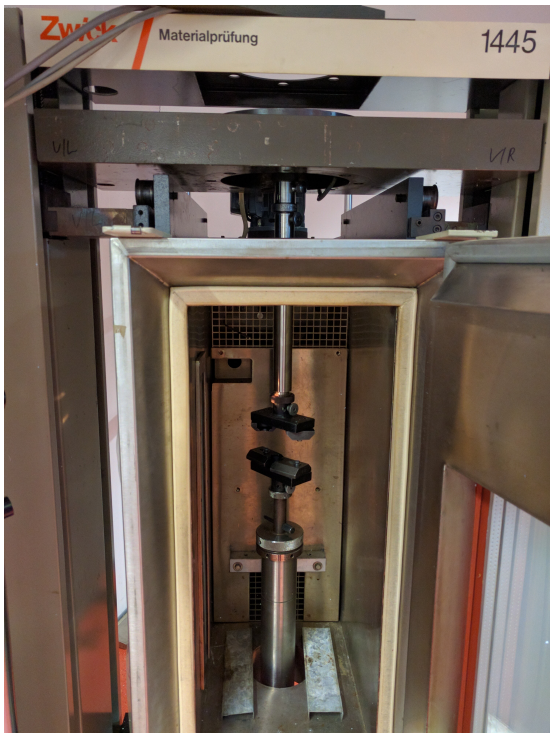

Figure 8.21: Uniaxial-tension test in a temperature controlled chamber on Zwick/Roell 1445 machine.

The quasi-static multi-hysteresis experiment at $v = 2mm/min$ ($\dot{\varepsilon} \approx 0.0017/s$) in Fig.1.1 was repeated, but this time in a temperature controlled chamber on Zwick/Roell 1445 which is shown

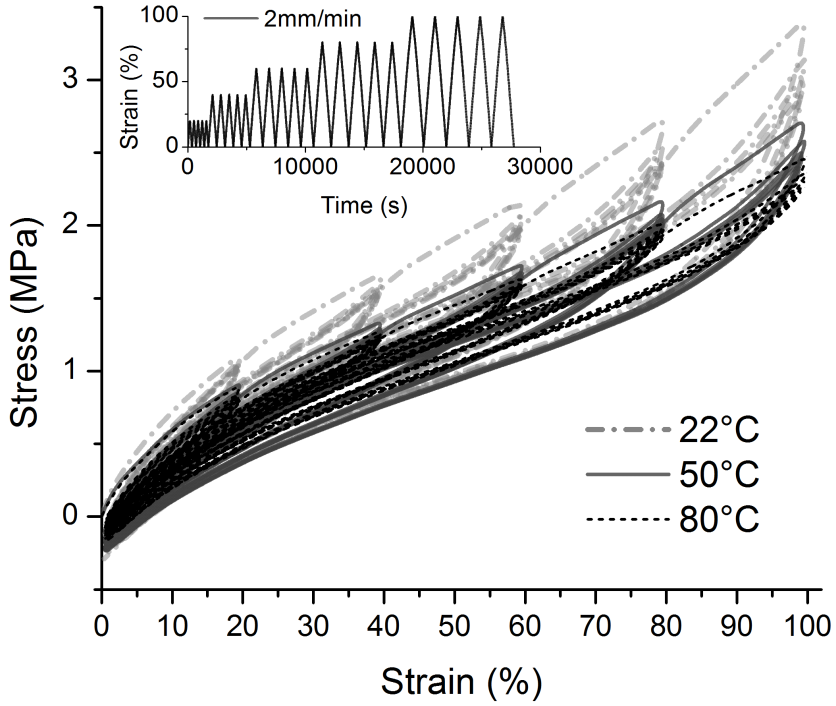

Figure 8.22: Temperature-dependent quasi-static uniaxial multi-hysteresis measurement of S50N1 sample at $v = 2mm/min$ ($\dot{\varepsilon} \approx 0.0017/s$). The inset shows the strain history.

in Fig.8.21. The temperature controlled chamber is designed to operate between $-60°C$ to $150°C$. For low temperature it makes use of Nitrogen gas while for high temperature it uses electric coils. With the help of temperature controlled chamber, two quasi-static multi-hysteresis experiments at elevated temperatures were carried out. The resulting behaviour can be observed in Fig.8.22. We can observe a pronounced temperature-dependent effects on the mechanical behaviour such as reduced stiffness and in-elastic effects: hysteresis, residual stress etc.

The stepwise loading and relaxation experiment in Fig.8.8 was repeated in temperature controlled chamber to characterise the material for both time and temperature dependent effects. The graphs in Fig.8.23 are the measurement curves conducted with a test velocity of $v = 20mm/min$ and $v = 500mm/min$ at room and elevated temperature conditions. In both the cases it can be observed that the amount of relaxation as well as hysteresis loops decrease with increase in temperature. On the other hand, due to entropy-elastic state of polymer the long-term relaxation stress ($t \to \infty$) increases with significant change of entropy [Juhre et al., 2013]. Therefore the stresses in Fig.8.23 first decrease with increase in temperature and then increase after a particular temperature.

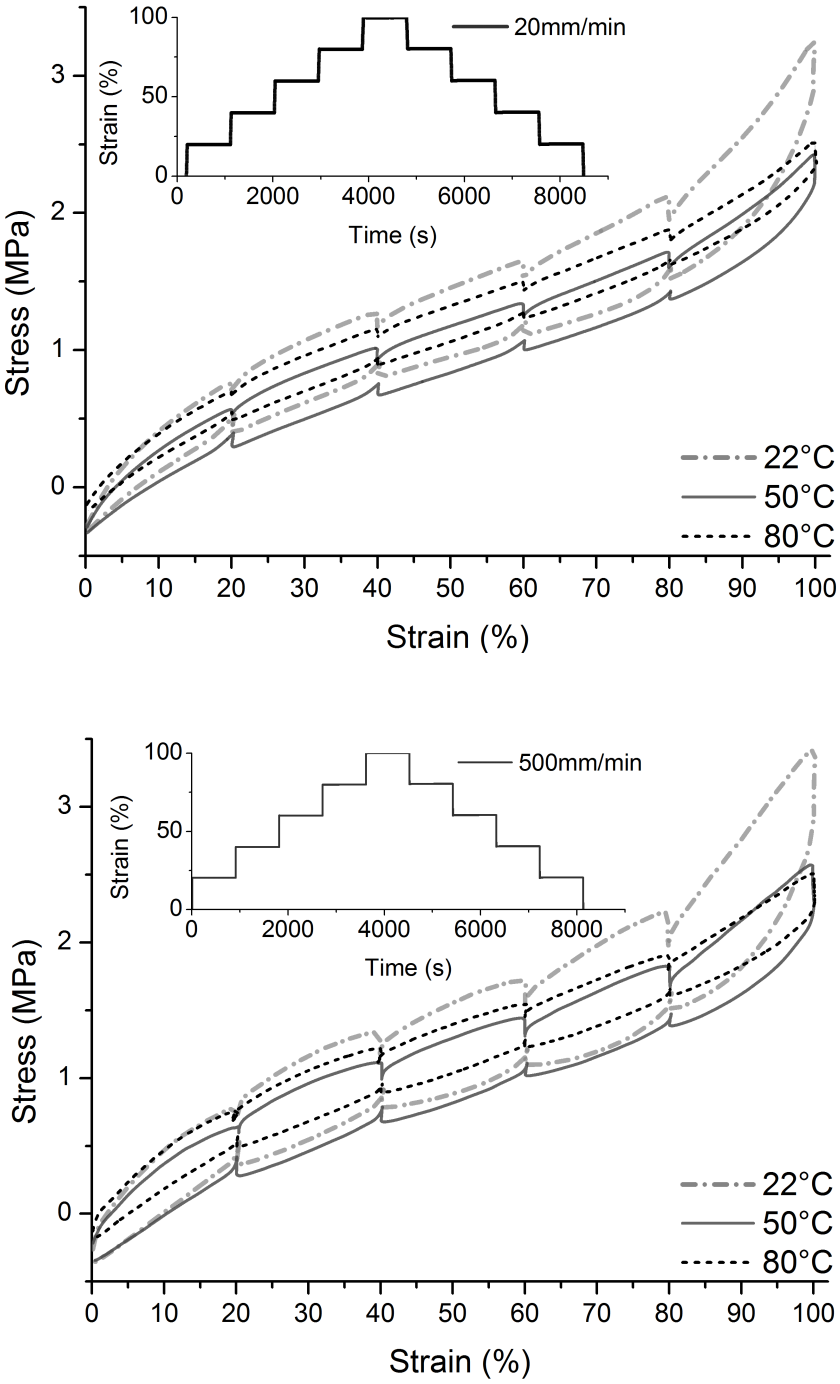

Figure 8.23: Temperature-dependent stepwise loading and relaxation measurements. Top: measurement speed at $v = 20mm/min$ ($\dot{\varepsilon} \approx 0.017/s$) and bottom: measurement speed at $v = 500mm/min$ ($\dot{\varepsilon} \approx 0.42/s$). The inset shows the strain history.

Chapter 9

Model prediction

9.1 Quasi-static fit

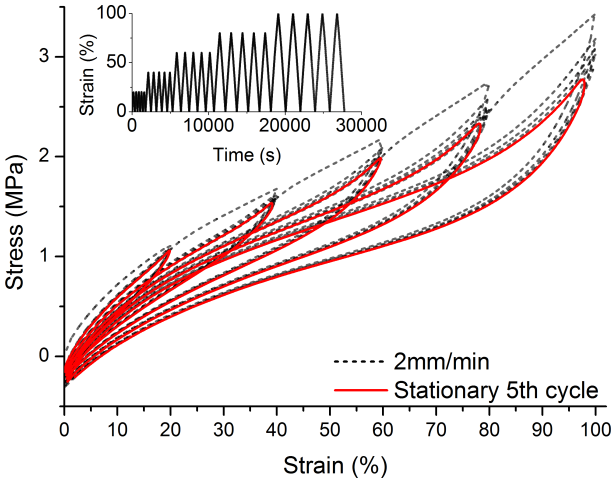

Figure 9.1: Dotted line: uniaxial tension multi-hysteresis measurement at $v = 2mm/min$; solid line: steady state cycles for the quasi-static parameter identification; inset shows the strain history.

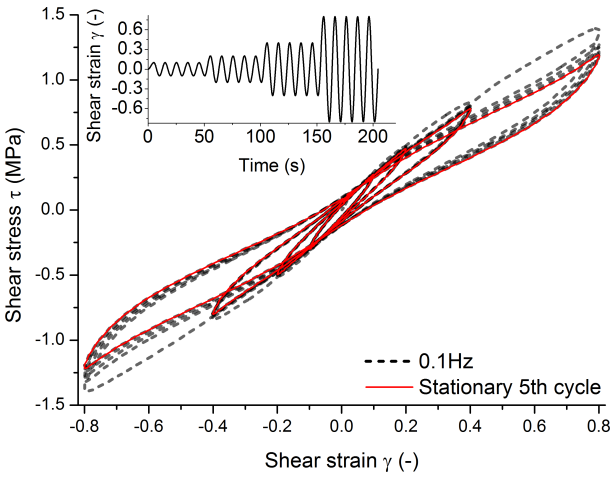

Figure 9.2: Dotted line: double-sided shear multi-hysteresis measurement at $f = 0.1Hz$; solid line: steady state cycles for the quasi-static parameter identification; inset shows the strain history.

We require reasonable material parameters for a successful prediction with a material model for a given strain history. At first the 5^{th} cycle of uniaxial multi-hysteresis measurement and simple shear were extracted as in Fig.9.1 and Fig.9.2, respectively. The reason behind this is that the multi-hysteresis loops were repeated 5 times at each strain amplitude to achieve a stationary behaviour, where it is considered that most of the inelastic properties of the material will no longer change drastically and achieves a steady-state response. The simultaneous fitting on stationary 5^{th} cycles of both uniaxial and simple shear results in the identification of 8 parameters for quasi-static DFM (Fig.9.3 & Tab.9.1). The first 3 parameters are for the matrix rubber and the next 4 parameters are related to the filler content in the matrix material. Here the parameters s_d and s_v are the quasi-static strengths of damaged and virgin clusters, respectively and $s_d < s_v$. The last parameter $T_{set,0}$ is the fitting factor for the residual stress which depends on the amount of filler content in the matrix material.

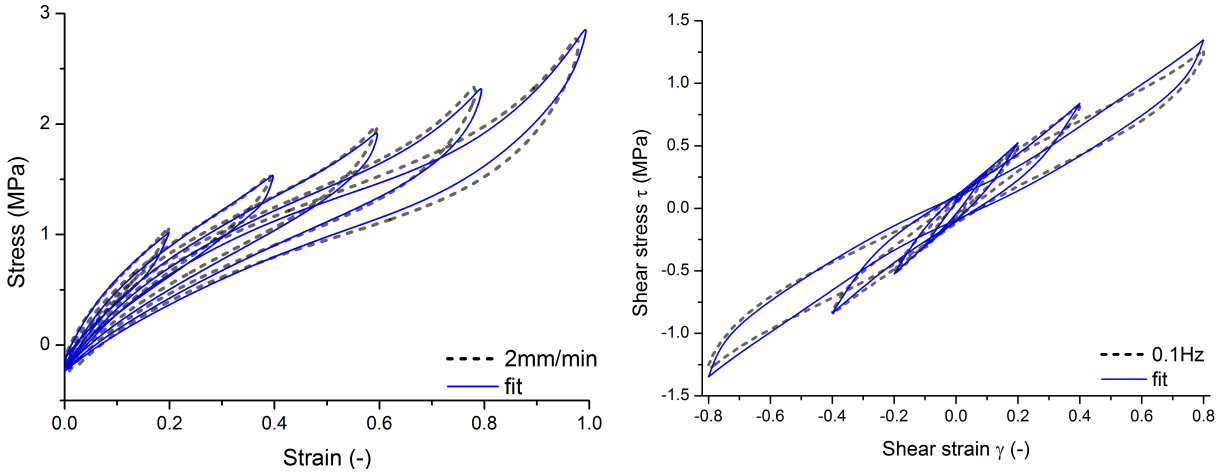

Figure 9.3: Quasi-static curve fit: left- 5^{th} cycle of uniaxial multi-hysteresis measurement (dotted line); right- 5^{th} cycle of double sided simple shear measurement (dotted line) with simultaneous fitted curves (solid line).

Table 9.1: Parameters of the quasi-static DFM obtained from the simultaneous fitting on uniaxial ($v = 2mm/min$) and simple shear ($f = 0.1Hz$) data.

Sample	G_c	G_e	n	s_d	s_v	χ_0	ϕ_{eff}	$\lvert T_{set,0}\rvert$
	MPa	MPa		MPa	MPa			MPa
S50N1	0.441	0.418	20.34	12.59	37.61	10.63	0.37	0.15

The fitted values of the three polymer and four filler related parameters appear physically reasonable. In particular, the cross-link modulus G_c has almost the same value as the entanglement modulus G_e indicating that the density of chain junctions (chemical cross-links and polymer filler couplings) is almost the same as the entanglement density. The entanglement modulus G_e of the natural rubber (NR) used in this study can be estimated independently by measuring the viscoelastic plateau modulus $G_N \approx 2G_e$ of the melt in the intermediate frequency regime before the glass transition appears. For NR one finds $G_N = 0.58MPa$ [Fetters et al., 1994] delivering for the entanglement modulus $G_e \approx 0.29MPa$, which is in fair agreement with the value of G_e in Tab.9.1. The slightly larger fitted value of G_e can be related to surface induced entanglements resulting from chain adsorption at the filler surface. The fitted segment number between successive trapped entanglements n is almost the same as the segment number n_e between successive entanglements, estimated from G_N, indicating that the trapping factor is close to one, i.e. almost all entanglements are trapped by cross-links.

The filler-specific fitting parameters of Tab.9.1 appear also reasonable, whereby the strength of virgin filler-filler bonds s_v is again found close to the value obtained by MD simulations [Froltsov et al., 2012]. The related mean cluster size $\chi_0 = 10.63$ appears physically reasonable as well. It agrees with expectations from TEM pictures of filler clusters in highly reinforced rubbers, i.e. on average the clusters are 10 times larger than the particles delivering about 100 particles per cluster if the fractal dimension of CCA clusters $d_f = 1.8$ is taken into account [Klüppel, 2003]. Finally the fitted effective filler volume fraction $\phi_{eff} = 0.37$ is somewhat larger than the real filler volume fraction $\phi = 0.26$ similar as in previous studies [Lorenz et al., 2011, 2012]. This is due to the fact that the carbon black particles are not spherical but structured. The difference is mainly related to the effect of occluded rubber that is hidden in voids of the structured particles

and acts like additional filler. The set stress T_{set} has no microscopic meaning but is simply empirical, so far.

During rupture of filler-filler bonds, voids may occur since the polymer is stretched strongly and yielding takes place, as observed e.g. in MD simulations [Froltsov et al., 2012]. Since the voids appear on nanoscopic length scales and the total volume of voids due to broken bonds is small compared to the sample volume, this has no significant effect on the constant volume assumption of the DFM. Indeed, the incompressibility or constant volume assumption is still a good approximation for filled rubbers. At room temperature, the yielding of the strongly immobilized polymer between adjacent filler particles which takes place during rupture of filler-filler bonds, can be considered to be almost irreversible and explains the irreversibility of the Mullins effect. Upon retraction of the sample, re-aggregation of bonds takes place and the polymer can relax back to its initial state. However, the polymer chains in the vicinity of the attractive filler particles relax very slowly back to the initial (equilibrium) configuration due to confinement effects. This delivers weaker bonds in the second or third deformation cycle, as described by the strength s_d of damaged filler-filler bonds.

9.2 Time-dependent fit

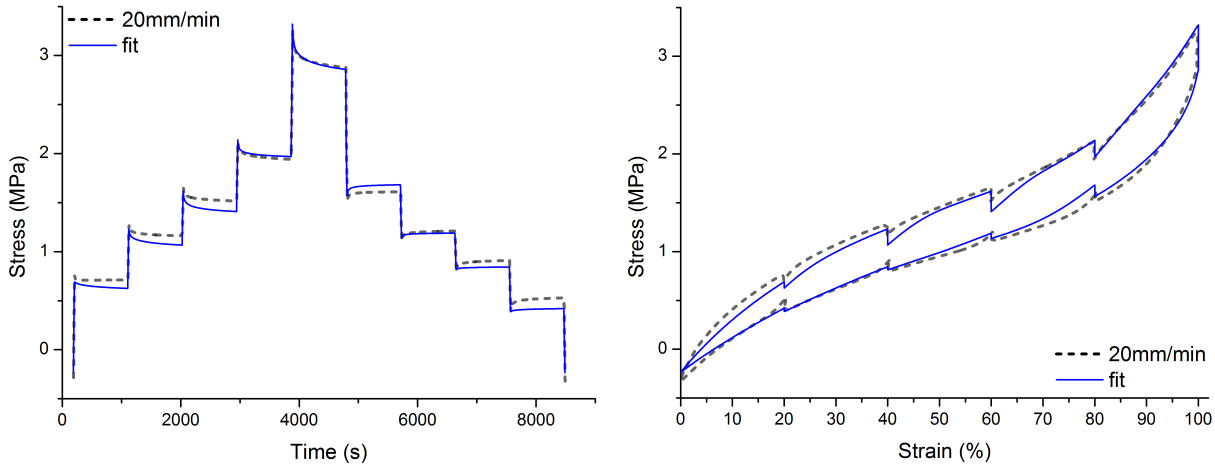

Figure 9.4: $v = 20mm/min$: measurement (dotted line) and fitted curves (solid line) using extended DFM.

After the identification of parameters for the quasi-static model we make use of 6 parameters out of 8 (except s_d and s_v) for the identification of parameters of the time-dependent DFM using curve fitting on $v = 20mm/min$ stepwise loading-relaxation data. The physical hypothesis in Juhre et al. [2013] states that the equilibrium part of the damaged cluster strength $s_{d,eq}$ is considered to be zero because, during the relaxation test the cluster stress tends to zero as $t \to \infty$. In addition, the parameters τ_d and τ_v are identical, since the same polymer molecules are responsible for the relaxation process. Further on, the exponent N is common for both the evolution functions of s_d and s_v.

However, in this work we have chosen to modify the claims of hypothesis by letting all the time-dependent parameters as free fitting variables during the fitting procedure. This results in total of 14 parameters for the time-dependent model where 6 will be from the quasi-static model fit which remain fixed where as the rest of the 8 parameters will vary during the fitting procedure.

Sample	G_c	G_e	n	$s_{d,eq}$	$s_{v,eq}$	χ_0	ϕ_{eff}	$\lvert T_{set,0}\rvert$	τ_d	η_d	τ_v	η_v	N_d	N_v
	MPa	MPa		MPa	MPa			MPa	$Pa^{N-1} \cdot s$	$Pa^N \cdot s$	$Pa^{N-1} \cdot s$	$Pa^N \cdot s$		
S50N1	0.441	0.418	20.34	0.354	17.29	10.63	0.37	0.15	$6.83x10^7$	$9.66x10^9$	$9.53x10^{23}$	$6.35x10^{25}$	6.52	16.13

Table 9.2: Identified parameters of extended DFM for NR compound.

This helps us to understand the influence of each parameter on the material model response. The corresponding fit (legend:"fit") can be seen in Fig.9.4 and the identified parameters of time-dependent DFM are shown in Tab.9.2. The parameter $s_{d,eq}$ is a non-zero value, but it is close to zero as described in hypothesis Juhre et al. [2013]. The parameter $s_{d,eq} < s_d$ of quasi-static model and similarly, $s_{v,eq}$ is also less than s_v. In general, the increase of these two parameters will increases the stress peaks and on the other hand decreases the rate of stress relaxation. The parameter τ influences the rate of relaxation, mainly the slope of loading part (when $\dot{\lambda} \neq 0$) after stress relaxation. As τ decreases, the rate of relaxation increases. The identified values of τ_d and τ_v are proximate to each other, while in the hypothesis Juhre et al. [2013] they are assumed to be equal. η is a tangent for the accumulated stress when $\dot{\lambda} \neq 0$. Unlike in hypothesis, in this paper, the identified parameters $N_d \neq N_v$. The parameter N mainly influences the rate of relaxation and to some extent the stresses. Despite investigating the influence of each parameter, it is difficult to assess the exact influence of all the free fitting parameters due to the given complexity of their physical interlinks to each other and also taking into account the statistical difference between the test specimens used for the experiments. Taking these sticking points into account the model fit is very satisfying.

9.3 Prediction of time-dependency

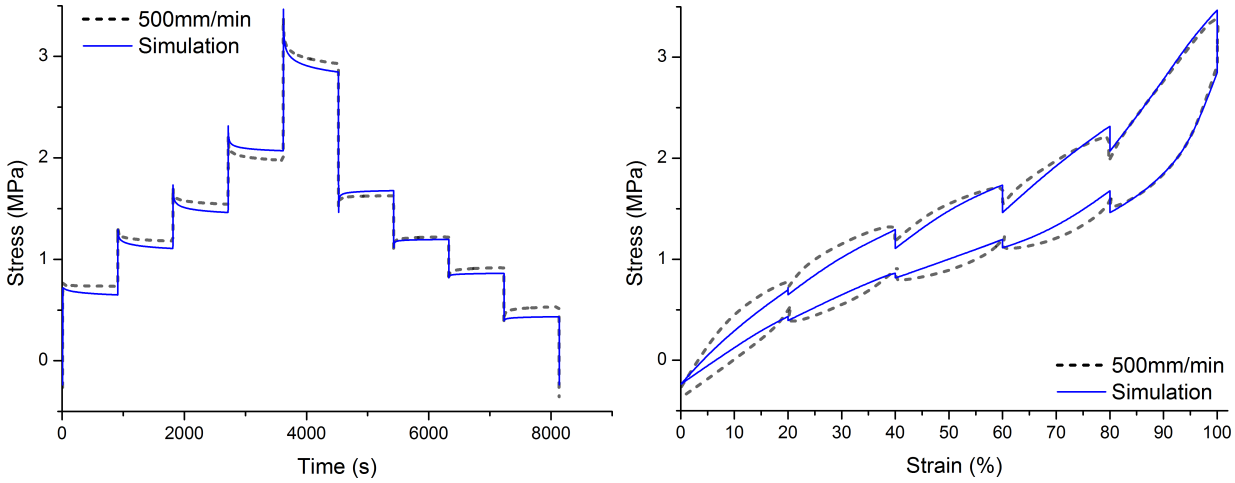

Figure 9.5: $v = 500mm/min$: measurement (dotted line) and simulated curves (solid line).

After the identification of parameters, the extended DFM was further validated against time-dependent experiments. It is to evaluate the ability of the model to reproduce the material behaviour using the same set of parameters that were identified by fitting on to $v = 20mm/min$, so that no new fitting is required. In accordance with this thought, model was validated against $v = 500mm/min$ data and the following result is shown in Fig.9.5. Apart from deviations to the measurement at small amplitudes, the model is able to estimate the material behaviour depending on the rate of loading.

9.4 Prediction of amplitude dependency

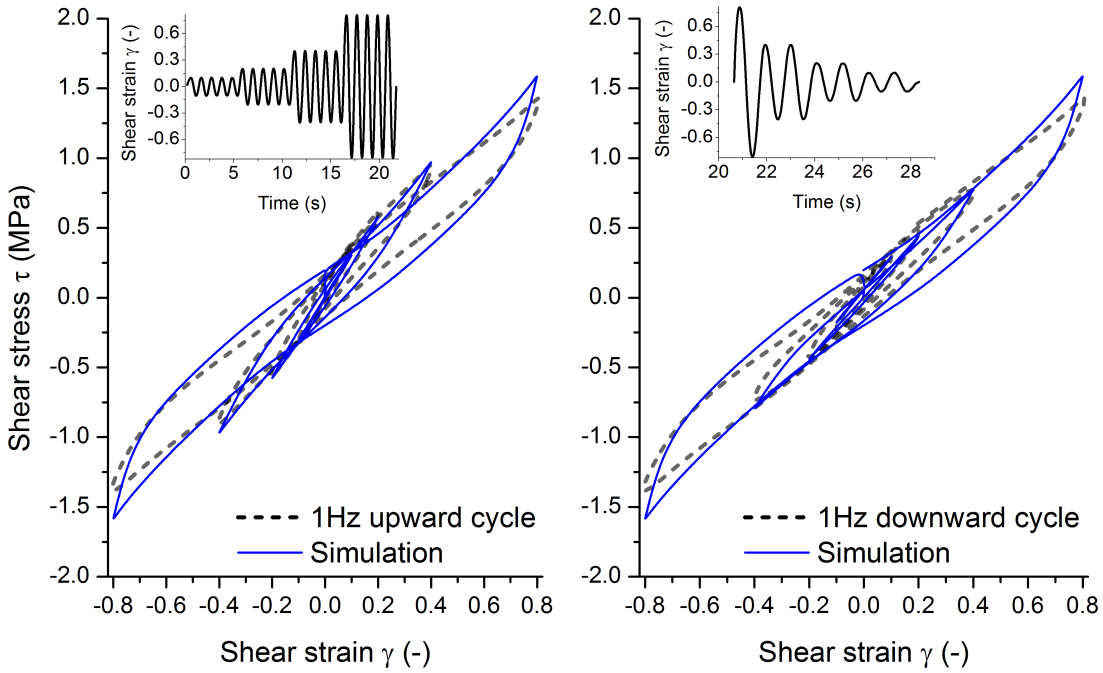

Figure 9.6: $f = 1Hz$ test data (dotted lines). Left: stationary 5^{th} upward loading cycle; right: 2^{nd} downward loading cycle compared with their corresponding simulated curves (solid lines); inset shows the strain history.

To investigate the Payne-effect without influence of the Mullins-effect, the specimen was subjected to double sided multi-hysteresis simple shear loading and the material model was validated against the outer and inner steady-state cycles of frequency $f = 1Hz$ and $10Hz$ test data as shown in Fig.9.6 and Fig.9.7, respectively.

The shear modulus G can be taken as the slope (peak to peak) of hysteresis curve at each strain amplitude:

$$G := \frac{\tau_{max} - \tau_{min}}{\gamma_{max} - \gamma_{min}}, \tag{9.1}$$

and the resulting graph is shown in Fig.9.8.

The dynamic flocculation model (DFM) considers the breakdown and re-aggregation of filler clusters in view of describing stress softening and hysteresis of filled elastomers at medium and large strain amplitudes. In this model, isolated filler clusters with a distinct size distribution are located separately in the rubber matrix and the stress on the filler clusters is transmitted by the matrix. Under quasi-static conditions, microscopic cluster stress and matrix stress are equal, allowing for a quite simple evaluation of the global cluster stress contribution (Eq.3.20). Accordingly, the DFM does not take into account that a filler network is formed at sufficient high filler concentration. This network can be considered to be composed of a space-filling configuration of filler clusters (with a distinct size distribution). At small strain, the stress in the filler network is transmitted directly between the filler clusters and hence the cluster strain equals the global strain. With increasing strain, a breakdown of the filler network takes place, which can be viewed as a random separation of filler clusters from the network. At a critical strain of about 10%, a gel-sol transition occurs and the stress of the filler network goes to zero. Above

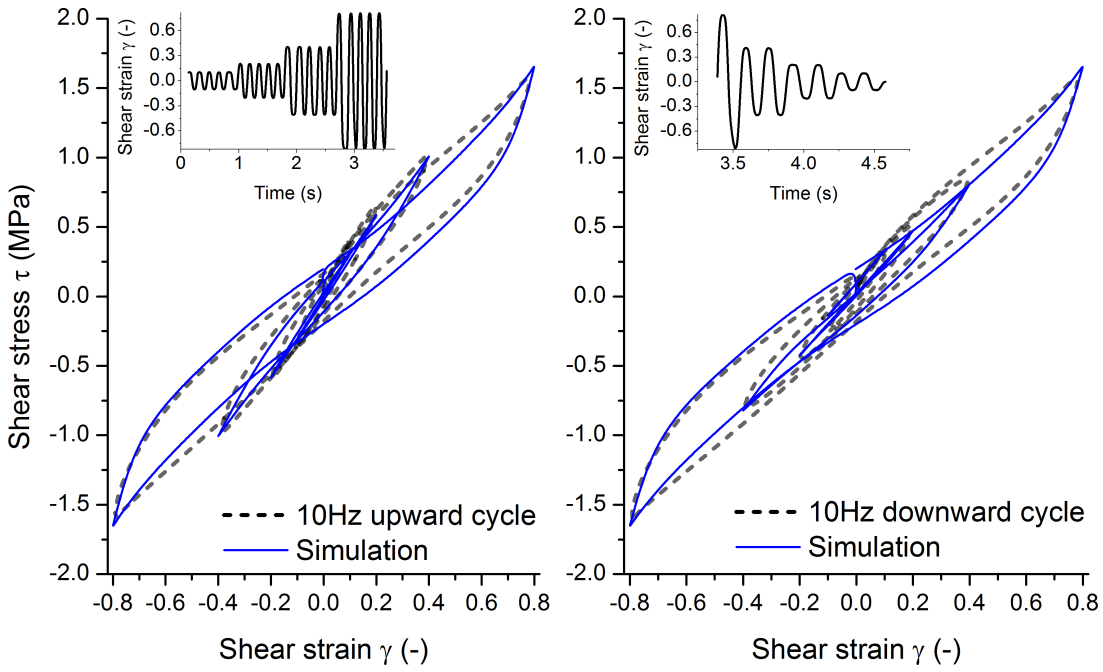

Figure 9.7: $f = 10Hz$ test data (dotted lines). Left: stationary 5^{th} upward loading cycle; right: 2^{nd} downward loading cycle compared with their corresponding simulated curves (solid lines); inset shows the strain history.

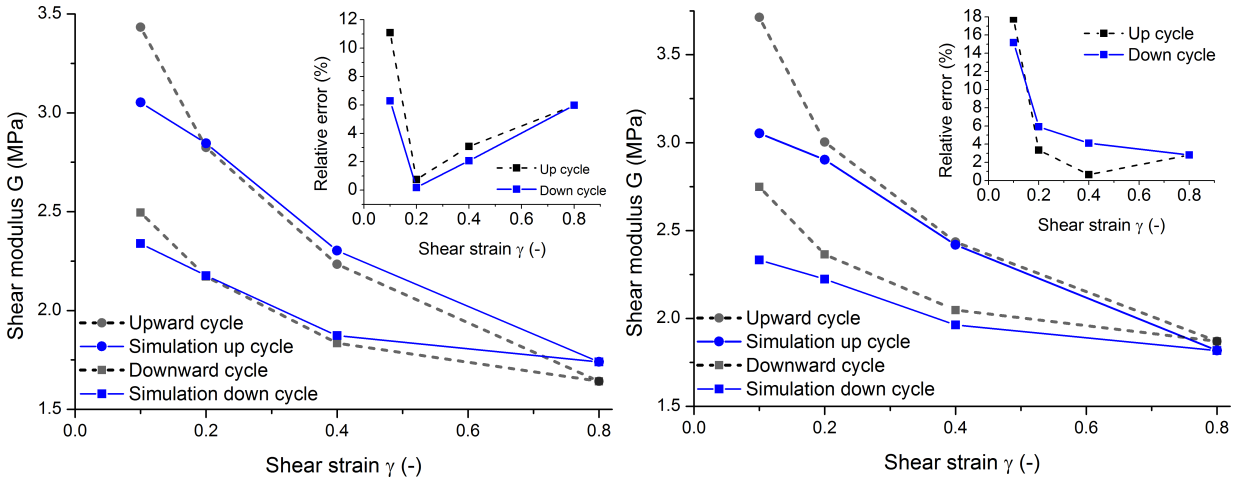

Figure 9.8: Peak to peak shear modulus of upward and downward loading cycles (dotted lines) of 1Hz (left) and 10Hz (right) compared with simulated curves (solid lines); the inset shows the estimated relative error.

the critical strain, only isolated clusters are present in the rubber and the non-linear response is well described by the DFM, just taking into account the hydrodynamic strain amplification of the polymer matrix. This scenario is shown schematically in Fig.9.9. It explains why in Fig.9.8 the experimentally obtained shear modulus is significantly larger than the one predicted by the DFM when the strain amplitude approaches the critical strain of about 10% from above. For lower strain values additional contributions of the filler network appear and so far that are not considered in the DFM. The inclusion of small strain contribution into the DFM will be a task of future work.

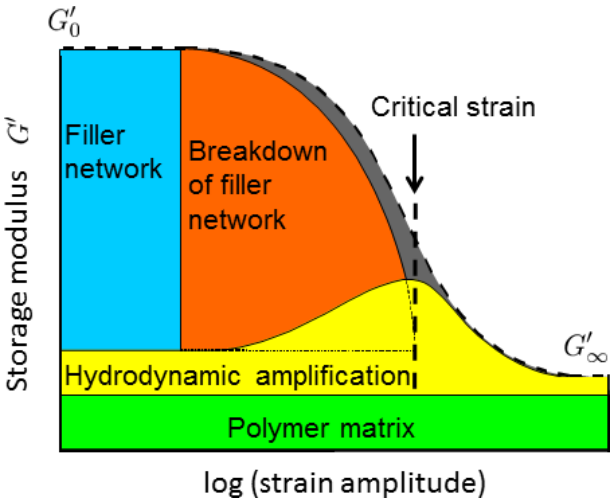

Figure 9.9: Schematic representation of Payne effect resulting from different contribution, as indicated [Vilgis et al., 2009].

Table 9.3: Input constants used for analytical calculation of temperature-dependent parameters.

E_d	E_v	R	θ_{ref}	θ_g
J/mol	J/mol	J/(mol K)	K	K
5000	3000	8.314	295	212

9.5 Thermo-hyperelastic fit

As only the uniaxial tension temperature-dependent tests were carried out in the subsection 8.5.4, the parameter identification in Tab.9.1 has not been used for further discussions. Instead, a new set of curve fitting procedure was followed to identify the temperature dependency of DFM parameters which were allowed to vary during the fitting process. The corresponding curves and parameters are displayed in Fig.9.10.

The temperature dependency of parameters are plotted in Fig.9.11. Although from equations (5.15) and (5.16) the thermo-physical relationship of moduli with temperature is linear, the characterised compound exhibits a different kind of behaviour. As we have used a polymer blend in this project, this result can be unique for S50N1 blend and not universally applicable because of the complexity behind the chemistry of blend rubber at the molecular level. The cross-link modulus G_c increases rapidly till $50°C$ and then the increase is marginal. Where as the entanglement modulus G_e decreases linearly with increasing temperature and the parameter n first decreases till $50°C$ and then increases rapidly. On the other hand, the strengths of cluster bonds s_d and s_v also follow the similar trend as parameter n, even though their dependency on temperature according to equations (5.17) and (5.18) is Arrhenius-like. The deviation of fit results to the analytical ones is the highest at $50°C$ with about $13MPa$ for s_v and about $6MPa$ for s_d and then the deviation reduces during $80°C$ to about $6MPa$ for s_v and about $3MPa$ for s_d. The deviation between the fit and analytical values of $T_{set,0}$ at $50°C$ is about $0.024MPa$ and is about $0.006MPa$ at $80°C$.

In Lorenz et al. [2012] the material parameters for the SBR compound with respect to temperature change is identified by using an analytical approach. In that work, the parameters except s_d,

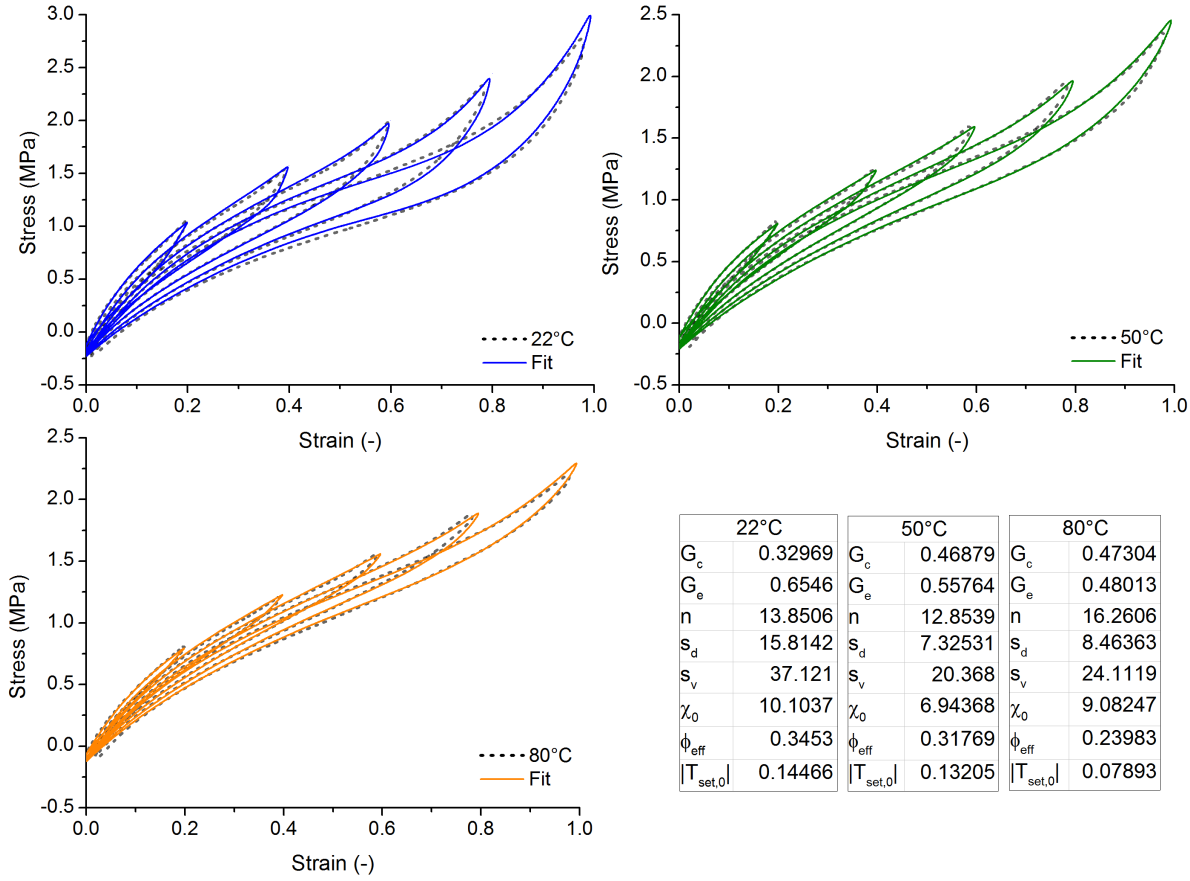

22°C		50°C		80°C	
G_c	0.32969	G_c	0.46879	G_c	0.47304
G_e	0.6546	G_e	0.55764	G_e	0.48013
n	13.8506	n	12.8539	n	16.2606
s_d	15.8142	s_d	7.32531	s_d	8.46363
s_v	37.121	s_v	20.368	s_v	24.1119
χ_0	10.1037	χ_0	6.94368	χ_0	9.08247
ϕ_{eff}	0.3453	ϕ_{eff}	0.31769	ϕ_{eff}	0.23983
$\lvert T_{set,0}\rvert$	0.14466	$\lvert T_{set,0}\rvert$	0.13205	$\lvert T_{set,0}\rvert$	0.07893

Figure 9.10: Temperature-dependent quasi-static curve fit: dotted lines - stationary 5^{th} cycle of uniaxial multi-hysteresis measurements in Fig.8.22; solid lines - free fit curves; tables - corresponding fit parameters (G_c, G_e, s_d, s_v and $T_{set,0}$ are given in MPa).

s_v and $T_{set,0}$ are kept constant and their values were identified from multi-hysteresis experiment measured at room temperature. With s_d, s_v and $T_{set,0}$ as temperature dependent parameters, the fit curves showed good agreement with the temperature dependent experiments. However, in our case, this procedure does not agree so well for NR blend compound. The calculated values of temperature-dependent parameters based on analytical solutions (equations (5.17), (5.18) and (5.19)) are given in Tab.9.4 and the used input constants to calculate them is given in Tab.9.3. The green and black dotted borders in Tab.9.4 represent analytically calculated parameters and reference parameters (θ_{ref}, $s_{d,ref}$, $s_{v,ref}$ and $T_{set,0,ref}$), respectively. On further fitting procedures it was observed that it becomes necessary to allow parameters like G_c, G_e and n to freely vary in order to get a good agreement with the experiments. The corresponding fits are shown in the Fig.9.12 and parameters are given in the Tab.9.5 with a dotted blue border around them.

Table 9.4: Analytically calculated temperature-dependent parameters of DFM.

θ	$s_d(\theta)$	$s_v(\theta)$	$\lvert T_{set,0}\rvert(\theta)$
K	MPa	MPa	MPa
295	15.814	37.121	0.144
323	13.252	33.386	0.108
353	11.313	30.362	0.085

The entries in the Tab.9.5 with brick-red border represent fixed parameters.

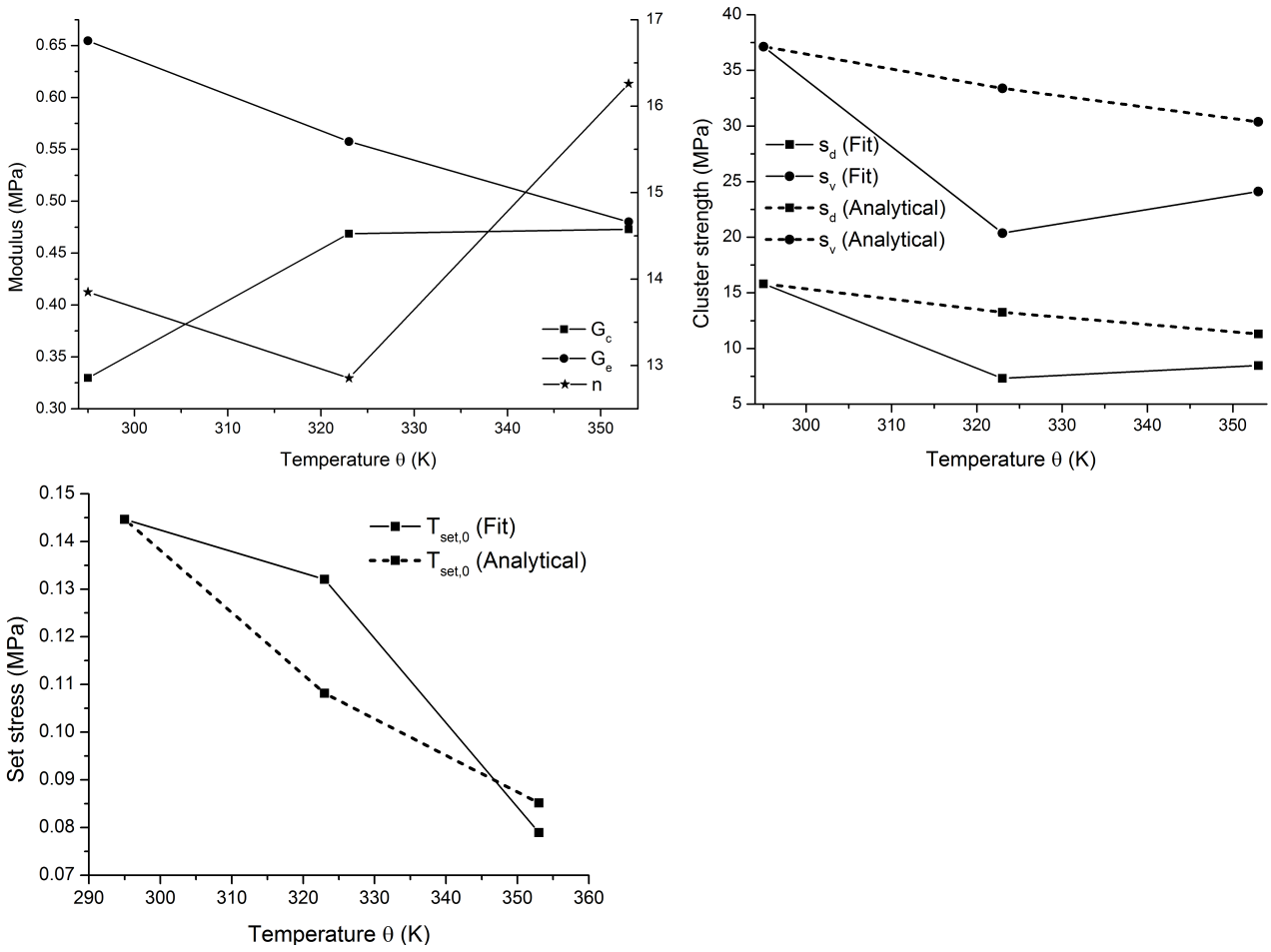

Figure 9.11: Plots of identified parameters from the free fit in Fig.9.10 and analytically determined parameters from Tab.9.4.

The constrained fit of G_c in the Fig.9.12 shows that it increases linearly with respect to temperature where as G_e decreases exponentially and the parameter n increases exponentially with respect to temperature. The decrease of G_e and increase of n are correlated because, from Eq.(5.16) the entanglement modulus G_e is inversely proportional to n,

$$G_e = \frac{1}{\sqrt{6}} R\theta \frac{\rho}{M_s\, n\, T_e}. \tag{9.2}$$

Another important point to be noted here is that the tendency of parameter G_e going towards zero as the temperature increases. Although the increase of G_c can be related to the entropy-elastic state of polymer matrix, it is not clear or theoretically difficult to assess the change of G_e due to

Table 9.5: Identification of rubber matrix parameters through constrained fit procedure.

θ	G_c	G_e	n	$s_d(\theta)$	$s_v(\theta)$	χ_0	ϕ_{eff}	$\lvert T_{set,0}\rvert(\theta)$
K	MPa	MPa		MPa	MPa			MPa
295	0.329	0.654	13.85	15.814	37.121	10.1	0.345	0.144
323	0.457	0.235	26.83	13.252	33.386	10.1	0.345	0.108
353	0.628	0.032	71	11.313	30.362	10.1	0.345	0.085

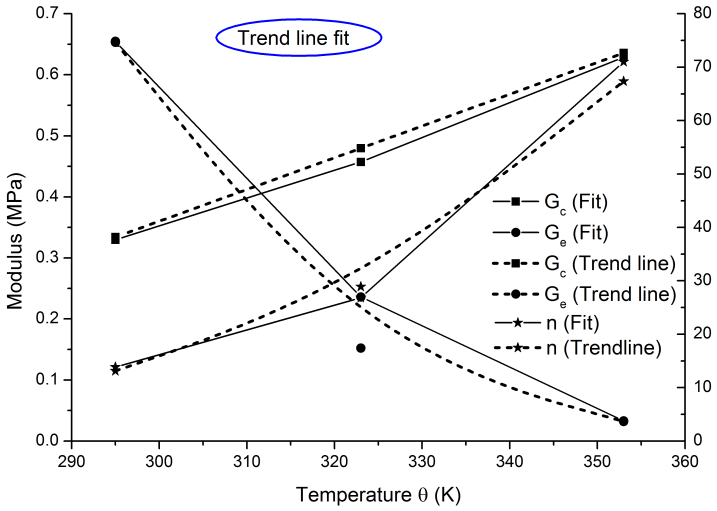

Figure 9.12: Plots of identified of rubber matrix parameters from the constrained fit in Tab.9.5 and the corresponding regression lines to determine the analytical equations.

Table 9.6: Analytically calculated parameters with blue border entries representing parameters of rubber matrix based on trend-line fit.

θ	$G_c(\theta)$	$G_e(\theta)$	$n(\theta)$	$s_d(\theta)$	$s_v(\theta)$	χ_0	ϕ_{eff}	$\lvert T_{set,0}\rvert(\theta)$
K	MPa	MPa		MPa	MPa			MPa
295	0.334	0.653	13.12	15.814	37.121	10.1	0.345	0.144
323	0.479	0.152	28.9	13.252	33.386	10.1	0.345	0.108
353	0.635	0.032	67.35	11.313	30.362	10.1	0.345	0.085

lack of information in this regard. Also the results may vary based on the polymer compound. One possible explanation can be found in Hamed and Hatfield [1989] where the characterisation of CB-rubber interaction is carried out using bound-rubber determination. According to their study the polymer chains adsorb onto the filler particles and if these chains are entangled then the trapped entanglements will have a significant effect on the material behaviour. During material flow, there is possibility of continual disentanglement and re-entanglement of chains which are adsorbed onto the filler particles. The ability of chains to re-entangle to each other is reduced. Therefore the decrease of parameter G_e with increasing temperature can be linked to such a phenomena of disentanglement and re-entanglement of chains adsorbed onto the filler particles which can vary with respect to temperature.

Finally from the constrained fit, the approaches to G_c, G_e and n were derived. Although, the temperature dependency of these parameters are not physically motivated, their phenomenological solutions are necessary to capture the actual tendency of the material behaviour. Analytical equations were derived based on the trend-line fit to the constrained fit curves as in Fig.9.12. The derived equations for θ_{ref}=295K are as follows

$$G_c = 1.534 \left(\frac{\theta}{\theta_{ref}}\right) - 1.1997, \tag{9.3}$$

$$G_e = 3 \cdot 10^6 \cdot e^{\left(-15.34 \cdot \frac{\theta}{\theta_{ref}}\right)}, \text{ and} \tag{9.4}$$

$$n = 0.0032 \cdot e^{\left(8.319 \cdot \frac{\theta}{\theta_{ref}}\right)}. \tag{9.5}$$

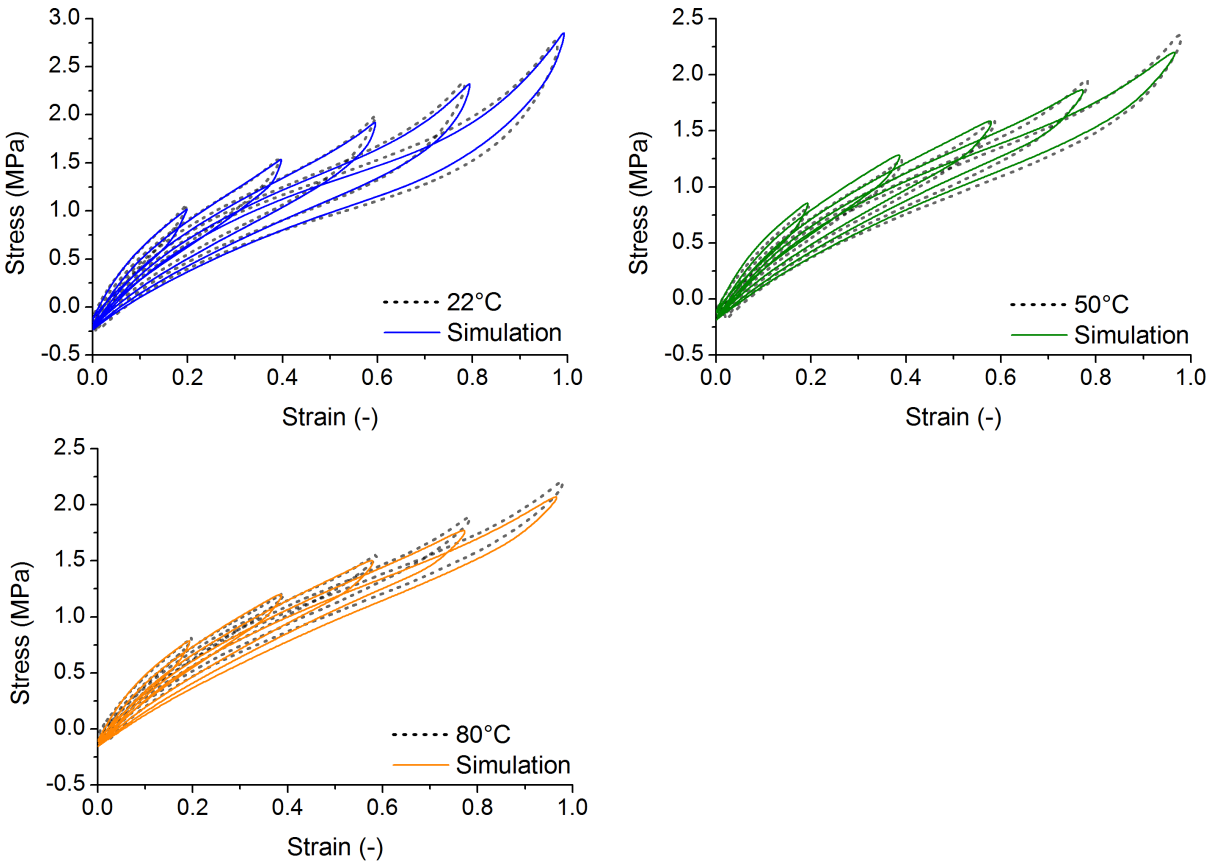

Figure 9.13: Temperature dependent quasi-static simulations based on parameters in Tab.9.6.

The final set of temperature-dependent parameters calculated based on analytical equations are given in Tab.9.6 with blue border entries representing parameters of rubber matrix based on trend-line fit. The temperature dependent quasi-static simulations based on parameters in Tab.9.6 are shown in Fig.9.13 and the simulation curves match very well to the actual behaviour.

9.6 Thermo-viscoelastic prediction

θ	$G_c(\theta)$	$G_e(\theta)$	$n(\theta)$	$s_{d,eq}$	$s_{v,eq}$	χ_0	ϕ_{eff}	$\lvert T_{set,0}\rvert(\theta)$	$\tau_d(\theta)$	η_d	$\tau_v(\theta)$	η_v	N_d	N_v
K	MPa	MPa		MPa	MPa			MPa	$Pa^{N-1} \cdot s$	$Pa^N \cdot s$	$Pa^{N-1} \cdot s$	$Pa^N \cdot s$		
295	0.334	0.653	13.12	0.739	19.43	10.1	0.345	0.144	$3.84\text{x}10^6$	$5.81\text{x}10^8$	$5.93\text{x}10^{21}$	$3.68\text{x}10^{23}$	5	15.46

Table 9.7: Start parameters for thermo-viscoelastic DFM identified from room temperature test.

The time- and temperature-dependent simulations of thermo-viscoelastic DFM was carried out to compare the prediction with actual relaxation curves measured at different temperatures. The start parameters for the simulation are identified using $v = 20mm/min$ relaxation measurement recorded at room temperature condition (Fig.8.23). The change of relaxation times $\tau_d(\theta)$ and $\tau_v(\theta)$ with respect to temperature are calculated according to the equations (5.23) and (5.24), respectively.

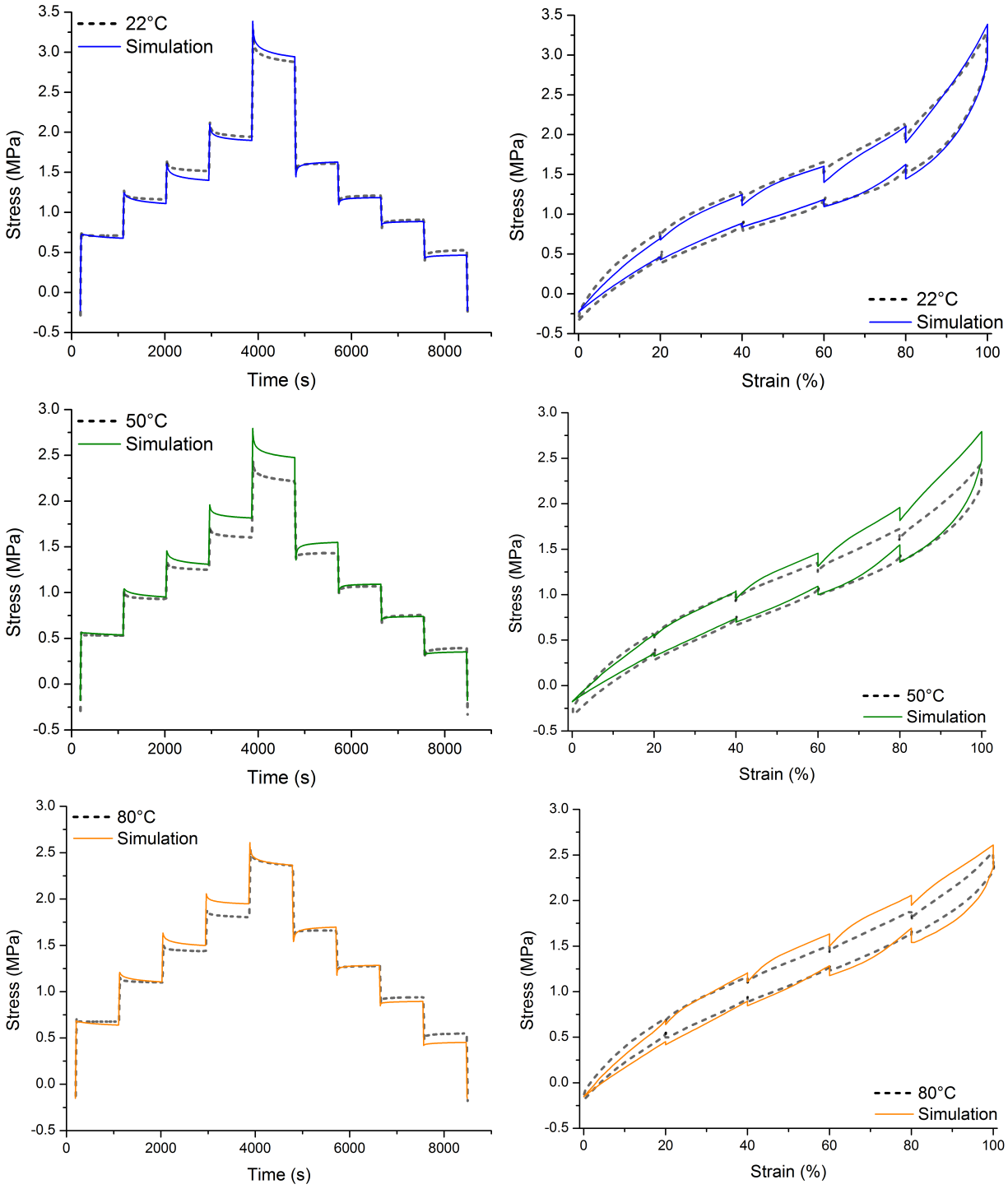

Figure 9.14: Dotted lines: temperature-dependent relaxation measurement at $v = 20mm/min$ ($\dot{\varepsilon} \approx 0.017/s$); solid lines: matreial behaviour prediction by time- and temparature-dependent DFM.

Fig.9.14 and Fig.9.15 shows the temperature-dependent simulation and experiment curves at $v = 20mm/min$ and $v = 500mm/min$, respectively. The results obtained for $22°C$ and $80°C$ shows that the thermo-viscoelastic DFM is able to reproduce the reasonable behaviour at these temperatures in par with the experiment. The tendency of the phenomena like reduced stress and hysteresis along with set stress are in agreement with the actual characteristics. In case of $50°C$, the simulation curves in the finite strain region deviates more from the actual behaviour

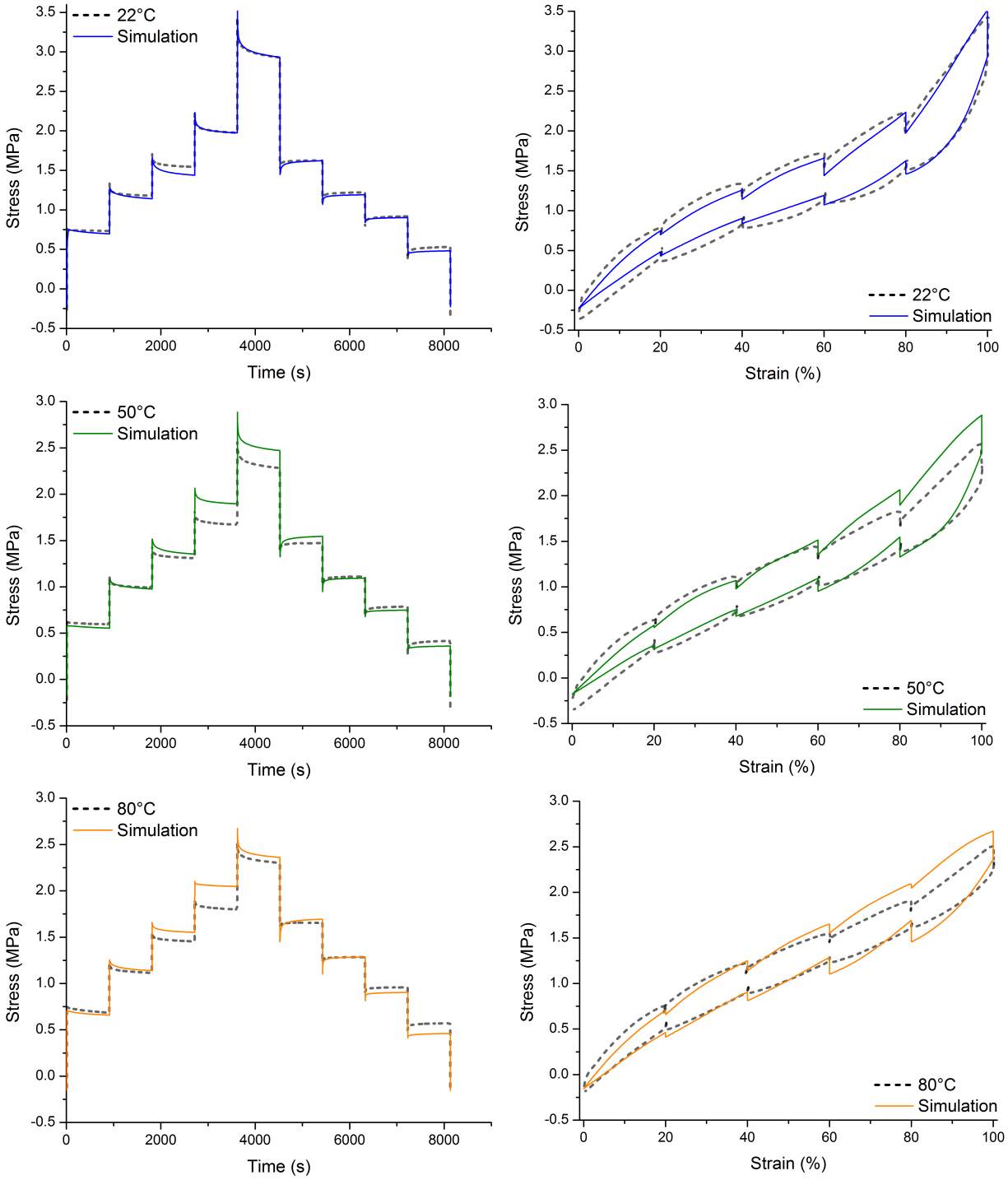

Figure 9.15: Dotted lines: temperature-dependent relaxation measurement at $v = 500mm/min$ ($\dot{\varepsilon} \approx 0.42/s$); solid lines: matreial behaviour prediction by time- and temparature-dependent DFM.

due to the overestimation of stresses and hysteresis. Although this deviation can also be observed in the results of $80°C$, it is not as much pronounced as $50°C$ results. This is also to do with the influence of time-dependency. The deviation in results of $50°C$ is more to do with the material characterisation particularly the temperature-dependency. If the parameters are well represented then this deviation can be marginal.

Chapter 10

FE simulation

10.1 Quasi-static analysis

In the tyre industry a simplified tyre model called *Grosch wheel* is often used to investigate various quantities that affect the tyre tread performance. Major topics like friction, traction, abrasion, rolling resistance and wear make use of this tyre model to assess the problems and enhance the product [Grosch, 1992, 1996, 2007]. The Grosch wheel is a very small solid rubber wheel with no tread patterns as shown in Fig.10.1. As this project is oriented towards developing the material model to investigate the truck tyre tread behaviour, we make use of the Grosch wheel simulations to visualise the outcome.

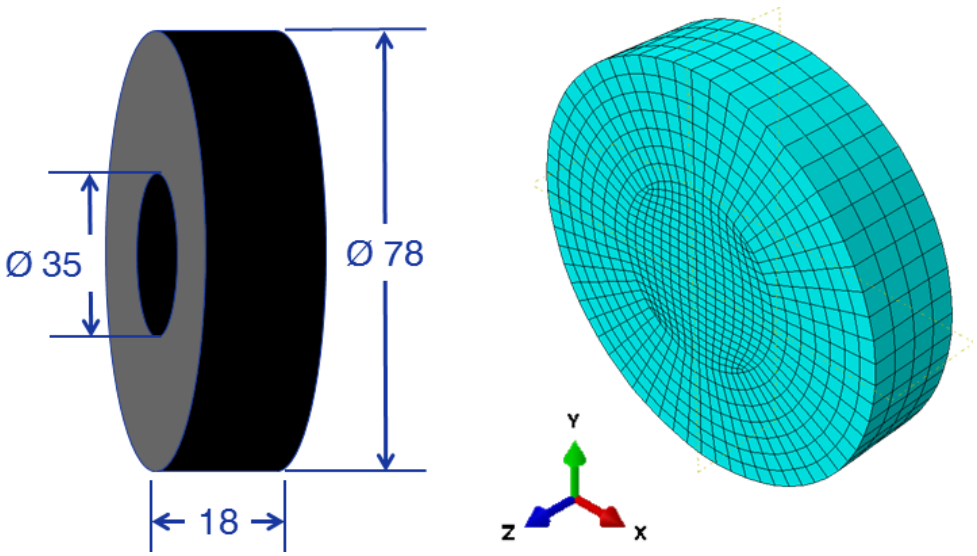

Figure 10.1: Left: Geometry of Grosch wheel (dimensions in mm); right: discretised FE model.

The discretised FE-model of Grosch wheel consists of inner shaft which is considered to be rigid due to its very high stiffness compared to rubber and the outer part is considered as deformable solid to which the DFM material model is assigned. Here we have done two sets of simulations. First set is only for demonstrating the stress softening effect during loading and the second set is the actual loading condition as per industry practise.

In the first set, a compression load of $1kN$ in the vertical direction was applied on the shaft. At the end of vertical load the wheel was compressed to about 10mm which is shown in Fig.10.2. In

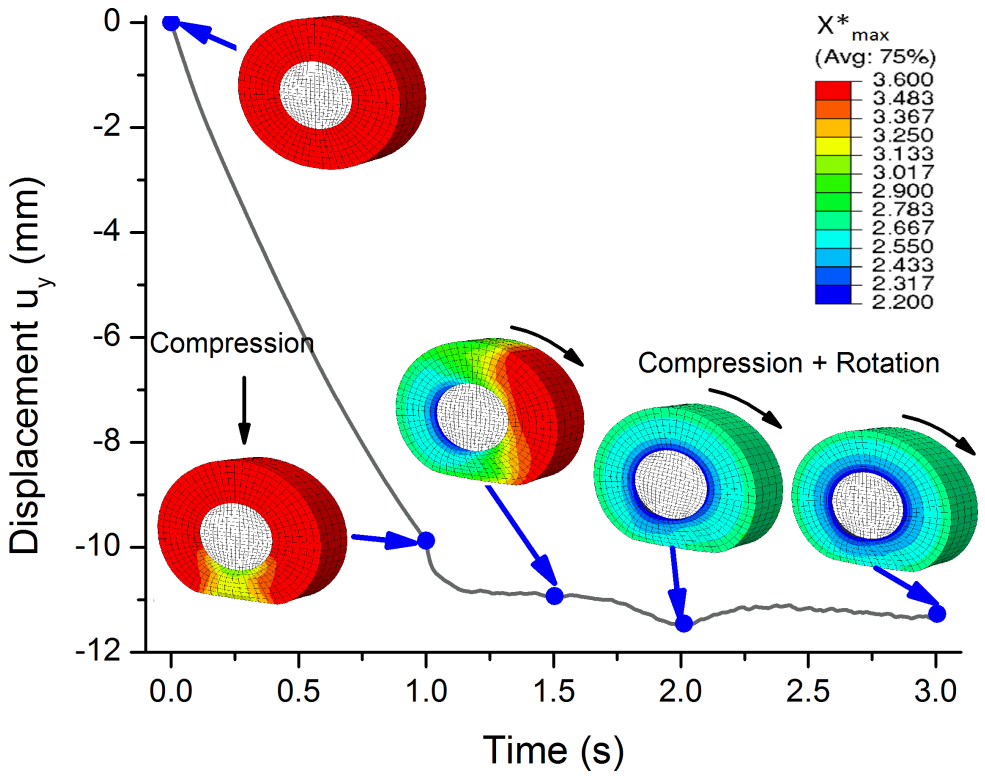

Figure 10.2: Quasi-static simulation of a compressed and rolling Grosch wheel. Plot: vertical displacement vs time; visualisation spectrum: stress softening expressed by the averaged amplification factor X^*_{max}. Arrows indicate the end of each loading step.

the following step the wheel rotates two times around its axis and rolls on the substrate. Despite the constant compression load of $1kN$, the displacement increases by about $1.5mm$ while the wheel completes the first revolution and then the displacement decreases by a fraction of mm at the end of second revolution. This is due to the stress softening effect and can be correlated to the decrease of the strain amplification factor X_{max}. As we use representative directions, at each integration point of the finite element mesh there will be α number of amplification factors $\overset{\alpha}{X}_{max}$. To obtain one single value of the average amplification factor X^*_{max} at each integration point, the amplification factors $\overset{\alpha}{X}_{max}$ in each space direction is averaged over α material lines as

$$X^*_{max} = \sum_{\alpha=1}^{n} \overset{\alpha}{w} \cdot \overset{\alpha}{X}_{max} \,. \tag{10.1}$$

Before the beginning of the load, the value of X^*_{max} equals 3.6 and then it decreases during compression and rolling of the wheel to a minimum value of 2.2. According to colour spectrum, the distribution of X^*_{max} is inhomogeneous along the radial direction. The minimum value of X^*_{max} can be found at the inner radius of rubber wheel near the shaft where the stresses are also high.

In the second set, the wheel was subjected to a static compression load of $75N$. This is the actual load case used for the tests in the industry to measure the foot print dimension. For the static load case, six compounds with two types of carbon-black filled NR blends each with three filler volume fractions are considered. The CB types chosen for the investigation are N121 and EB262. They are different from each other with respect to their particle size, surface area, and percolation threshold, etc. Even though there is only a filler fraction difference of 5phr between

Table 10.1: DFM parameters of 6 compounds used for the static Grosch wheel simulations.

Sample	G_c	G_e	n	s_d	s_v	χ_0	ϕ_{eff}	$\lvert T_{set,0}\rvert$
	MPa	MPa		MPa	MPa			MPa
S30N1	0.236	0.265	32.24	6.33	28.94	12.42	0.25	0.0588
S40N1	0.23	0.45	12	10	30	9	0.28	0.135
S50N1	0.329	0.654	13.85	15.81	37.12	10.1	0.345	0.144
S35EB2	0.206	0.568	12	3.106	13.55	5.816	0.32	0.11
S45EB2	0.252	0.659	13.33	6.05	18.44	7.501	0.36	0.126
S55EB2	0.201	0.779	16.69	10.9	38.49	9.94	0.44	0.182

the low, medium and highly filled compounds of EB262 and N121, from the energy density it appears like N121 30phr is equivalent of EB262 35phr, N121 40phr is equivalent of EB262 45phr and so on. The compounds are given a sample name like $S30N1$ and $S35EB2$. The first character stands for NR of type SMR 20, the numbers in second and third position are the filler fraction in phr, and then the following characters and number corresponds to the type of CB. The identified parameters of quasi-static DFM for the investigated compounds are given in the Tab.10.1.

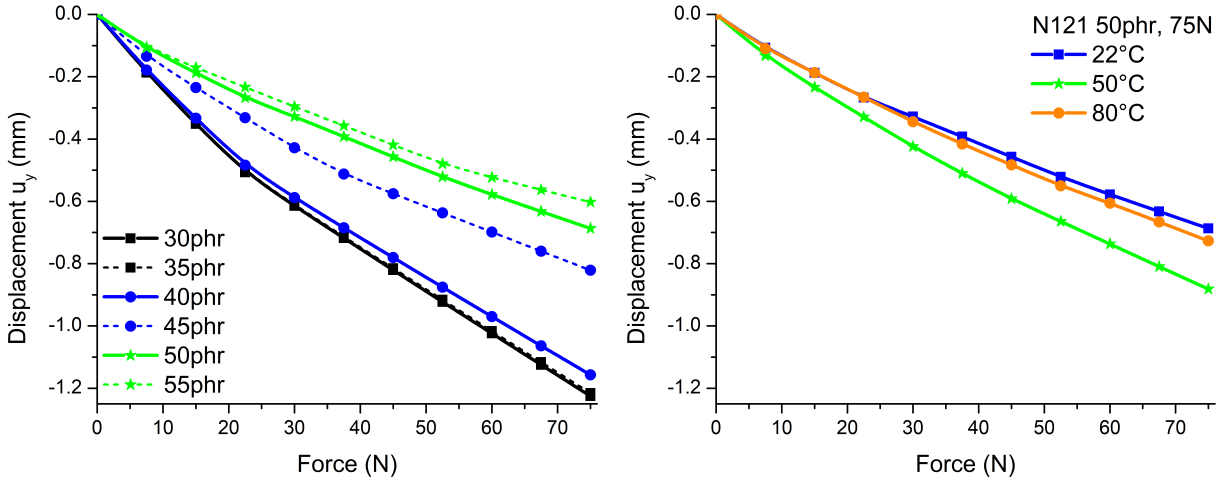

Figure 10.3: Static analysis of Grosch wheel. The deformation behaviour of: (left graph) six types of carbon-black compounds under the compression load of $75N$, and (right graph) the compound N121 50phr under the load of $75N$ and at different temperatures.

The vertical displacement of the Grosch wheel for the given load are plotted in the Fig.10.3. The displacement u_y for the case of low filled compounds remain the same with respect to applied load (left graph in Fig.10.3). In case of medium filled compounds the deviation in their behaviour is more pronounced. The S45EB2 shows more stiff behaviour compared to S40N1 with a displacement difference of about 30%. The deviation in the stiffnesses of S50N1 and S55EB2 are marginal when compared to medium filled compounds. The significant deviation in the material behaviour of medium filled compounds can be due to the difference between their percolation threshold. Although both CBs are highly active and the filler concentration of compounds used in this work are already above the percolation threshold (necessary for building network of fillers), the percolation activity is more pronounced for EB262 45phr than for N121 40phr. The right graph in the Fig.10.3 shows the displacement for the given load of $75N$ at different temperatures.

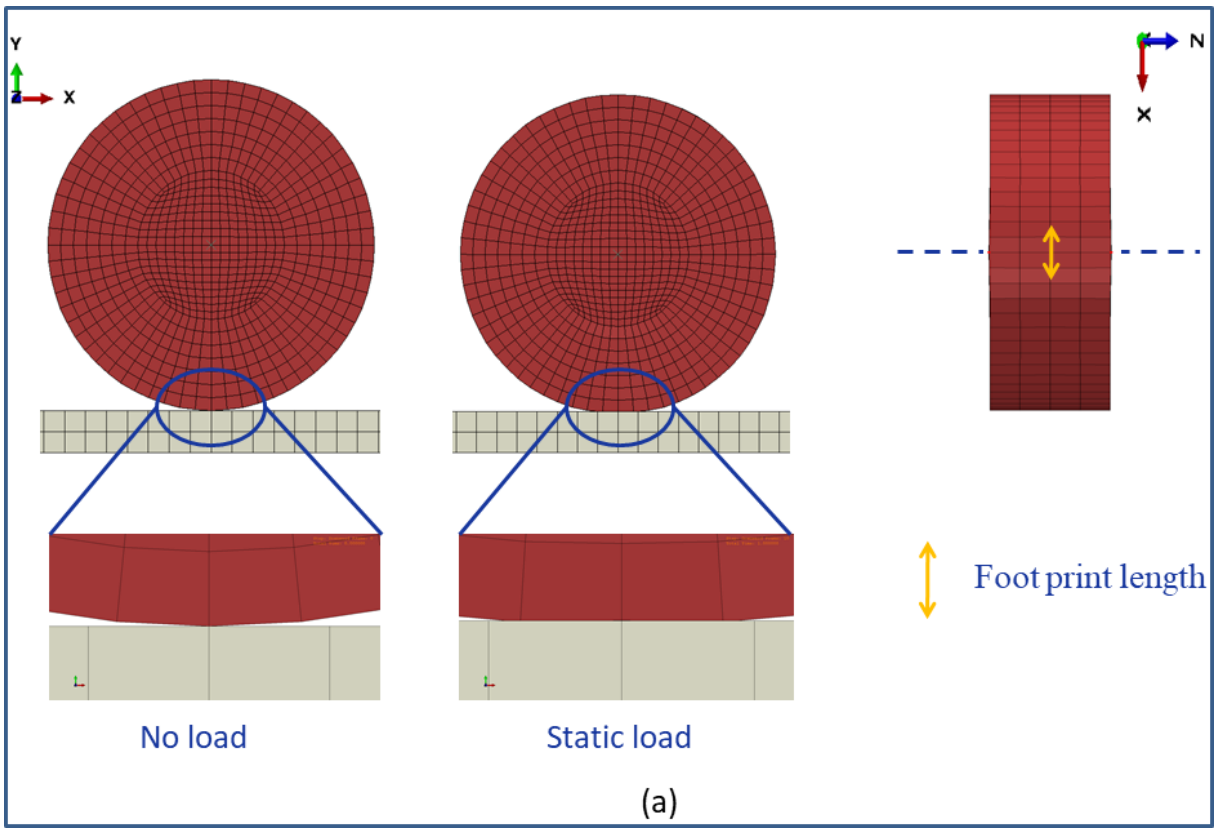

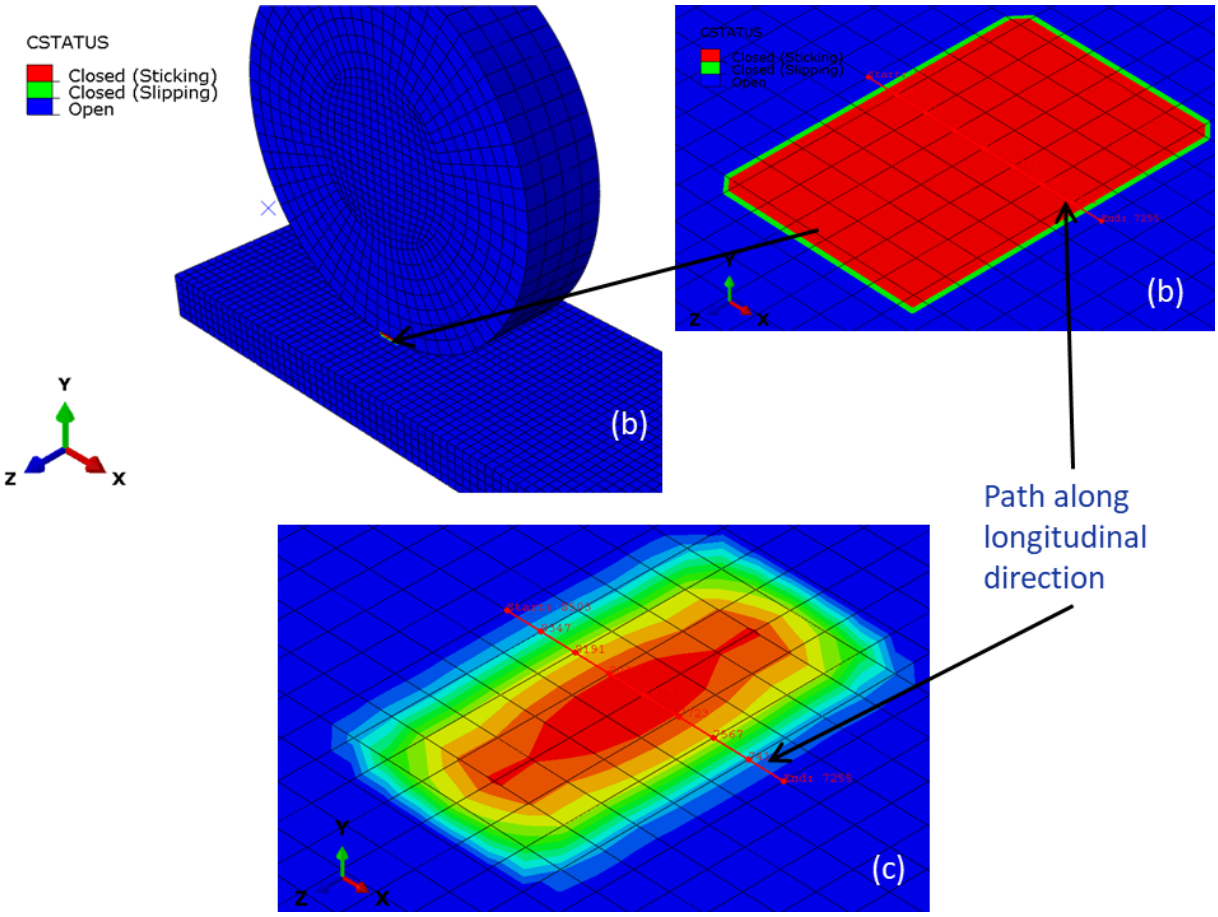

Figure 10.4: (a) The contact formation between the compressed Grosch wheel and the substrate under quasi-static loading condition, (b) CSTATUS shows the status of contact between the wheel and the substrate, and (c) contour plot of vertical contact force.

With an increasing temperature from RT to 80°C, the material stiffness first reduces and then it increases. This kind of behaviour is not that was expected in reference to quasi-static material characterisation in the Fig.9.13, but if we look at the variation of parameters during free fit in the Fig.9.11 which shows how the parameters are influenced by the temperature evolution. The same can also be observed in the figures 9.14 and 9.15, where the stiffness reduces at first for 50°C and then increases for 80°C. The parameters which are generally identified through homogeneous tests deliver a slightly different response due to inhomogeneous deformation during component simulation which involves complex loading cases. Therefore this kind of behaviour can be considered reasonable. The left graph in the Fig.10.3 also shows how the material stiffness improves with respect to increase in the filler content and therefore improves the component response to loading.

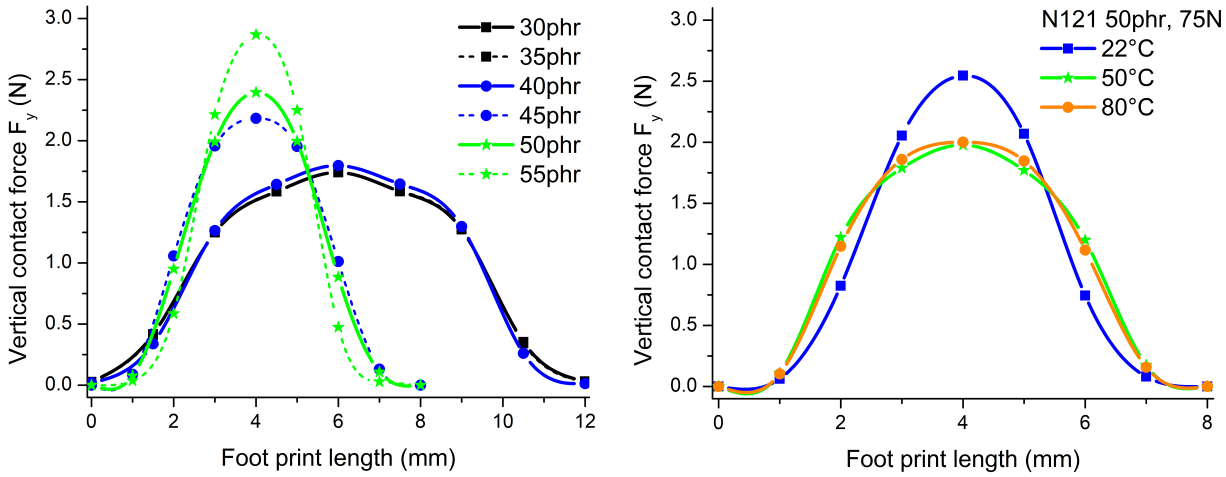

Figure 10.5: Vertical contact force versus foot print length of: (left graph) different compounds taken along the preselected longitudinal path, and (right graph) the compound N121 50phr at different temperatures.

When the tyre is in motion, the tyre load and velocity generate forces at the interface of the tire and the road. These forces act in two planes within this interface region, called the contact area or footprint area (Fig.10.4). The vertical contact forces are a function of tire factors and operational factors. It is these factors which determine how the tire distributes contact pressures across its tread width and the peak contact forces achieved. From the simulations in the Fig.10.3, the vertical component acting in the "y" direction and the foot print lengths for different compounds are taken along the preselected longitudinal path (shown in the plots (b) and (c) of the Fig.10.4) are plotted in the Fig.10.5. The vertical forces generated in the footprint form a bell shaped non-uniform function over the length of the contact. Peak vertical contact forces are achieved in the central region of the contact area. The foot print length has been taken using CSTATUS which shows the status of contact between the bodies (see Fig.10.4). CSTATUS shows both stick and slip if the contact bodies have friction between them, and if the contact is considered to be frictionless then only stick part appears in CSTATUS. The contact forces increase and the foot print lengths decrease with respect to increasing filler content in the compound (left graph of Fig.10.5) and with respect to increasing temperature, the peak of contact forces decreases where as the width of bell shape curve across the central region of foot print length increases (right graph of Fig.10.5).

Table 10.2: The rotational velocities of Grosch wheel considered for dynamic simulation.

Wheel radius	Velocity	Angular velocity	RPS or f
[mm]	[km/h]	[rad/s]	[s^{-1} or Hz]
	5	35.61	5.66
39	10	71.22	11.33
	20	142.45	22.66

10.2 Time-dependent dynamic analysis

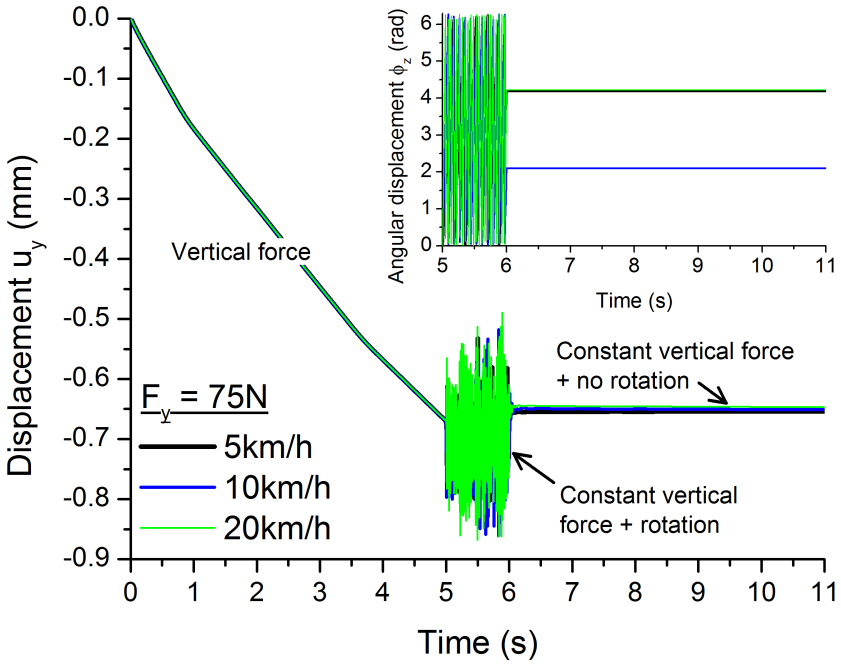

Figure 10.6: Dynamic simulation of Grosch wheel using time-dependent DFM. Vertical force of 75N followed by rotation of wheel at different angular velocity under constant vertical load, and finally modal analysis. Inset shows the angular displacement of wheel during rotation and modal analysis steps.

In case of practical scenario the tyre will be subjected to various complex operating conditions like vehicle velocity and dynamics, road surface, and weather, etc. Compared to the stationary loads, transient loads are the most dominant forces acting on the tyre when the vehicle is on movement. That means the tyre analysis should not be limited to stationary loading conditions but the dynamic analysis needs to be carried out to understand the tyre response to transient loads.

Accordingly the Grosch wheel was simulated with dynamic loading condition using time-dependent DFM. For the simulations, only 75N of vertical load and S50N1 compound parameters have been used. The analysis includes three steps which is as shown in Fig.10.6. First step is the vertical force of 75N which was applied on the wheel with a step time of 5 seconds. This dynamic simulation time corresponds to the quasi-static response of 50phr compound to 75N load which is as shown in the middle-left graph of Fig.10.3. Second one is the wheel rotation step in which the wheel rotates at different velocities under constant vertical pre-force and the rotational frequencies which are provided in the Tab.10.2. In this step neither substrate nor the wheel has

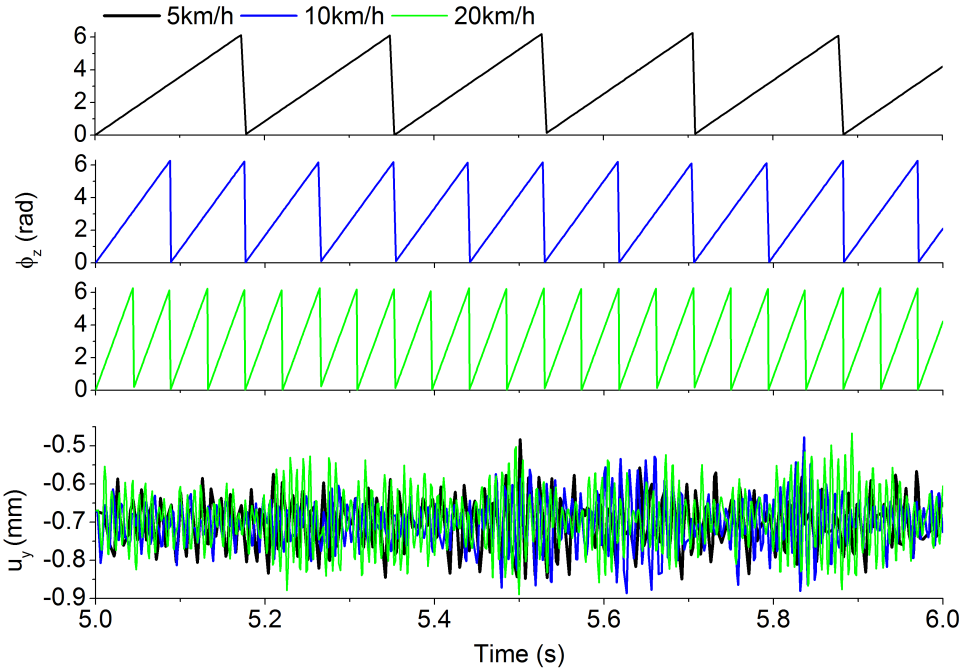

Figure 10.7: The vibration or noise response 'u_y' of rotating wheel to the given input ϕ_z.

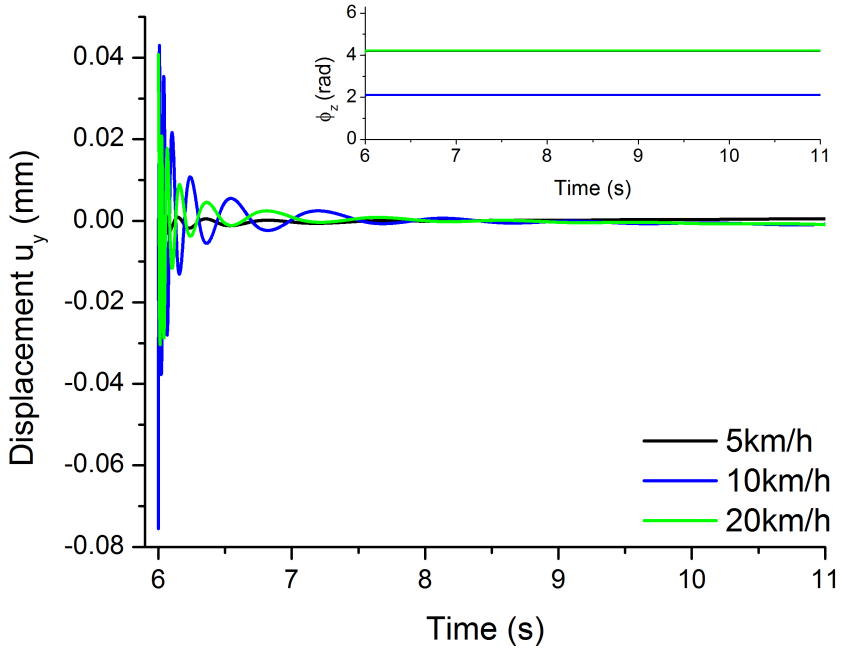

Figure 10.8: Modal analysis of wheel after the rotation at different speeds. The oscillation response of wheel under constant vertical force and without any rotation of wheel.

translational motion. That means, all the degrees of freedom (DOFs) of substrate was constrained and the wheel rotates on the substrate at a stationary translational position. The simulation time for all the rotating velocities are 1 second. Upon rotation, the wheel generates a kind of vibration or noise response which can be seen in the magnified time scale graphs of Fig.10.7. In this work only the vertical reaction amplitude is considered for the vibration analysis. This response has been further analysed using amplitude and power spectra. The third step involves modal analysis of wheel. This is to analyse the oscillation response of wheel after the end of

rotation. When the wheel rotation comes to an end, the rotational frequencies in the previous step generates an oscillatory motion as in Fig.10.8 which dissipates over time. This response is not periodic as the frequency of each wave varies. In this section we have tried to analyse these responses using Fast Fourier Transform (FFT) and Power Spectral Density (PSD). Although there is no experimental data available to assess the results, some literatures related to this topic like Smith and Garcia [2013] has been referred to present the analysis findings.

10.2.1 Vibration analysis

Vibration is about frequencies and is often analysed using a tool called vibration response spectrum. This is particularly suitable for random vibration inputs where as the pure sinusoidal vibration can be dealt with time domain methods.

Accordingly, the frequency and power spectral analysis are used to investigate the models behaviour during different rotational velocities, mesh size and friction. The Fourier analysis is used to de-construct a signal into its individual sine wave components. The result is vibration amplitude as a function of frequency, which lets us perform analysis in the frequency domain (or spectrum) to gain a deeper understanding of the vibration profile. Although the Fast Fourier Transforms (FFTs) are great at analysing vibration when there are a finite number of dominant frequency components, but the power spectral densities (PSD) are used to characterise random vibration signals.

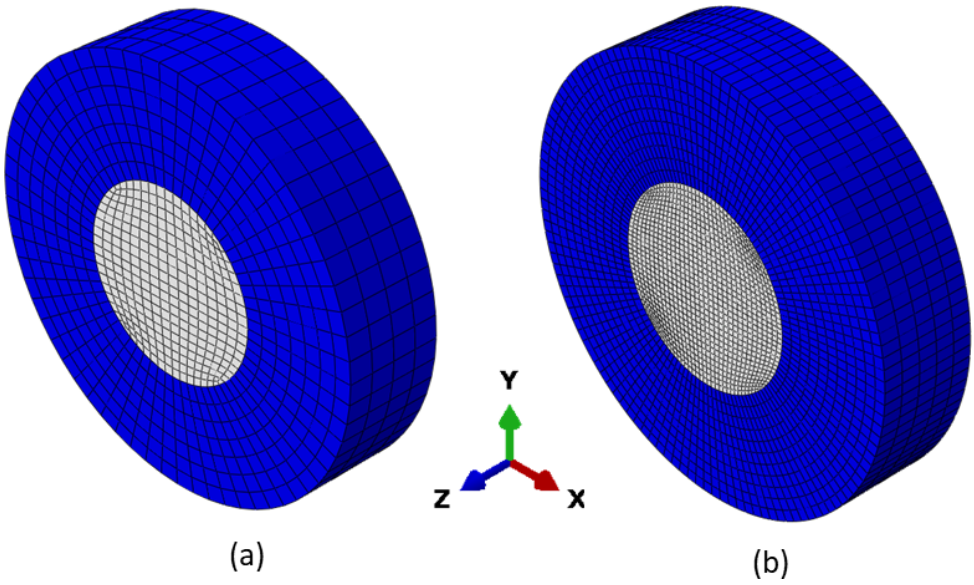

Figure 10.9: Discretised Grosch wheel. (a) Coarse mesh with element size 4mm and (b) fine mesh with element size 1mm.

The vibration response of rotating Grosch wheel has been investigated based on the FE mesh size which is as shown in the Fig.10.9. This is to confirm whether the vibrations are caused by the dynamic forces or due to numerical abnormalities such as the mesh size. For example, if the wheel is discretised with coarse mesh, then the wheel will have less number of nodes in contact with the substrate. As the discretised circumference of the wheel is not perfectly curved, this can generate unrealistic response during rolling. In case of fine mesh, the mesh size was reduced to 1mm. However, we observed that, for both the cases the vibration response is somewhat similar in shape and form. This confirms that the vibration is caused by the dynamic forces from

the wheel-substrate contact interaction. In addition, the simulations were carried out with and without using friction between wheel and substrate. The coefficient of friction was considered to be 0.5.

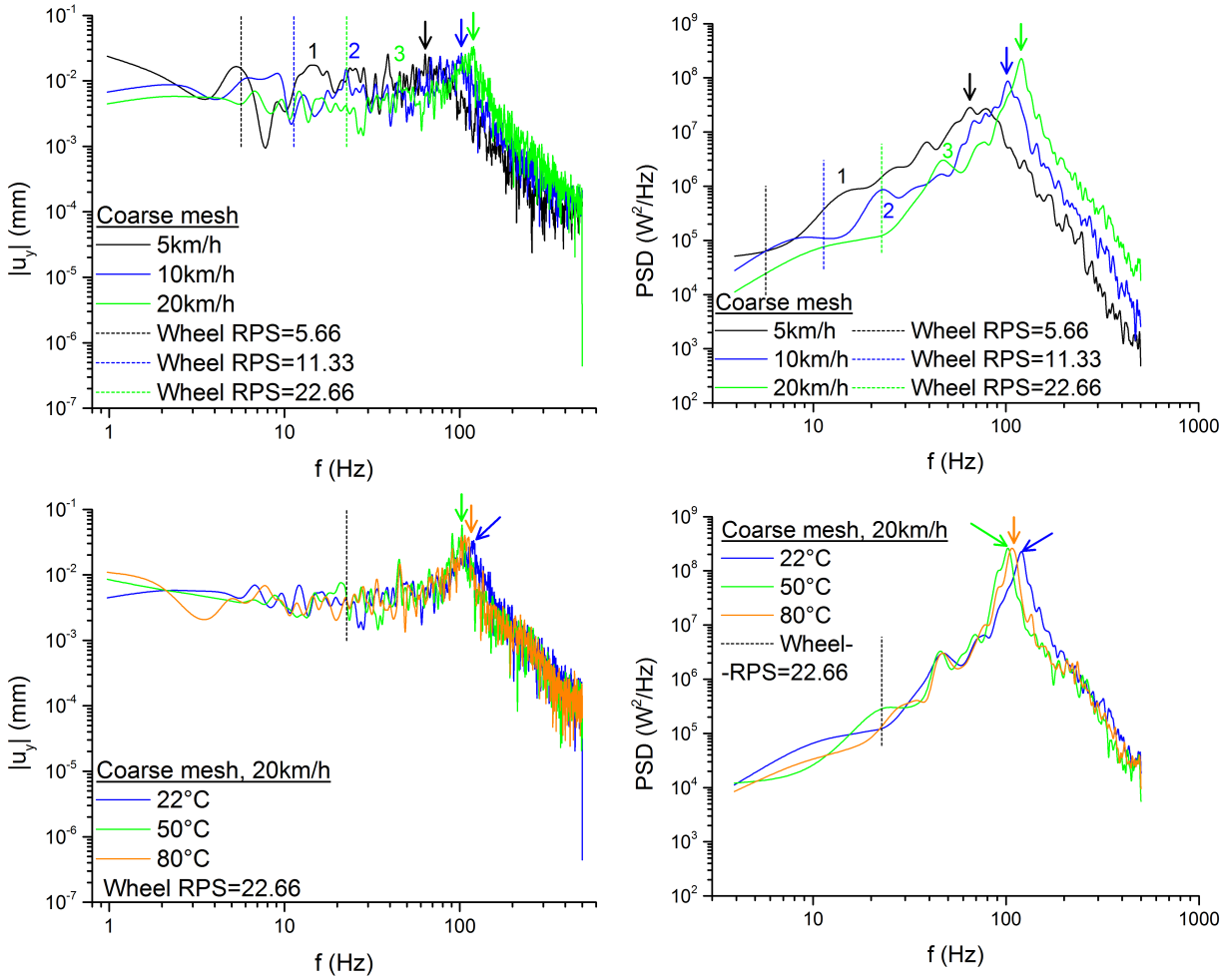

Figure 10.10: Coarse mesh without friction. Top: vertical displacement response as a function of frequency (left) and the corresponding power spectral density (right). Bottom: FFT of vibration response of wheel at different temperatures (left) and the corresponding PSD.

The figures 10.10 and 10.11 show single sided amplitude spectrum of vertical displacement u_y on the left side and the corresponding power spectral density graphs on right side. The mean value has been subtracted from the vibration data as our focus is only on fluctuations.

FFT of vibration signal shows at which frequencies the vibrations cause the greatest amplitudes. Where as the power spectral density graph shows where in the frequency spectra the vibrations have the largest energy per second. The power was calculated using

$$P = F_y \cdot \dot{u}_y \tag{10.2}$$

Where F_y is the static vertical force of $75N$ and $\dot{u}_y$ is the rate of displacement or velocity of vibration amplitude. PSD of power P of vibration signal is expressed in W^2/Hz. The largest power does not mean that the vibration amplitudes have to be very big, just that the

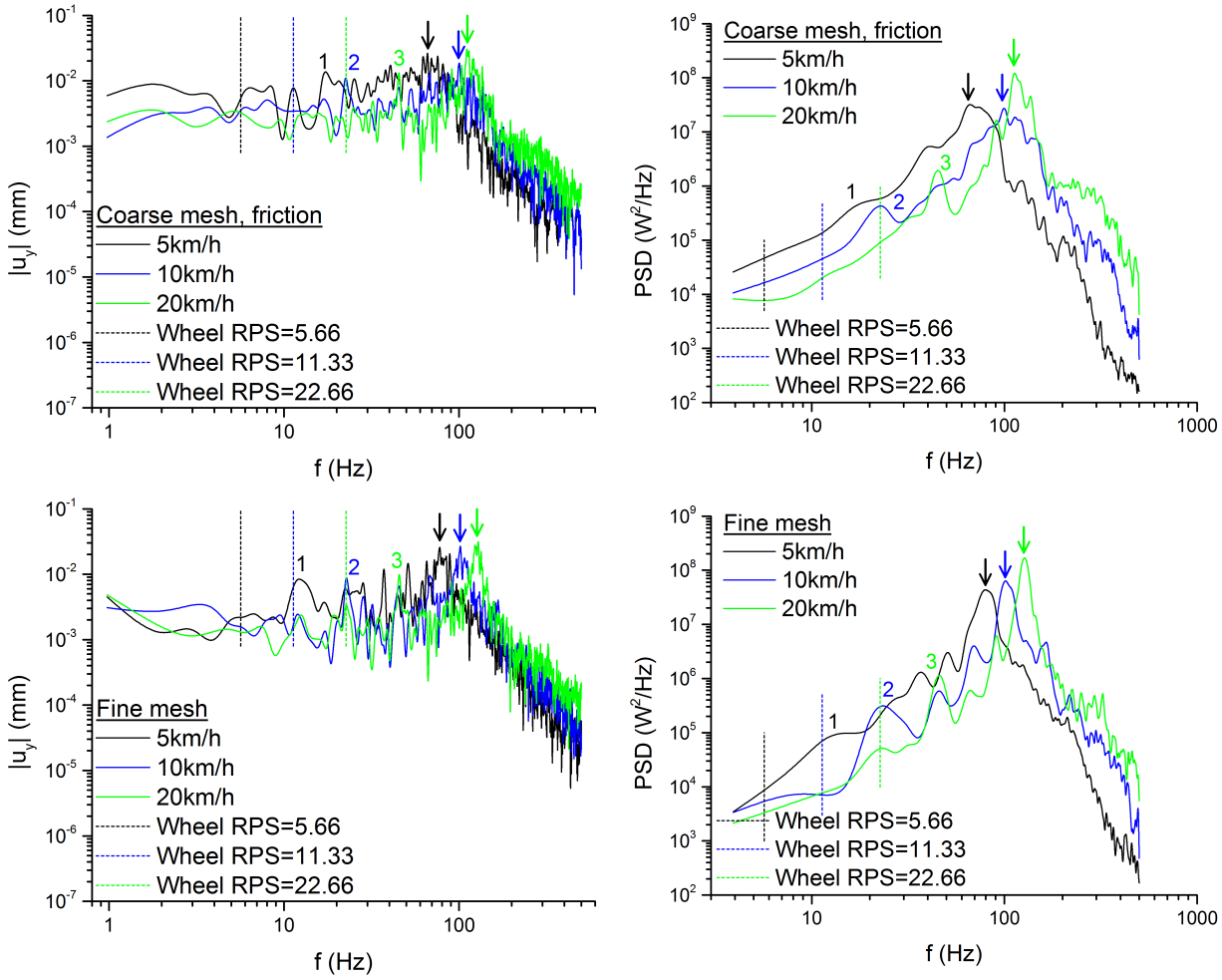

Figure 10.11: FFT of vibration response of wheel and the corresponding PSD. Top: Coarse mesh with friction and bottom: fine mesh without friction.

transmitted effect is large and more difficult to cancel out. The down arrows ↓ marked on each of the graphs show the peak of both displacement amplitudes and PSDs over the spectrum. The values of frequency, amplitude and PSD corresponding to these peaks are given in Tab.10.3. The temperature dependent graphs for the case of rotational velocity $20kmh$ is also provided in bottom half of Fig.10.10 and the corresponding peak values are given in Tab.10.4. These peak values vary with respect to rotational velocity of wheel as well as temperature. Apart from this, in the figures 10.10 and 10.11 the first peaks or bumps of displacement amplitude/PSD in relation with rotating frequencies of the wheel are marked as numbers from 1 to 3 and the values are given in Tab.10.5. The first bump frequencies for different mesh size and with friction are similar and these bumps are generated at those frequencies which are approximately close to the second harmonic of wheel rotation frequencies. At the end of this sub-section the Fig.10.12 shows the PSDs based on mesh size and friction plotted separately for each wheel rotation frequency. This figure just has graphs rearranged from figures 10.10 and 10.11. The graphs depending on the mesh size and friction show similar tendency in shape and form and the first peak and maximum peak frequencies are also very proximate to each other (refer Tab.10.3 and Tab.10.5).

Table 10.3: The values of frequency, amplitude and PSD corresponding to the maximum peaks of amplitude spectrum and power spectral density of wheel vibration.

Velocity	Symbol	Coarse mesh without friction			Coarse mesh with friction			fine mesh without friction		
		f	u_y	PSD	f	u_y	PSD	f	u_y	PSD
[km/h]		[Hz]	[mm]	$[W^2/Hz]$	[Hz]	[mm]	$[W^2/Hz]$	[Hz]	[mm]	$[W^2/Hz]$
5	↓	64	0.026	2.99x10^7	66	0.026	3.58x10^7	78	0.026	4.56x10^7
10	↓	102	0.028	9.21x10^7	100	0.018	2.82x10^7	102	0.027	7.01x10^7
20	↓	120	0.034	25.77x10^7	110	0.03	12.84x10^7	128	0.0314	17.9x10^7

Table 10.4: The values of frequency, amplitude and PSD corresponding to the maximum peaks of amplitude spectrum and power spectral density of temperature dependent wheel vibration.

Velocity	Temperature	Symbol	Coarse mesh without friction		
			f	u_y	PSD
[km/h]	[°C]		[Hz]	[mm]	$[W^2/Hz]$
20	22	↓	120	0.034	25.77x10^7
	50	↓	103	0.057	2.73x10^7
	80	↓	107	0.040	2.73x10^7

Table 10.5: The first displacement amplitude peak in relation with rotating frequency of wheel.

Velocity	Number	Wheel rotation frequency	Coarse mesh without friction	Coarse mesh with friction	fine mesh without friction
		f			
[km/h]		[Hz]			
5	1	5.66	14.4	17	12
10	2	11.33	22.6	22.6	22.6
20	3	22.66	45	45.3	45.7

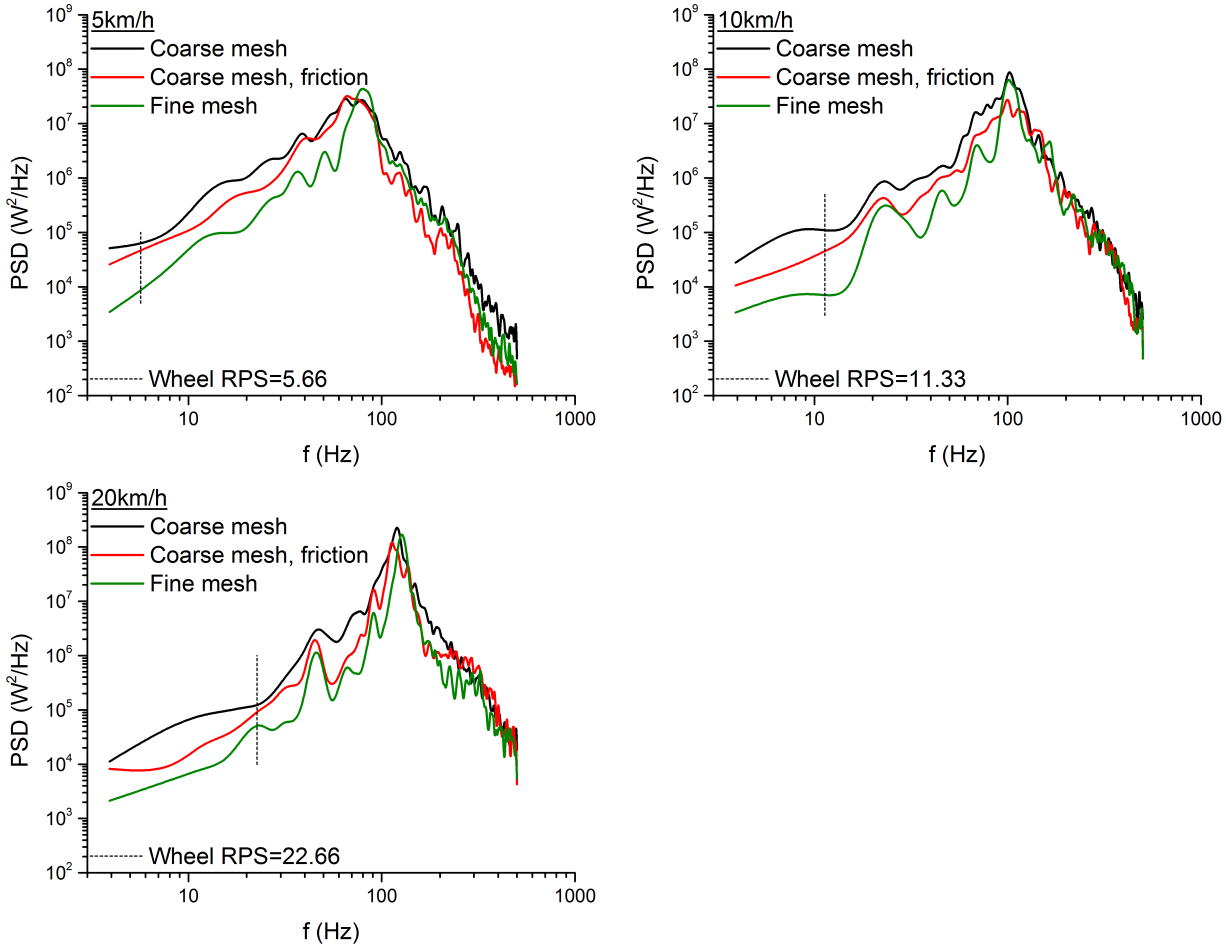

Figure 10.12: From the figures 10.10 and 10.11, comparison of PSDs with respect to mesh size of FE model and friction between the wheel and substrate.

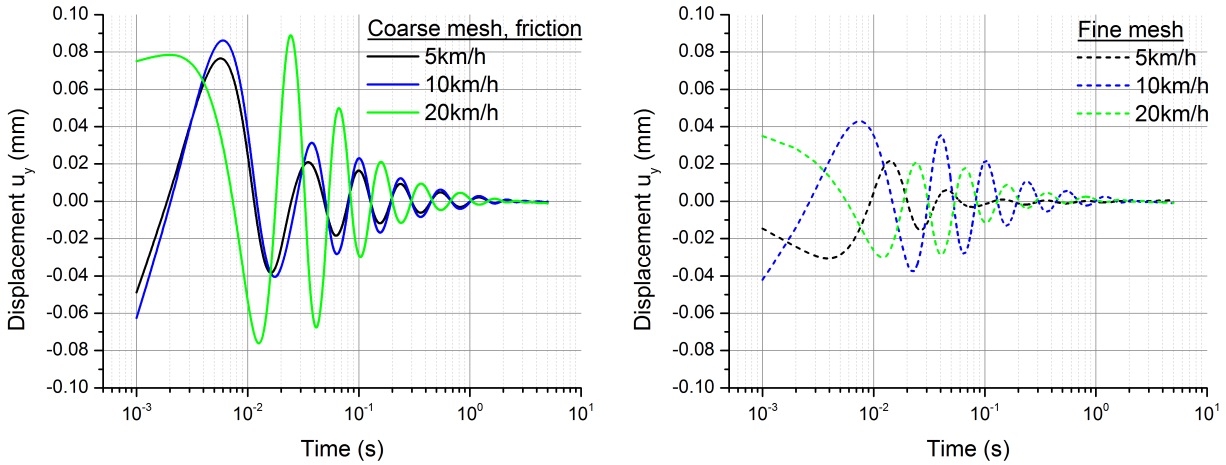

Figure 10.13: Modal analysis of wheel in dependence of rotational velocity. Coarse mesh with friction(left) and fine mesh without friction (right).

10.2.2 Modal analysis

The oscillation created by the rotation of the wheel at different rotational velocities is investigated using modal analysis. The Fig.10.13 shows oscillating response of wheel (Fig.10.8) in the

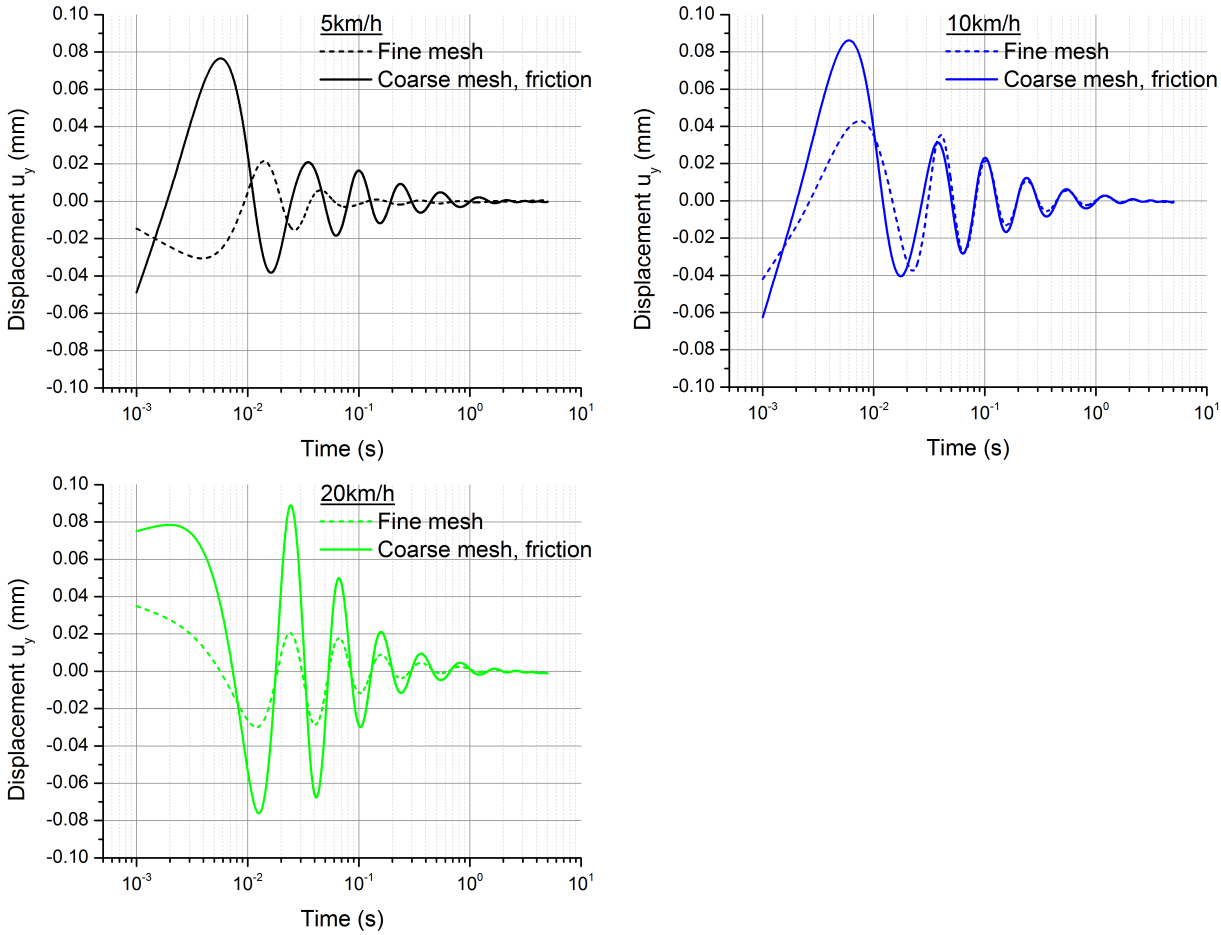

Figure 10.14: From the Fig.10.13, comparing the oscillation response of wheel in dependence of mesh size of FE model.

logarithmic time scale. It is important to note that the response is not periodic. That means the periodicity of each wave is not repetitive. Therefore the behaviour is not harmonic and the damping frequency of decaying signal keeps on changing over time. Therefore we again make use of FFT and PSD to understand the response over frequency spectrum. In this subsection only the simulation results of coarse mesh with friction and fine mesh without friction are discussed. In case of coarse mesh with friction, the response of $5km/h$ and $10km/h$ are in same phase, where as the response of $20km/h$ has a phase shift compared to other two velocities. In contrast, the simulation results with fine mesh shows that the oscillation response of all the three velocities are in different phase to each other.

In case of coarse mesh with friction, the displacement amplitudes of oscillation are monotonically increasing with respect to increasing velocity where as for fine mesh the amplitude of $10km/h$ is higher than of $20km/h$. The reason is not clear because this was not the same with vibration signal as in Fig.10.11. This ambiguity is also reflected in PSD curves of fine mesh in Fig.10.15. The curves in Fig.10.13 are once again rearranged in Fig.10.14 according to the rotational velocities. In this figure we can observe that the responses of $10km/h$ and $20km/h$ are in same phase where as the $5km/h$ responses are not. The displacement amplitude for the coarse mesh with friction simulation is higher than for fine mesh without friction due to the resistance at the contact surface.

In the Fig.10.15, the single sided amplitude spectra and the corresponding PSDs for different

mesh size and friction are displayed. The resulting curves or the fluctuations are similar in shape and form for all the rotating velocities. From the PSD graphs we can see that the first two peaks or bumps of power coincide with the wheel rotation frequencies of $11.33Hz$ and $22.66Hz$.

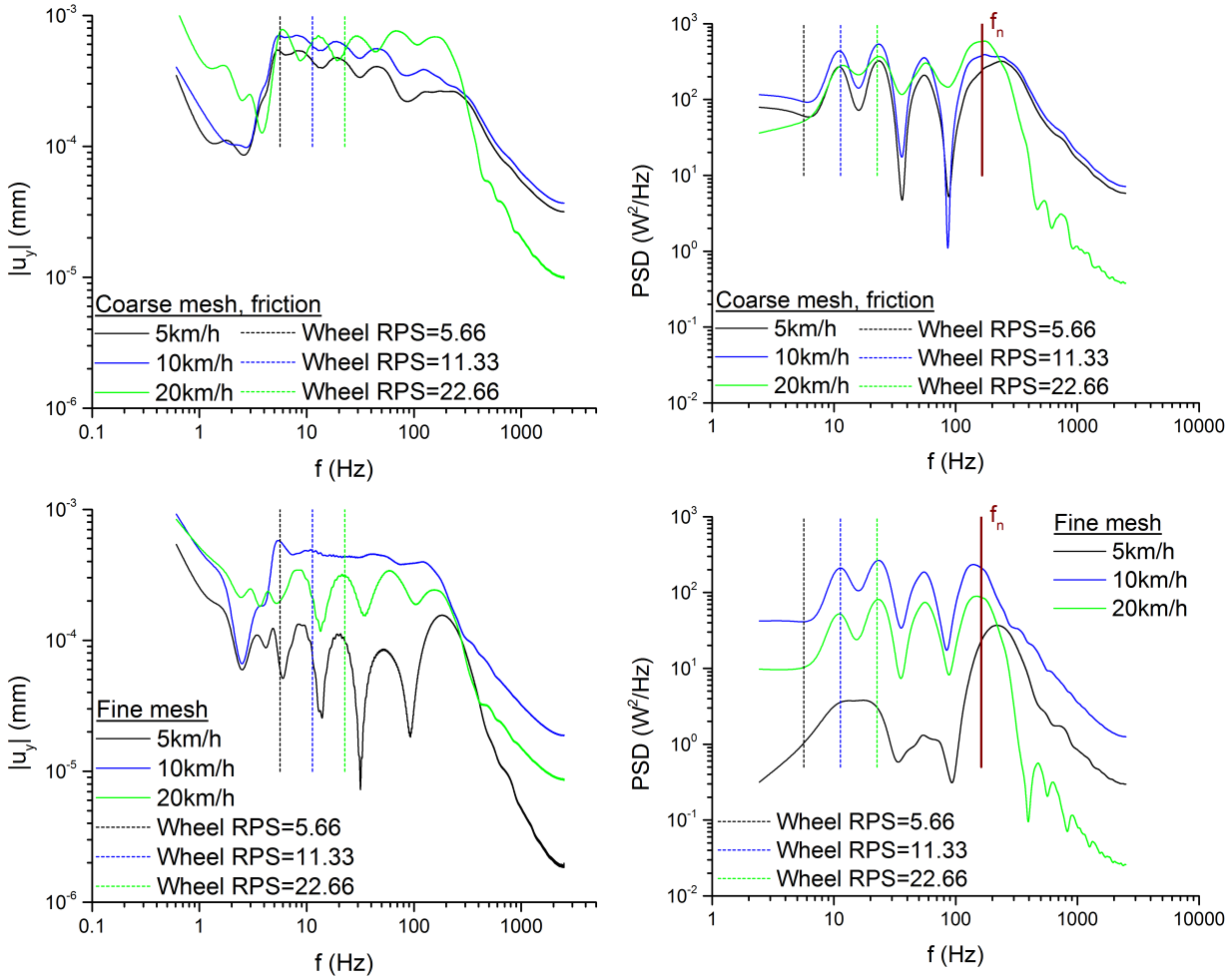

Figure 10.15: FFT of modal response of wheel and the corresponding PSD. Top: Coarse mesh with friction and bottom: fine mesh without friction.

If we consider the wheel to be equal to a 1-D spring of stiffness k and mass M, then the natural angular velocity ω_n can be written as

$$\omega_n = \sqrt{\frac{k}{M}}. \tag{10.3}$$

Then the resulting natural frequency f_n will be

$$f_n = \frac{1}{2\,\pi}\,\omega_n. \tag{10.4}$$

The stiffness k=$97.8kN/m$ was calculated from the tangent to the quasi-static force-displacement curve. Volume of the wheel is considered to be $0.86\text{x}10^{-4}m^3$ and the corresponding mass M of the wheel is $0.0946kg$. The resulting natural angular velocity ω_n is $1016.7rad/s$ and the natural frequency f_n is $162Hz$.

Beyond $5Hz$ the rotational forces generate oscillation in the wheel. This oscillation gets amplified when the frequency of oscillation equals the natural frequency f_n of the body called resonance

and is marked as red line in the Fig.10.15. Finally the Fig.10.16 shows the rearranged graphs of Fig.10.15 based on the wheel rotational velocities.

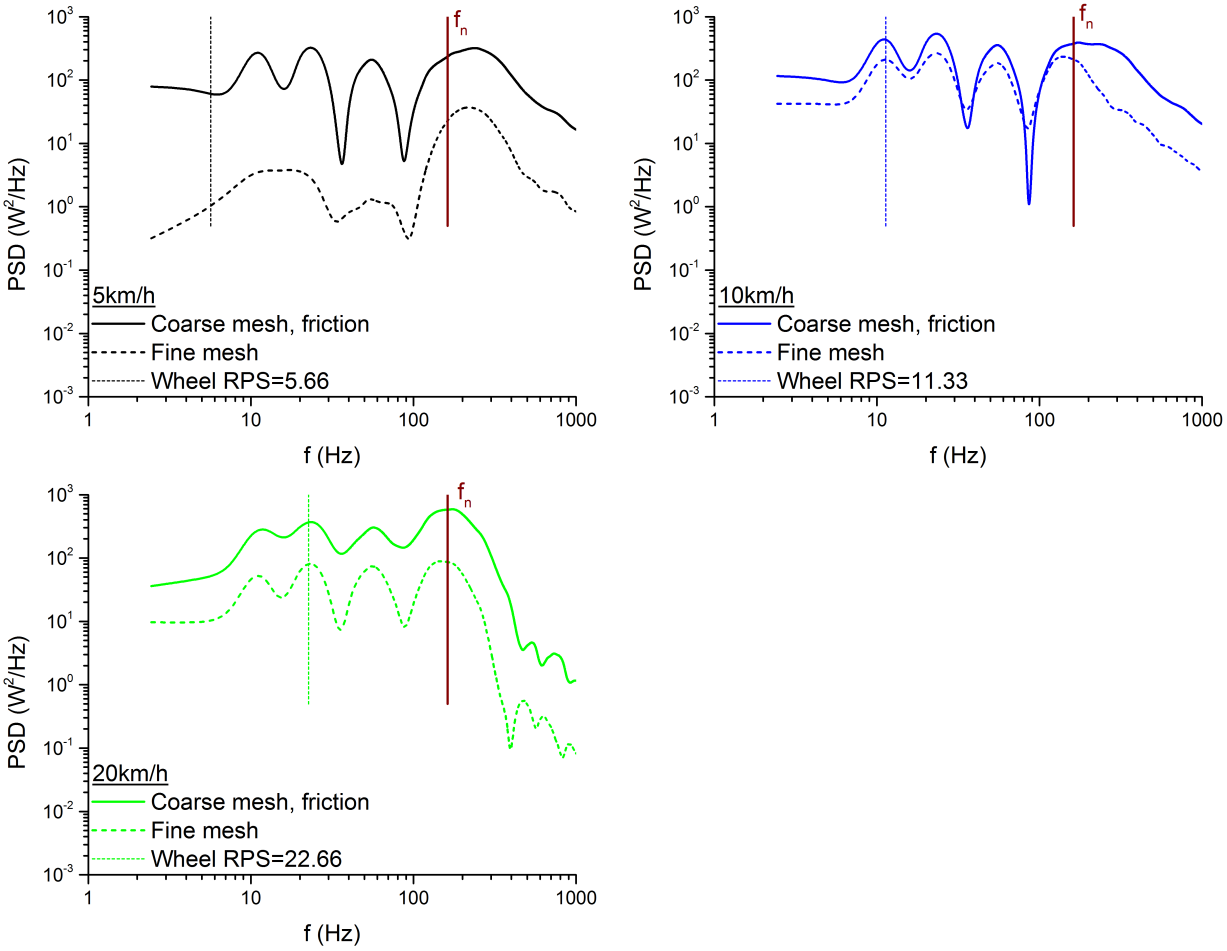

Figure 10.16: From the Fig.10.15, comparing the oscillation response of wheel in dependence of mesh size of FE model.

10.3 Thermo-mechanical coupling

In this section the thermo-mechanically coupled Zener model was used to simulate the temperature evolution due to mechanical dissipation. As the DFM is not completely developed to couple the temperature-displacement equations, this section does not include simulations of the DFM. The Tab.10.6 shows the parameters for the simulation of thermo-mechanically coupled Zener model. Out of these parameters, C_{10}, μ_0 and τ are not actual, that means they are not determined from actual experiments and therefore the results are superficial and only for exhibiting the thermo-mechanical analysis. Other parameters like K_{mod} is taken based on the concept of representative directions. ρ and α_T are based on the literature survey. E_a is taken to be equivalent of E_d in Tab.9.3. The parameters like C_p and κ are based on the actual experiments where as k_{stat} and k_{conv} are the fit parameters which are determined from the analytical simulation shown in next chapter.

The coupled thermo-mechanical simulation was done on dumbbell specimen. The geometry and full FE model is shown on the left side of Fig.10.17. As dumbbell is geometrically symmetric

Table 10.6: Parameters of the 1-D thermo-viscoelastic Zener model.

C_{10}	0.35	MPa	θ_{amb}	295	K
μ_0	0.9	MPa	θ_{ref}	295	K
τ	1.0	s	E_a	5 x 10^3	J/mol
K_{mod}	1000	MPa	R	8.314	$J/(K\,mol)$
ρ	1.1 x 10^{-9}	$tonne/mm^3$	α_T	9.87 x 10^{-5}	K^{-1}
			C_p	1.52 x 10^6	$J/(tonne\,K)$
			κ	0.221 x 10^{-3}	$W/(mm\,K)$
			k_{stat}	47 x 10^{-6}	$W/(mm^2\,K)$
			k_{conv}	47 x 10^{-6}	$W\,s/(mm^3\,K)$

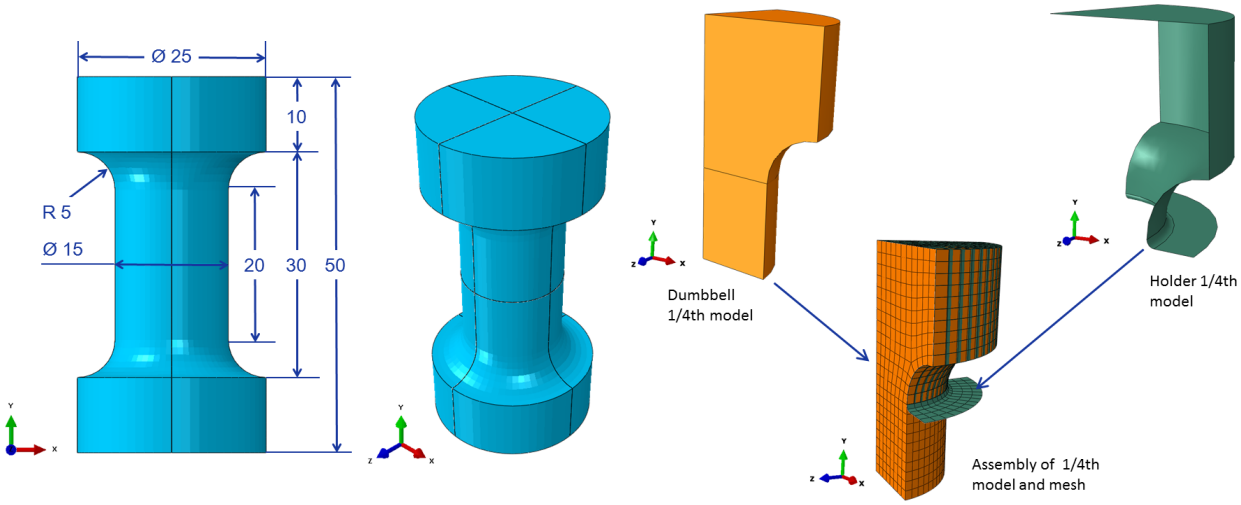

Figure 10.17: Left: Geometry and 3D FE model of dumbbell specimen; right: assembly and mesh of $\frac{1}{4}$th FE models.

in circular as well as in axial direction, it is beneficial from the point of FE simulation to take only the $\frac{1}{4}$th of actual geometry. Accordingly we have considered the $\frac{1}{4}$th of dumbbell and holder FE models and their corresponding assembly and mesh is shown on the right side of Fig.10.17. Holder is considered to be rigid and is constrained by the reference point RF. The displacement boundary conditions are applied on the assembly which is shown in Fig.10.20. The full model deformations in the Fig.10.20 are obtained by mirroring the $\frac{1}{4}$th assembly on symmetry planes. The contact boundary condition between dumbbell and holder is defined using interaction properties. The friction coefficient is taken as 0.5.

During the simulation, the dumbbell was subjected to time-dependent load of $v = 500mm/min$. The loading history is given in Fig.10.19 where, first 10 cycles are 50% stretch and the next 5 cycles are 100% stretch of the dumbbell. The resulting temperature evolution is taken from the nodes, one at the core and another at the surface. The temperature of both the nodes remain same till first 2 cycles of 50% stretch and then they deviate from each other due to increase in exchange rate of heat at the boundary. The temperature evolution accelerates at first few cycles and then slows down till it reaches a stabilised state where the growth remains unchanged. This phenomena of temperature evolution is dependent on the energy dissipation of hysteresis cycles. As the hysteresis loops are larger during transient cycles, the material dissipates more energy and in turn converted into heat. When the heat generation within the body exceeds the heat diffusion

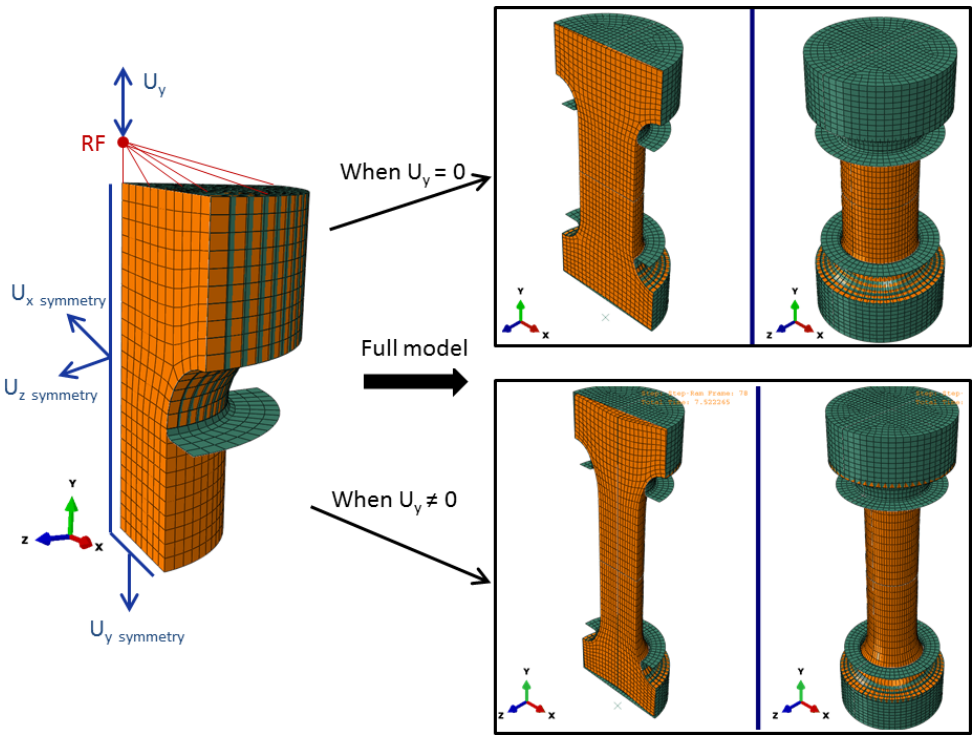

Figure 10.18: Defined boundary conditions on $\frac{1}{4}$th assembly and their corresponding full model deformation.

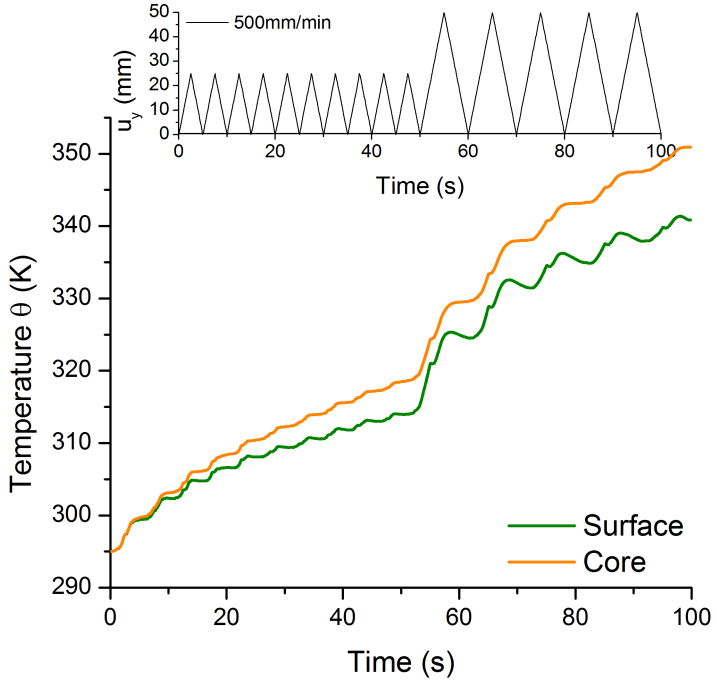

Figure 10.19: Temperature evolution over time. Inset shows the loading history.

through the material, the inner temperature of the body keeps on rising. As the hysteresis loops tend towards stable or stationary behaviour, the balance between the internal heat generation and the heat diffusion through material reaches an equilibrium. The temperature difference between the core and surface nodes at the end of loading is around 10°C. Cyclic experiment in the next chapter upholds the above discussion.

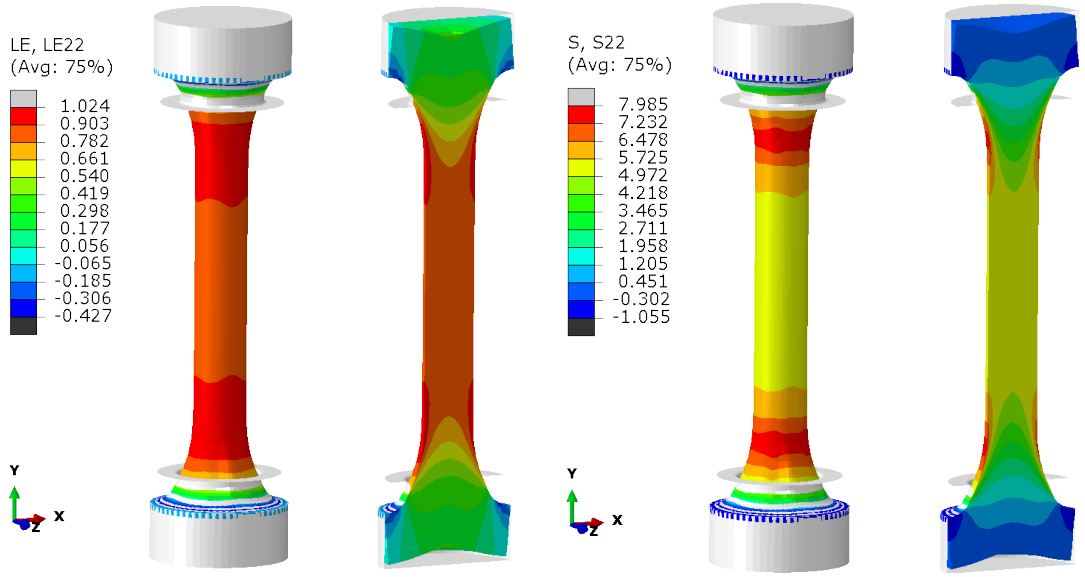

Figure 10.20: Visualisation of strain and stress at the end of loading in the normal direction y. Left: Logarithmic stain; right: Cauchy stress.

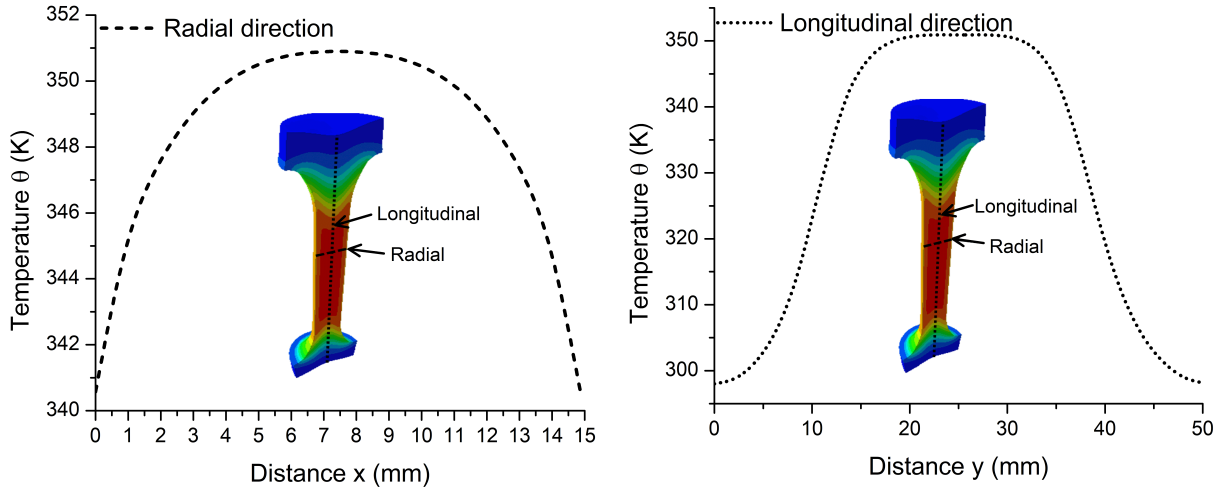

Figure 10.21: Direction dependent temperature distribution curves at the end of loading. Left: along radial direction; right: along axial direction. Inset shows the defined directions on dumbbell FE model.

Fig.10.20 shows the stress and strain in the stretch direction at the end of loading history. Maximum stress and strain can be seen at the curves where the material can undergo continuous damage and ultimately fails at this spot. The temperature spectrum at core and surface is shown in Fig.10.22. The temperature distribution on the surface is homogeneous along the axial direction till the curves. It is inhomogeneous in the inner section both along the axial as well as in the radial direction due to heat flux. The temperature change along the predefined paths in radial and axial directions are shown in Fig.10.21. Along radial direction it is like U shape in reverse. In case of axial direction the change is also like U shape in reverse, but with a flat top (plateau). These results can be compared with the actual measured results as shown in figures 11.8 and 11.9.

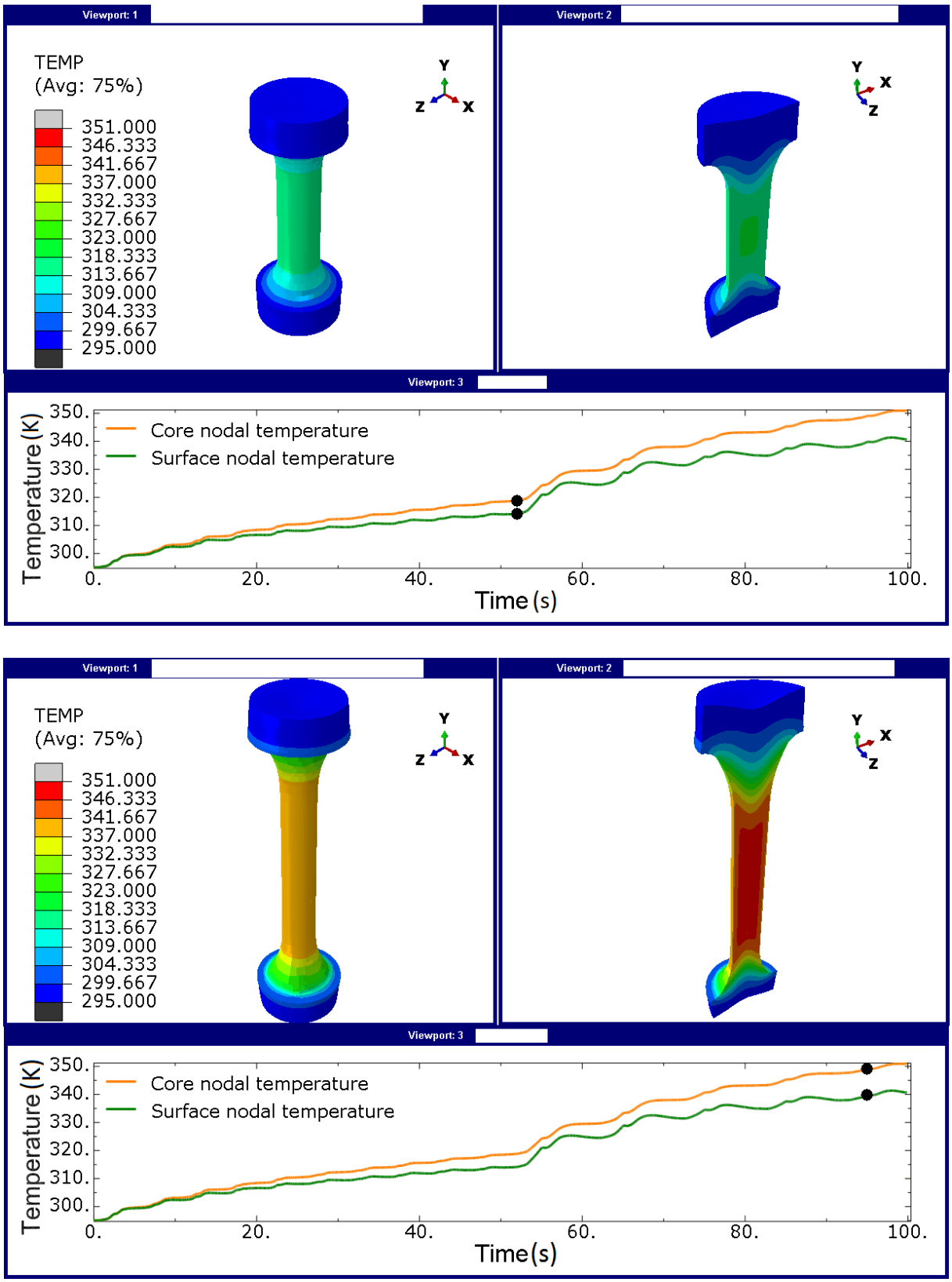

Figure 10.22: Visualisation of surface and core temperatures at the peaks of 50% and 100% loading.

Chapter 11

Internal heat generation

In this chapter, an analytical simulation of self heating of rubber component during cyclic loading is presented. For that we make use of analytical model proposed by Carslaw and Jaeger [1959] and for implementation, Fritzsche and Klüppel [2011b] has been referred. The aim of this chapter is to present the evolution of temperature within the body due to self heating and the analytical estimation of internal and surface temperatures during cyclic loading. The results are compared with thermal images and curves. In addition, the simulation parameter "heat exchange coefficient" k_{stat} is identified through curve fitting on measured surface temperature.

11.1 Experiment - harmonic loading

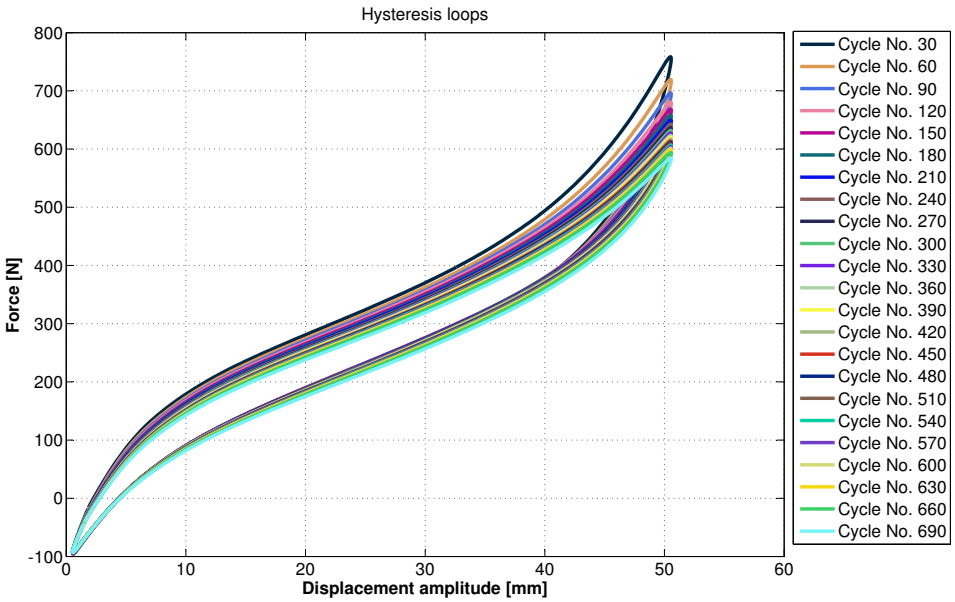

Figure 11.1: Cyclic loading at $f = 1Hz$. Hysteresis loops taken at every $30s$.

The hysteretic loops in Fig.11.1 were obtained from harmonic loading test carried out on MTS machine. A Dumbbell sample was stretched to 100% strain at a frequency of $f = 1Hz$. In the figure, only loops at an interval of $30s$ has been displayed. This is because if the program is set

to save the loops every second then it would be a huge amount of data to save and on the other hand, machine also makes a pause of few microseconds to save each loop. Hence it was opted to save loops every $30s$. Although the aim was to carry out the test till $30min$ in order to obtain a constant surface temperature, the sample failed earlier at about $705s$, which is as shown in the Fig.11.2.

Figure 11.2: A crack propagation due to high stresses at the corner lead to sample failure. Material failed after $705s$.

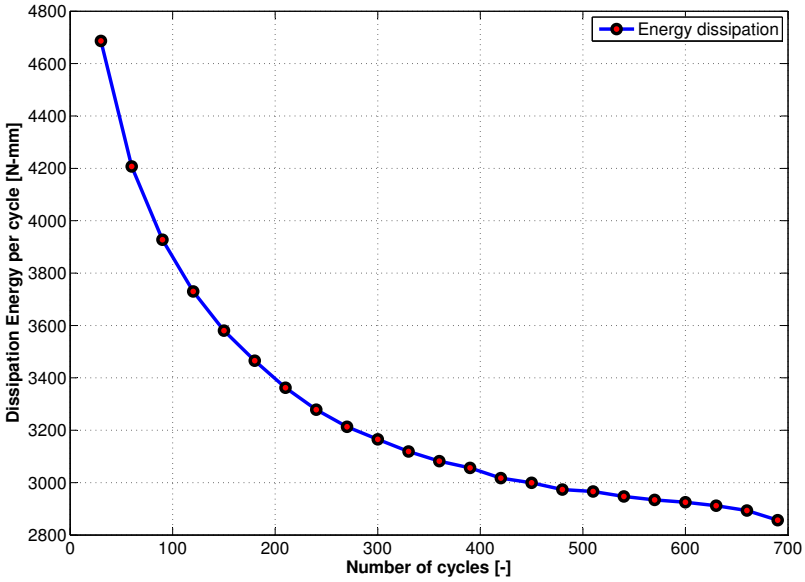

Figure 11.3: Dissipated energy per cycle vs number of cycles.

A continuous decrease of stiffness as well as hysteresis can be observed in the Fig.11.1. The hysteretic behaviour of material is the cause of energy dissipation and this leads to heat build up. The evolution of temperature in turn affects the mechanical behaviour and thereby results in reduced hysteresis and stress softening of material. The exponential decrease of energy dissipation per cycle is shown in Fig.11.3. The energy dissipation is nothing but the area within hysteresis loop and is the difference between the integral of force-displacement product of loading and unloading curves. Using trapezoidal quadrature rule, the energy dissipation can be approximated

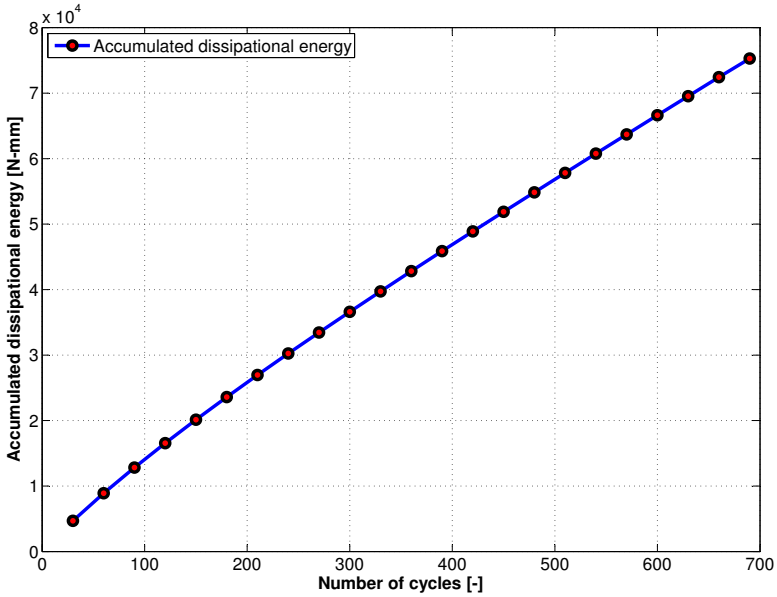

Figure 11.4: Accumulated dissipated energy over number of cycles.

as

$$E_{diss} = \frac{1}{2}\left(u_n \cdot F_n - u_1 \cdot F_1\right) \sum_{i=1}^{n} \left(u_{i+1} \cdot F_i - u_i \cdot F_{i+1}\right), \tag{11.1}$$

where u and F are displacement and force, respectively.

Fig.11.4 shows the accumulated dissipated energy over number of cycles to determine the total amount of dissipated energy which is transferred to heat. Then the average dissipated energy can be calculated by dividing the total dissipated energy by number of cycles.

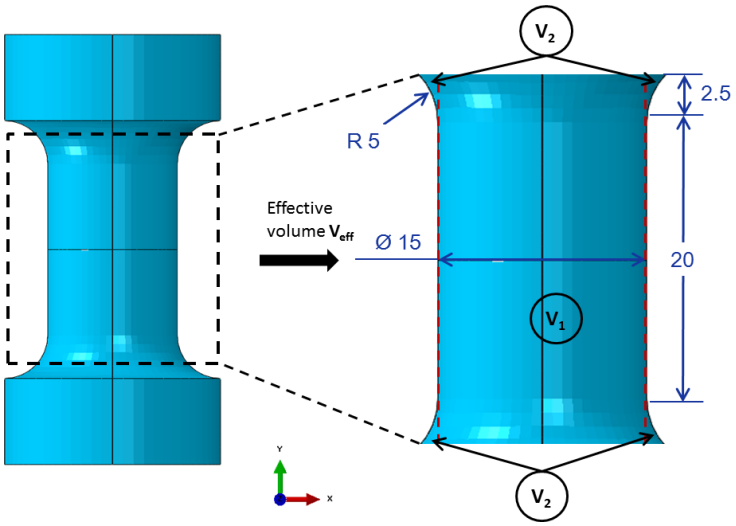

Figure 11.5: Schematic of dumbbell sample to calculate the effective volume.

The dissipation power or the dissipation energy rate can be calculated using the form,

$$\mathscr{D}^m = \frac{E_{diss,avg}}{V_{eff}} \cdot f \cdot 10^{-3}, \tag{11.2}$$

Table 11.1: Energy dissipation of hysteresis cycles and the corresponding dissipation power of measured sample.

Accumulated energy dissipation	$E_{diss,avg}$	V_{eff}	$\mathscr{D}^m$
$N\,mm$	$N\,mm$	mm^3	W/mm^3
75298	3273.8	4950.8	0.00066127

where $E_{diss,avg}$, V_{eff} and f are the average dissipation energy, effective volume of dumbbell sample and frequency, respectively. The effective volume is not the volume of whole dumbbell sample rather it is the deformation volume as shown in Fig.11.5. As the rest of the volume is clamped, it's contribution to dissipation is negligible. The effective volume is an additive split of two parts. The volume v_1 can be directly calculated from the formula of a cylinder $\pi \cdot R_1^2 \cdot h_1$. Where R_1 is $7.5mm$ and h_1 is $20mm$. The volume v_2 can be calculated as

$$V_2 = 2 \cdot \sum_{i=1}^{n} \pi \cdot \left(R_i^2 - R_1^2\right) \cdot \Delta h_i, \tag{11.3}$$

where R_i is the radius of curved profile, R_1 is the radius of cylinder 1 and Δh_i is the incremental height of profile. The total height of cylinder 2 is $2.5mm$. The multiplication pre-factor 2 in Eq.(11.3) is for the volume of curved profiles on both the sides. Tab.11.1 shows the corresponding calculated values of energy dissipation for the measured sample.

11.2 Heat conduction in a cylinder

From the first law of thermodynamics, the reduced form of balance of internal energy without external heat source can be expressed as

$$\dot{U} = \mathscr{D}^m - \nabla q, \tag{11.4}$$

where $\dot{U}$ is the rate of internal energy and q is the heat flux the through material. The increase of temperature in the material is due to increase of internal energy caused by the combination of heating due to dissipation and heat loss through body and surface heat fluxes.

The rate of internal energy is equal to $C_p \cdot \rho \cdot \dot{\theta}$ and q is equal to $-\kappa \left(\frac{\partial \theta}{\partial x} + \frac{\partial \theta}{\partial y} + \frac{\partial \theta}{\partial z}\right) = -\kappa\, \nabla\theta$. Therefore by rewriting the Eq.(11.4) we obtain,

$$\begin{aligned} C_p \cdot \rho \cdot \dot{\theta} &= \mathscr{D}^m + \kappa\, \nabla^2 \theta, \\ &= \mathscr{D}^m + \kappa \left(\frac{\partial^2 \theta}{\partial x^2} + \frac{\partial^2 \theta}{\partial y^2} + \frac{\partial^2 \theta}{\partial z^2}\right). \end{aligned} \tag{11.5}$$

With thermal diffusivity $\varsigma = \dfrac{\kappa}{C_p\, \rho}$, Eq.(11.5) becomes

$$\left(\frac{\partial^2 \theta}{\partial x^2} + \frac{\partial^2 \theta}{\partial y^2} + \frac{\partial^2 \theta}{\partial z^2}\right) - \frac{1}{\varsigma}\, \dot{\theta} = -\frac{\mathscr{D}^m}{\kappa} \tag{11.6}$$

In the Eq.(11.6), heat loss through the material can be described using heat flux in three directions. For dumbbell like sample, the concept of flow of heat in an infinite circular cylinder from Carslaw and Jaeger [1959] can be considered. In this, the heat flux has been considered only in

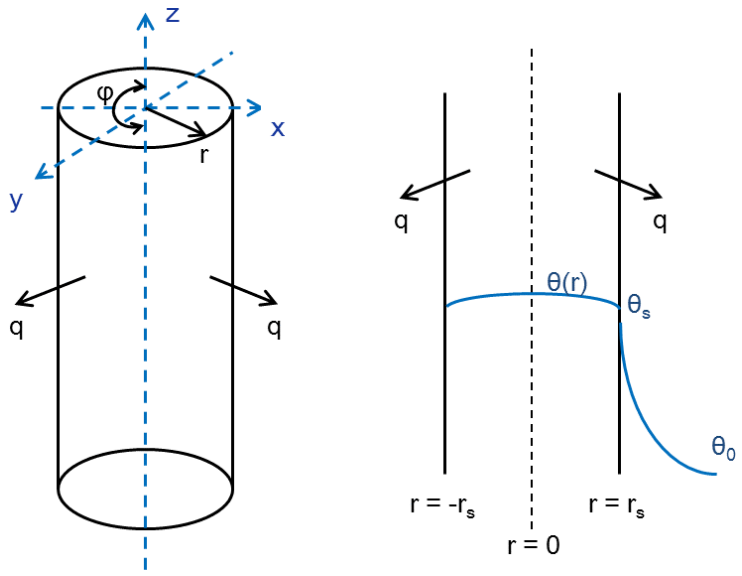

Figure 11.6: Left: simplified dumbbell sample as a cylinder of infinite length with coordinates and heat flux only in radial direction; right: schematic representation of temperature profile within and outside the sample [Fritzsche and Klüppel, 2011b].

radial direction and thereby neglecting heat loss in z-direction (Fig.11.6). With only one variable r, two dimensional description of heat transportation can be defined and the approximation is considered to be more accurate compared to other geometries. Accordingly, the Eq.(11.6) for the case of circular cylinder results in,

$$\left(\frac{\partial^2\theta}{\partial r^2}+\frac{1}{r}\frac{\partial\theta}{\partial r}\right)-\frac{1}{\varsigma}\dot{\theta}=-\frac{\mathscr{D}^m}{\kappa}. \tag{11.7}$$

With an assumption of linear heat transfer at the surface, the boundary condition for $r = r_s$ can be written as

$$\begin{aligned}&\kappa\frac{\partial\theta}{\partial r}+k_{stat}\left(\theta-\theta_0\right)=0, \quad \text{or}\\ &\frac{\partial\theta}{\partial r}+\mathscr{F}_1\left(\theta-\theta_0\right)=0,\end{aligned} \tag{11.8}$$

with $\mathscr{F}_1=\dfrac{k_{stat}}{\kappa}$. k_{stat} can be referred to as the surface conductance or the heat exchange coefficient. As $\mathscr{F}_1 \to 0$ then, no flux across the surface, i.e., $\dfrac{\partial\theta}{\partial r}=0$ and as $\mathscr{F}_1 \to \infty$, temperature may be constant, or a function of time, or position, or both.

11.3 Heat generation within an infinite cylinder

For the initial condition, when $t = 0$ then $\theta(r,t) = \theta_0$, which is a constant initial surrounding temperature over the cross section. For $t > 0$ with $\mathscr{D}^m$ = constant, the resulting partial

differential equation after applying the boundary condition can be written as

$$\theta(r,t) = \theta_0 + \underbrace{\frac{\mathscr{D}^m \cdot r_s^2}{4 \cdot \kappa}\left(1 - \frac{r^2}{r_s^2} + \frac{2}{r_s \cdot \mathscr{F}_1}\right)}_{①} - \underbrace{\frac{2 \cdot \mathscr{F}_1 \cdot \mathscr{D}^m}{r_s \cdot \kappa} \sum_{n=1}^{\infty} e^{-\varsigma \cdot c_n^2 \cdot t} \frac{J_0(r \cdot c_n)}{c_n^2 \left(\mathscr{F}_1^2 + c_n^2\right) J_0(r_s \cdot c_n)}}_{②}, \tag{11.9}$$

where c_n with n = 1,2,... are the positive square roots of the function $c \cdot J_1(r_s \cdot c) - \mathscr{F}_1 \cdot J_0(r_s \cdot c) = 0$ and J_n are Bessel functions of order n and can be written as

$$J_n(z) = \sum_{i=0}^{\infty} \frac{-1^i \left(\frac{z}{2}\right)^{n+2\,i}}{i!\ (n+i)!}. \tag{11.10}$$

The ① in Eq.(11.9) refers to the maximum temperature that has developed in the material during loading due to self heating and it depends on power of dissipation $\mathscr{D}^m$ and radius r and it does not depend on time, where as ② refers to the heat loss over time and this part is derived in the next section.

11.4 Heat loss through surface

The Eq.(11.11) for the case of heat loss through surface due to heat flux can be writte as

$$\dot{\theta} = \frac{1}{\varsigma}\left(\frac{\partial^2 \theta}{\partial r^2} + \frac{1}{r}\frac{\partial \theta}{\partial r}\right) \qquad for \quad 0 < r < r_s \tag{11.11}$$

with $\mathscr{D}^m = 0$.

If the circular cylinder is considered with an initial temperature $\vartheta(r)$,

$$\theta(r,t) = \frac{2}{r_s^2} \sum_{n=1}^{\infty} e^{-\varsigma \cdot c_n^2 \cdot t} \frac{c_n^2 \cdot J_0(r \cdot c_n)}{\left(\mathscr{F}_1^2 + c_n^2\right) J_0^2(r_s \cdot c_n)} \int_0^{r_s} r \cdot \vartheta(r) \cdot J_0(r \cdot c_n)\, dr \tag{11.12}$$

By considering $\vartheta(r) = \vartheta \equiv$ constant, then a simple solution of Eq.(11.12) can be written as

$$\theta(r,t) = \frac{2 \cdot \mathscr{F}_1 \cdot \vartheta}{r_s} \sum_{n=1}^{\infty} e^{-\varsigma \cdot c_n^2 \cdot t} \frac{J_0(r \cdot c_n)}{\left(\mathscr{F}_1^2 + c_n^2\right) J_0(r_s \cdot c_n)} \tag{11.13}$$

By writing $\beta_n = r_s \cdot c_n$, $\mathscr{T} = \dfrac{\varsigma \cdot t}{r_s^2}$ and $\mathscr{F}_2 = r_s \cdot \mathscr{F}_1$, in order to introduce dimensionless quantities, the Eq.(11.13) can be rewritten as

$$\theta(r,t) = 2 \cdot \mathscr{F}_2 \cdot \vartheta \sum_{n=1}^{\infty} e^{-\beta_n^2 \cdot \mathscr{T}} \frac{J_0\left(\frac{r \cdot \beta_n}{r_s}\right)}{\left(\mathscr{F}_2^2 + \beta_n^2\right) J_0(\beta_n)}, \tag{11.14}$$

where β_n with n = 1,2,... are the positive square roots of the function $\beta \cdot J_1(\beta) - \mathscr{F}_2 \cdot J_0(\beta) = 0$. The first six roots, β_n are provided in ***Appendix IV, Table III*** of Carslaw and Jaeger [1959].

11.5 Temperature measurement

Surface and core temperatures of the measured sample were captured using infrared thermo camera. Two sets of experiments were conducted to measure these temperatures. Surface temperature was recorded during the cyclic loading test as in Fig.11.1. As the sample failed after 690s, the results only upto this time have been displayed in Fig.11.7. The temperature profile on the surface of sample along it's length is given in Fig.11.8. This profile can be compared with the numerical simulation result in Fig.10.21.

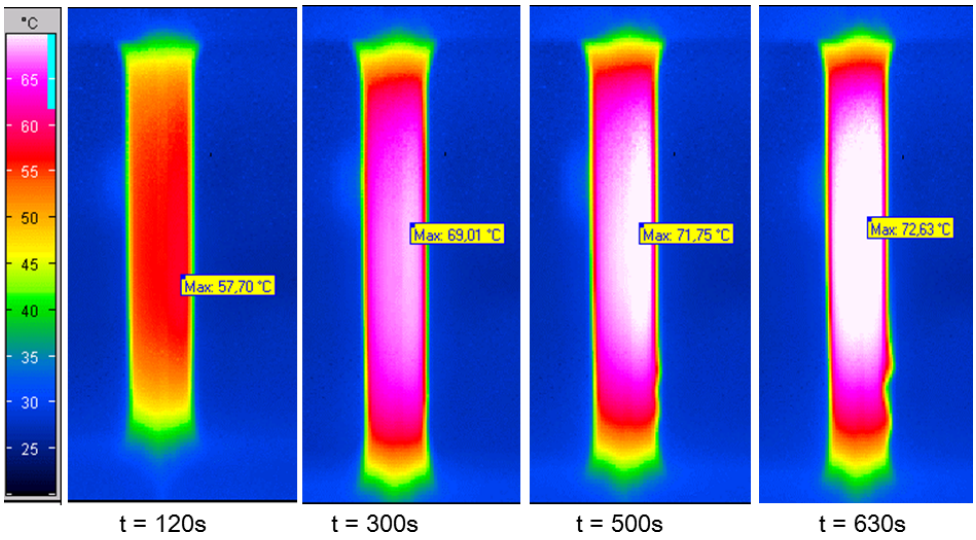

Figure 11.7: Measured surface temperatures during cyclic loading in Fig.11.1.

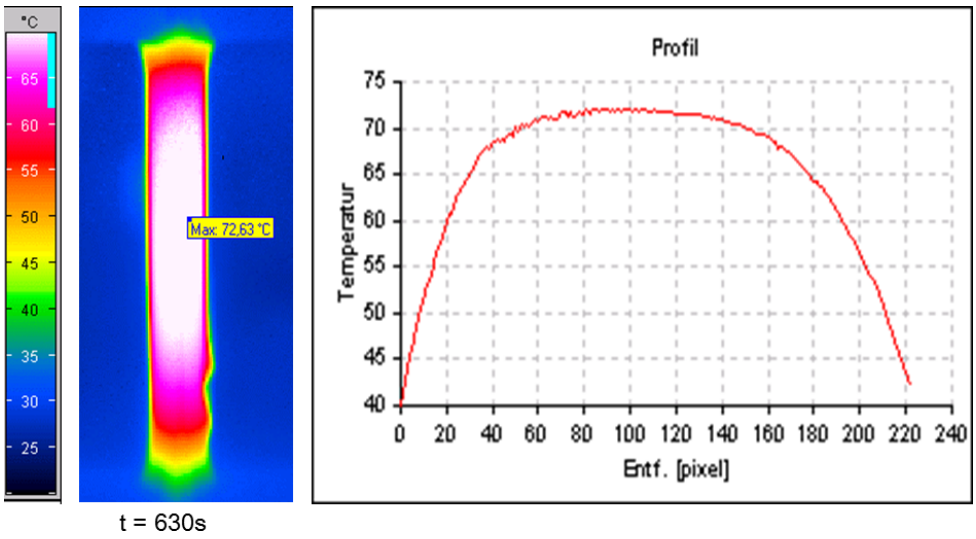

Figure 11.8: Surface temperature profile measured along the length of dumbbell sample.

For measuring the core temperature another measurement was carried out till 300s and then the sample was cut in the middle. 16 pictures were taken per second for about 5min. The temperature picture of cut sample in Fig.11.9 which was captured as soon as the sample was cut shows the max. temperature at the centre of temperature isotherms and it is about 85.81°C. The temperature profile can be compared with the numerical simulation result in Fig.10.21.

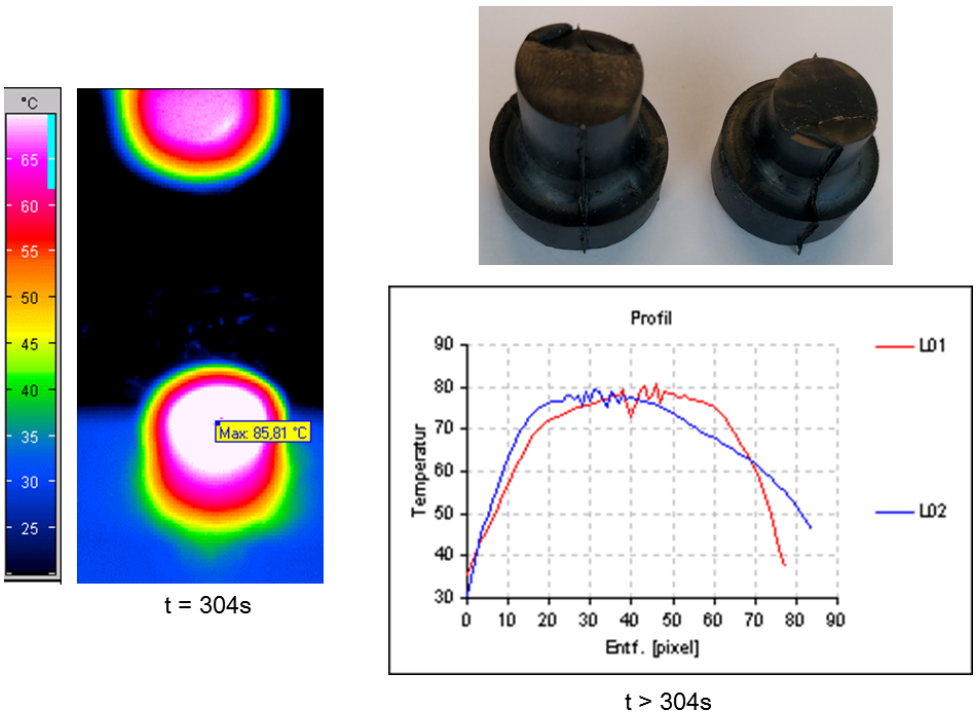

Figure 11.9: Measured core temperature at the cut section after $300s$ of cyclic loading and the temperature profiles along vertical direction ($L01$) and horizontal direction ($L02$).

Table 11.2: Parameters used for the simulation of heat generation.

C_p	ρ	ς	κ
$J/(tonne\,K)$	mm^3	mm^2/s	$W/(mm\,K)$
1.52 x 10^6	1.1 x 10^{-9}	0.1339	0.22 x 10^{-3}

11.6 Simulation results

The model was programmed in Matlab. The program includes calculation of effective volume of sample, energy dissipation and corresponding power from the dynamic cyclic test. Input parameters are taken from the experiments mentioned in the chapter ***Experiments*** and are highlighted in Tab.11.2. One input parameter that was identified during simulation was the temperature exchange coefficient k_{stat}. This parameter is not directly measurable or one can say that a measurement method is not yet established. Hence this parameter has to be identified from the curve fit procedure. During the simulation this value was varied to fit the simulated curve to that of surface temperature measurement by infrared camera in Fig.11.10. The estimated value of k_{stat} is given in Tab.11.3. The identified value of k_{stat} is also used in the numerical simulation.

The Fig.11.10 shows measured surface temperature and the fit curve. The temperature estimation agrees very well with the measured data by adjusting the value of k_{stat}. After estimating the tendency of temperature change over the surface, the core temperature was simulated and was compared to the measured core temperature which is as shown in Fig.11.11. The simulated result is over estimated compared to the measured value because the measured core temperature is not accurate. Even a similar experimental inaccuracy is mentioned in Fritzsche and Klüppel [2011b] where the core temperature was measured by using temperature sensor. In that work, the deviation in results of investigated compounds is about $2-10°C$. In our case the difference

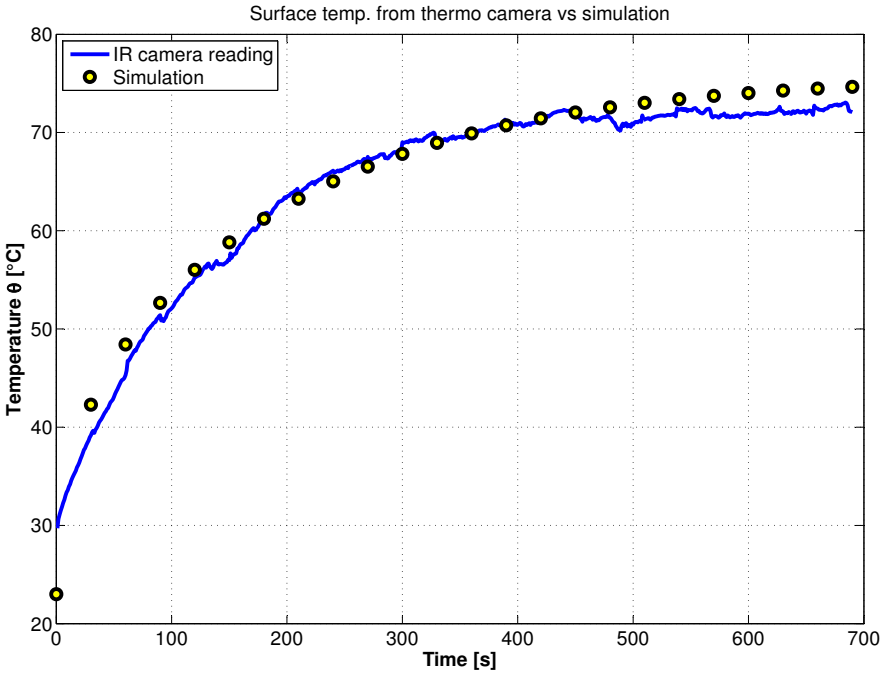

Figure 11.10: Estimation of surface temperature.

Table 11.3: Estimated value of heat exchange coefficient k_{stat} and comparison of surface and core temperatures of simulation and experiment.

	Heat exch. coeff. k_{stat}	Initial temp. θ_0	time t	Surface temp. θ_s	Core temp. θ_c	Temp. diff. $\Delta\theta$
	$W/(mm^2\,K)$	$°C$	s	$°C$	$°C$	$°C$
Simulation	47 x 10^{-6}	23	≈ 300	68	90.5	22.5
Experiment		23	≈ 300	69	85.81	16.81

is about $4-5$°C. Considering this point into account and the uncertainty of the measurement, the simulated result can be regarded as reasonable. The temperature difference between core and surface is given in Tab.11.3 and the deviation compared to experiment is around 5.5°C and is largely due to inaccurate measured core temperature.

Fig.11.12 shows the simulated temperature profile at different times along the radial direction of sample. At time $t = 0$, the temperature over the radius is constant i.e., θ_0 and when $t > 0$, temperature starts increasing. The simulated temperature profile till 180°C is strange because the core temperature is cooler than the surface temperature. Also the increase of surface temperature is faster compared to core temperature (Fig.11.13) and in the Fig.11.14 we can see that the heat loss profile at the surface is different to that of core where the temperature decrease is not exponential during short time loading. Despite, the temperature profile beyond 180°C is reasonable where the maximum temperature is more pronounced at the centre of the sample (r=0). Although the reason is not completely clear, this can be either due to the limitations of the model in short time scale or may be due to wrong implementation.

Fig.11.13 shows heating of material during loading. The temperature gradient is high in the

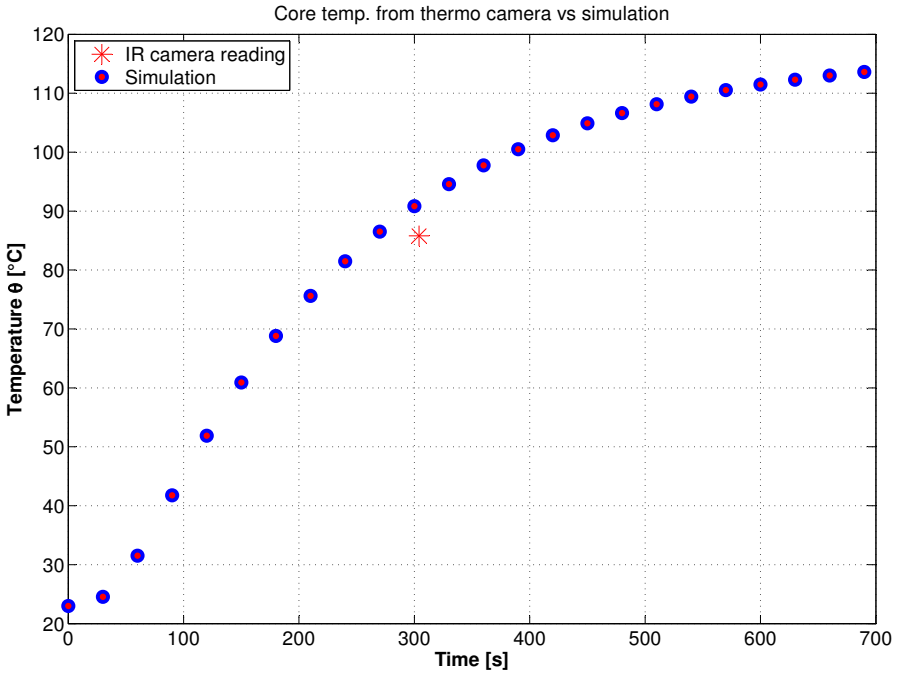

Figure 11.11: Simulation of core temperature.

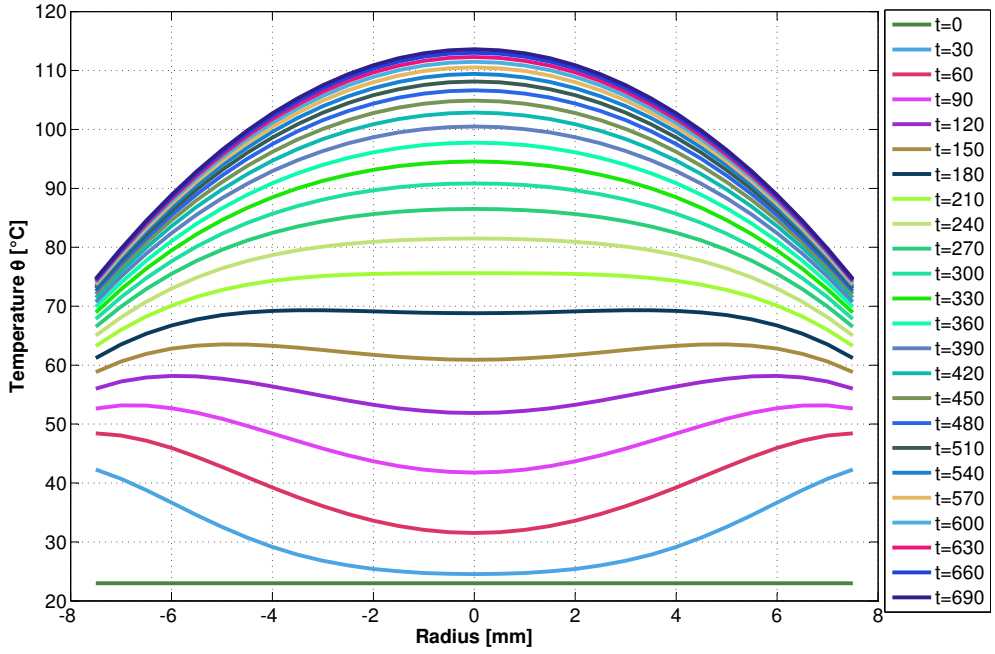

Figure 11.12: Time-dependent temperature profile over radius of sample.

short times of loading and then the gradient decreases over time till the temperature reaches plateau due to balance of energy dissipation and the heat flux trough surface. The heat loss graph in the Fig.11.14 shows the exponential decrease of sample temperature to the surrounding

or the initial temperature θ_0.

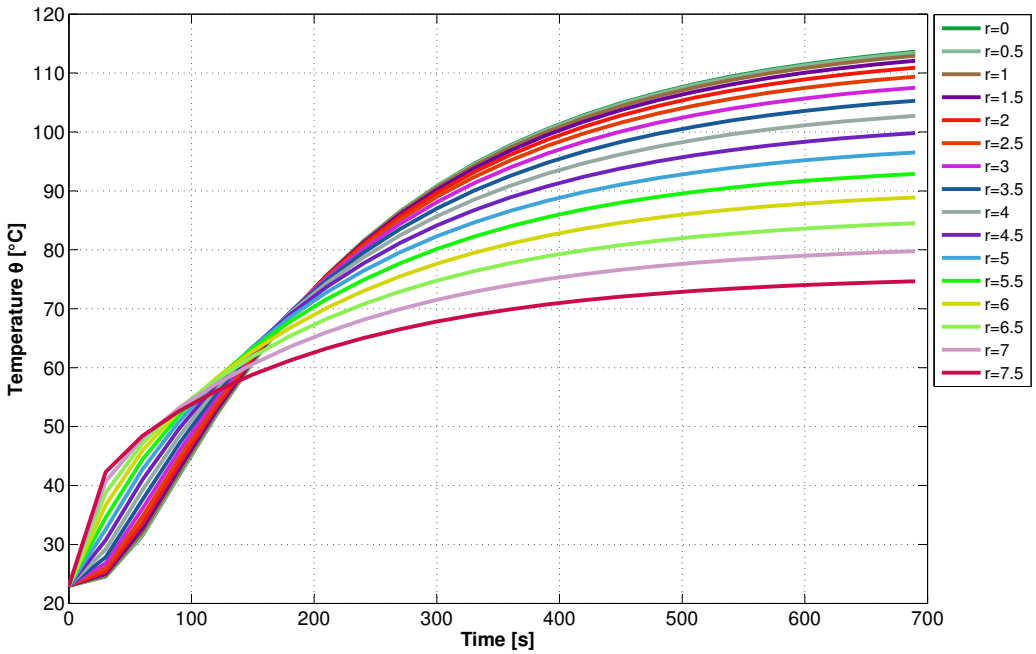

Figure 11.13: Temperature increase due to heating over time along the radius of sample.

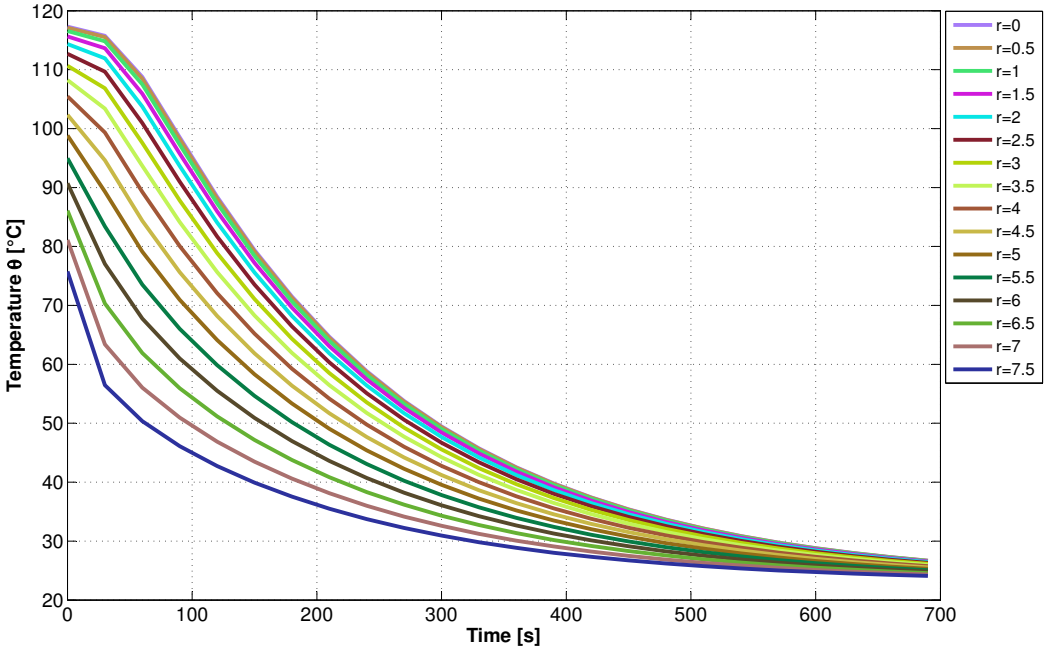

Figure 11.14: Heat loss over time along the radius of sample.

Chapter 12

Summary and outlook

The earlier works on Dynamic Flocculation Model (DFM) which are highlighted in the foregone chapters have exhibited the ability of microstructure-based model to describe various inelastic effects that a conventional hyperelastic model can not. The model describes the phenomena like hydrodynamic reinforcement of rubber elasticity and stress softening effect by means of strain amplification caused by stiff cluster bonds. The filler induced hysteresis of reinforced elastomers is due to breakdown and re-aggregation of filler clusters has been introduced using an integral over the damaged section of the cluster size distribution. The material parameters of DFM are interpreted as real physical quantities which help the model to reproduce the quasi-static stress/strain behaviour for the given strain deformation. The one dimensional constitutive model which is implemented into FE program using the concept of representative directions allows the user to simulate complex components, visualise the effects exerted by the loading and understand the shortcomings that can be improved later in further development. Virtual component development using material models such as DFM shortens the development time along with better approximation of actual problems.

The prediction of time-dependent effects using extended micro-mechanical DFM shows good agreement with the experiments displaying its ability to reproduce the deformation behaviour with time and strain rate as well as amplitude dependency using time-dependent parameters of damaged cluster strength $s_d(t)$ and the virgin cluster strength $s_v(t)$, under multi modal deformation histories. The evolution equation realised to include the time-dependent effects into the model is simple. As its concept is related to the filler induced rupture and recovery of so-called cluster bridges, the relaxation function is considered to be physically reasonable. Although the time-dependent material parameter characterisation was done mainly on uniaxial tension, the material model reproduces the material behaviour in shear mode as well. Below critical strain the extended DFM describes the reversible softening phenomenon observed during amplitude dependency (Payne effect) with minimal error.

The quasi-static and viscoelastic DFM was isothermal and simulating the mechanical response to the variation in temperature was not possible. Hence there was a scope to extend the model further to include the temperature effects and also coupling of temperature-mechanical response of the material. From the DMA master curve it was observed that in the rubber-elastic plateau, the temperature dependence of the material behaviour is dominated by that of filler network. Accordingly, Arrhenius-like thermal activation of strength of filler cluster bonds are used to describe the temperature effects. From the previous works it was observed that, describing only the strength of filler cluster bonds as temperature dependent is not sufficient to get the reasonable

material behaviour due to the absence of entropy-elastic effects of rubber matrix in the model. Therefore in addition to that, the moduli of rubber matrix are also considered to be temperature dependent. Although a physically motivated solution was not obtained, their phenomenological solutions were necessary to capture the tendency. The permanent set behaviour is taken into account empirically by a simple analytical function depending on temperature change and glass transition temperature θ_g. The simulation of thermo-hyperelastic DMA showed a good agreement with temperature controlled quasi-static experiments.

For thermo-viscoelasticity, from the time-temperature superposition principle, the Arrhenius-like dependence of filler-filler bonds with respect to change in temperature is considered by using temperature-dependent relaxation time $\tau(\theta)$. Despite deviation in simulated results of thermo-viscoelastic prediction, model was able to demonstrate the change in stiffness, hysteresis and set stress with respect to temperature change. The coupled temperature-displacement simulations using Zener model shows the self-heating of rubber due to energy dissipation. Although the results are not supported by any experiment, as a reference the results like temperature difference between core and surface and the temperature profiles can be compared to the measurements of infrared camera. Finally the analytical simulation to estimate core and surface temperature of cylindrical sample matches very well with the data and pictures recorded by infrared thermo camera. The temperature profile in short times are not well represented by the analytical model and the reason may be due to the functional abnormality or due to the parameters that are still not well characterised.

As the fully coupled thermo-viscoelastic DFM requires entropy contribution of filler clusters that is not yet included in the formulation due to unavailable quantities to fulfil the balance equations, there is a scope in the future work to couple the response of thermo-mechanical behaviour. In parallel to what DFM is developed on, there are also papers contributing on developing physical models with different approaches. A remark can also be added here concerning strain amplification factor where, Domurath et al. [2012] refers to the violation of energy conservation law which contradicts the approach of amplification factor on local strain field. The hydrodynamic amplification factor X which is multiplied to the strain is much higher than the amplification factor proposed by Einstein [1906] and Smallwood [1945] and it leads to an unequal macroscopic and microscopic energy dissipations. Accordingly an approach is under way for the DFM with a recent work in progress by Plagge and Klüppel [2016] which makes use of stress and strain amplification approach in agreement with Domurath et al. [2012]. The resulting modified DFM describes stress-softening and hysteresis in uniaxial tension which is similar to the existing DFM and the other viscoelastic effects like rate-dependent stress relaxation and thermo-viscoelasticity are the future works. The compatibility of FE implementation of such a model based on convolution mechanism is yet to be checked and therefore the work in this direction is yet to be progressed.

The joint project called *LORRY* an acronym given for LOw Rolling Resistance tYre, involves group of institutions around Europe for a collective development of commercial tyre for heavy duty vehicles. This includes the development of so-called CD Tire model which is a thermo-mechanical tire model from Fraunhofer ITWM, Kaiserslautern for full tyre simulation. This makes use of a material model to predict the temperature creation and propagation and then its effect on rolling resistance. This so-called CD Tire is a complete 3D shell based model for tread layer, steel cord layer, carcass layer, rubber layer and inflation pressure. For the tyre tread, a visco-elasto-plastic material model has been considered to calculate the temperature using dissipated energy into heat. A earlier proposal was to replace this phenomenological model with

a more realistic physical model such as DFM. However as DFM is not completely coupled for thermo-mechanical analysis, the future work can also consider the task to connect this missing link.

Bibliography

J. Aboudi. Micromechanics-based thermoviscoelastic constitutive equations for rubber-like matrix composites at finite strains. *International Journal of Solids and Structures*, 41:5611–5629, 2004. doi:10.1016/j.ijsolstr.2004.04.039.

A.F.M.S. Amin, A. Lion, S. Sekita, and Y. Okui. Nonlinear dependence of viscosity in modeling the rate-dependent response of natural and high damping rubbers in compression and shear: Experimental identification and numerical verification. *International Journal of Plasticity*, 22: 1610–1657, 2006. doi:10.1016/j.ijplas.2005.09.005.

L. Anand, N. M. Ames, V. Srivastava, and S. A. Chester. A thermo-mechanically-coupled theory for large deformations of amorphous polymers. part i: formulation. *International Journal of Plasticity*, 25:1474–1494, 2009. doi:10.1016/j.ijplas.2008.11.004.

D. Balzani, A. Gandhi, M. Tanaka, and J Schröder. Numerical calculation of thermo-mechanical problems at large strains based on complex step derivative approximation of tangent stiffness matrices. *Computational Mechanics*, 55:861–871, 2015. doi:10.1007/s00466-015-1139-0.

R. Behnke, H. Dal, and M. Kaliske. An extended tube model for thermo-viscoelasticity of rubber-like materials: Theory and numerical implementation. *Constitutive Models for Rubber VII*, pages 87–92, 2012.

J. Bergstrom and M. Boyce. Constitutive modeling of the large strain time-dependent behavior of elastomers. *Journal of the Mechanics and Physics of Solids*, 46:931–954, 1998. doi:10.1016/S0022-5096(97)00075-6.

N. Billon. New constitutive modeling for time-dependent mechanical behavior of polymers close to glass transition: Fundamentals and experimental validation. *Journal of Applied Polymer Science*, 125(6):4390–4401, 2012. doi:10.1002/app.36598.

J. Bonet and R. D. Wood. *Nonlinear Continuum Mechanics for Finite Element Analysis*. Cambridge University Press, 2 edition, 2008. URL http://klancek.si/sites/default/files/datoteke/files/bonet-woodnonlinearcontinuummechanics2ndedition.pdf.

A. Boukamel, S. Méo, O. Débordes, and M. Jaeger. A thermo-viscoelastic model for elastomeric behaviour and its numerical application. *Archive of Applied Mechanics*, 71:785–801, 2001. doi:10.1007/s004190100191.

H. S. Carslaw and J. C. Jaeger. *Conduction of heat in solids*. Oxford Science Publication, 2 edition, 1959. URL https://www.scribd.com/doc/63559781/Carslaw-and-Jaeger-Conduction-of-Heat-in-Solids-1959-ISBN-0198533683.

D. Christ and S. Reese. A finite element model for shape memory alloys considering thermo-

mechanical couplings at large strains. *International Journal of Solids and Structures*, 46: 3694–3709, 2009. doi:10.1016/j.ijsolstr.2009.06.017.

B. Dippel, M. Johlitz, and A. Lion. Thermo-mechanical couplings in elastomers - experiments and modelling. *Zeitschrift für Angewandte Mathematik und Mechanik (ZAMM)*, 95:1117–1128, 2014. doi:10.1002/zamm.201400110.

J. Domurath, M. Saphiannikova, G. Ausias, and G. Heinrich. Modelling of stress and strain amplification effects in filled polymer melts. *Journal of Non-Newtonian Fluid Mechanics*, 171–172:8–16, 2012. doi:http://dx.doi.org/10.1016/j.jnnfm.2012.01.001.

J.B. Donnet. Nano and microcomposites of polymers elastomers and their reinforcement. *Composites Science and Technology*, 63:1085–1088, 2003. doi:10.1016/S0266-3538(03)00028-9.

S.F. Edwards and T. Vilgis. The effect of entanglements in rubber elasticity. *Polymer*, 27(4): 483–492, 1986. doi:10.1016/0032-3861(86)90231-4.

F. Ehrburger-Dolle, I. Morfin, F. Bley, F. Livet, G. Heinrich, S. Richter, L. Piche, and M. Sutton. Xpcs investigation of the dynamics of filler particles in stretched filled elastomers. *Macromolecules*, 45(21):8691–8701, 2012. doi:10.1021/ma3013674.

A. Einstein. Eine neue bestimmung der moleküldimensionen. *Ann. Phys.*, 19:289–306, 1906. doi:10.1002/andp.19063240204.

L. J. Fetters, D. J. Lohse, D. Richter, T. A. Witten, and A. Zirkel. Connection between polymer molecular weight, density, chain dimensions, and melt viscoelastic properties. *Macromolecules*, 27(17):4639–4647, 1994. doi:10.1021/ma00095a001.

M. Freund and J. Ihlemann. Generalization of one-dimensional material models for the finite element method. *Zeitschrift für Angewandte Mathematik und Mechanik (ZAMM)*, 90:399–417, 2010. doi:10.1002/zamm.200900352.

M. Freund, H. Lorenz, D. Juhre, J. Ihlemann, and M. Klüppel. Finite element implementation of a microstructure based model for filled elastomers. *International Journal of Plasticity*, 27: 902–919, 2011. doi:10.1016/j.ijplas.2010.10.003.

J. Fritzsche and M. Klüppel. Structural dynamics and interfacial properties of filler-reinforced elastomers. *Journal of Physics: Condensed Matter*, 23, 2011a. doi:10.1088/0953-8984/23/3/035104.

J. Fritzsche and M. Klüppel. Simulation of the internal sample temperature of rubber components during cyclic deformation. *Kautschuk Gummi Kunststoffe*, 64(6):44–51, 2011b. URL https://www.researchgate.net/publication/288454100_Simulation_of_the_internal_sample_temperature_of_rubber_components_during_cyclic_deformation_authors.

J. Fröhlich, W. Niedermeier, and H.-D. Luginsland. The effect of filler-filler and filler-elastomer interaction on rubber reinforcement. *Composites: Part A*, 36:449–460, 2005. doi:10.1016/j.compositesa.2004.10.004.

V. A. Froltsov, M. Klüppel, and G. Raos. Molecular dynamics simulation of rupture in glassy polymer bridges within filler aggregates. *Physical review E*, 86:041801, 2012. doi:10.1103/PhysRevE.86.041801.

K. A. Grosch. Abrasion of rubber and its relation to tire wear. *Rubber chemistry and technology*, 65:78–106, 1992. doi:http://dx.doi.org/10.5254/1.3538609.

K. A. Grosch. The rolling resistance, wear and traction properties of tread compounds. *Rubber chemistry and technology*, 69:495–568, 1996. doi:10.5254/1.3538383.

K. A. Grosch. Goodyear medalist lecture. rubber friction and its relation to tire traction. *Rubber chemistry and technology*, 80:379–411, 2007. doi:http://dx.doi.org/10.5254/1.3548172.

G. R. Hamed and S. Hatfield. On the role of bound rubber in carbon black reinforcement. *Rubber chemistry and technology*, 62(1):143–156, 1989. doi:http://dx.doi.org/10.5254/1.3538213.

P. Haupt. *Continuum Mechanics and Theory of Materials*. Springer-Verlag Berlin Heidelberg, 2002. URL http://www.springer.com/de/book/9783540431114.

P. Haupt and A. Lion. On finite linear viscoelasticity of incompressible isotropic materials. *Acta Mechanica*, 159:87–124, 2002. doi:10.1007/BF01171450.

G. Heinrich, E. Straube, and G. Helmis. Rubber elasticity of polymer networks: theories. *Adv. Polym. Sci.*, 85:33–87, 1988. doi:10.1007/BFb0024050.

P. Höfer and A. Lion. Modelling of frequency-and amplitude-dependent material properties of filler-reinforced rubber. *Journal of the Mechanics and Physics of Solids*, 57:500–520, 2009. doi:10.1016/j.jmps.2008.11.004.

G. A. Holzapfel. *Nonlinear Solid Mechanics: A Continuum Approach for Engineering*. John Wiley & Sons, Inc., 2000. URL http://eu.wiley.com/WileyCDA/WileyTitle/productCd-0471823198.html.

G. Huber and T. A. Vilgis. Universal properties of filled rubbers: mechanisms for reinforcement on different length scales. *Kautschuk Gummi Kunststoffe (KGK)*, 52:102–107, 1999.

J. Ihlemann. Kontinuumsmechanische nachbildung hochbelasteter gummiwerkstoffe. *In: Fortschr.-Ber. VDI Reihe. VDI Verlag.*, 18(288), 2003.

M. Johlitz, B. Dippel, and Alexander Lion. Dissipative heating of elastomers: a new modelling approach based on finite and coupled thermomechanics. *Continuum Mechanics and Thermodynamics*, 28:1111–1125, 2015. doi:10.1007/s00161-015-0469-7.

A. R. Johnson and C. J. Quigley. A viscohyperelastic maxwell model for rubber viscoelasticity. *Rubber Chemistry and Technology*, 65:137–153, 1992. doi:10.5254/1.3538596.

D. Juhre. Basics of continuum mechanics (academic lecture script), technical university of braunschweig, 1-97., 2010.

D. Juhre, R. Raghunath, M. Klüppel, and H. Lorenz. A microstructure-based model for filled elastomers including time-dependent effects. *Proceedings of the 8th European Conference on Constitutive Models for Rubbers, ECCMR. Constitutive Models for Rubber*, VIII:293–298, 2013. doi:10.1201/b14964-53.

M. Kaliske and G. Heinrich. A formulation of rubber elasticity and viscoelasticity with damage for finite element simulations. *Kautschuk Gummi Kunststoffe (KGK)*, 53:110–117, 2000.

Y. Kantor and I. Webman. Elastic properties of random percolating systems. *Phys Rev Lett*, 52: 1891–1894, 1984. doi:10.1103/PhysRevLett.52.1891.

M. Klüppel. The role of disorder in filler reinforcement of elastomers on various length scales. *Advances in Polymer Science*, 164:1–86, 2003. doi:10.1007/b11054.

M. Klüppel and J. Schramm. A generalized tube model for rubber elasticity and stress softening of filler reinforced elastomer systems. *Macromol. Theory Simul.*, 9:742–754, 2000. doi:10.1002/1521-3919(20001201)9:9<742::AID-MATS742>3.0.CO;2-4.

M. Klüppel, R. H. Schuster, and G. Heinrich. Structure and properties of reinforcing fractal filler networks in elastomers. *Rubber Chem. Technol.*, 70:243, 1997. doi:10.5254/1.3538429.

M. Klüppel, H. Menge, H. Schmidt, H. Schneider, and R. H. Schuster. Influence of preparation conditions on network parameters of sulfur cured natural rubber. *Macromolecules*, 34(23): 8107–8116, 2001. doi:10.1021/ma010490v.

M. Klüppel, J. Meier, and M. Dämgen. Modeling of stress softening and filler induced hysteresis of elastomer materials. *Constitutive Models for Rubber IV*, pages 171–177, 2005.

S. Kohjiya, A. Katoh, T. Suda, J. Shimanuki, and Y. Ikeda. Visualisation of carbon black networks in rubbery matrix by skeletonisation of 3d-tem image. *Polymer*, 47(10):3298–3301, 2006. doi:10.1016/j.polymer.2006.03.008.

G. (ed.) Kraus. *Reinforcement of elastomers*, volume 6. Interscience, New York, 1965. doi:10.1002/pol.1968.150061129.

N. H. Kröger, R. Raghunath, and D. Juhre. Extension of dfm and morph in representative directions to viscous effects via prony series approach. *Proceedings in Applied Mathematics and Mechanics (PAMM*, 16(1):363–364, 2016. doi:10.1002/pamm.201610170.

L. Laiarinandrasana, R. Piques, and A. Robisson. Visco-hyperelastic model with internal state variable coupled with discontinuous damage concept under total lagrangian formulation. *International Journal of Plasticity*, 19:977–1000, 2003. doi:10.1016/S0749-6419(02)00089-X.

Jean L. Leblanc. Rubber-filler interactions and rheological properties in filled compounds. *Prog. Polym. Sci.*, 27:627–687, 2002. doi:10.1016/S0079-6700(01)00040-5.

C. Lin and Y. Lee. Strain-dependent dynamic properties of filled rubber network systems. *Macromol. Theory Simul.*, 5(6):1075–1104, 1996. doi:10.1002/mats.1996.040050605.

C. Lin and Y. Lee. Strain-dependent dynamic properties of filled rubber network systems, 2: The physical meaning of pparameter in the l-n-b model and their applicability. *Macromol. Theory Simul.*, 6(2):339–350, 1997. doi:10.1002/mats.1997.040060203.

A. Lion. Constitutive modelling in finite thermoviscoplasticity: A physical approach based on nonlinear rheological models. *International Journal of Plasticity*, 16:469–494, 2000. doi:10.1016/S0749-6419(99)00038-8.

A. Lion. Phenomenological modelling of strain-induced structural changes in filler-reinforced elastomers. *Kautschuk Gummi Kunststoffe (KGK)*, 58(4):157–162, 2005. URL `http://www.neue-verpackung.de/ai/resources/409e86f2472.pdf`.

A. Lion and C. Kardelky. The payne effect in finite viscoelasticity: constitutive modelling based on fractional derivatives and intrinsic time scales. *International Journal of Plasticity*, 20: 1313–1345, 2004. doi:10.1016/j.ijplas.2003.07.001.

A. Lion, J. Retka, and M. Rendek. On the calculation of predeformation-dependent dynamic modulus tensors in finite nonlinear viscoelasticity. *Mechanics Research Communications*, 36: 653–658, 2009. doi:10.1016/j.mechrescom.2009.02.005.

V.M. Litvinov, R.A. Orza, M. Klüppel, M. van Duin, and P.C.M.M. Magusin. Rubber-filler interactions and network structure in relation to stress-strain behavior of vulcanized, carbon black filled epdm. *Macromolecules*, 44(12):4887–4900, 2011. doi:10.1021/ma2007255.

H. Lorenz. *Mikrostruktur-basierte Modellierung des mechanischen Verhaltens gefüllter Elastomere*. PhD thesis, Department of Mechanical Engineering, Technical University of Dresden, 2012.

H. Lorenz and M. Klüppel. Microstructure based modeling of arbitrary deformation histories of filler-reinforced elastomers. *Journal of the Mechanics and Physics of Solids*, 60:1842–1861, 2012. doi:10.1016/j.jmps.2012.06.013.

H. Lorenz, M. Freund, D. Juhre, J. Ihlemann, and M. Klüppel. Constitutive generalization of a microstructure based model for filled elastomers. *Macromolecular Theory and Simulations*, 20:110–123, 2011. doi:10.1002/mats.201000054.

H. Lorenz, M. Klüppel, and G. Heinrich. Microstructure-based modelling and fe implementation of filler-induced stress softening and hysteresis of reinforced rubbers. *Zeitschrift für Angewandte Mathematik und Mechanik (ZAMM)*, 92(8):608–631, 2012. doi:10.1002/zamm.201100172.

H. Luo, M. Klüppel, and H. Schneider. Study of filled sbr elastomers using nmr and mechanical measurements. *Macromolecules*, 37(21):8000–8009, 2004. doi:10.1021/ma035985u.

J.M. Martinez, A. Boukamel, S. Méo, and S. Lejeunes. Statistical approach for a hyper-visco-plastic model for filled rubber: Experimental characterization and numerical modeling. *European Journal of Mechanics A/Solids*, 30:1028–1039, 2011. doi:10.1016/j.euromechsol.2011.06.013.

B. Marvalova. Viscoelastic properties of filled rubber. experimental observations and material modelling. *Engineering Mechanics*, 14(1/2):81–89, 2007. URL `http://www.engineeringmechanics.cz/pdf/14_1_081.pdf`.

J. G. Meier, J. Mani, and M. Klüppel. Analysis of carbon black networking in elastomers by dielectric spectroscopy. *Physical review B*, 75:054202, 2007. doi:10.1103/PhysRevB.75.054202.

C. Miehe and S. Göktepe. A micro-macro approach to rubber-like materials. part ii: The micro-sphere model of finite rubber viscoelasticity. *Journal of the Mechanics and Physics of Solids*, 53:2231–2258, 2005. doi:10.1016/j.jmps.2005.04.006.

C. Miehe, S. Göktepe, and F. Lulei. A micro-macro approach to rubber-like materials-part i: the non-affine micro-sphere model of rubber elasticity. *Journal of the Mechanics and Physics of Solids*, 52:2617–2660, 2004. doi:10.1016/j.jmps.2004.03.011.

E. L. Mullins and N. R. Tobin. Stress softening in rubber vulcanizates, part i. *Journal of Applied Polymer Science*, 9:2993, 1965. doi:10.1002/app.1965.070090906.

C. Naumann and J. Ihlemann. Thermomechanical material behaviour within the concept of representative directions. *Constitutive Models for Rubber VII*, pages 107–112, 2012.

B. Omnes, S. Thuillier, P. Pilvin, Y. Grohens, and S. Gillet. Effective properties of carbon black filled natural rubber: Experiments and modeling. *Composites: Part A*, 39:1141–1149, 2008. doi:10.1016/j.compositesa.2008.04.003.

A. Papon, H. Montes, F. Lequeux, J. Oberdisse, K. Saalwachter, and L. Guy. Solid particles in

an elastomer matrix: impact of colloid dispersion and polymer mobility modification on the mechanical properties. *Soft Matter*, 8:4090–4096, 2012. doi:10.1039/C2SM06885K.

J. Plagge and M. Klüppel. A physically based model of stress softening and hysteresis of filled rubber including rate- and temperature dependency. *International Journal of Plasticity*, 2016. doi:http://dx.doi.org/10.1016/j.ijplas.2016.11.010.

W. Pyckhout-Hintzen, S. Westermann, A. Wischnewski, M. Monkenbusch, and D. Richter. Direct observation of nonaffine tube deformation in strained polymer networks. *Physical review letters*, 110:196002, 2013. doi:10.1103/PhysRevLett.110.196002.

R. Raghunath, D. Juhre, and M. Klüppel. A physically motivated model for filled elastomers including strain rate and amplitude dependency in finite viscoelasticity. *International Journal of Plasticity*, 78:223–241, 2016. doi:10.1016/j.ijplas.2015.11.005.

S. Reese. A micromechanically motivated material model for the thermo-viscoelastic material behaviour of rubber-like polymers. *International Journal of Plasticity*, 19:909–940, 2003. doi:10.1016/S0749-6419(02)00086-4.

S. Reese and S. Govindjee. A theory of finite viscoelasticity and numerical aspects. *International Journal of Solids and Structures*, 35:3455–3482, 1998a. doi:10.1016/S0020-7683(97)00217-5.

S. Reese and S. Govindjee. Theoretical and numerical aspects in the thermo-viscoelastic material behaviour of rubber-like polymers. *Mechanics of Time-Dependent Materials*, 1:357–396, 1998b. doi:10.1023/A:1009795431265.

M. Rendek and A. Lion. Amplitude dependence of filler-reinforced rubber: Experiments, constitutive modelling and fem-implementation. *International Journal of Solids and Structures*, 47: 2918–2936, 2010. doi:10.1016/j.ijsolstr.2010.06.021.

C. O. Rodas, F. Zaïri, and M. Naït-Abdelaziz. Filler effects on the heat build-up of filled rubbers during fatigue: Experimental observations and constitutive modelling. *Constitutive Models for Rubber IX*, pages 173–179, 2015.

H. M. Smallwood. Limiting law of the reinforcement of rubber. *Rubber Chemistry and Technology*, 18(2):292–305, 1945. doi:http://dx.doi.org/10.5254/1.3546730.

E. Smith and H. Garcia. Wheel induced vibrations on heavy vehicles. pages 1–45, 2013. URL `https://www.diva-portal.org/smash/get/diva2:753968/FULLTEXT01.pdf`.

E. Straube, V. Urban, W. Pyckhout-Hintzen, and D. Richter. Sans investigations of topological constraints and microscopic deformations in rubber-elastic networks. *Macromolecules*, 27(26): 7681–7688, 1994. doi:10.1021/ma00104a025.

T.A. Vilgis, G. Heinrich, and M. Klüppel. *Reinforcement of polymer nano-composites: theory, experiments and applications*, volume 12. Cambride University Press, New York, 2009. doi:10.1017/CBO9780511605314.

M. J. Wang, W. J. Patterson, and G. B. Ouyang. Dynamic stress-softening of filled vulcanizates. *Proceedings of the spring ACS rubber division meeting, Montreal*, 1996.

J. A. Weiss. *A constitutive model and finite element representation for transversely isotropic soft tissues*. PhD thesis, University of Utah, 1994. URL `http://mrl.sci.utah.edu/papers/jaw_diss.pdf`.

T. A. Witten, M. Rubinstein, and R. H. Colby. Reinforcement of rubber by fractal aggregates. *J. Phys. II France*, 3:367–383, 1993. doi:10.1051/jp2:1993138.

D. Wollscheid and A. Lion. Predeformation- and frequency-dependent material behaviour of filler-reinforced rubber: Experiments, constitutive modelling and parameter identification. *International Journal of Solids and Structures*, 50:1217–1225, 2013. doi:10.1016/j.ijsolstr.2012.12.015.